# Group IV Epitaxy for Advanced Nano- and Optoelectronic Applications

Stephan Wirths

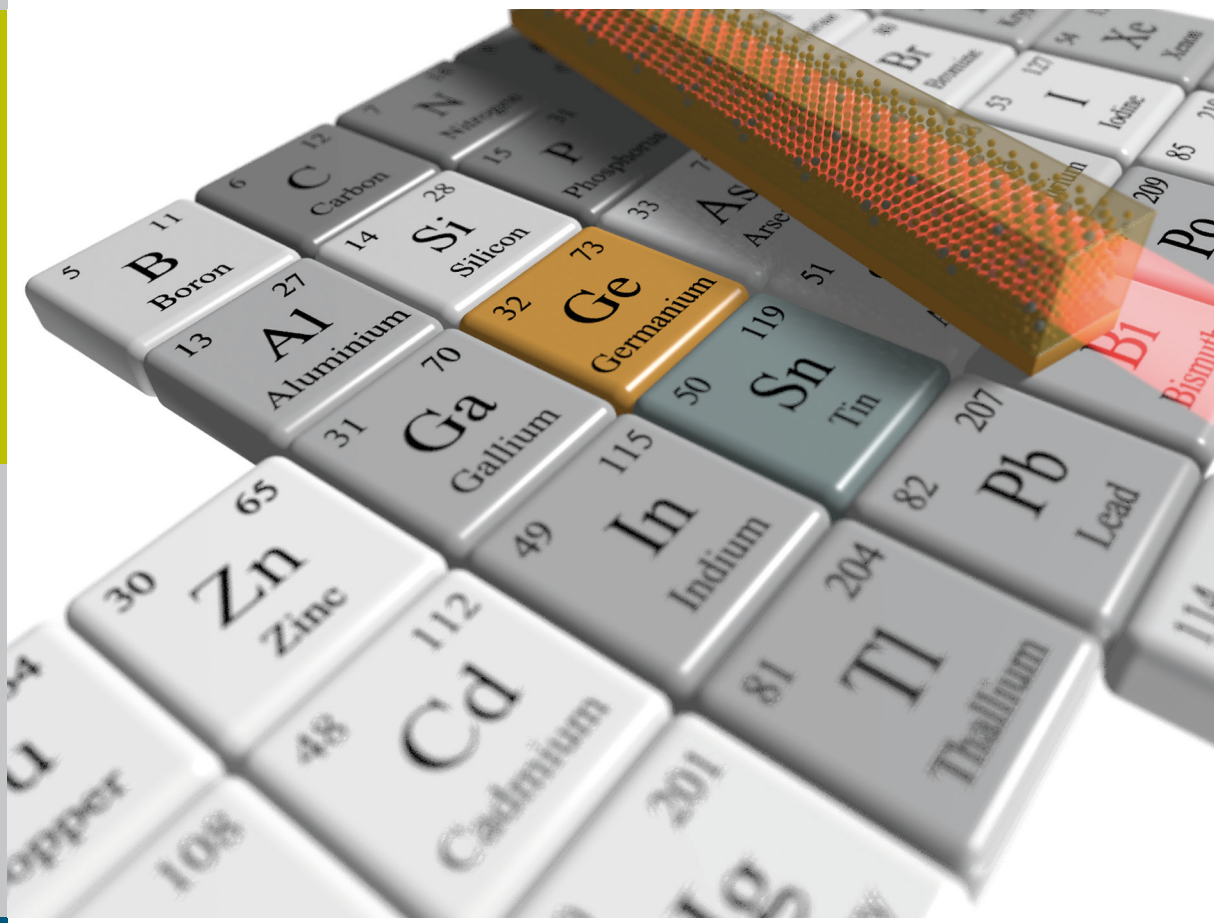


Schlüsseltechnologien / Key Technologies
Band / Volume 123
ISBN 978-3-95806-132-3

JÜLICH
FORSCHUNGSZENTRUM

Schriften des Forschungszentrums Jülich
Reihe Schlüsseltechnologien / Key Technologies Band / Volume 123

Forschungszentrum Jülich GmbH
Peter Grünberg Institute
Semiconductor Nanoelectronics (PGI-9)

# Group IV Epitaxy for Advanced Nano- and Optoelectronic Applications

Stephan Wirths

Schriften des Forschungszentrums Jülich
Reihe Schlüsseltechnologien / Key Technologies Band / Volume 123

ISSN 1866-1807 ISBN 978-3-95806-132-3

Bibliographic information published by the Deutsche Nationalbibliothek.
The Deutsche Nationalbibliothek lists this publication in the Deutsche Nationalbibliografie; detailed bibliographic data are available in the Internet at http://dnb.d-nb.de.

| | |
|---|---|
| Publisher and Distributor: | Forschungszentrum Jülich GmbH<br>Zentralbibliothek<br>52425 Jülich<br>Tel: +49 2461 61-5368<br>Fax: +49 2461 61-6103<br>Email: zb-publikation@fz-juelich.de<br>www.fz-juelich.de/zb |
| Cover Design: | Grafische Medien, Forschungszentrum Jülich GmbH |
| Printer: | Grafische Medien, Forschungszentrum Jülich GmbH |
| Copyright: | Forschungszentrum Jülich 2016 |

Schriften des Forschungszentrums Jülich
Reihe Schlüsseltechnologien / Key Technologies, Band / Volume 123

D 82 (Diss. RWTH Aachen University, 2015)

ISSN 1866-1807
ISBN 978-3-95806-132-3

The complete volume is freely available on the Internet on the Jülicher Open Access Server (JuSER) at www.fz-juelich.de/zb/openaccess.

# Abstract

Sn-based group IV semiconductors have attracted increasing scientific interest during the last decade due to their exciting electronic properties, such as a fundamental direct bandgap or high carrier mobility. Whereas these properties have been predicted already in the early 1980's, the quality of epitaxially grown GeSn and SiGeSn layers on Si and Ge substrates has been limited owing to the low solid solubility of Sn in (Si)Ge ($< 1$ at.%) and the large lattice mismatch ($> 15$ %). Hence, the enormous potential of these material systems regarding their implementation in nano- and optoelectronics has not been exploited to date. A low temperature reduced pressure chemical vapour process using commercially available Ge- and Sn-precursors, namely $Ge_2H_6$ and $SnCl_4$, is developed for the growth of GeSn and SiGeSn epilayers directly on Si(001) and on Ge-buffered Si(001). Sn concentrations far beyond the solid solubility of Sn in (Si)Ge are achieved. High growth rates at low growth temperatures assure exceptionally high monocrystalline quality evidenced by exhaustive layer characterization, i.e. transmission electron microscopy, Rutherford backscattering spectrometry, X-ray diffraction or photoluminescence. Moreover, it is shown that the plastic strain relaxation of these (Si)GeSn epilayers on Ge/Si(001) takes place mostly via edge dislocations rather than via treading dislocations as well-known in other group IV systems, i.e. SiGe/Ge. Subsequently, dedicated heterostructures are used for admittance and optical characterization. Highly biaxially tensile strained Ge and GeSn layers grown on GeSn strain relaxed buffer layers are used to fabricate metal oxide semiconductor capacitors in order to investigate the interfacial quality between these narrow bandgap semiconductors and high-k dielectrics. For the investigation of the Nickel metallization process of GeSn and SiGeSn epilayers, Sn concentration above 10 at.% are used. Furthermore, the transition from an indirect to a fundamental direct group IV semiconductor is presented by means of temperature dependent PL measurements on a set of high Sn content GeSn epilayers. Strain relaxed GeSn layers with a Sn concentration of 12.6 at.% grown on Si(001) substrates exhibit high modal gain values at cryogenic temperatures. Finally, the first demonstration of lasing action in direct bandgap group IV Fabry-Perot cavities is presented.

# Zusammenfassung

Zinn-basierte Legierungen, ausschließlich bestehend aus Elementen der 4. Hauptgruppe des Periodensystems, haben innerhalb der letzten zehn Jahre ein gesteigertes wissenschaftliches Interesse auf sich gezogen. Bereits seit Anfang der 1980er Jahre sind die hochinteressanten elektronischen Eigenschaften, wie etwa eine fundamental direkte Bandlücke oder hohe Ladungsträgerbeweglichkeiten, dieser Halbleiter bekannt. Allerdings haben die niedrige Löslichkeit des Zinns in Ge oder SiGe und die hohe Gitterfehlanpassung das Wachstum von hochqualitativen GeSn und SiGeSn Schichten auf Si Substraten erheblich eingeschränkt. Somit konnte das enorme Potential dieses Materialsystems in Bezug auf dessen Anwendung in der Nano- und Optoelektronik noch nicht vollständig ausgenutzt werden. Ein Tieftemperatur-Prozess für die chemische Gasphasenabscheidung unter reduziertem Druck mit kommerziell erwerblichen Ge- und Sn-Präkursoren wie $Ge_2H_6$ und $SnCl_4$ für das epitaktische Wachstum von GeSn und SiGeSn Legierungen direkt auf Si(001) und auf Ge-gepufferten Si(001) Substraten ist in dieser Arbeit entwickelt worden. Die in die Schichten eingebauten Zinn Konzentrationen übersteigen hierbei die im thermischen Gleichgewicht möglichen Werte bei weitem. Hohe Wachstumsraten bei niedrigen Wachstumstemperaturen ermöglichen außergewöhnlich gute Schichtqualitäten, die mittels Transmissionselektronenmikroskopie, Rutherford-Rückstreu-Spektrometrie, Röntgendiffraktometrie oder Photolumineszenz (PL) nachgewiesen worden sind. Weiterhin wird gezeigt, dass sich die plastische Relaxation dieser Schichten von der des gut bekannten SiGe/Si Systems unterscheidet. Nachfolgend, werden ausgewählte Heterostrukturen mittels Admittanz und optischer Charakterisierung untersucht. Hochgradig zugverspannte Ge und GeSn Schichten, die auf teilrelaxierten GeSn Pufferschichten aufgewachsen worden sind, werden für die Herstellung von Metal-Oxid-Halbleiter Kondensatoren verwendet, die wiederum der Charakterisierung der Grenzschichten zwischen den hochverspannten Halbleitern und den eingesetzten Dielektrika mit hohen Dielektrizitätskonstanten dienen. Für die Untersuchung des Metallisierungsprozesses von GeSn und SiGeSn Schichten werden Zinn Konzentrationen von über 10 at.% verwendet. Schließlich wird der Übergang von einem indirekten zu einem fundamental direkten Gruppe IV Halbleiter präsentiert. Hierfür sind temperaturabhängige PL Messungen an einem prädestinierten Probensatz durchgeführt worden. Teilrelaxierte GeSn Schichten gewachsen auf Si(001) Substraten und mit einer Zinn Konzentration von 12.6 at.% zeigen hohe optische Verstärkung bei tiefen Temperaturen. Darüber hinaus wird zum ersten Mal Lichtverstärkung durch stimulierte Emission von Strahlung (lasing) in Gruppe IV Halbleitern mit fundamental direkter Bandlücke präsentiert.

# Contents

# Chapter 1

## Introduction

Nowadays, computing systems and consequently integrated circuits (ICs) set the pace not only for CMOS industries but also widely for the whole society. In accordance with the ever increasing demand for mobile devices, like smartphones or tablet personal computers, the internet data transfer has grown exponentially over the last decades leading in turn to a tremendous increase of power consumption. Within the 28 years, from 1984 till 2012, the worldwide internet traffic in total amounts to 1.2 zettabytes, that are $1.2 \times 10^{21}$ bytes or 1.2 billion terabytes. It is predicted that this number will increase until 2017 to 1.4 zettabytes per year [1]. In order to tackle the resulting power consumption crisis, both optoelectronics and nanoelectronics have to be revolutionized. Here, the traditional way of device scaling, the steady increase of the processor speed by ever increasing the number of transistors in *integrated circuits* (ICs) might reach its limits. Already since more than 10 years or so, the widening gap between the exponentially increasing number of transistors on a single chip and the delivered performance of the chip, known as *Moore's gap*, illustrates this restriction. New transistor concepts such as *Tunnel field effect transistors* (TFETs) based on band-to-band tunneling rather than on thermal emission as in conventional *metal oxide semiconductor field effect transistors* (MOSFETs) are prominent alternatives, due to the capability to beat the physically limited subthreshold swing (60 mV/dec) of MOSFETs [2]. In this context, simulation results have shown that Sn-based alloys are promising candidates to realize complementary TFET scaled logic for low power applications [3, 4]. Moreover, it is well-known that not only the active but also the passive elements of ICs, such as interconnects, usually made of Cu and low-k dielectrics, produce a vast power dissipation via heating. A smart way to solve this problem is to avoid heating by replacing the on-chip partially or chip-to-chip electrical interconnects by optical interconnects. The application of photons for the data and information transfer requires less energy and provides higher speed at the same time compared to their RC limited Cu-counterparts. These so-called *Electronic-Photonic Integrated Circuits* (EPICs) consist of several optoelectronic key devices, since the electrical information has to be modulated onto the light and read out again. The key devices are a light source, a modulator to convert electrical in optical signals, waveguides to transport the modulated light to the detector where the optical signals are read out and converted to electrical signals again. Here, the ultimate vision is to employ a single material system for both electronic and photonic devices, that is, *monolithic integration*. Since Si is the material of choice for ICs for many decades, a group IV solution is highly desired, so group IV photonics comes into play. The big dream, frequently also called the *Holy Grail*, of group IV photonics is an efficient laser source, since for the goal of combining electronic with photonic ICs a monolithically in-

tegrated group IV laser is the missing piece. All other main components like waveguides [5], photo-detectors [6] and modulators [7] can already be fabricated in a CMOS environment, i.e. Si- or Ge-based. However, an efficient group IV light source, i.e. a laser diode, has not been achieved, yet. This is due to the fundamental indirect bandgap of Si and Ge, which makes first order transitions from the conduction band at the Γ-valley to the top valence band highly unlikely compared to second order transitions including phonons. Hence, complex hybrid integration techniques have been developed to combine III-V laser sources with Si waveguides [8] possessing, however, severe drawbacks like alignment issues or thermal mismatch prohibiting a large scale photonic integration so far.
The lack of a direct bandgap group IV semiconductor, thus, an efficient group IV light emitter prohibits the large scale integration of Si photonics. Furthermore, the indirect band-to-band tunneling, the fairly large bandgap and the absence of suitable heterostructures in Si-based devices restrict the efficiency of group IV low power TFETs to date. The use of GeSn as optically active gain or channel material with its lower and potentially direct bandgap compared to fundamentally indirect Ge (0.66 eV) and Si (1.12 eV) provides a viable solution to overcome the obstacles in both fields photonics and electronics. In the scope of this thesis, the huge potential of (Si)GeSn alloys employed as active laser material and channel material for novel CMOS applications will be demonstrated.

This thesis is subdivided into five chapters. Each of the three main chapters is introduced by an overview about the state-of-the-art science in the corresponding field. Subsequently to this introductory **chapter 1**, the epitaxial growth of GeSn and SiGeSn layers is presented in **chapter 2**. The growth kinetics as well as the crystalline and optical quality of Ge and (Si)GeSn epilayers on Si(001) and Ge buffered Si(001) are investigated. In addition, the plastic strain relaxation of Sn-based alloys on Ge is addressed. Highly biaxial tensile strained Ge and GeSn (sGe, sGeSn) have been grown on partially relaxed GeSn buffer layers, that are electrically characterized in **chapter 3**. Metal oxide semiconductor capacitors using sGe(Sn)/GeSn/Ge/Si heterostructures are fabricated and electrically studied via admittance characterization. Special attention is paid to the thermal budget during processing and the interfacial quality between the highly strained and narrow bandgap semiconductor and the dielectric. The following **chapter 4** treats the interaction of light with GeSn and SiGeSn alloys under low and high excitation as well as stimulated emission. Temperature dependent photoluminescence along with gain measurements provide the essential ingredients for lasing action, which will be demonstrated in the last part of this chapter via optically pumped GeSn Fabry-Perot cavities. **Chapter 5** provides a brief summary and conclusion of the work as well as an outlook.

# Chapter 2

## Si-Ge-Sn Epitaxy

More than 30 years ago, in 1982, GeSn alloys have been mentioned in literature for the first time as possible direct bandgap group IV semiconductors with unusually high carrier mobilities [9]. Although GeSn has been considered as a hypothetical alloy, due to the low solid solubility of Sn in Ge [10], groups have succeeded in growing microcrystalline and monocrystalline GeSn layers in the 1980's and 1990's. Recently, the scientific interest in CVD grown metastable GeSn and SiGeSn layers has risen abruptly, owing to the need of novel transistor channel materials and stressor layers as well as to the increasing demand for Si photonics to integrate photonics with electronics.
In the following chapter, the epitaxial growth and structural characterization of GeSn binary and SiGeSn ternary alloys is presented using an industrial-compatible 200 mm *reduced-pressure chemical vapor deposition* (RP-CVD) tool. Here, particular attention is paid to the growth kinetics of (Si)GeSn on Si(001) as well as on *Ge virtual substrates* (Ge-VS) in the low growth temperature regime. The high optical quality of the grown layers is verified by room temperature *photoluminescence* (PL) measurements. Partially strain relaxed and high Sn-content GeSn layers are used as epitaxial buffer layers for overgrown tensile strained Ge and GeSn.
Parts of the presented results of this chapter have been published in [11, 12, 13, 14, 15, 16].

### 2.1 Background

The group IV element Sn located below Ge in the periodic table undergoes a phase transition at 13.2 °C from so-called $\alpha$-Sn (gray Sn) to metallic $\beta$-Sn (white Sn). The former has a diamond cubic structure - just as crystalline C, Si or Ge - with a zero bandgap. The crystalline bonds of $\alpha$-Sn are not strong covalent as for their group IV counterparts but they are rather at the border between covalent and metallic [18]. Moreover, along with the phase transition, the volume of the material decreases by approx. 26 % [19]. This makes the synthesis of $\alpha$-Sn rather challenging. Farrow *et al.* [20] developed a MBE-based growth technique to deposit high quality $\alpha$-Sn films on InSb and CdTe at 25 °C, which have been used subsequently by other groups to grow and analyze $\alpha$-Sn layers by photoemission spectroscopy [19] regarding their band structure. These measurements have confirmed that the *Groves-Paul model* (GP) [21] describes the band structure quite well. According to this model, $\alpha$-Sn is a semimetal with an inverted band structure, that is, the conduction and valence bands are bent downwards and upwards, respectively. As

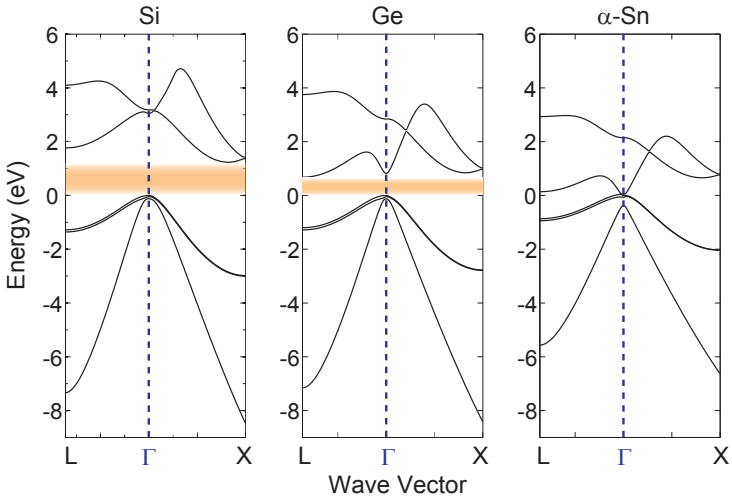


**Figure 2.1:** Electronic band structure of Si, Ge and $\alpha$-Sn (Data taken from [17]).

a result, the bandgap at the center of the Brillouin zone is negative, $E_{g,\Gamma} = -0.41\,\text{eV}$ (c.f. table 2.1). This electronic band structure differs significantly from band structures of other group IV elements like Si or Ge (c.f. Fig. 2.1), but are comparable to those of HgTe or HgS. However, the zero bandgap limits the applicability of $\alpha$-Sn. Recently, Ansari *et al.* [18] have proposed to use $\alpha$-Sn for a *confinement modulated gap transistor* (CMGT). Here, a transition from a semimetal to a semiconductor with bandgaps larger than 2 eV is predicted due to quantum confinement, similar to methods that are used to open the bandgap in graphene nanoribbons [22].

The knowledge about the electronic band structure of $\alpha$-Sn is essential in order to predict the properties of its alloys with Ge and Si. The bandgaps at 0 K for the Γ- and L-point are given in table 2.1. In contrast, Ge is a group IV semiconductor with an indirect bandgap at the L-point within the Brillouin zone, see Fig. 2.1, and at room temperature the Γ-valley lies energetically 140 meV above the L-valleys [23]. In Si the difference in energy between the highest valence band maximum (Γ-point) and the lowest conduction band minimum (X-point) is approx. 1.12 eV, whereas the local conduction band minimum at the Γ-point is approx. 2.3 eV higher. The bandgaps at 0 K are summarized in table 2.1. These values suggest that the bandgaps at the center of the Brillouin zone and the L-point shrink significantly for GeSn and SiGeSn alloys for increasing Sn concentration. However, the Γ-valley is supposed to decline faster compared to the L-valleys, since the difference $E_{g,\Gamma,Ge} - E_{g,\Gamma,\alpha-Sn}$ is larger than $E_{g,L,Ge} - E_{g,L,\alpha-Sn}$ and $E_{g,\Gamma,\alpha-Sn} < E_{g,L,\alpha-Sn}$. As a consequence GeSn alloys are expected to become fundamental direct bandgap group IV semiconductors for a certain Sn content. In the case of SiGeSn ternary alloys this indirect to direct transition strongly depends on the Si concentration since incorporating Si into a

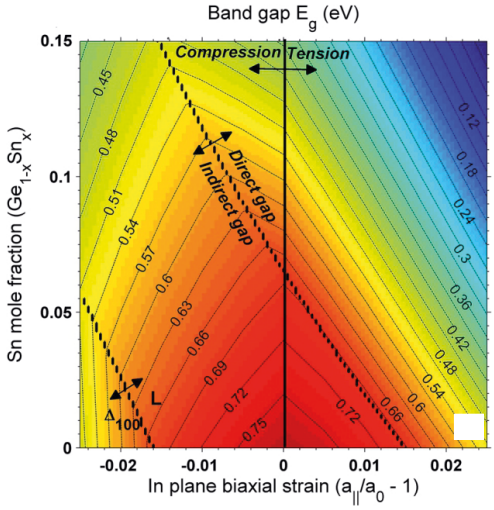


**Figure 2.2:** Contour plots of the lowest energy band in GeSn as function of the Sn concentration and applied strain [26].

GeSn crystal will increase the bandgap at the Γ-valley faster than at the L-valleys, which means that a higher amount of Sn is required to achieve the direct bandgap nature. The bandgaps of unstrained $Ge_{1-x}Sn_x$ and $Si_yGe_{1-x-y}Sn_x$ crystals at the critical points of the Brillouin zone can be calculated using [17, 24]:

$$E_i(x) = E_i^{Ge}(1-x) + E_i^{Sn}x + b_i^{GeSn}x(1-x), \tag{2.1}$$

$$\begin{aligned} E_i(x,y) &= E_i^{Ge}(1-x-y) + E_i^{Sn}x + E_i^{Si}y + b_i^{GeSn}x(1-x-y) \\ &+ b_i^{SiGe}y(1-x-y) + b_i^{SiSn}xy, \end{aligned} \tag{2.2}$$

where $E_i^{Ge,Si,Sn}$ are the critical points of elemental Ge, Si and α-Sn, respectively, and $b_i^{GeSn,SiGe,SiSn}$ are the bowing parameters that give the deviation from the linear interpolation.

| | Si | Ge | α-Sn |
|---|---|---|---|
| $E_{g,\Gamma}$ (eV) (0 K) | 3.3 | 0.892 | −0.408 |
| $E_{g,L}$ (eV) (0 K) | 2.0 | 0.744 | 0.120 |
| $E_{g,X}$ (eV) (0 K) | 1.2 | 0.901 | 0.910 |
| $C_{11}$ (GPa) | 166 | 129 | 69 |
| $C_{12}$ (GPa) | 64 | 48 | 29 |
| $C_{44}$ (GPa) | 80 | 68 | 36 |

**Table 2.1:** Material properties of Si, Ge and α-Sn [23, 24, 25].

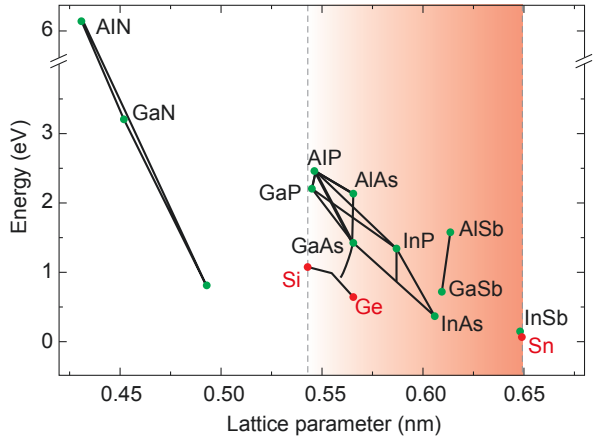


**Figure 2.3:** Bandgap energy as function of the lattice constant for all group IV and a variety of III/V semiconductors (Data taken from [27]).

Another essential parameter for the electronic band structure is the strain of the material. Via so-called *strain engineering* the properties of a semiconductor can be significantly changed. In the case of GeSn, Gupta *et al.* [26] theoretically determined the influence of biaxial strain - compressive as well as tensile - on the band structure of GeSn based on the nonlocal empirical pseudopotential method. The main results of their study can be seen in Fig. 2.2. For unstrained GeSn they predict a transition from a fundamental indirect to direct bandgap at 6.5 at.%. As will be shown experimentally in chapter 4 this underestimates the required Sn concentration for the transition. However, this value can be significantly decreased for increasing tensile strain (Fig. 2.2), i.e. for elemental Ge the required strain for a direct bandgap nature amounts to approx. 1.5 % which is slightly lower than other published values of 1.6 % [28] and 1.9 % [29]. In order to achieve tensile strain in GeSn alloys fully or partially relaxed GeSn layers can be used. The growth of such buffer layers as well as tensile strained Ge and GeSn will be demonstrated in chapter 2.2.3. For increasing compressive strain the needed Sn content steadily increases, i.e. $x_{Sn} = 15$ at.% is assumed to be necessary for a 1.5 % compressively strained GeSn epilayer.

On the one hand, the chemical and electronic differences between Si, Ge and $\alpha$-Sn provide exciting new material properties. On the other hand, however, these differences represent a serious obstacle for the fabrication, i.e. epitaxial growth, of alloys composed of these elements. The two main challenges are the low solid solubility of $\alpha$-Sn in Ge as well as in Si and the large difference in lattice constants between $\alpha$-Sn (6.493 Å), Ge (5.658 Å) and Si (5.431 Å). As can be seen in Fig. 2.3 it is actually one of the largest lattice mismatches among all group IV and most III/V semiconductors. As a consequence, growing smooth layers with high crystalline quality, i.e. low density of defects, is challenging.

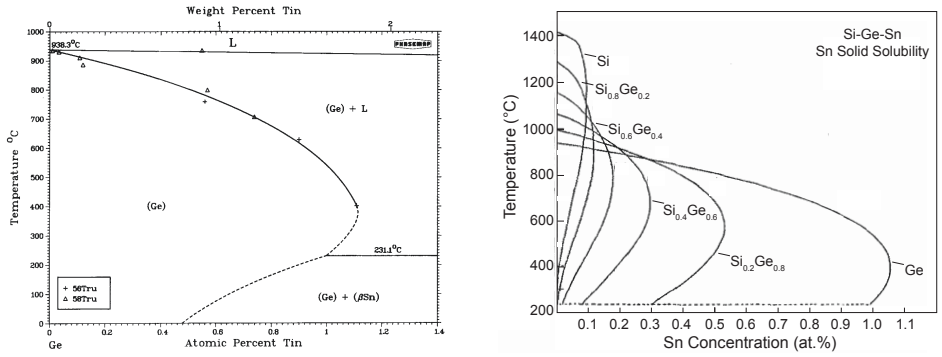


(a) (b)

**Figure 2.4:** Phase diagrams of the (a) Ge-Sn system for high Ge concentrations [36] and the (b) Si-Ge-Sn system for various SiGe compositions [10].

For heteroepitaxy of semiconductors with a large lattice mismatch the so-called *Stranski-Krastanov* (SK) growth mode occurs. After a few 2D monolayers (*wetting layer*) a 3D growth mode leads to nucleation and finally severe surface roughening. Even for the Ge/Si(001) system with a lattice mismatch of approximately 4.2 % the SK growth mode cannot be avoided. However, in the last 16 years several CVD-based growth techniques have been developed, e.g. thick, graded SiGe buffer layers [30], epitaxial necking [31, 32] or the two temperature method [33, 34, 35], in order to fabricate device-grade Ge epilayers on Si(001).

In Fig. 2.4 (a) the phase diagram of the Ge-Sn system is displayed for high Ge concentrations [36]. According to these calculations the maximum solubility of Sn in Ge is approx. 1.1 at.%, whereas it is even lower (< 1 at.%) at the eutectic temperature. There are solely two small regions to find a single phase in equilibrium, namely for GeSn with $x_{Sn} < 1$ at.% and SnGe with $x_{Ge} < 0.6$ at.% (not shown here). Above the melting temperature of Sn, which is 231.1 °C ($\sim$ 500 K), a two phase mixture can be found consisting of $Ge_{1-x}Sn_x$ with $x < 0.01$ and liquid $\beta$-Sn. Below this temperature, the $\beta$-Sn is solid within the two phase mixtures. The phase diagram for the Si-Ge-Sn system for low Sn concentrations and various SiGe compositions is shown in Fig. 2.4 (b). Obviously the solubility of Sn in SiGe alloys decreases significantly for increasing Si content. The solubility in pure Si is $\leq 0.1$ at.%.

Thus, for the epitaxial growth of (Si)GeSn alloys with technologically and scientifically relevant Sn concentrations exceeding 1 at.%, growth conditions far beyond equilibrium have to be met in order to avoid phase separation. The latter may occur via surface segregation or bulk precipitation of Sn, i.e. $\beta$-Sn. Surface segregation is indeed a severe issue for Sn-based epitaxy, since it is energetically more favorable for Sn atoms in a Ge matrix to change their position with Ge adatoms on the surface. For a small surface coverage

of approx. 0.1 monolayers the surface energy is constant, i.e. it does not depend on the surface coverage, and a linear segregation model can be assumed [37]:

$$n_S = \Delta_S \cdot n, \tag{2.3}$$

where $n_S$ is the concentration of surface adatoms and $n$ is the bulk concentration of Sn. $\Delta_S$ is the segregation length, which should be kept as low as possible to avoid Sn surface segregation. For low temperatures $\Delta_S$ strongly depends on the temperature (kinetic branch of $\Delta_S$), hence the segregation length is small for low temperatures and/or high growth rates. The exchange rate between subsurface Sn atoms and Ge adatoms can be reduced at lower temperatures, and the time slot for this exchange becomes smaller for higher growth rates. It is assumed [37], that during the epitaxial growth the surface segregation is the predominant process regarding phase separation. Bulk precipitation of $\beta$-Sn is more likely to occur during post-growth processing, i.e. *rapid thermal annealing* (RTA) [38].

Despite of all these challenges the first metastable microcrystalline GeSn alloy has been fabricated by UV laser annealing of sputtered, amorphous GeSn [39] shortly after the demonstration of $\alpha$-Sn deposition by Farrow *et al.* [20]. Several additional studies on microcystalline and amorphous GeSn followed and have paved the route for the monocrystalline epitaxial growth of metastable GeSn layers [40, 41, 42, 43, 44]. Here, the main deposition technique has been *molecular beam epitaxy* (MBE). Moreover, different kind of substrates such as Ge, GaAs or InSb have been employed to reduce the lattice mismatch and improve the epitaxy. Till the late 1990's MBE remained the primary method to deposit GeSn epilayers with reasonable crystalline quality [45, 46] in order to investigate growth conditions, band structure as well as optical properties [47, 48]. However, the required very low growth temperatures $100 - 200\,^{\circ}\mathrm{C}$ during MBE deposition to avoid Sn segregation leads to epitaxial breakdown at elevated Sn concentrations and unsuitable layer thicknesses [49]. Thus, around the year 2000 it has become clear that the crystalline quality of the layers grown so far have not been good enough for any devices and the scientific activity has dropped.

The lack of suitable Sn precursors hindered the epitaxial growth of GeSn and SiGeSn layers using CVD techniques until the early 2000s. Owing to the low Sn-H bond energy, Sn hydrides are unstable at room temperature. The group of Kouvetakis and Menéndez *et al.* at the Arizona State University (ASU) introduced *ultra high vacuum* (UHV) CVD of high quality GeSn and SiGeSn epilayers using a deuterium stabilized Sn precursor ($SnD_4$) [50, 51, 52]. In 2011 *atmospheric pressure* (AP) CVD of GeSn using digermane ($Ge_2H_6$) along with commercially available $SnCl_4$ has been demonstrated by Vincent *et al.* [53]. By means of these two techniques device-grade Sn-based semiconductors have been fabricated for a variety of applications, e.g. photodiodes [54, 55, 56], photodetectors [57, 58] or MOSFETs [59] and the scientific interest has revived.

However, neither device-grade pseudomorphic layers grown on Ge-VS nor high quality relaxed layers with Sn concentrations above 10 at.%, that is, fundamental direct (Si)GeSn alloys, have been demonstrated using above-mentioned CVD techniques, so far. The development of those layers would enable the fabrication of new classes of group IV devices

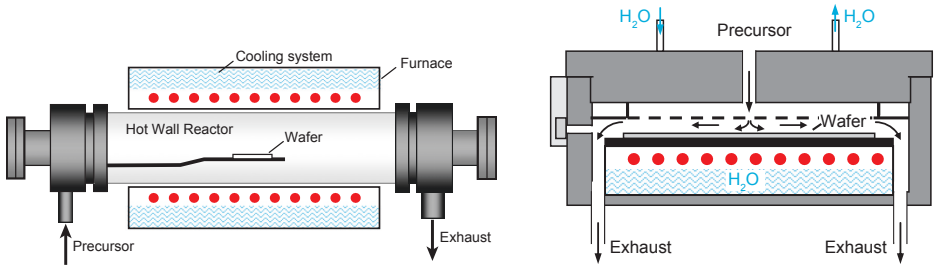


**Figure 2.5:** Schematics of (a) horizontal and (b) vertical (showerhead) CVD reactor designs (after [60]).

such as (Si)GeSn lasers or direct bandgap TFETs. In the following, the epitaxial growth of GeSn binary and SiGeSn ternary alloys will be presented using a *reduced pressure* (RP) CVD tool and a precursor combination of $Ge_2H_6$, $SnCl_4$ and $Si_2H_6$. The growth kinetics and crystalline quality of such epilayers with Sn concentrations above 10 at.% employing Cl-based precursor will be discussed.

## 2.2 Reduced-Pressure CVD of Si-Ge-Sn Alloys

As far as group IV epitaxy is concerned the most common reactor design consists of a horizontal reactor chamber, which is heated from the top and bottom, see Fig. 2.5 (a). For this study a AIXTRON TRICENT 200 mm metal cold-wall RP CVD reactor is used, which has been designed for industrial applications. The precursors along with the carrier gas are led into the reaction chamber via a showerhead (vertical reactor design see Fig. 2.5 (b)). The wafer is placed on a graphite susceptor that is heated solely from underneath using 9 infrared (IR) lamps. Both the showerhead as well as the IR lamps are cooled with water. Consequently, the temperature of the showerhead is below 120 °C at any process step and inside the growth chamber a temperature gradient is built up. The growth temperature is measured with 6 thermocouples placed inside the susceptor. This reactor design has been developed initially for the epitaxial growth of III-V semiconductors in order to prevent premature cross reactions between the various precursors prior to the growth chamber [61]. Furthermore, it assures uniform gas distribution over the whole wafer as well as low total gas consumption.
Prior to the growth process the native oxide on the substrate surface is etched using a Semitool Raider single wafer cleaning tool. Here, two 200 mm chambers provide etch processes based on the reaction between HF and $SiO_2$. Bath- as well as HF-vapor processes are used to assure hydrophobic, H-terminated Si- or Ge surfaces. Inside the CVD growth chamber residual oxide is removed by employing a pre-epi bake step at approx. 1000 °C

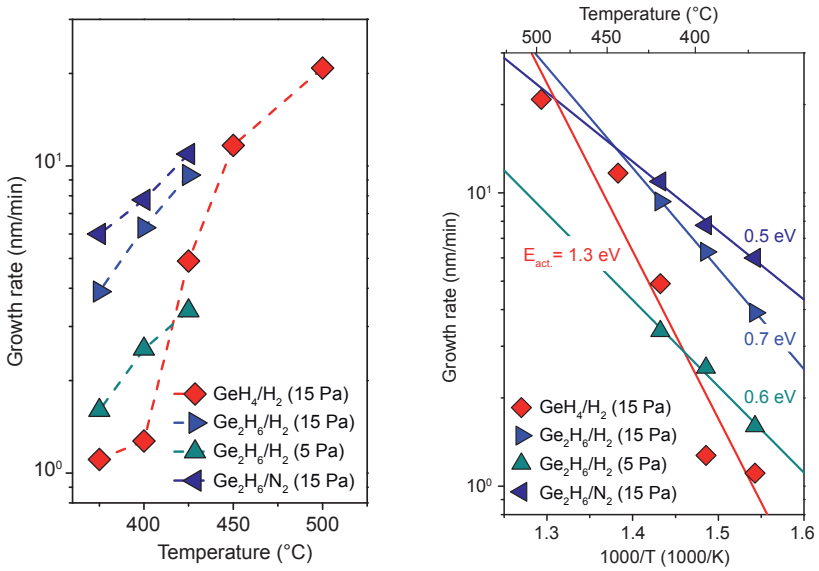


**Figure 2.6:** (a) Ge growth rate as function of temperature for various Ge-precursors ($GeH_4$, $Ge_2H_6$) and carrier gases ($H_2$, $N_2$). (b) Arrhenius plot for the Ge growth.

for 3 min in an $H_2$ ambient.
First, the deposition of monocrystalline Ge layers is investigated using $GeH_4$ and $Ge_2H_6$ (diluted in $H_2$) in combination with $N_2$ and $H_2$ as carrier gases. The goal is, to determine the appropriate combination of Ge-precursor and carrier gas for the required low temperature epitaxy of Sn-based alloys. Special emphasis is placed on achieving high growth rates at low temperatures along with high crystalline quality and smooth layer morphology.

### Low Temperature Ge Growth

As discussed at the beginning of this chapter, far non-equilibrium growth conditions, i.e. high deposition rates at low growth temperatures, are required in order to overcome the low solid solubility of Sn in Ge and Si. Thus, first the deposition of Ge epilayers at low temperatures is investigated employing the most commonly used precursor for Ge epitaxy, namely $GeH_4$, and the next higher order Ge hydride, $Ge_2H_6$.
It is well known that $GeH_4$ is suitable to grow monocrystalline Ge layers at temperatures between $350 - 750\,°C$ [62, 32, 33, 63, 64, 34, 35], however, the achieved growth rates at

very low growth temperatures might be too low for Sn-based epitaxy. Due to this large temperature range there has been no need to investigate higher order germane precursors in contrast to silicon epitaxy, where $Si_2H_6$ [65], $Si_3H_8$ [66] and $Si_5H_{12}$ [67] have been used. Whereas the first report on CVD-grown monocrystalline Ge layers using $Ge_2H_6$ in a horizontal RP-CVD reactor [68] has been published 2012 there has been no study using a vertical reactor chamber.
In Fig. 2.6 (a) the growth rate as function of growth temperature is shown for Ge epilayers grown at a constant reactor pressure of 60 mbar and a total gas flow of a few slm. $GeH_4$ and $Ge_2H_6$ partial pressures of 5 Pa and 15 Pa are used in combination with $H_2$ or $N_2$ as carrier gas. At 450 °C a growth rate of 10 nm/min is measured for germane, which quickly decreases to approximately 1 nm/min at 375 °C. In comparison, the growth rate is much higher, $4 - 6$ nm/min, for $T_{gr} = 400$ °C for the deposition with digermane. However, it drops to $< 3$ nm/min for a three times lower partial pressure, $p_{Ge_2H_6}$. Switching from $H_2$ to $N_2$ as carrier gas leads to an increase of the deposition rate by a factor of 1.2-1.5 for temperatures between $375 - 425$ °C and $p_{Ge_2H_6} = 15$ Pa. These values are significantly lower compared those obtained for $GeH_4$ ($3 - 4\times$ [68]), but very close to the results of Gencarelli *et al.* [68]. The Ge growth rate at low temperatures in the case of germane is limited by the desorption of hydrogen from the surface. So, if the carrier gas is switched to $N_2$ the amount of open surface sites increases and so does the growth rate. In contrast, for the growth using digermane this dependence on open sites on the surface seems to be much weaker. Therefore, it is assumed that $Ge_2H_6$ can either grow without open surface sites or creates them via surface reactions [68]. A similar behavior has been observed for Si epitaxy using neopentasilane [67]. Here, a growth mechanism has been suggested, which is based on a concerted reaction of simultaneous bond breaking and bond forming. Sturm *et al.* [67] postulated that the Si-Si bond of the $Si_2H_6$ molecule will brake up that are weaker than the Si-H bonds, and subsequently one $SiH_3$ fragment (radical) will form $SiH_4$ with H occupying surface sites. This $SiH_4$ molecule will be desorbed from the surface and the remaining $SiH_3$ fragment will bond to the vacated surface site. Thus, no open surface site is required for the growth.
The growth rate as function of the inverse temperature, also known as *Arrhenius plot*, is displayed in Fig. 2.6 (b). From this dependence the activation energy, $E_{act}$, can be determined by means of a linear fit and the following expression:

$$R(T) = A \cdot \exp\left(\frac{E_{act}}{k_B T}\right), \tag{2.4}$$

where $R(T)$ is the temperature dependent growth rate, $A$ is a constant and $k_B$ is the Boltzmann constant. The activation energy decreases by nearly a factor of two by switching the precursor from germane ($E_{act} = 1.3$ eV) to digermane ($E_{act} = 0.7$ eV) at a precursor partial pressure of 15 Pa and $H_2$ carrier gas. Whereas a further decrease is observed for a lower $p_{Ge_2H_6}$ of 5 Pa, $E_{act} = 0.6$ eV, the lowest activation energy of $E_{act} = 0.5$ eV is found when $N_2$ is employed as carrier gas. The values for $GeH_4$ are in fair agreement with those for $Ge_2H_6$ in [68], whereas $E_{act} = 0.7$ eV for $p_{Ge_2H_6} = 15$ Pa is less than half of the results for $p_{Ge_2H_6} \approx 30$ Pa in [68]. However, they are indeed significantly higher

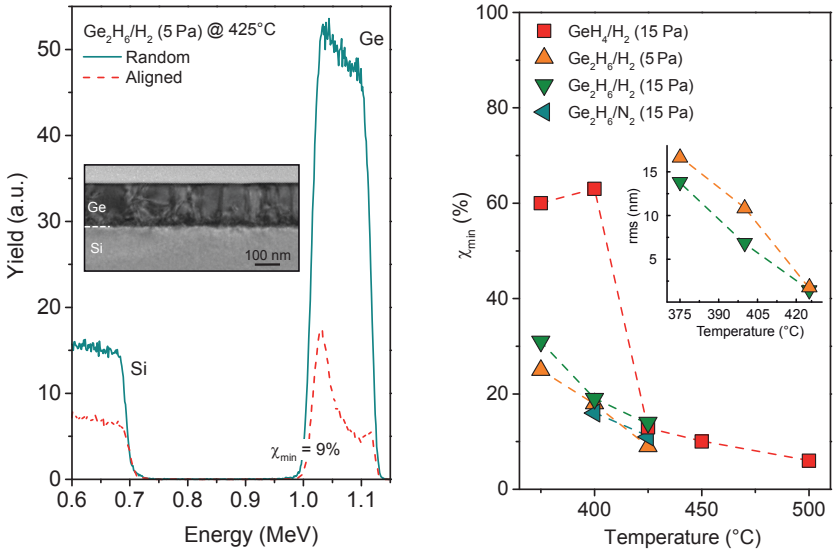


(a) (b)

**Figure 2.7:** (a) RBS random and channeling spectra of a 150 nm Ge layer grown on Si(001) at 425 °C using $Ge_2H_6$ and $H_2$ as carrier gas. Inset: TEM image. (b) $\chi_{min}$ as function of growth temperature for various combinations of precursor and carrier gas. The inset shows the rms roughness as function of growth temperature.

compared to activation energies (approx. 0.3 eV) in a diffusion limited growth regime [33]. In addition, the growth rate here depends on the temperature and the precursor partial pressure. Hence, the growth regime under investigation is most likely a transition between a fully kinetically- and diffusion limited regime, which is in agreement with the findings in [68] identifying a fully kinetically limited growth at 275 °C. The significantly lower activation energy for $GeH_4$ compared to the $Ge_2H_6$ growth at identical conditions might be another indication that the $Ge_2H_6$ growth does not require open sites on the surface and that $GeH_3$ radicals accelerate hydrogen desorption from the surface.
In order to study the crystalline quality of the grown layers *Rutherford backscattering spectrometry* (RBS) measurements are carried out as well as *transmission electron micrographs* (TEM) are taken. In Fig. 2.7 (a) the RBS channeling and random spectra are shown for a 150 nm Ge layer grown on Si(001) at 425 °C with $p_{Ge_2H_6} = 5$ Pa and $H_2$ carrier gas. The ratio between the aligned and random spectra right behind the surface peak at approx. 1.1 MeV is called minimum yield value, $\chi_{min}$, and is a measure for the crystalline quality of the epilayer. Here, a $\chi_{min}$ of 9 % is found. Towards the interface of the Ge layer and the Si substrate at $1.00 - 1.05$ MeV the channeling signal increases due to the defects at the interface, mainly misfit dislocations, induced by the lattice mismatch between Si

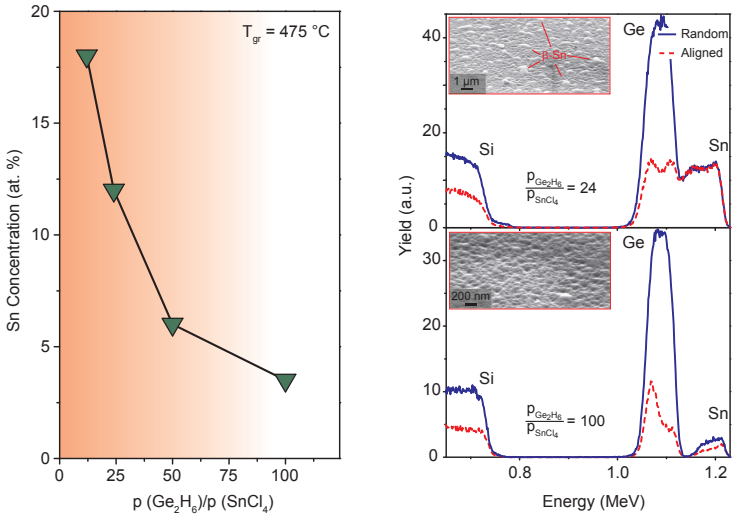


**Figure 2.8:** (a) Sn concentration as function of the partial pressure ratio between $Ge_2H_6$ and $SnCl_4$. (b) RBS spectra for GeSn depositions using partial pressure ratios between $Ge_2H_6$ and $SnCl_4$ of 24 (top) and 100 (bottom). Insets: SEM images.

and Ge. The large density of defects, especially at the Ge/Si interface can also be seen in the TEM image in the inset of Fig. 2.7 (a). The $\chi_{min}$ of Ge epilayers as function of the growth temperature is shown in Fig. 2.7 (b). Whereas the absolute minimum of approx. 5 % is obtained for Ge grown at 500 °C with $GeH_4$, layers grown at low temperatures using $Ge_2H_6$ exhibit a higher crystalline quality. Note, for $T_{gr} \leq 400\,°C$ the $\chi_{min}$ in the case of $GeH_4$ increases rapidly to $> 60\,\%$. The roughness of the layers is measured by *atomic force microscopy* (AFM) and the rms results of $4 \times 4\,\mu$m scans are presented in the inset of Fig. 2.7 (b). For decreasing growth temperature the roughness increases. This is owed to the reduced mobility of adsorbed precursor molecules on the growth surface.
In summary, it has been shown that higher growth rates and higher crystalline quality can be obtained in the low temperature regime by using a higher order germane precursor. In the next section, the growth kinetics of GeSn and SiGeSn layers are presented using $Ge_2H_6$ as Ge precursor.

### 2.2.1 Si-Ge-Sn Growth Kinetics

Since it has been shown that in the case of Ge deposition, the highest growth rates at low growth temperatures can be achieved using $Ge_2H_6$ and $N_2$ as carrier gas this combi-

nation is used for the epitaxial growth of GeSn and SiGeSn layers. Regarding a suitable Sn precursor, there have been reports mainly on two sources in literature. The group of Menéndez and Kouvetakis has introduced $SnD_4$ [50, 51, 52]. However, stannane is rather unstable at room temperature [53, 69] and so Vincent *et al.* [53] suggested to use commercially available $SnCl_4$. In this study the latter Sn precursor is used. Owing to the fact that $SnCl_4$ is liquid at room temperature a bubbler system is employed with $H_2$ as carrier gas. Whereas all layers have been grown using identical reactor pressure ($p_{tot} = 60\,\text{mbar}$) and total gas flow of a few slm, the growth temperature as well as the precursor partial pressures are varied systematically.

For a growth temperature of 475 °C the Sn concentration of $Ge_{1-x}Sn_x$ layers grown on Si(001) - measured via RBS - as function of the partial pressure ratio between $Ge_2H_6$ and $SnCl_4$ is presented in Fig. 2.8 (a). A strong decrease of the Sn concentration from 18.0 at.% to 3.5 at.% is observed when the partial pressure ratio is raised from 12 to 100. However, RBS channeling spectra and *scanning electron micrographs* (SEM) indicate strong surface segregation of most probably $\beta$-Sn and poor crystalline quality of layers grown with a partial pressure ratio $< 100$. The RBS spectra of GeSn samples grown with ratios of 24 and 100 are displayed in the top and bottom part of Fig. 2.8 (b), respectively. For the Ge signal a $\chi_{min}$ of approx. 35 % is observed, no channeling occurs for the Sn signal, i.e. $\chi_{min} = 100\,\%$. Moreover, the front edge as well as the back edge of the Si and Ge signals are flattened, due to the roughened surface induced by the $\beta$-Sn segregation (c.f. inset of the top part of Fig. 2.8 (b)). Due to the growth temperature which is well above the melting point of Sn (approx. 500 K) the metal on the surface is melt and resemble droplets. In contrast, nearly no Sn droplets are observed for the higher partial pressure ratio, $p_{Ge_2H_6}/p_{SnCl_4}$, of 100. The $\chi_{min}$ values are lowered to $\chi_{min}(Ge) = 12\,\%$ and $\chi_{min}(Sn) = 50\,\%$ and the edges of the Si and Ge signals are steeper. At these growth conditions, a continuous even though rough GeSn layer is grown with a Sn concentration of 3.5 at.% and a Sn substitutionality of approx. 50 %.

In order to substitutionally incorporate a higher amount of Sn atoms lower growth temperatures as well as lower $p_{SnCl_4}$ at a constant $p_{Ge_2H_6}$ are investigated in the following. Again, the total pressure of the reactor chamber and the total gas flow are kept constant. The temperature dependence of the Sn content within GeSn layers grown directly on Si(001) with $SnCl_4$ partial pressures of 0.6 Pa and 1.3 Pa are displayed in Fig. 2.9 (a). As the growth temperature declines the Sn concentration increases for both partial pressures. Whereas the maximum content within the investigated parameter window is 10 at.% observed at $T_{gr} = 375\,°\text{C}$ and $p_{SnCl_4} = 1.3\,\text{Pa}$, below that temperature no GeSn layer with reasonable high crystalline quality can be grown. For growth temperatures $\leq 425\,°\text{C}$ a higher Sn concentration is determined for the higher $p_{SnCl_4}$. All layers exhibit a significantly improved crystalline quality regarding their $\chi_{min}$ ($< 21\,\%$) compared to the samples presented in Fig. 2.8 (b). The $\chi_{min}$ values are lowered by more than a factor of two indicating a substitutional incorporation of Sn atoms of at least 80 %. Exemplary, the Sn signal of RBS spectra measured for a 90 nm GeSn layer grown at 400 °C is shown in the inset of Fig. 2.9 (a). A Sn concentration of 6.5 at.% is obtained that is nearly

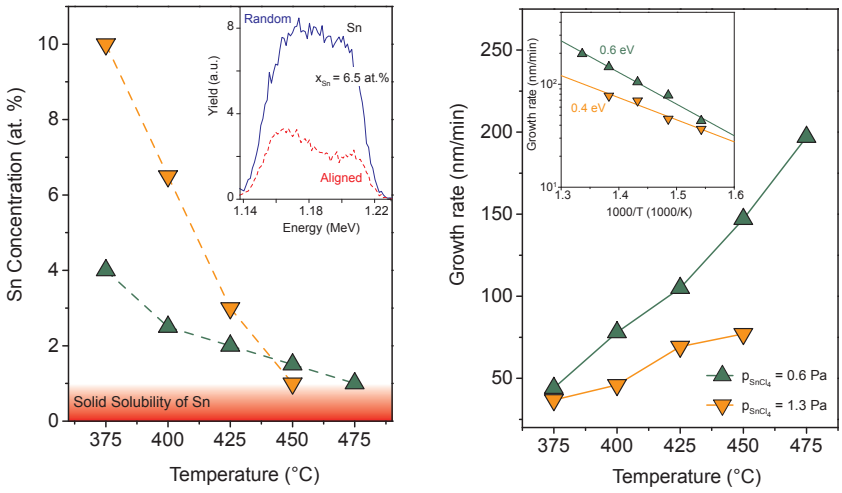


(a) (b)

**Figure 2.9:** (a) $x_{Sn}$ as function of the growth temperature for constant $p_{Ge_2H_6} = 120\,\text{Pa}$ and two different $p_{SnCl_4}$. Inset: RBS spectra of a GeSn layer grown at 400 °C (b) Growth rate as function of growth temperature. Inset: Arrhenius plot.

homogeneously distributed throughout the whole layer; a slight decrease towards the surface (higher energies) can be seen. Towards the GeSn/Si interface the aligned spectrum increases due to defects induced by the large lattice mismatch similar to Ge/Si interfaces (c.f. Fig. 2.7 (a)).

Regarding the temperature dependence of the growth rates that are presented in Fig. 2.9 (b), the values decrease with decreasing temperature, owed to the reduced thermal cracking of $Ge_2H_6$. The growth rates lie between 37 nm/min at 375 °C and 200 nm/min at 475 °C. Here, the GeSn deposition especially at higher temperatures with the lower $p_{SnCl_4}$ is faster and comparable to the growth rates without $SnCl_4$. Hence, the addition of $SnCl_4$ reduces the growth rate and results in higher Sn concentrations. At 375 °C, however, the difference between the growth rates is rather small. The activation energy, as shown in the inset of Fig. 2.9 (b), decreases from 0.6 eV ($p_{SnCl_4} = 0.6\,\text{Pa}$) - that is similar to the activation energy for Ge deposition (c.f. Fig. 2.6 (b)) - to 0.4 eV ($p_{SnCl_4} = 1.3\,\text{Pa}$).

These results clearly evidence that the achieved growth rates for the temperature range between 375 °C and 475 °C are high enough to avoid Sn segregation at the surface and bulk precipitation, and, therefore, enables the growth of GeSn epilayers with Sn concentrations exceeding the equilibrium solid solubility of Sn in Ge by more than one order of magnitude. Compared to Ge layers grown at comparable temperatures, but with lower digermane partial pressures, the $\chi_{min}$ values are comparable at least for temperatures $\leq 400\,°\text{C}$. The following section deals with the incorporation of Si into GeSn based on

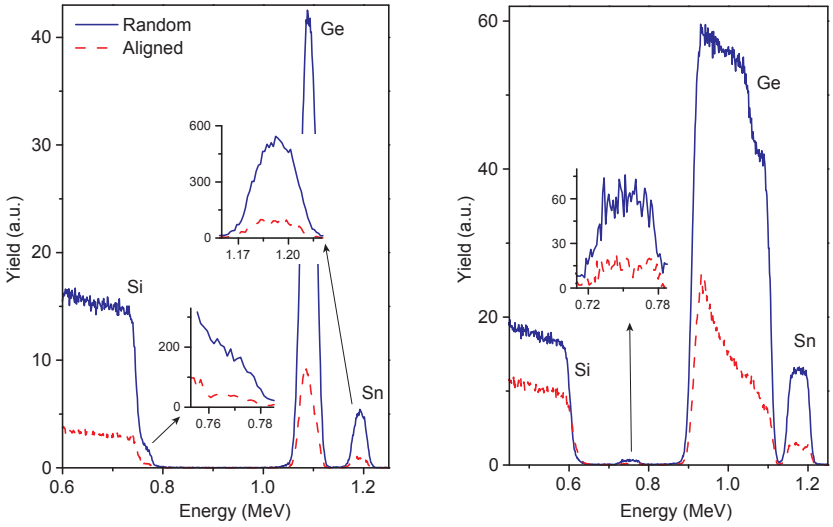


(a) SiGeSn/Si(001) (b) SiGeSn/Ge/Si(001)

**Figure 2.10:** RBS spectra of (a) 45 nm $Si_{0.12}Ge_{0.84}Sn_{0.04}$ grown directly on Si at 425 °C and (b) 85 nm $Si_{0.04}Ge_{0.85}Sn_{0.11}$ grown on Ge-buffered Si at 350 °C.

the above results.

### Incorporation of Si into GeSn

The great advantage of ternary alloys is the possibility to decouple band engineering from the lattice constant [70]. This opens a novel degree of freedom for future optoelectronic as well as nanoelectronic device applications. Despite the formidable perspectives of these materials there are only two groups that succeeded in growing such alloys using CVD [71, 52]. Furthermore, no systematic growth study has been presented so far for the used precursor combination.
On the basis of the epitaxial results on GeSn, the identical digermane partial pressure of 120 Pa and a constant $SnCl_4$ partial pressure of 0.6 Pa is employed for the following investigation as well as pure $Si_2H_6$ as Si precursor. In contrast to the GeSn growth study Ge-buffered Si(001) substrates have been used as well. The $140 - 250$ nm thick Ge buffer layers have been grown at 425 °C with $H_2$ as carrier gas and a digermane partial pressure of 5 Pa.
SiGeSn layers have been grown using a growth temperature range between 350 °C and 475 °C and subsequently analyzed via RBS regarding the Si and Sn concentration as well as the crystalline quality. Typical RBS spectra of two SiGeSn layers are displayed in

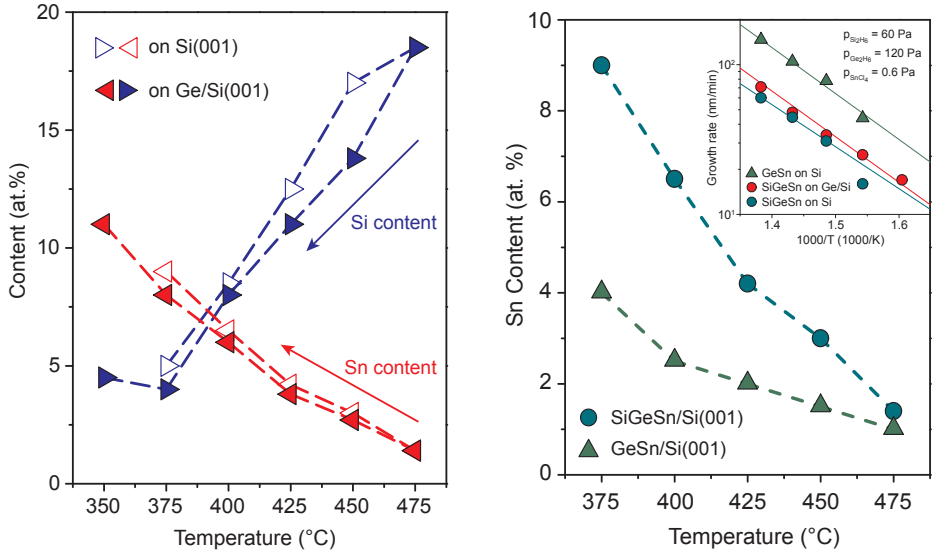


**Figure 2.11:** (a) $x_{Sn}$ and $x_{Si}$ as function of the growth temperature for SiGeSn epilayers grown directly on Si(001) and Ge-buffered Si(001). (b) Temperature dependent $x_{Sn}$ for GeSn/Si(001) and SiGeSn/Si(001). Inset: Arrhenius plot.

Fig. 2.10 (a) and (b) grown directly on Si(001) at 425 °C and Ge-buffered Si(001) at 375 °C, respectively. Besides the strong Ge signal around 0.9 MeV and 1.1 MeV, Si and Sn peaks are clearly visible. Well-defined plateaus in the Sn and Si signals (c.f. Fig. 2.10 (b)) proof homogeneous distribution throughout the whole SiGeSn layer. The aligned spectra exhibit comparable $\chi_{min}$ values of approx. 15 % for all three elements indicating a substitutionality of Si and Sn atoms in the Ge lattice of at least 85 %. The values are independent of the growth temperature using a constant partial pressure ratio between all three precursors, and they are slightly lower compared to the values obtained for GeSn alloys. Dechanneling is seen towards the SiGeSn/Si(001) and SiGeSn/Ge interface, respectively, owed to the relaxation induced defects due to the large lattice mismatch. No indication of Sn segregation or bulk precipitation is observed.
The determined Si and Sn concentrations as function of the growth temperature are presented in Fig. 2.11 (a). The composition of the SiGeSn ternaries clearly depends on the growth temperature. In addition, the temperature window is increased for layers grown on Ge-buffered Si(001). Whereas SiGeSn layers cannot be deposited directly on Si(001) at 350 °C the use of a Ge buffer layer enables epitaxial growth of SiGeSn at this growth temperature. The Si content decreases steadily from 19 at.% to 4 at.% going from 475 °C to 350 °C due to the reduced cracking efficiency of $Si_2H_6$. The Sn concentration is

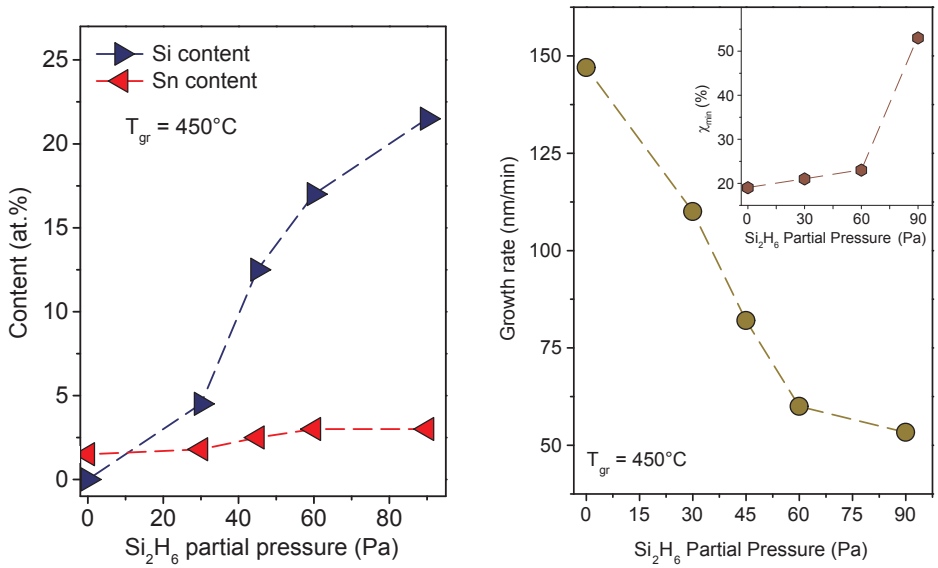


**Figure 2.12:** (a) $x_{Sn}$ and $x_{Si}$ and (b) growth rate as function of $p_{Si_2H_6}$ grown at 450 °C. The inset of (b) displays the $\chi_{min}$ for various $p_{Si_2H_6}$.

limited to 9 at.% at 375 °C without Ge buffer and can be increased to 11 at.% at 350 °C. Overall there is nearly no change in composition between layers grown on buffered Si(001) or directly on Si(001).

The Sn content of GeSn and SiGeSn layers using identical $p_{Si_2H_6}$ and $p_{SnCl_4}$ are compared in Fig. 2.11 (b). Nearly for all temperatures the Sn concentration is doubled in the ternary alloys. In the inset of Fig. 2.11 (b) the growth rate of SiGeSn on Si and Ge over 1000/T is displayed. The growth rates of GeSn on Si for $p_{SnCl_4} = 0.6$ Pa are plotted for comparison. The activation energies for all three materials are approx. 0.6 eV. However, the growth rate for GeSn is twice as high as for SiGeSn. Thus, adding $Si_2H_6$ into the growth chamber results in a significant decrease of the growth rate. Moreover, these findings provide evidence for the assumption that the incorporation of Sn atoms into Ge or SiGe depends on the growth rate; for a lower growth rate the Sn content increases.

In order to gain deeper insight into the relation between growth rate and Sn incorporation, SiGeSn layers have been grown at 450 °C at constant $p_{SnCl_4}$ as well as $p_{Ge_2H_6}$ and different $p_{Si_2H_6}$ ($0 - 90$ Pa), see Fig. 2.12. Indeed, a similar effect is observed. Both the Si and Sn concentration increase for higher $p_{Si_2H_6}$ (c.f. Fig. 2.12 (a)); whereas $x_{Si}$ gets five times higher for an increase of the disilane partial pressure by a factor of three, $x_{Sn}$ is doubled. Taking the growth rate into consideration (Fig. 2.12 (b)) the same dependence between $x_{Sn}$ and growth rate is observed. If the growth rate is halved the Sn concentration is

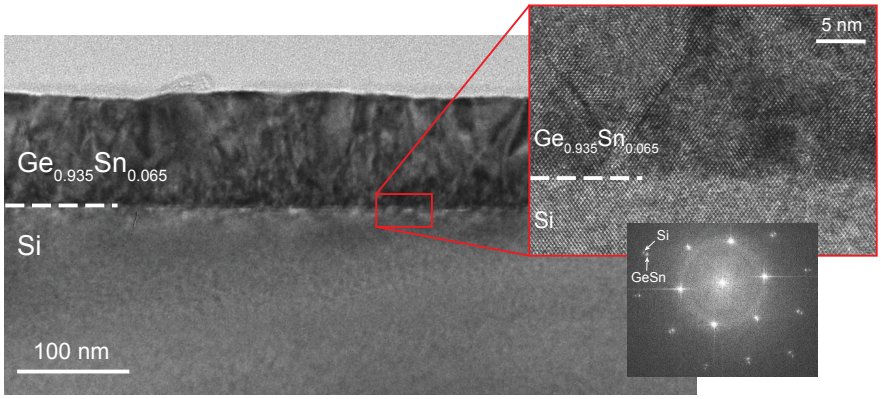


**Figure 2.13:** Transmission electron micrographs of $Ge_{0.935}Sn_{0.065}$ grown directly on Si(001) and a GeSn/Si close up. The inset shows the selected area diffraction pattern.

doubled. Furthermore, for too high $p_{Si_2H_6}$ (90 Pa) the layer quality degrades as evidenced by the $\chi_{min}$ of approx. 50 % (inset of Fig. 2.12 (b)).

### 2.2.2 Crystalline and Optical Quality of Pseudomorphic and Partially Relaxed GeSn and SiGeSn Epilayers

After having determined the appropriate growth parameters including growth temperature range and partial pressures for $Si_2H_6$, $Ge_2H_6$ and $SnCl_4$ to fabricate metastable GeSn and SiGeSn alloys with Sn concentrations exceeding the solid solubility of Sn in Ge by far, the next section addresses the crystalline quality of various Sn-based epilayers and heterostructures. Whereas in the case of SiGeSn ternary alloys no study is published concerning electronic device performance, yet, the device grade quality of GeSn layers with Sn concentrations $\leq$ 8 at.% has been proven by several groups (c.f. chapter 2.1). However, high quality GeSn and SiGeSn layers containing Sn concentrations above 10 at.% grown pseudomorphically on Ge have not been published so far. In addition, the lack of fully or partially relaxed (Si)GeSn epilayers with suitable optical quality prohibits their application for optically active devices up to now.
Thus, the focus of this section rests on the study of the crystalline quality of pseudomorphic as well as partially relaxed $Ge_{1-x}Sn_x$ and $Si_yGe_{1-x-y}Sn_x$ epilayers targeting high Sn concentrations grown on Si(001). Moreover, partially relaxed GeSn buffer layers are used to apply tensile strain in overgrown Ge and GeSn layers.
In a previous study from 2005 [72] it has been suggested to employ cubic GeSn layers as template on Si(001) for high quality Ge or III-V epitaxy thereon. Atomically flat epilayers directly grown on Si(001) by CVD ($Ge_2H_6$ and $H_3GeGeH_3$) are claimed, which reveal low defectivity and high thermal stability compared to former studies using MBE

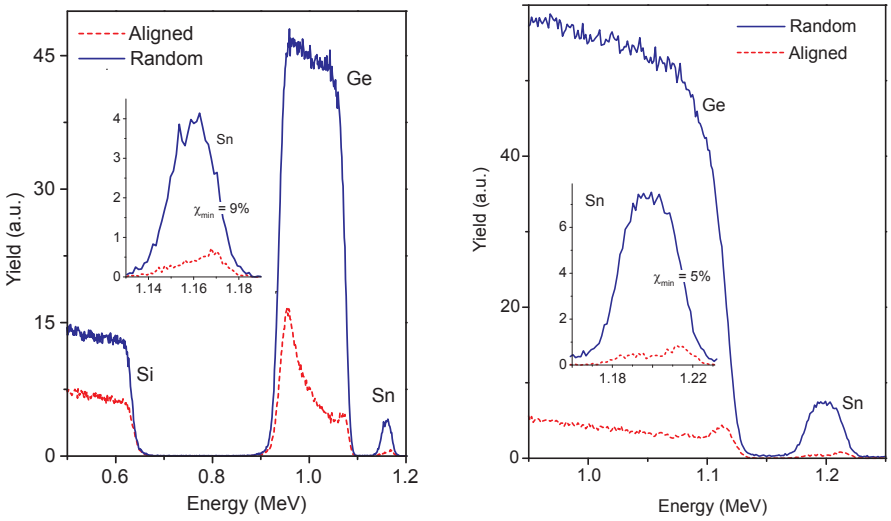


**Figure 2.14:** RBS spectra for (a) 32 nm $Ge_{0.955}Sn_{0.045}$ and (b) 45 nm $Ge_{0.94}Sn_{0.06}$ on top of a *in-situ* grown and a $2.5 - 2.7\,\mu$m thick Ge buffer layer [73], respectively.

[46] and GaAs- as well as Ge-deposition on top of $Ge_{0.98}Sn_{0.02}$ buffer layers have been demonstrated. However, GeSn buffer layers with comparable structural and morphological properties containing higher Sn concentrations directly grown on Si(001) have not been reported, yet. These findings are rather surprising, since the large lattice mismatch in the GeSn/Si system is supposed to result in a surface roughening after a thin wetting layer formation and as a consequence in a high defective epilayer like in the case of low temperatures Ge deposition on Si [34, 73, 35].
The GeSn and SiGeSn layers presented here that are grown directly on Si(001), exhibit $\chi_{min}$ values between 15 % and 21 %. In order to gain additional information about the layer quality TEM images are taken. In Fig. 2.13 a typical image of a $Ge_{0.935}Sn_{0.065}$ layer grown at 400 °C is shown. A large number of defects within the layer and at the GeSn/Si interface is observed (c.f. closeup view) that also move up to the sample surface. No defects going into the Si substrate as well as no $\beta$-Sn precipitation have been found throughout all investigated GeSn and SiGeSn epilayers. The *selected area diffraction* pattern (SAD) reveals monocrystalline $Ge_{0.935}Sn_{0.065}$ and the separation of Si- and GeSn-spots indicate strain relaxation. These findings are similar to the low temperature deposition of Ge on Si(001) rather than to the findings presented in Ref. [72].
A common route to improve the crystalline quality of epilayers in heteroepitaxy is to decrease the lattice mismatch between the epilayer and the substrate. Thanks to the resultant reduced roughening, the defect density can be significantly improved. The most

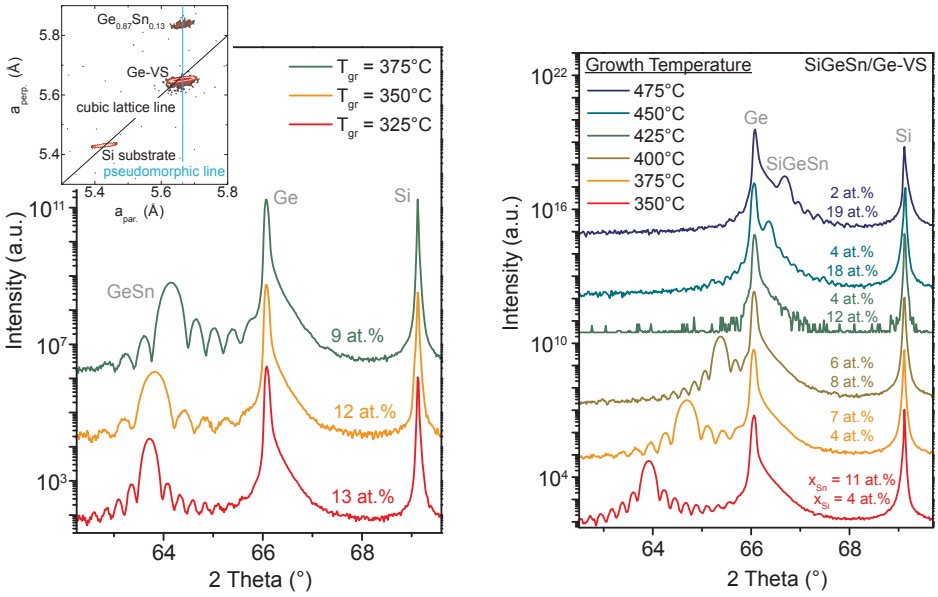


**Figure 2.15:** XRD $\theta/2\theta$-scans of (a) GeSn and (b) SiGeSn layers grown on Ge-VS at 325 °C < $T_{gr}$ < 475 °C. The inset displays the XRD-RSM of 40 nm $Ge_{0.87}Sn_{0.13}$/Ge-VS.

obvious way to achieve this for (Si)GeSn is to employ Ge buffer layers grown on Si(001), so called *Ge virtual substrates* (Ge-VS) [34, 73, 35]. This (Si)GeSn/Ge-VS system is comparable to SiGe/Si heterostructures in terms of lattice mismatch. The effect of approximately 4 Ge atoms in SiGe is similar to the one of 1 Sn atom in GeSn [37]. Hence, the lattice mismatch of $Ge_{0.925}Sn_{0.075}$ to Ge is comparable to the mismatch of $Si_{0.70}Ge_{0.30}$ to Si. The difference in crystalline quality of (Si)GeSn layers grown on two different types of Ge-VS is demonstrated in the following.

A 150 − 250 nm thick *in-situ* grown Ge-VS using $T_{gr}$ = 425 °C and $p_{Ge_2H_6}$ = 5 Pa is compared to 600 − 2700 nm thick Ge buffer layers provided by the University of Warwick and LETI. Details about the properties of these layers can be found in Refs. [73, 35]. In Fig. 2.14 RBS spectra of a 32 nm $Ge_{0.955}Sn_{0.045}$ (a) and a 45 nm $Ge_{0.94}Sn_{0.06}$ (b) layer on top of an *in-situ* grown and a thick Ge-VS are presented, respectively. Compared to the (Si)GeSn layers grown directly on Si the crystalline quality for such layers grown on Ge is significantly improved, as indicated by $\chi_{min}$ values of 9 % (*in-situ* grown Ge-VS) and 5 % (thick Ge-VS) for both the Ge and Sn signal. The former numbers are identical to those of the bare Ge-VS presented above. Thus, the quality of the (Si)GeSn layers is limited to the Ge buffer quality and complete Sn substitutionality is achieved. The lower minimum yield of 5 % is close to the value of structurally perfect Si (3 %) and comparable

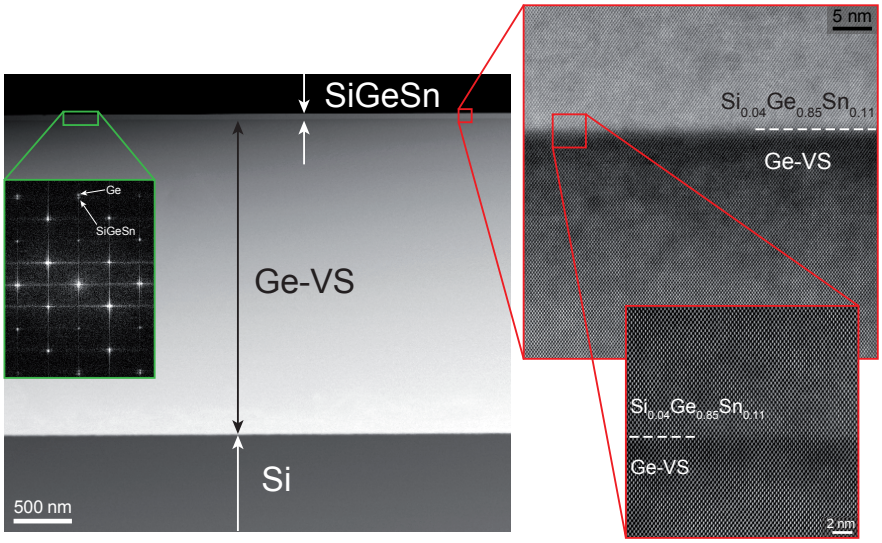


**Figure 2.16:** Low magnification *high angle annular dark field scanning transmission electron micrograph* (HAADF/STEM) of a 50 nm $Si_{0.04}Ge_{0.85}Sn_{0.11}$ layer grown on a 2.7 $\mu$m thick Ge-VS. High resolution STEM image and SAD of the SiGeSn/Ge-VS interface.

to pseudomorphic SiGe layers grown on Si.
Subsequently, GeSn and SiGeSn epilayers grown on thick Ge-VS are analyzed via *X-ray diffraction* (XRD) $\theta/2\theta$-scans and *reciprocal space maps* (RSM). The results for samples grown between 325 °C and 475 °C with Si and Sn concentrations up to 19 at.% and 13 at.%, respectively, are shown in Fig. 2.15. The layer thicknesses are between 25 nm and 65 nm. Without exception, well-shaped GeSn and SiGeSn peaks besides the Si and Ge peaks are observed that are surrounded by thickness fringes on both sides. This indicates pseudomorphic layers with high crystalline quality as well as sharp interfaces and surfaces. In the inset of Fig. 2.15 (a) the XRD-RSM of a 40 nm thick $Ge_{0.87}Sn_{0.13}$ layer is displayed. Here, the peak of the epilayer lies perfectly on the pseudomorphic line above the Ge-VS, which means the in-plane lattice constant, $a_{par}$, of GeSn and Ge are identical, whereas the out-of-plane lattice constant, $a_{perp}$, of the GeSn is larger. This proof of pseudomorphic growth is found for all presented layers in Fig. 2.15. The appearance of the fringes is independent of the growth temperature. Accordingly, the GeSn peaks shift towards lower angles if the Sn concentration is increased, that is, $a_{perp}$ is increased. Owing to the larger cubic lattice constant of GeSn compared to Ge a tetragonal distortion of the GeSn crystal occurs. $a_{par}$ is identical to Ge, thus, according to the Poisson effect, $a_{perp}$ has to increase. Using the bowing corrected Vegard's law [74]:

$$a_0^{\mathrm{Ge_{1-x}Sn_x}} = a_0^{\mathrm{Ge}}(1-x) + a_0^{\mathrm{Sn}}x + b^{\mathrm{GeSn}}x(1-x), \tag{2.5}$$

where $b^{\mathrm{GeSn}}$ is the bowing parameter, that amounts to 0.041 Å [74], and $a_0^{\mathrm{Ge,Sn}}$ are the cubic lattice constants of Ge and $\alpha$-Sn, the Sn concentrations are determined, see Fig. 2.15 (a), which confirm the RBS results. This evidences the full substitutionality of the Sn atoms into the Ge host lattice. In the case of SiGeSn, the SiGeSn peaks shift towards higher angles for a increasing $x_{Si}/x_{Sn}$-ratio. The cubic lattice constants of SiGeSn and Ge perfectly match for Si and Sn concentrations of 12 at.% and 4 at.%, respectively (olive curve in Fig. 2.15 (b)), thus, the XRD peaks overlay. The $x_{Si}/x_{Sn}$-ratio of three, when the lattice constants of SiGeSn and Ge match, is in good agreement with results of [75, 76] taking the +0.16 % tensile strain of the Ge-VS into consideration. For a further increase of this ratio the lattice constant of SiGeSn becomes smaller compared to Ge and consequently pseudomorphic layers (light and dark blue curve in Fig. 2.15 (b)) become tensile strained. The out-of-plane lattice constant is smaller than $a_{perp}$ of Ge and the XRD SiGeSn peak lies between the Ge and the Si peak. The obtained strain values from these XRD measurements lie between +0.4 % (tensile strain) and −1.9 % (compressive strain). Additionally, TEM analysis is carried out on these pseudomorphic layers. A *high angle annular dark field scanning transmission electron micrograph* (HAADF/STEM) of a 50 nm $Si_{0.04}Ge_{0.85}Sn_{0.11}$ layer grown on a 2.7 $\mu$m thick Ge-VS is displayed in Fig. 2.16 as well as a high resolution STEM image and a SAD pattern of the SiGeSn/Ge-VS interface. Neither dislocations in the SiGeSn layer or at the SiGeSn/Ge-VS interface nor any $\beta$-Sn precipitation have been found. The SAD spots of SiGeSn and Ge are in-plane superposed and slightly departed in the out-of-plane direction indicating identical in-plane but different out-of-plane lattice constants. This provides an independent evidence for the coherent growth. The determined change of $a_{perp}$ that is equivalent to a compressive strain of −1.6 % is in perfect agreement with the corresponding XRD-RSM result.

### Plastic Strain Relaxation of (Si)GeSn Epilayers on Ge-VS

Apart from pseudomorphic (Si)GeSn epilayers grown on Ge with high monocrystalline quality, fully or partially relaxed alloys can be employed for a variety of applications as mentioned above. The strain relaxation of GeSn and SiGeSn on thick Ge-VS is presented and discussed in the following. As shown above GeSn layers can be grown pseudomorphically, thus, nearly defect-free on Ge. However, due to the larger cubic lattice constant of GeSn compared to Ge the thickness of fully strained layers is limited by the critical thickness for plastic strain relaxation [77, 78]. Up to a certain layer thickness elastic strain induced by the lattice mismatch between the substrate, here Ge, and the epilayer can be accumulated within the GeSn epilayer. This strain increases with lattice mismatch, hence higher Sn concentrations. At a certain layer thickness that exponentially depends on the lattice mismatch [77], it is energetically more favorable for the system to form *misfit dislocations* (MDs) at the interface between the epilayer and the substrate in order to relief the stress within the epilayer [79]. If the layer thickness is further increased the density of MDs at the interface raises and consequently the degree of strain relaxation.

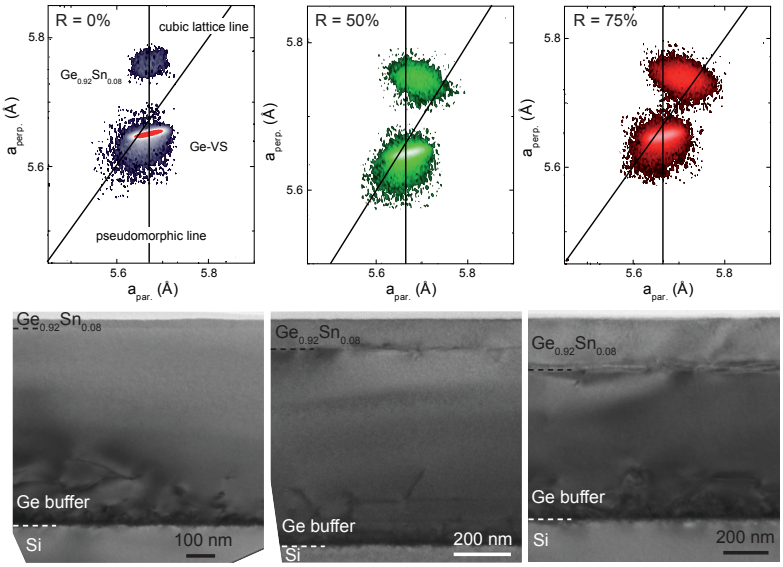


**Figure 2.17:** Top row: XRD-RSM of $Ge_{0.92}Sn_{0.08}$ layers with thicknesses of 30 nm (left), 90 nm (middle) and 195 nm (right). Bottom row: the corresponding TEM micrographs.

In the SiGe/Si system the MD formation at the interface is necessarily accompanied by the creation and glide of 60° *threading dislocations* (TDs) [79]. The resulting high defect density of those strain relaxed SiGe layers leads to a significant degradation of crystalline as well as optical quality [30].
In Fig. 2.17 XRD-RSM and TEM results of $Ge_{0.92}Sn_{0.08}$ grown on 600 nm Ge-VS [35] with thicknesses ranging from 30 nm over 90 nm to 195 nm are presented. Whereas the diffraction peak of the 30 nm layer (top left) is perfectly aligned to the pseudomorphic line of the Ge-VS, the peaks of the thicker layers are shifted towards the cubic lattice line. This means that the in-plane lattice of the thinnest GeSn and the Ge-VS match and both the in-plane and out-of-plane lattice constants of the thicker layers approach the bulk lattice constant of $Ge_{0.92}Sn_{0.08}$. In the TEM images the evolution of the defect formation can be traced. In the case of the fully strained layer (bottom left) no defects are found within the layer and at the interface towards the Ge-VS. Solely in the lower part of the Ge-VS there are defects due to its growth process [35]. For the 90 nm thick $Ge_{0.92}Sn_{0.08}$ layer (bottom middle) defects are obviously formed at the GeSn/Ge-VS interface and an even higher density of defects is obtained for the thickest sample (bottom right). In addition, in the latter case the dislocations seem to form loops extending into the Ge-VS. However, slightly above the interface up to the surface a nearly perfect crystalline quality is obtained for the partially relaxed GeSn layers.
For a deeper analysis a low magnification TEM micrograph of a partially relaxed, 225 nm

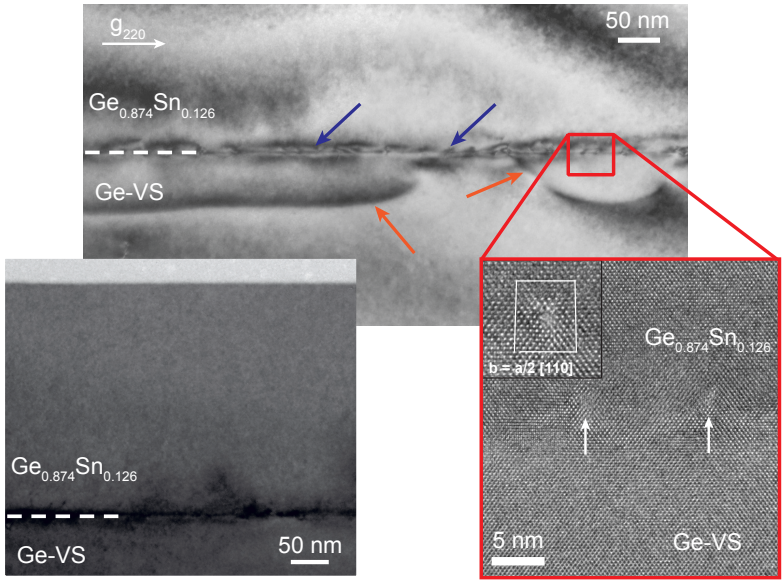


**Figure 2.18:** Low magnification and high resolution TEM images of a 225 nm thick $Ge_{0.874}Sn_{0.126}$ layer and its interface to the Ge-VS.

thick $Ge_{0.874}Sn_{0.126}$ layer as well as high resolution closeups of the GeSn/Ge interface are shown in Fig. 2.18. Here, the micrograph is taken in a (220) 2-beam condition in order to increase the contrast at the dislocations. A crystalline layer with smooth surface without Sn precipitation is observed. No crystal defects are found in the GeSn "bulk", whereas at the GeSn/Ge interface a high density of misfit dislocations (blue arrows) with a mean spacing of 12.5 nm is observed. In addition to the misfit defects at the interface, dislocation loops (orange arrows) are formed in the Ge-VS and pinned at the GeSn/Ge interface. These dislocation half-loops may be an indication of a particular relaxation mechanism. The large number of bulk point defects, typical for very low temperature epitaxy [37], is assumed to be the origin of these dislocation loops via climb processes. The enlargement of the loops by acquiring additional point defects during growth is accompanied by the extension of the interface misfit segments. This in turn leads to plastic strain relaxation. A similar relaxation model has been observed in Si/SiGe heterostructures starting with low temperature buffer layers prior to the growth of a strain relaxing graded SiGe layer [80, 81, 82]. With low temperature Si buffer layers threading dislocations are prevented from propagating into the SiGe layer [83] leading to very low threading dislocation densities $\leq 10^4\,\mathrm{cm}^{-2}$. The type of the misfit dislocations was studied by measuring the Burgers vector tilting the sample 3° off the (110) pole around the (220) direction (see Fig. 2.18). Lomer dislocations with Burger's vectors of a/2 [110] and edge dislocations with Burgers vectors of a/4 [110] are found. This type of dislocations is known to be the

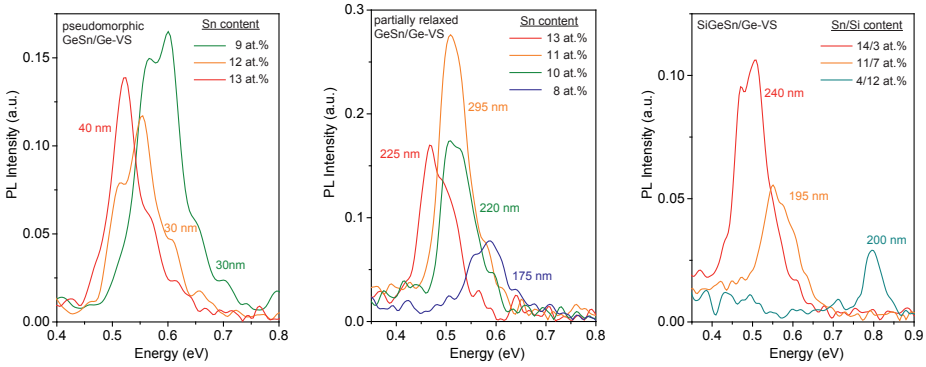


(a) (b) (c)

**Figure 2.19:** Room temperature PL spectra of (a) pseudomorphic GeSn, (b) partially relaxed GeSn and (c) pseudomorphic and partially relaxed SiGeSn layers.

most efficient one regarding strain relaxation [84]. Apparently, no threading dislocation reaching the sample surface can be seen. By counting the threading dislocations within many micrographs I estimate a threading dislocation density (TDD) below $5 \times 10^6\,\mathrm{cm}^{-2}$. Similar observations are made for partially strain relaxed SiGeSn layers with 14 at.% Sn and 3 at.% Si suggesting a relaxation mechanism akin to the one obtained in GeSn.

The optical quality of pseudomorphic and partially strain relaxed GeSn and SiGeSn layers is analyzed by means of room temperature *photoluminescence* (PL). Here, a continuous-wave solid-state laser emitting at a wavelength of 532 nm is focused to a spot size of approx. 5 $\mu$m. The emitted luminescence is analyzed using a Fourier transform infrared spectrometer and detected with a liquid nitrogen-cooled InSb detector with a cut-off at 0.27 eV.

Figure 2.19 (a) shows the PL results of pseudomorphic GeSn layers with Sn concentrations between 9 at.% and 13 at.% and thicknesses of $30 - 40$ nm. The measured signal is stemming from direct transitions between the Γ-valley and the valence bands, since at room temperature electrons are thermally excited from the L- into the Γ-valley [85, 86]. A detailed PL analysis including temperature dependence is presented in chapter 4. The clear peaks are superimposed by Fabry-Perot oscillations due to the Ge-VS [87] and red-shifted with increasing Sn content. The highest intensity is observed for the $Ge_{0.81}Sn_{0.09}$ layer, which might indicate a superior layer quality.

In the case of partially relaxed GeSn, see Fig. 2.19 (b), the intensity increases with increasing Sn concentration except for a $Ge_{0.87}Sn_{0.13}$ epilayer with a thickness of 225 nm.

PL spectra of relaxed and fully strained SiGeSn layers are presented in Fig. 2.19 (c). Again, the intensity increases, whereas the peak position is shifted to lower energies for increasing $x_{Sn}/x_{Si}$ ratio.

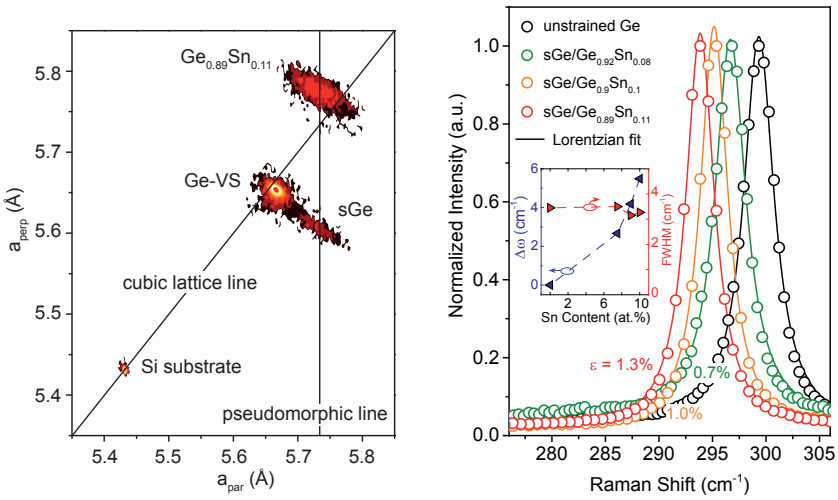


(a) (b)

**Figure 2.20:** (a) XRD-RSM of a sGe/$Ge_{0.89}Sn_{0.11}$/Ge-VS heterostructure. (b) Normalized Raman spectra for various tensile strained Ge layers grown on GeSn strain relaxed buffer layers. Inset: Peak shift vs. Sn concentration.

### 2.2.3 Highly Tensile Strained Ge and GeSn

The high quality, partially strain relaxed $Ge_{1-x}Sn_x$ and $Si_yGe_{1-x-y}Sn_x$ layers are subsequently used as buffer layers, so-called *strain relaxed buffer layers* (SRBs), to introduce tensile strain in overgrown Ge and $Ge_{1-z}Sn_z$ (with $z < x$). The strain in overgrown Ge(Sn) layers can be adjusted by choosing the appropriate Sn content or by the degree of relaxation of the buffer. In order to measure the applied strain in the topmost epilayers, XRD-RSM and Raman spectroscopy are carried out.

Figure 2.20 (a) shows the XRD-RSM of a 70 nm strained Ge layer on a 250 nm $Ge_{0.89}Sn_{0.11}$ SRB. A 73 % buffer relaxation results in a 1.4 % biaxial tensile strained Ge layer coherently grown on top. This obtained value is close to the required biaxial tensile strain for the indirect to direct bandgap transition in Ge [28, 29] and exceeds by far previously reported strain levels using GeSn SRBs [88, 38].

Complementary Raman spectra of three differently tensile strained Ge layers as well as unstrained bulk Ge are shown in Fig. 2.20 (b). GeSn SRBs with Sn concentrations ranging from 8 at.% to 11 at.% are used. By means of Lorentzian fits the shifts of the tensile strained Ge layers, $\Delta\omega$, towards lower wavenumbers are extracted (see inset of Fig. 2.20 (b)). The incorporated strain can be determined via [89]:

$$\Delta\omega = b\epsilon_{||}, \tag{2.6}$$

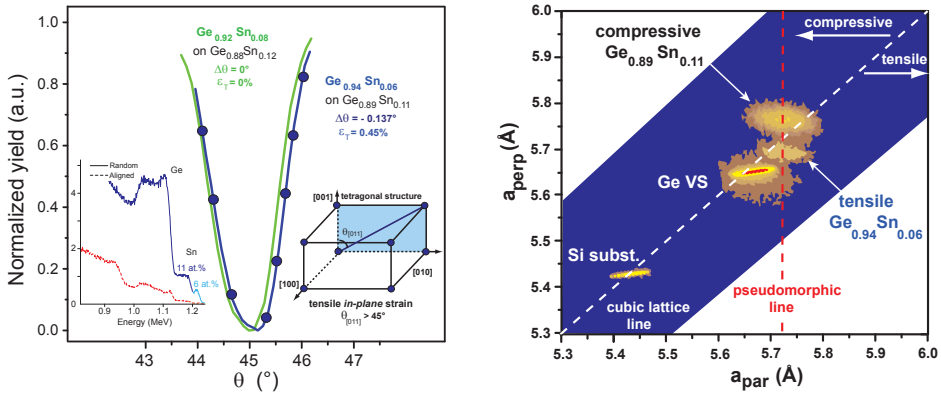


**Figure 2.21:** (a) RBS ion channeling angular yield scans of sGeSn/GeSn/Ge-VS heterostructures. Inset: RBS spectra of $sGe_{0.94}Sn_{0.06}$ grown on a GeSn SRB. (b) XRD-RSM of a $sGe_{0.94}Sn_{0.06}/Ge_{0.89}Sn_{0.11}$/Ge-VS heterostructure.

where $\epsilon_{||}$ is the biaxial strain and $b = -415\,\mathrm{cm}^{-1}$ [90]. The obtained strain values are in agreement with the XRD results. Moreover, the symmetry of the Ge vibration modes as well as the strain independent *full width at half maximum* (FWHM) values slightly above $3\,\mathrm{cm}^{-1}$ indicate high crystalline quality.
Similar partially strain relaxed $Ge_{1-x}Sn_x$ SRBs are employed to fabricate fully strain relaxed or tensile strained $Ge_{1-y}Sn_y$ epilayers with $y < x$. Here, the quantitative determination of the applied strain within the thin layers is a challenging task. Hence, besides XRD-RSM measurements, RBS ion channeling angular yield scans are carried out that provide the absolute angles between different crystal directions. This technique allows to extract the full strain tensor [91]. These channeling scans are performed through the [001] sample normal and the [110] direction within the (100) plane using solely the Sn backscattering signal of the topmost layer. Note, a 10 nm Ge interlayer is grown between the GeSn SRB and the topmost GeSn in order to facilitate the separation of the Sn signals. A sketch of a tetragonal distorted lattice is shown in the inset of Fig. 2.21 (a). For unstrained crystals the angle between the [001] and [110] direction equals 45 °. If the layer is tensile strained larger angles are measured. The angular scans in Fig. 2.21 (a) clearly exhibit that a 25 nm $Ge_{0.92}Sn_{0.08}$ layer grown on top of a 295 nm $Ge_{0.88}Sn_{0.12}$ SRB is fully strain relaxed. The measurement of a 30 nm $Ge_{0.94}Sn_{0.06}$/265 nm $Ge_{0.89}Sn_{0.11}$/Ge-VS heterostructure shows a angular deviation of $\Delta\theta^{GeSn}_{[110]} = 45\,^\circ - \Delta\theta_{[110]} = -0.137\,^\circ$ within the thin layer evidencing a tetragonal strain of 0.45 %. This corresponds to a biaxial tensile strain of approx. 0.4 %. Furthermore, the RBS random and aligned spectra of this structure shown as inset in Fig. 2.21 (a) provides a $\chi_{min}$ of approx. 6 % without dechanneling at the sGeSn/GeSn SRB interface indicating high crystalline quality.

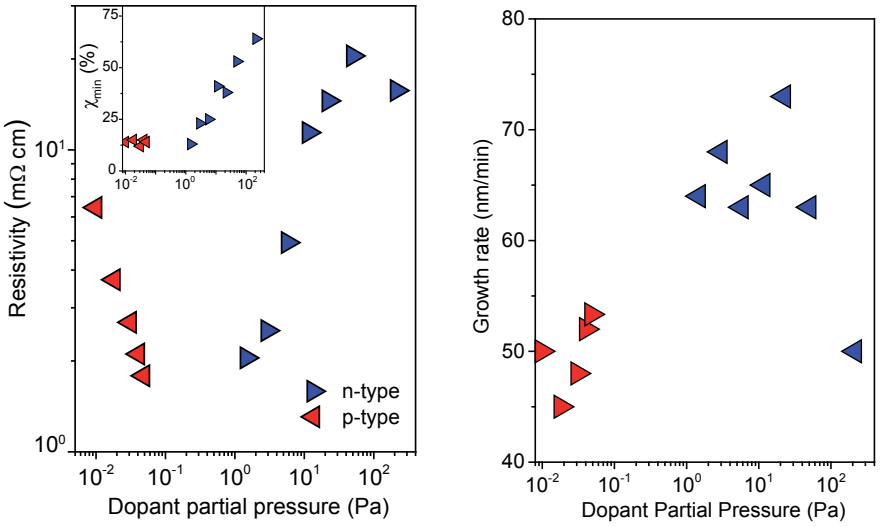


(a) (b)

**Figure 2.22:** (a) Resistivity, $\chi_{min}$ and (b) growth rate of n- and p-type doped SiGeSn layers grown at 425 °C as function of dopant partial pressure.

The corresponding XRD-RSM is displayed in Fig. 2.21 (b). Along with peaks stemming from the Si substrate and the Ge-VS two GeSn peaks lie on both sides of the cubic lattice line. For the $Ge_{0.89}Sn_{0.11}$ buffer layer a degree of relaxation, $R$, of approx. 69 % is measured. The peak of the topmost layer is found on the pseudomorphic line of the $Ge_{0.89}Sn_{0.11}$ buffer evidencing coherent epitaxial growth. The use of these layers for MOSFET applications is addressed in chapter 3.

### 2.2.4 Doping

In order to study the dopant incorporation and its influence on (Si)GeSn epitaxy on Si(001) and Ge-VS sheet resistance measurements have been performed. For efficient carrier injection, a uniform carrier distribution and low electrical current doped (Si)GeSn epilayers with low sheet resistivity are required. SiGeSn:P and SiGeSn:B layers have been grown at 425 °C using $B_2H_6$ (100 ppm in $H_2$) and undiluted $PH_3$ precursors. At these low growth temperatures hydrogen desorption is known to be one of surface reactions that limits the growth process, i.e. growth rate. $B_2H_6$ is supposed to enhance the hydrogen desorption, hence much lower partial pressures are needed to achieve reasonably high doping concentrations compared to $PH_3$.
In Fig. 2.22 (a) the resistivity as a function of the dopant partial pressure is shown. For

increasing dopant partial pressure the SiGeSn layer's resistivity decreases for the Boron case and increases for the case of Phosphorous. In the latter case, a reduced layer quality has been found for $PH_3$ partial pressures above 10 Pa through an increase of the $\chi_{min}$ (see inset of Fig. 2.22 (a)). In Si epitaxy it has been shown that high $PH_3$ partial pressures might lead to P segregation and, thus, layer quality degradation. This could be also the case for the SiGeSn growth, since in our study rather large $PH_3$ partial pressures have been used. The growth rates for doped ternaries do not show any dopant partial pressure dependence (c.f. Fig. 2.22 (b)) at least at a constant growth temperature of 425 °C. Interestingly enough, the growth rate for SiGeSn:P is higher than for SiGeSn:B layers. In the latter case growth rates comparable to undoped SiGeSn (45 nm/min) have been obtained. Since large $Si_2H_6$ (60 Pa) and $Ge_2H_6$ (120 Pa) partial pressures have been utilized the rather small amount of $B_2H_6$ does not significantly affect the growth rate. As shown above a higher amount of $Si_2H_6$ results in reduced growth rates compared to GeSn binaries. Additionally, Meyerson *et al.* [92] have demonstrated preferential $PH_3$ adsorption over Si hydrides, that is, more $PH_3$ molecules might get adsorbed compared to $Si_2H_6$ reducing its effect on the growth rate, hence, faster growth can be achieved. The large amount of P atoms on interstitial lattice sites leads to a fast drop of the electrical active dopant concentration of more than one order of magnitude. On the other hand, for higher $B_2H_6$ partial pressures more B atoms are incorporated on Ge lattice sites leading to increased dopant activation up to $2 \times 10^{19}\,cm^{-3}$ without layer quality degradation. The amount of B incorporated is limited here by the high dilution of the $B_2H_6$ (100 ppm) while pure $PH_3$ (100 %) is used for P doping, which allows higher doping levels.

## 2.3 Summary

The epitaxial growth of GeSn binary and SiGeSn ternary alloys using RP-CVD and a precursor combination of $Ge_2H_6$, $Si_2H_6$ and $SnCl_4$ has been investigated. Here, special attention has been paid to the crystalline and optical quality of fully strained and partially relaxed, high Sn content (Si)GeSn epilayers. Using partially strain relaxed GeSn buffer layers, overgrown Ge and GeSn layers have been biaxially tensile strained. Dopant incorporation in SiGeSn ternaries has been studied.

- It has been shown that GeSn as well as SiGeSn alloys can be epitaxially grown on Si(001) within the temperature window of $375 - 475\,°C$. Here, temperature dependent Sn and Si concentrations of max. 10 at.% and 19 at.% have been achieved. Decreasing the partial pressure of $SnCl_4$ at constant $p_{Ge_2H_6}$ results in a lower growth rate. The addition of $Si_2H_6$ also leads to a reduced growth rate but at the same time higher Sn concentrations compared to the GeSn growth are obtained.

- By means of Ge buffer layers (Ge-VS) the growth temperature window for (Si)GeSn layers is extended to $325 - 475\,°C$. As a consequence higher Sn concentrations of max. 13 at.% are determined. Owing to the reduced lattice mismatch nearly defect-free pseudomorphic (Si)GeSn layers can be grown.

- High quality, strain relaxed GeSn alloys are obtained by exceeding the critical thicknes for plastic strain relaxation. The relaxation occurs mainly via 90 ° Lomer misfit dislocations rather than 60 ° threading dislocations. Hence low threading dislocation densities of approx. $5 \times 10^6\,cm^{-2}$ are estimated.

- Both fully strained and partially relaxed (Si)GeSn epilayers exhibit room temperature photoluminescence. The peak positions shift according to the bandgap of the alloys.

- By means of partially relaxed GeSn buffer layers with Sn concentrations of 11 – 12 at.% and degrees of strain relaxation of approx. 70 % high biaxial tensile strain of up to 1.4 % and 0.4 % are applied to coherently overgrown Ge and $Ge_{0.94}Sn_{0.06}$, respectively.

# Chapter 3

## Electrical Characterization

In the following chapter Si-Ge-Sn heterostructures, whose epitaxial growth and structural characterization have been discussed in chapter 2, are employed to investigate essential building blocks of nanoelectronic devices, i.e. gate stack and source/drain contacts. Thanks to the developed surface reaction enhanced CVD growth mode, high quality strain relaxed $Ge_{1-x}Sn_x$ buffer layers (SRBs) with large lattice constants are synthesized and used as biaxial stressor layer for elemental Ge and $Ge_{1-y}Sn_y$ (with $y < x$). This enables the epitaxial growth of novel, highly tensile strained Ge (sGe) and GeSn (sGeSn) semiconductors, that are supposed to provide superior electron and hole mobility compared to sSi and unstrained Ge. At the beginning of this chapter, a brief discussion is provided about the potential of these novel materials to be employed as channel materials in *metal-oxide-semiconductor field effect transistors* (MOSFET) or *tunnel field effect transistors* (TFET). The following characterization of the interface quality between these highly tensile strained layers and high-k oxide layers, i.e. $HfO_2$ and $Al_2O_3$, goes beyond the state-of-the-art, since the main focus so far has been put on biaxial compressively strained GeSn layers [59, 93, 94, 95]. Prior to the fabrication and characterization of *MOS capacitors* (MOSCAPs) using sGe and sGeSn, the theory of admittance characterization for small bandgap MOSCAPs is described. Subsequently, a detailed analysis of the surface passivation, Sn diffusion during *forming gas annealing* (FGA) and *Capacitance-Voltage* (CV) characteristics follows. Finally, GeSn and SiGeSn layers pseudomorphically grown on Ge(001) containing up to 12 at.% Sn and 18 at.% Si are used in order to study the phase formation, morphology and conductive properties of NiGeSn ternary and NiSiGeSn quaternary alloys suitable as low resistance metallic contacts.

### 3.1 GeSn as Channel Material

Two of the most prominent routes to boost the electronic device performance of transistors in integrated circuits (ICs) in order to keep up with Moore's law are to improve the conductive properties of the channel material (sSi) of field effect devices, i.e. enhance the carrier mobility, or to introduce novel device architectures like FinFETs and Tunnel FETs. Recently, great progress has been achieved by implementing new channel materials such as SiGe alloys or Ge in MOSFET devices [96, 97, 98, 99, 100]. Since these materials provide higher bulk hole mobility [101] compared to Si, they might be a choice for the next generation of p-MOSFETs, in particular if one keeps in mind that the bulk hole mobility

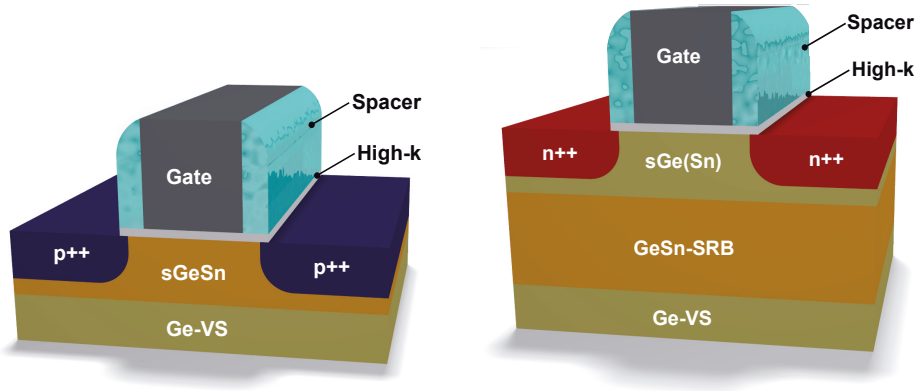


(a) p-MOSFET (b) n-MOSFET

**Figure 3.23:** (a) p-type and (b) n-type MOSFETs based on Ge and GeSn alloys exhibiting high carrier mobilities.

in Ge is highest amongst all semiconductors including group III/V compounds [97]. Moreover, strain engineering is essential for Ge-based materials in order to outperform sSi [102], because of its well-known and highly optimized properties in terms of mobility enhancement, surface passivation, scaling and process optimization. Compressively strained GeSn channel p-MOSFETs grown on Ge virtual substrates containing up to 7 at.% have been investigated by several groups [93, 103, 104] and they exhibit a significant mobility boost compared to Ge control devices. Introducing tensile strain is known to be even more beneficial in terms of carrier mobility, however there are rather few studies on tensile strained GeSn- [14, 105, 106] and GeSn n-MOSFETs [59] so far.
The carrier mobility in a semiconductor is mainly affected by the carrier effective mass and the scattering mechanisms that are related to the electronic band structure. Hence, manipulating the band structure may lead to a significant carrier mobility enhancement [101]. In this regard, the most efficient techniques are to add atoms of a different element into the host lattice via alloying or to introduce strain. Recently, Sau *et al.* [107] suggested that alloying Ge with Sn might lead to an even increased bulk mobility of holes and electrons compared to elemental Ge, opening a path towards high performance group IV p- and n-MOSFETs on the same material platform. Furthermore, GeSn binary alloys coherently grown on Ge substrates (c.f. Fig. 3.23 (a)) exhibit large compressive strain, as shown in chapter 2, leading to a split of the light hole (LH) and heavy hole (HH) valence band degeneracy and in turn to reduced intervalley phonon scattering. Here, the valence band splitting, $\Delta E_{HH-LH} = E_{HH} - E_{LH}$, increases with the amount of substitutional Sn atoms, i.e. for $x_{Sn} = 10$ at.% a splitting of approx. 90 meV has been predicted [108]. Thus, the layer structure shown in Fig. 3.23 (a) might be beneficial for p-MOSFETs. By means of GeSn SRBs high tensile strain can be introduced to elemental Ge and GeSn

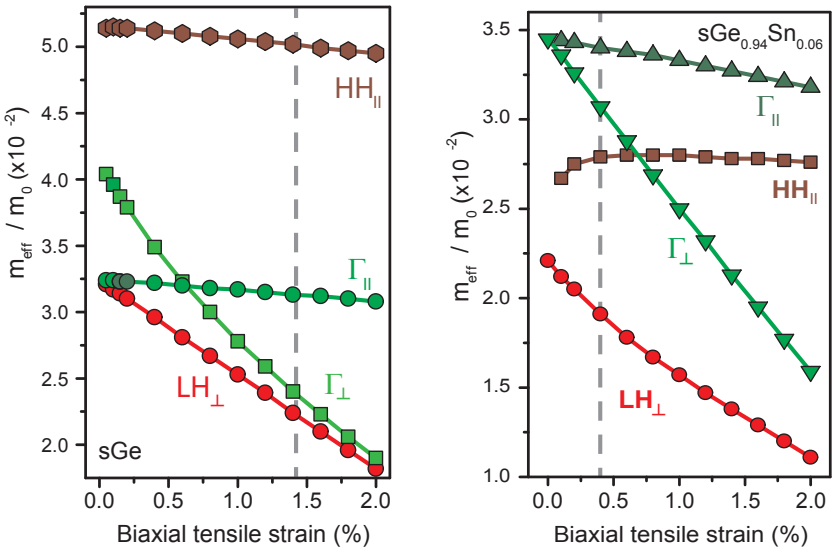


**Figure 3.24:** Effective masses as function of biaxial strain for (a) strained Ge and (b) strained GeSn containing 6 at.% Sn. The gray lines represent the experimentally achievable strain values.

layers as illustrated in Fig. 3.23 (b). Besides the valence band splitting this offers the possibility to achieve a direct bandgap group IV semiconductor. If the Γ valley with its low effective mass is pulled below the L valleys electrons start to populate states of this band lying in the center of the Brillouin zone. The increased occupancy of the Γ band would lead to a large increase of the electron mobility up to 25000 $cm^2$/Vs [107, 101]. Those layers are very promising for future n-MOSFETs.

In cooperation with the University of Leeds, band structure calculations (c.f. Fig. 3.24 and 3.25) have been carried out based on the $8 \times 8$ k·p method including strain effects [109] and experimental epitaxial results. In Fig. 3.24 the effective masses of tensile strained Ge (a) and GeSn (b) at room temperature for the HH, LH and Γ are presented. Here, 6 at.% Sn are assumed and the experimentally achievable strain levels are marked with dashed gray lines. All investigated masses decrease with increasing strain. The strongest change is observed for the transversal masses, $LH_{\perp}$ and $\Gamma_{\perp}$, whereas the longitudinal masses, $HH_{||}$ and $\Gamma_{||}$, only slightly change with biaxial tensile strain for both investigated materials. Comparing unstrained Ge and GeSn, the lowest effective masses for holes are observed for the alloy. Even for the experimentally achievable strain levels of 1.4 % in Ge the effective hole masses are still below those values of moderately strained $Ge_{0.94}Sn_{0.06}$. These results indicate that alloying Ge with Sn and applying tensile strain might result in superior hole

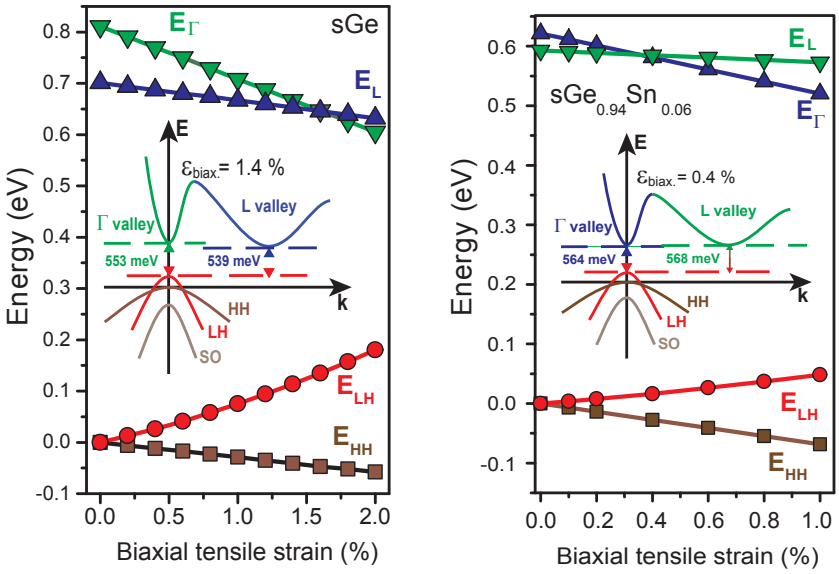


**Figure 3.25:** Conduction band valley energies of the Γ- and L-point as well as HH and LH energies for (a) biaxial tensile strained Ge and (b) GeSn with 6 at.%.

mobility compared to Ge devices. In the case of the electron effective masses the 1.4 % strained Ge exhibits lower values compared to 0.4 % strained GeSn. However, the lowest masses may be also achieved in highly tensile strained GeSn with 6 at.% Sn.

### Sn-Based Heterostructures for Tunnel FETs

Compared to conventional MOSFETs, whose principle is based on thermionic emission, the current in TFETs is dominated by band-to-band tunneling from source to channel. The high energy part of the Fermi distribution of carriers in the source is effectively cut-off, that is, the electronic system is "cooled" down, allowing subthreshold slopes below 60 mV/decade [2, 110]. Due to these steeper slopes a significant reduction of the device supply voltage can be achieved [2]. The main challenge for the optimization of TFETs, i.e. Si TFETs, however, is to overcome rather poor on-currents. In this regard the most important parameter is the transmission probability, $T_{WKB}$, which can be calculated using the *Wentzel-Kramer-Brillouin* (WKB) approximation [111, 112]:

$$T_{WKB} \approx \exp\left(-\frac{4\lambda\sqrt{2m*}\sqrt{E_g^3}}{3q\hbar(E_g+\Delta\Phi)}\right). \tag{3.7}$$

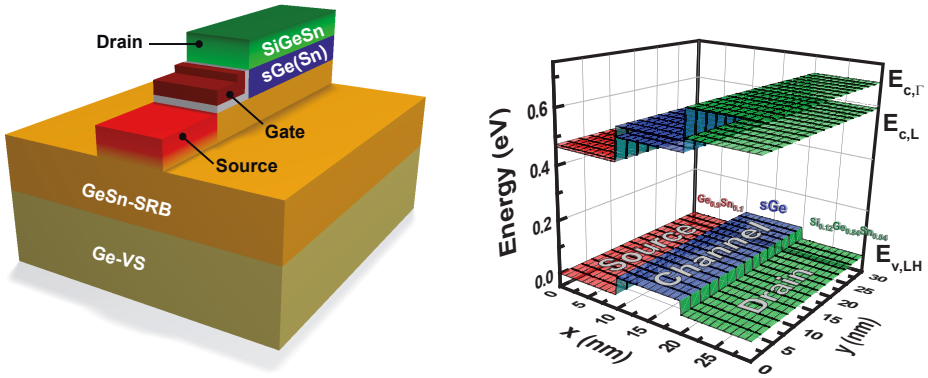


(a) (b)

**Figure 3.26:** (a) TFET design based on a direct bandgap group IV semiconductor, i.e. sGe or sGeSn. The corresponding band alignment of this heterostructure is shown in (b).

Here, $m^*$ is the effective mass, $E_g$ is the bandgap, $\lambda$ is the screening tunneling length and $\Delta\Phi$ is the energy window of carriers that are able to tunnel into the channel. Based on this equation, low bandgap semiconductors providing low effective masses are ideal materials for source/channel junctions in TFETs.
The tunneling process, hence the on-current, in indirect semiconductors like Si or Ge is dominated by indirect tunneling processes, where the required change of momentum of the tunneling carrier is provided by phonon absorption or emission. In contrast, for fundamental direct bandgap semiconductors no phonon is necessary for the band-to-band tunneling, which might lead to an enhanced tunneling probability [3], hence, higher on-currents. Since the off-current is also based on tunneling processes, i.e. from the channel into the drain, large bandgap semiconductors with an indirect bandgap are advantageous. The simulated energies at the critical points in the Brillouin zone (LH, HH, Γ- and L-point) of Ge and $Ge_{0.94}Sn_{0.06}$ as function of biaxial tensile strain are shown in Fig. 3.25. For increasing strain the bandgap of both materials shrinks significantly. Whereas the transition from an indirect to direct semiconductor in Ge occurs at a strain level $> 1.5\,\%$, less strain ($0.4\,\%$) is needed in $Ge_{0.94}Sn_{0.06}$. Moreover, the LH and HH split increases with biaxial tensile strain. For the layers under investigation in this chapter with the highest tensile strain, i.e. $1.4\,\%$ strained Ge and $0.4\,\%$ strained $Ge_{0.94}Sn_{0.06}$, the calculated bandgaps amount to 539 meV and 564 meV, respectively. Here, only the sGeSn layer is claimed to provide a fundamental direct bandgap. Nonetheless, both materials are promising channel materials in future TFET devices.
A possible layer structure of a group IV TFET based on strained Ge or GeSn as direct bandgap channel material is displayed in Fig. 3.26 (a). The GeSn-SRB - in this example with a Sn concentration of 10 at.% - epitaxially grown on a Ge-VS is used to tensile strain

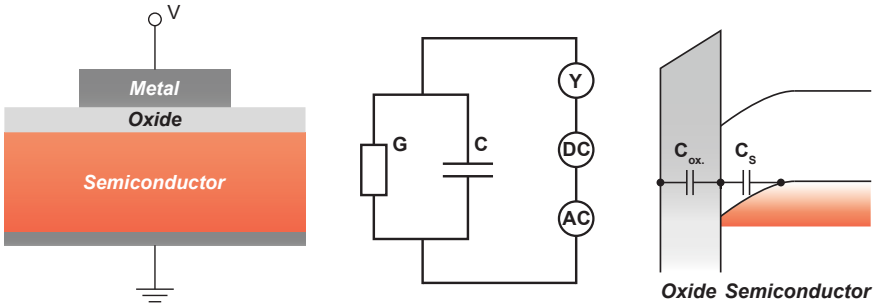


**Figure 3.27:** (left) Layer structure of a MOSCAP. (middle) Equivalent circuit including a DC biasing and AC probing signal. (right) The capacitance consists of two contributions, namely the oxide capacitance $C_{ox}$ and the semiconductor capacitance $C_S$.

the Ge or GeSn layer on top and at the same time act as the source electrode. For the band structure calculations this $Ge_{0.9}Sn_{0.1}$ SRB is assumed to be fully strain relaxed. For the drain side a SiGeSn layer is suggested with 4 at.% Sn and 12 at.% Si to ensure a large indirect bandgap and consequently reduced tunneling at the channel/drain junction. The calculated electronic band diagram for such a structure is shown in Fig. 3.26 (b); all $Ge_{1-y}Sn_y$ layers with $y < 0.1$ including elemental Ge ($y = 0$) grown directly on cubic $Ge_{0.9}Sn_{0.1}$ undergo the desired indirect to direct transition. Furthermore, the simulation results show that the tensile strained $Si_{0.12}Ge_{0.84}Sn_{0.04}$, used as drain contact, indeed provide a larger indirect bandgap compared to the channel material. Thus, this concept fulfills the requirement of a small tunneling barrier at the source/channel junction, in order to achieve high on-current, and simultaneously it allows for the reduction of both the ambipolar behavior and the leakage current.

## 3.2 Strained (Si)Ge(Sn) Metal-Oxide-Semiconductor Capacitors

Although Si provides lower bulk carrier mobility compared to Ge, which was the initial channel material of transistors, the digital revolution was mainly driven by ICs relying on transistors with Si channels. This tremendous success is owed to the high quality and chemical stability of the $SiO_2$/Si interface formed naturally when Si is exposed to air. On the contrary Ge suffers from a rather poor $GeO_x$/Ge ($1 \leq x \leq 2$) interface quality, especially in terms of electrical properties. However, recent success concerning the surface passivation of bulk Ge [113, 94] including gate dielectric deposition [114, 115] has again enabled the integration of Ge into high performance MOSFETs. For the implementation of new semiconductors (non-Si) as channel materials in MOSFET or TFET devices the gate stack formation is known to be one of most critical issues. Here, the surface passivation

of the channel material is the key process, in order to achieve high quality semiconductor-dielectric interfaces, i.e. low density of interfacial trap states, low hysteresis etc. Especially for TFET applications a superior gate control is required making a detailed study of the semiconductor-dielectric interface indispensable.
In this section the interface properties of differently strained Ge and GeSn surfaces and various high-k dielectrics, namely $Al_2O_3$ and $HfO_2$, are investigated. The main analysis has been done via admittance characterization (C-V and G-V measurements) of Ge, sGe and sGeSn MOSCAPs. In order to apply tensile strain GeSn SRBs are used, whose epitaxial growth and characterization have been demonstrated in chapter 2. Due to the metastable nature of GeSn alloys and the tendency of Sn atoms to segregate towards the sample surface, special attention needs to be drawn to Sn-diffusion and strain relaxation during capacitor processing via *time of flight secondary ion mass spectrometry* (ToF-SIMS), XRD-RSM and TEM analysis. First, the principle of MOSCAP characterization is presented mainly based on standard MOS admittance theory developed for Si-based devices [111, 116]. However, in the case of non-Si and low bandgap semiconductors, this treatment has to be expanded to ensure proper data interpretation regarding *interfacial trap densities* ($D_{it}$), *flatband voltage* ($V_{fb}$) shifts, doping or fixed oxide charges. These extensions to the admittance theory have been introduced by Martens *et al.* [117]. On the basis of these findings, temperature dependent ($300\,K - 80\,K$) admittance experiments for sGe and sGeSn MOSCAPs are presented and discussed.
On the left of Fig. 3.27 the sketch of a MOSCAP layer structure is shown. An oxide layer is deposited on top of the semiconductor most likely by *Atomic Layer Deposition* (ALD). By means of a topmost metal plate and an ohmic contact at the bottom of the semiconductor, the structure can be biased using a DC voltage source. A probing AC signal is additionally applied in order to measure the admittance of the MOSCAP:

$$Y = G + i\omega C. \tag{3.8}$$

Here $G$ and $C$ depict the conductance and capacitance, respectively. The admittance is measured using a Keithley 4200-SCS parameter analyzer. The equivalent circuit of an admittance measurement of a MOSCAP is shown in the middle of Fig. 3.27. Whereas from the maximum capacitance, $C_{ox}$, the *equivalent oxide thickness* (EOT) can be determined, the doping concentration can be extracted using the depletion capacitance dominated by the semiconductor capacitance, $C_S$. For an ideal MOSCAP these capacitances are connected in series (c.f. on the right in Fig. 3.27). All measurements are carried out within the frequency range between 1 kHz and 1 MHz, hence, the following theoretical considerations are limited to this range as well.

### 3.2.1 Ideal MOSCAP

For an ideal MOSCAP, charges solely inside the semiconductor and the metal are considered, whereas interface trap states and any kind of oxide charges are neglected. Moreover,

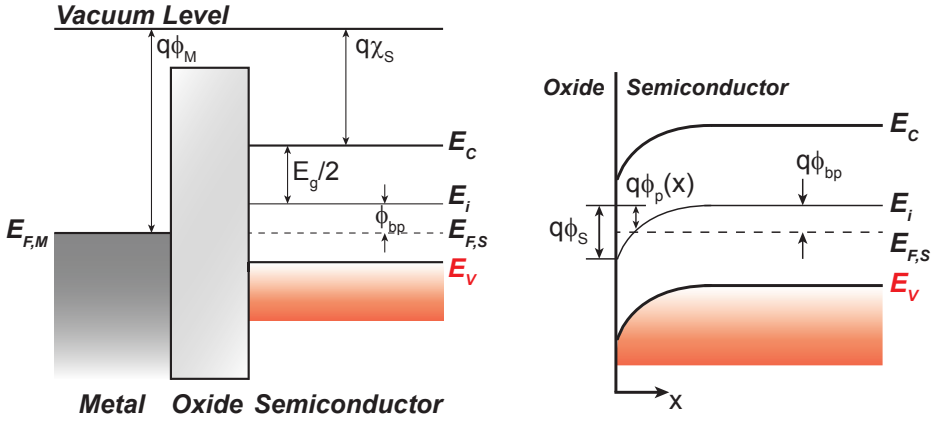


(a) $V = 0V$ (b) $V < 0V$

**Figure 3.28:** (a) Sketch of the band structure of an ideal MOSCAP structure for $V = 0\,\mathrm{V}$. A detailed description can be found in the text. (b) Oxide-Semiconductor interface for $V < 0\,\mathrm{V}$. The surface potential is labeled with $\phi_S$.

it is assumed, that no carrier transport occurs under DC biasing conditions, that is, the resistivity of the oxide is supposed to be infinitely high. The band structure of such an ideal MOSCAP for $V = 0\,\mathrm{V}$ and a p-type doped semiconductor is displayed in Fig. 3.28 (a). Here, $E_C$ and $E_V$ represent the band edges of the conduction and valence band, $E_{F,M}$ and $E_{F,S}$ are the Fermi-levels of the metal plate and the semiconductor, $E_g$ is the bandgap energy, $\phi_M$ is the metal workfunction, $\chi_S$ is the electron affinity of the semiconductor and $\phi_{bp}$ represents the Fermi-potential with respect to the midgap $E_i$. If the difference between $\phi_M$ and the semiconductor workfunction is zero the conduction and valence bands are flat, *flat band condition*, and can be expressed via [111]:

$$\phi_{M,S} = \phi_M - \left(\chi_S + \frac{E_g}{2q} + \phi_{bp}\right) = 0. \tag{3.9}$$

In Fig. 3.28 (b) a more detailed band diagram of the oxide-semiconductor interface is presented for $V < 0\,\mathrm{V}$ in order to introduce the surface potential $\phi_S$. The spatial dependency of the potential $\phi_p(x)$ is given by [111]:

$$\phi_p(x) \equiv \frac{E_i(x) - E_i(\infty)}{q}. \tag{3.10}$$

At the surface of the semiconductor, $\phi_p(x = 0) \equiv \phi_S$ and is called *surface potential*. If the MOSCAP is biased, the following conditions can be distinguished depending on the position of the surface potential with respect to the Fermi-level (c.f. Fig. 3.29):

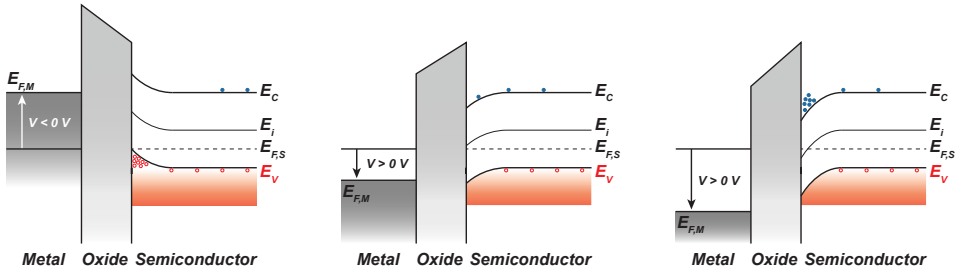


(a) Accumulation (b) Depletion (c) Inversion

**Figure 3.29:** Band diagrams for the three main regimes of an ideal p-type MOSCAP. (a) accumulation of majority carriers is achieved for a negative DC bias. If the voltage is increased, the region close to the interface is depleted (b) from majority carriers until, finally, minority carriers are attracted to the inversion layer (c).

(i) $\phi_S < 0$ (Accumulation of majority carriers): For a negatively applied voltage majority carriers (holes in a p-type semiconductor) accumulate at the surface of the semiconductor and the bands are bent upwards.

(ii) $\phi_S = 0$ (Flat band condition): In an ideal MOS capacitor - absence of oxide carriers and differences in workfunctions - this condition is achieved for 0 V.

(iii) $\phi_{bp} > \phi_S > 0$ (Depletion of majority carriers): A slight positive voltage results in a depletion of majority carriers and thus a lower hole concentration compared to the bulk close to the interface which leads to a downward band bending.

(iv) $2\phi_{bp} > \phi_S > \phi_{bp}$ (Weak inversion): If the voltage is further increased minority carriers from the bulk are attracted towards the surface and at a certain point the minority carrier density exceeds the majority carrier density at the surface.

(v) $\phi_S > 2\phi_{bp}$ (Strong inversion): The Fermi-level at the surface is far above the midgap level.

An ideal CV characteristic of a $SiO_2$-Si MOSCAP (p-type with $N_h = 10^{17}\,cm^{-3}$, $A = 5 \times 10^{-4}\,cm^{-2}$ and $t_{ox.} = 10\,nm$) [118] is displayed in Fig. 3.30 (a). The main regimes, namely accumulation, depletion and inversion, can be easily identified. For gate voltages below 0 V, accumulation occurs and the capacitance reaches $C_{ox}$. For slightly higher bias voltages the semiconductor is depleted and the residual capacitance stems mainly from ionized dopant atoms. If the gate voltage is further increased inversion sets in. Additionally, in Fig. 3.30 (b) simulations of an ideal n-type Ge MOSCAP are shown illustrating the variation of depletion capacitance with doping density [119]. The CV curve

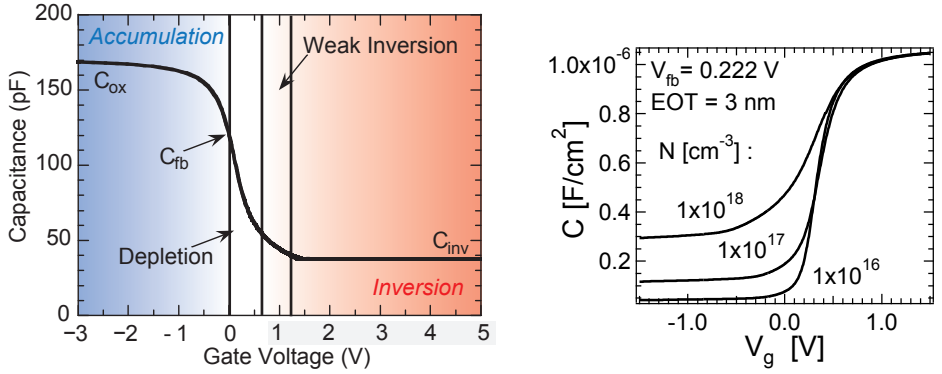


**Figure 3.30:** (a) CV characteristic of an ideal Si MOSCAP (data taken from [118]) and (b) the influence of doping on the CV curve [119].

is stretched out and the depletion and inversion capacitance increase if the semiconductor exhibits a higher dopant concentration, since $C_S \approx \epsilon_S / w_{depl.} \propto \epsilon_S \sqrt{qN}$[1].

### 3.2.2 Influence of Interface Traps on Narrow Bandgap MOSCAPs

Interface traps may lead to severe performance degradation in electronic devices, i.e. enhanced scattering at the dielectric-channel interface due to interface traps will result in mobility reduction and, hence, lower on-currents. Moreover, a large $D_{it}$ strongly effects admittance characteristics, especially for non-Si, narrow bandgap MOSCAPs, as will be described in the following. That in turn might lead to erroneous extraction of important device parameters like EOT, $V_{fb}$ and doping levels. Thus, achieving a $D_{it}$ as low as possible is one of the major goals of gate stack formation. In the case of the well-known $SiO_2$/Si interface, very low $D_{it}$ values in the range of $10^{10}\,cm^{-2}eV^{-1}$ are achievable, due to the optimized FGA resulting in effective saturation of dangling bonds with atomic hydrogen. Hence, the influence of the $D_{it}$ on CV curves is rather low. Even without performing FGA resulting in $D_{it} \approx 10^{12}\,cm^{-2}eV^{-1}$, the effect of interface traps on the CV characteristic is small, because of the much higher accumulation layer density in Si (approx. $10^{13}\,cm^{-2}$). Simulation results have shown [119] that the effect for $SiO_2$/Si interfaces is limited to an additional interface trap capacitance in the depletion regime [116], also known as frequency dependent $D_{it}$ *bump*. For a high quality interface with a low $D_{it}$ ($1 \times 10^{11}\,cm^{-2}eV^{-1}$) steep and well-shaped CV curves can be obtained without any frequency dispersion. In contrast, for low bandgap semiconductors like Ge or III/V

[1] $\epsilon_S$ and $w_{depl.}$ depict the dielectric constant and the depletion width of the semiconductor. $q$ is the elemental charge and N is the dopant concentration.

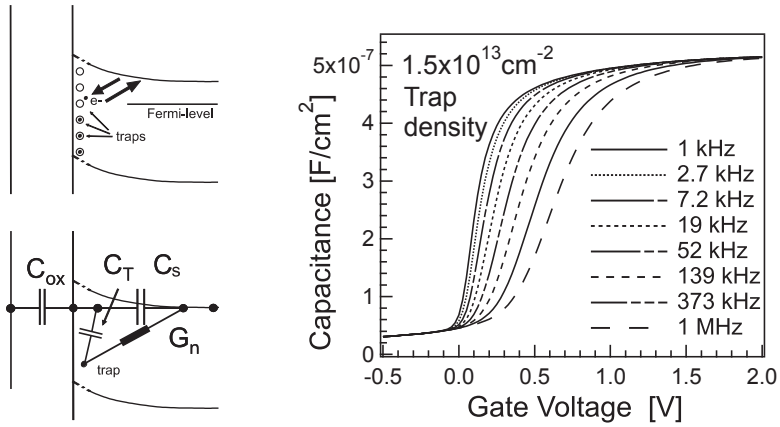


(a) (b)

**Figure 3.31:** (a) In depletion electrons trapped in interface states may interact with the majority energy band that requires the addition of a trap induced capacitance and conductance in the equivalent circuit [119]. (b) Simulation of a GaAs MOSCAP with a $D_{it}$ of $\approx 1.5 \times 10^{13}\,\mathrm{cm}^{-2}$ [119].

compounds higher $D_{it}$ levels are usually obtained that have in addition a much stronger influence on admittance characteristics [120, 117, 121] compared to $SiO_2$/Si interfaces. Here, high $D_{it}$ levels can be identified by a stretch-out of the CV [122, 123] and an additive admittance, i.e. capacitance, besides the MOS admittance [124, 123]. The stretch-out is caused by a reduced Fermi-level movement, due to the large number of interface traps. Carriers of the semiconductor are trapped in interface traps located closer to the oxide, which results in a reduced band bending inside the semiconductor. Less band bending in turn means less steep CV curves. In order to discuss the effect on the depletion, Fig. 3.31 (a) shows the according band diagram and equivalent circuits for interface traps energetically distributed inside the bandgap of the semiconductor [119]. Interface traps are charged and discharged according to the probing AC signal, whereas the kind of trap, which is filled and at which position inside the bandgap is determined by the applied DC bias that defines the position of the Fermi-level inside the bandgap. Besides the oxide capacitance, $C_{ox}$, and the semiconductor capacitance, $C_S$, an additional trap capacitance needs to be added as well as a conductance, since the capture and emission of electrons by a trap is a dissipating process. According to reference [125] the capacitance, $C_{it}$, and conductance, $G_{it}$, of a single trap inside the bandgap can be expressed via:

$$C_{it} = \frac{qD_{it}}{1+(\omega\tau_{it})^2}, \tag{3.11}$$

$$\frac{G_{it}}{\omega} = \frac{qD_{it}\omega\tau_{it}}{1+(\omega\tau_{it})^2}. \tag{3.12}$$

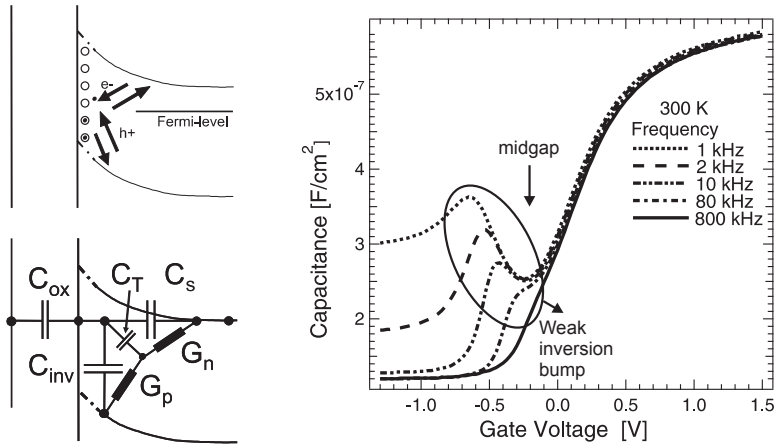


(a) (b)

**Figure 3.32:** (a) In weak inversion electrons trapped in interface states may interact with the majority and minority energy band that requires the addition of a trap induced capacitance and two conductances in the equivalent circuit [119]. (b) Frequency dependence of an n-type Ge/$GeO_xN_y$ CV curve [117].

Where $\tau_{it}$ is the time needed to exchange charge carriers between the trap and conduction or valence band depending on the position of the Fermi-level. Note, $\tau_{it}$ depends exponentially ($\propto \exp(-q\Delta E/k_BT)$) on the energy distance between the trap and majority carrier band edge, $\Delta E$. The admittance becomes accordingly:

$$Y = \left((i\omega C_{ox})^{-1} + (G_{it} + i\omega(C_{it} + C_S))^{-1}\right)^{-1}. \tag{3.13}$$

$G_{it}/\omega$ peaks at $f = 1/2\pi\tau_{it}$ and $C_{it} = 2G_{it}/(\omega q)$. The interface trap capacitance will dominate the oxide capacitance, hence, the CV characteristic, if so-called *weak Fermi-level pinning* sets in at $D_{it} > C_{ox}/q$. This results in a strong frequency dispersion in depletion or *frequency dependent flatband shift*, see Fig. 3.31 (b). At higher frequencies traps far away from the band edges are no longer able to respond and, as a consequence, the capacitance decreases compared to lower frequencies. This weak Fermi-level pinning effect has been observed for example in GaAs MOSCAPs [126, 127, 128]. For very high interface trap densities a vertical down-shift in accumulation for increasing frequency is observed due to an extreme stretch-out.

### Inversion regime

However, the interface traps not only affect the depletion regime, as for $SiO_2$/Si interfaces, but also the weak inversion. Here, the model and the equivalent circuit have to be ex-

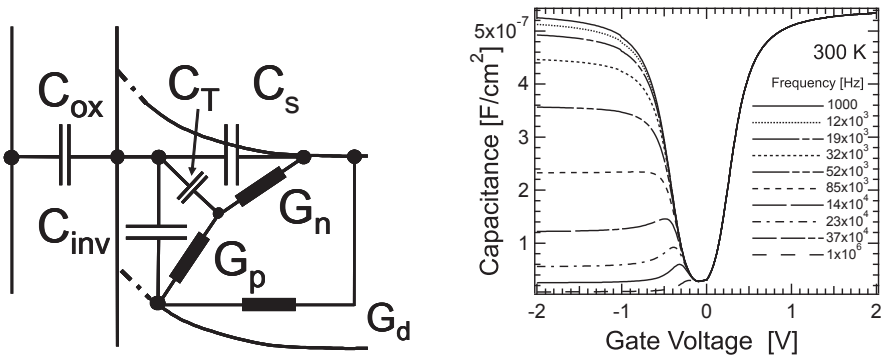


(a) (b)

**Figure 3.33:** (a) Equivalent circuit including the inversion generation induced conductance [119]. (b) Simulation of an n-type Ge MOSCAP considering strong inversion response [119].

tended, as presented in Fig. 3.32. In contrast to depletion, carriers captured in interface traps may interact not only with the majority energy band, but also with the minority carriers band, see Fig. 3.32 (a). This in turn leads to an additional conductance $G_p$ and a trap induced capacitance, $C_T$, in weak inversion besides $C_{ox}$, $C_S$ and $C_{inv}$, as shown in the equivalent circuit at the bottom of Fig. 3.32 (a). This interaction with the majority as well as minority energy band strongly depends on the bandgap of the semiconductor. That is why this so-called *weak inversion response* does not occur for $SiO_2$-Si interfaces for the given frequency (1 kHz to 1 MHz) and temperature (300 K to 80 K) range.
The weak inversion response in narrow bandgap semiconductors induce a weak inversion bump, that is frequency dependent. Martens *et al.* [117] have demonstrated that this effect is indeed observable in Ge-based MOSCAPs, see Fig. 3.32 (b). Since $\tau_{it}$ exponentially depends on the temperature, the kind of traps that respond to the applied frequency varies also strongly with temperature. Electrons trapped in states near midgap are not able to interact with the valence or conduction band at low temperatures, thus, the observable trap energy window shifts towards the band edges with decreasing temperature. As a consequence, it might be possible to observe a frequency dependent $V_{fb}$ shift due to a high density of interface states exclusively at low temperature [117].
Another essential mechanism in inversion to be considered is *inversion generation*. In order to fulfill the required charge neutrality in inversion, the supply of minority carriers to the inversion layer is also provided by carriers from the bulk by diffusion or generation-recombination processes. Especially, the *diffusion induced inversion response* or *strong inversion response* becomes significant for small bandgap semiconductors and superimposes the weak inversion response. This contribution might be taken into account by inserting a diffusion-induced conductance, $G_d$, into the equivalent circuit, as shown in

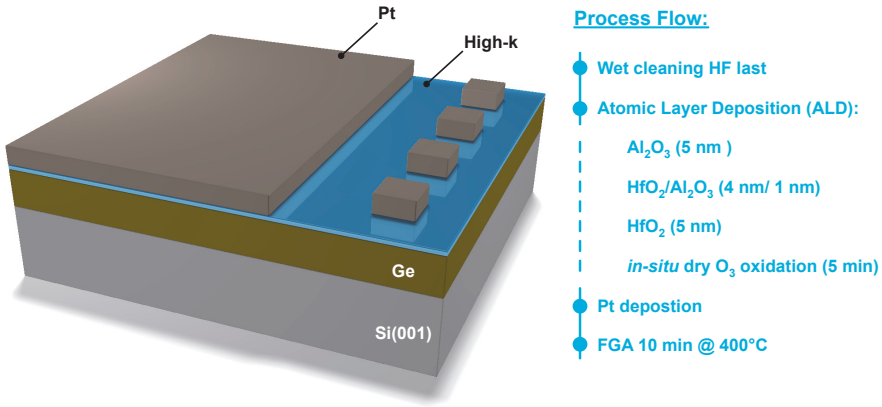


**Figure 3.34:** (left) Sketch of a processed MOSCAP structure with large and small Pt pads using Ge-VS. (right) Ge-MOSCAP process flow.

Fig. 3.33 (a) that is proportional to the mobility of the minority carriers and the intrinsic carrier concentration. The effect of the strong inversion response on the CV characteristic of Ge-MOSCAPs is presented in Fig. 3.33 (b). These simulation results [119] indicate a strong frequency dispersion in inversion. Notably, at frequencies below 85 kHz the inversion capacitance remains constant and reaches the value of the oxide capacitance at 1 kHz. Moreover, the shape of the CV curve resembles more and more a U-shape for lower frequencies. This tendency becomes stronger for lower bandgaps or at higher temperatures, i.e. the U-shape appears at higher frequencies.
In conclusion, the admittance characteristics of narrow bandgap MOSCAPs differ significantly from those of Si MOSCAPs mainly due to the increased interaction of interface traps with the energy bands as well as the increased strong inversion response. Thus, the correct interpretation of admittance characteristics of low bandgap MOSCAPs requires frequency and temperature dependent measurements as will be shown in the following for tensile strained Ge- and GeSn-MOSCAPs as well as for Ge-VS control devices.

### 3.2.3 Dielectric-Ge Interface Passivation

The aforementioned poor structural and electrical properties of dielectric-Ge interfaces strongly hampered the integration of Ge as channel material into microelectronics. In literature, numerous methods for Ge-passivation have been studied, for instance nitridation [129, 130, 131] or Si-passivation [132, 133]. However, it turned out that the most promising approach relies on the formation of a $GeO_x$ or $GeSnO_x$ *interfacial control layer* (IL) by either *electron cyclotron resonance* (ECR) plasma post oxidation [134, 135, 136, 137] or $O_3$ oxidation [59]. Prior to the electrical characterization of strained Sn-based MOSCAPs,

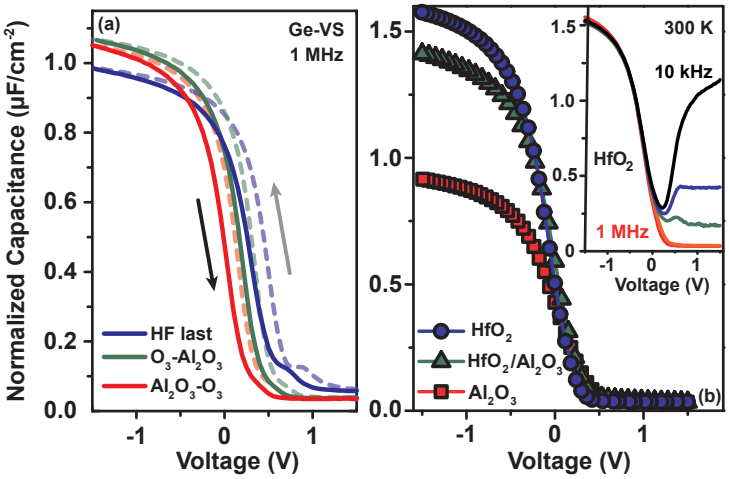


**Figure 3.35:** (a) Room temperature CV curves (at 1 MHz) of a Ge MOS capacitor with $Al_2O_3$ gate dielectric. (b) CV characteristics of Ge MOSCAPs with $HfO_2$, $HfO_2/Al_2O_3$ and $Al_2O_3$ dielectric (at 1 MHz). The inset shows the frequency dependence between 10 kHz and 1 MHz at room temperature.

dielectric-Ge interfaces are studied, in order to optimize the surface passivation. Here, different *in-situ* $O_3$ dry oxidation steps after the wet-chemical cleaning (HF last) are under investigation.

In Fig. 3.34 the sketch of a Ge-VS MOSCAP structure as well as a summary of the process are shown. First, the samples are cleaned with an HF:$H_2O$ (1:100) (in the following called *HF last*) wet solution to remove the native $GeO_x$ oxide. The surface cleaning is followed by an ALD of the dielectric, i.e. $Al_2O_3$ and/or $HfO_2$. Metallic contacts made of Pt are deposited afterwards using *electron beam evaporation* (EBE). Finally, the MOSCAP process ends with a standard FGA (ambient: 4 % $H_2$ in $N_2$) for 10 min at 400 °C. The devices are measured in a top-top configuration between a large and a small pad (c.f. Fig. 3.34). Since the capacitances are added inversely, the capacitance of the large pad is negligible. A series equivalent circuit is used for the CV measurements and the measured capacitance is normalized to the smaller pad size.

The CV characteristics at 1 MHz for three differently processed $Pt/Al_2O_3/Ge$ gate stacks are displayed in Fig. 3.35 (a). For the sample without $O_3$ treatment at all, a reduced accumulation capacitance as well as a bump at approx. 0.8 V is observed. In contrast, applying an *in-situ* $O_3$ oxidation step prior (green lines) or after (red lines) the dielectric deposition results in smooth and steep CV curves and a reduced hysteresis that is due to oxide charge trapping. For all three devices the flatband voltage is shifted to positive voltages. However, if the oxidation step follows after the $Al_2O_3$ deposition, this shift is minimized to 0.15 V. Thus, this $O_3$ oxidation step is applied for all MOSCAP structure

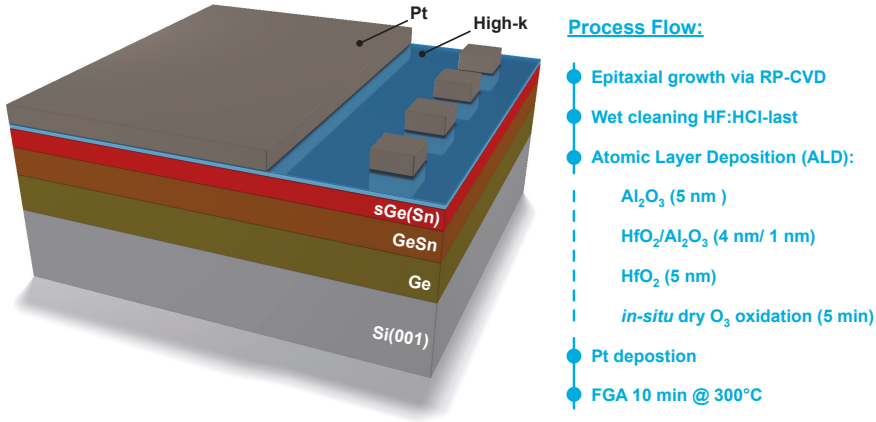


**Figure 3.36:** (left) Sketch of a processed strained Ge(Sn) MOSCAP structure with large and small Pt pads. (right) MOSCAP process flow.

in the following either after the complete dielectric deposition of 5 nm $Al_2O_3$ and $HfO_2$ or after the first nm of $Al_2O_3$ in the $HfO_2/Al_2O_3$ (4 nm/1 nm) case.
A comparison for the three different gate stacks on Ge is presented in Fig. 3.35 (b). Well-behaved CV curves at 1 MHz are measured and the highest accumulation capacitance is found for $HfO_2$/Ge stacks, due to the higher effective dielectric constant of $HfO_2$ compared to $Al_2O_3$. The frequency dependent measurements for all three samples do not exhibit any frequency dependent flatband voltage shift in depletion, see inset of Fig. 3.35 (b). The increased weak and strong inversion response observed for lower frequencies is attributed to the small bandgap of Ge. By means of the conductance method, $D_{it}$ levels at room temperature of $1 \times 10^{12}\,cm^{-2}eV^{-1}$ and $5 \times 10^{12}\,cm^{-2}eV^{-1}$ are determined for 5 nm $Al_2O_3$ and 5 nm $HfO_2$ on Ge, respectively. This increase can be explained by the intermixing of $HfO_2$ and $GeO_x$ that can be avoided by inserting an $Al_2O_3$ IL as interdiffusion control layer [138]. These values similar to present state-of-the-art results show that the employed process for the gate stack formation on Ge is suitable for high quality dielectric-Ge interfaces.

### 3.2.4 Dielectric-Tensile Strained Ge(Sn) Interface Passivation

Compressively strained GeSn layers have been studied by several groups for the use as channel material in MOSFET devices exhibiting superior performance compared to Ge control devices [93, 103, 104]. However, there have been only a few groups reporting on high-k-GeSn interfaces. In this section, MOSCAPs based on tensile strained Ge and GeSn layers are fabricated and characterized.

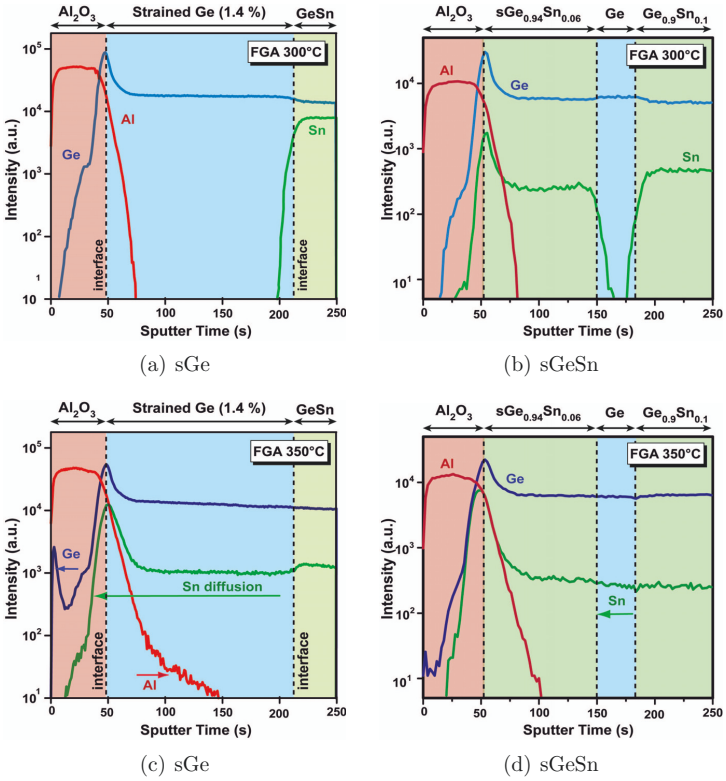


(a) sGe (b) sGeSn

(c) sGe (d) sGeSn

**Figure 3.37:** ToF-SIMS measurements of processed sGe (a) and (c) and sGeSn (b) and (d) MOSCAPs. FGA temperatures of 300 °C and 350 °C are used in order to investigate the thermal stability of the MOSCAP structures.

### Sample preparation

The above described MOSCAP process is used for the fabrication and characterization of tensile strained GeSn-based MOSCAPs, namely sGe MOSCAPs with $\epsilon = 1.1\,\%$ and $\epsilon = 1.4\,\%$ as well as $sGe_{0.94}Sn_{0.06}$ MOSCAPs with $\epsilon = 0.4\,\%$. Gupta *et al.* [94] have shown that a conventional HF last cleaning step is not sufficient for high quality dielectric-GeSn interfaces, but HCl needs to be added. So, the wet cleaning step prior to the dielectric deposition has been modified. Parallel to the GeSn-based MOSCAPs, Ge control devices have been processed in the same batch. In Fig. 3.36 a sketch of the MOSCAP structure as well as the complete process flow are shown. The growth temperature of the whole heterostructure amounts to 350 °C in order to incorporate the highest possible Sn concentration into the $200 - 300\,\text{nm}$ thick GeSn SRBs. Prior to the electrical characterization

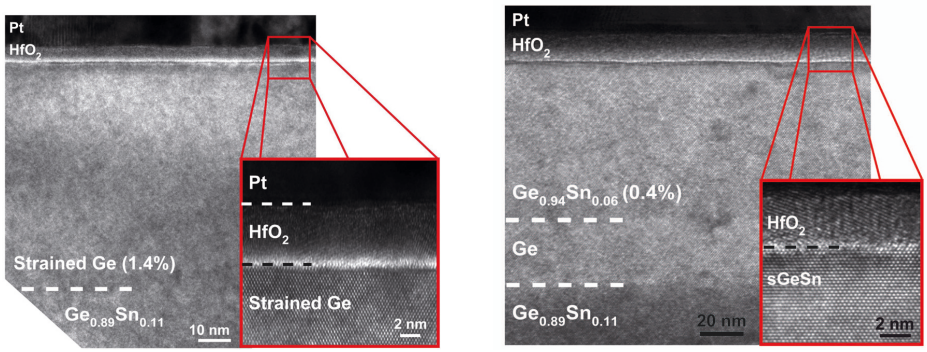


(a) sGe (b) sGeSn

**Figure 3.38:** TEM micrographs of (a) sGe and (b) sGeSn MOSCAPs. The insets show high resolution images of the dielectric-semiconductor interface.

the thermal stability of these MOSCAP structures has been investigated in terms of strain relaxation and Sn segregation towards the sample surface.
In Fig. 3.37 ToF-SIMS measurements of $Al_2O_3$/sGe(Sn)/GeSn-SRB/Ge-VS heterostructures are presented for FGA temperatures of 300 °C as well as 350 °C. For the lower annealing temperature, the measurements indicate homogeneous Sn distribution throughout the whole heterostructure and abrupt GeSn/Ge as well as $Al_2O_3$/GeSn interfaces (Fig. 3.37 (a) and (b)). Merely, a moderate Ge diffusion into the oxide layer is observed. The increasing Ge and Sn signals towards the oxide-sGe(Sn) interface are due to matrix effects. The applied tensile strain within the layers has been conserved at 300 °C as proven by XRD-RSM. However, if the annealing temperature is increased to 350 °C severe Sn as well as Ge diffusion occurs (Fig. 3.37 (c) and (d)). Ge atoms tend to diffuse even through the topmost oxide layer, whereas the Sn atoms stop within the $Al_2O_3$. Thus, in order to avoid Sn segregation and strain relaxation the overall thermal budget is limited to 300 °C for these heterostructures. The TEM micrographs in Fig. 3.38 show the top interfaces of processed sGe ($\epsilon = 1.4\,\%$) and sGeSn ($\epsilon = 0.4\,\%$) MOSCAPs with 5 nm $HfO_2$ dielectric and a thermal budget limited to 300 °C. Within the 70 nm strained Ge and the 30 nm strained GeSn neither any indication for threading dislocations nor misfit dislocations at the abrupt interfaces towards the GeSn SRB have been found. The latter finding confirms the XRD-RSM results evidencing complete strain conservation after processing. Moreover, the surfaces towards the dielectrics appear smooth and without Sn precipitation. However, it is not possible to verify if a $GeO_x$ or $GeSnO_x$ IL has been built up by the ALD ozone process step. The interface quality has been further investigated by room temperature as well as low temperature CV characteristics of differently processed sGe and sGeSn MOSCAP in the following.

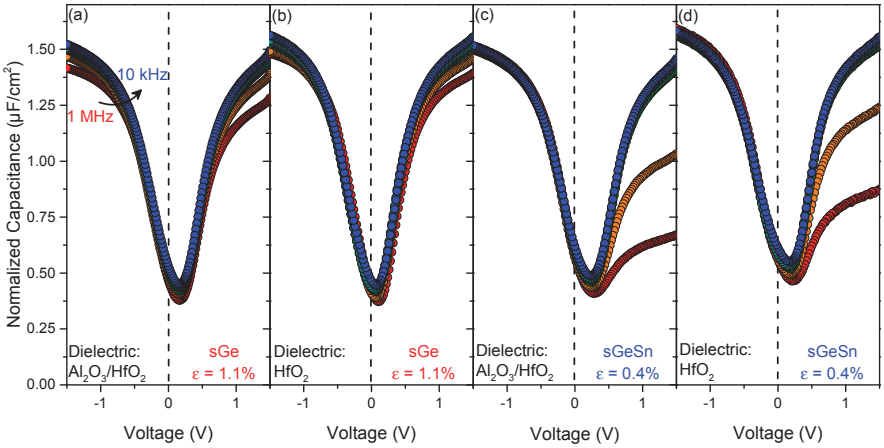


**Figure 3.39:** Frequency dependence at room temperature of sGe ($\epsilon = 1.1\,\%$) (a) and (b) as well as $sGe_{0.94}Sn_{0.06}$ ($\epsilon = 0.4\,\%$) (c) and (d) MOSCAP with $Al_2O_3$ and $HfO_2$ as gate dielectrics.

### Electrical characterization

In Fig. 3.39 room temperature CV characteristics of sGe and $sGe_{0.94}Sn_{0.06}$ MOSCAPs as function of frequency are displayed. Here, the applied strain in the devices amounts to 1.1 % and 0.4 % for the sGe and sGeSn capacitors, respectively. Two different stacks of dielectrics are used, namely $Al_2O_3/HfO_2$ (Fig. 3.39 (a) and (c)) and a single $HfO_2$ layer (Fig. 3.39 (b) and (d)). Strikingly enough, all four investigated devices exhibit p-type behavior. This can be understood by considering the growth conditions of these heterostructures. It is well-known that the CVD growth at very low temperatures leads to the incorporation of vacancies which in turn may result in an enhanced p-type background doping of the epilayer. This might be also the reason for $C_{min}$-values observed between 0.37 V and 0.47 V. In this connection, the values for sGeSn MOSCAPs are slightly higher. The oxide capacitances at 1 MHz amount to 1.41 $\mu F/cm^2$ (sGe) and 1.51 $\mu F/cm^2$ (sGeSn) for the $Al_2O_3/HfO_2$ stack and 1.48 $\mu F/cm^2$ (sGe) and 1.59 $\mu F/cm^2$ (sGeSn) for the $HfO_2$ layer. As expected higher EOT values are determined without an $Al_2O_3$ interlayer comparable to the results of the Ge-VS MOSCAPs (c.f. chapter 3.2.3). Interestingly enough, the EOT values are higher for the sGeSn devices and the $V_{fb}$ is slightly shifted towards negative voltages. However, for all four frequency dependent measurements no frequency dependent $V_{fb}$ shift is observed indicating no Fermi-level pinning at the dielectric-semiconductor interface. Hence, the Fermi-level can be easily moved inside the bandgap by varying the DC gate voltage. Furthermore, especially for the strained Ge devices no frequency dependent inversion bump (c.f. chapter 3.2.2) can be seen. Due to the small bandgap of

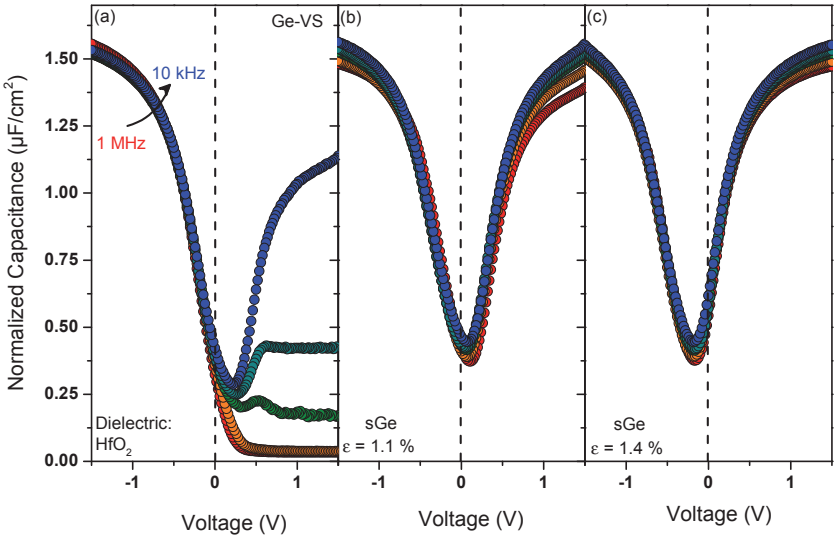


**Figure 3.40:** Frequency dependence at room temperature of differently strained (a) $\epsilon = 0.16\,\%$ (b) $\epsilon = 1.1\,\%$ and (c) $\epsilon = 1.4\,\%$ Ge MOSCAP with $HfO_2$ as gate dielectric.

these layers diffusion induced inversion response might superimpose the weak inversion response. In strong inversion, a smaller frequency dispersion is obtained for the elemental MOSCAPs which might be another hint for the smaller bandgap of these layers. On the other hand, this dispersion is slightly larger for the $Al_2O_3/HfO_2$ stack for both types of devices. This could be an indication, that indeed a $GeO_x$ and $GeSnO_x$ IL has been formed. In order to gain more information about the dependence of the CV characteristics on the bandgap, three frequency dependent CV measurements are presented in Fig. 3.40 for Ge MOSCAPs with tensile strain levels of 0.2 %, 1.1 % and 1.4 %. By comparing elemental MOSCAPs the influence of Sn atoms can be excluded. The deformation potentials for Ge are well-known, hence the strain can be computed quite accurately, whereas for GeSn also the contribution of Sn atoms on substitutional lattice sites has to be considered in the band structure calculations, which might lead to inaccuracies, not only because of the yet not well-determined bowing parameters for GeSn. Moreover, the quality of dielectric-semiconductor surface is supposed to be nearly identical. The calculated bandgaps for the MOSCAP structures under investigation are $E_g = 0.57\,\text{eV}$ and $E_g = 0.54\,\text{eV}$ for 1.1 % and 1.4 % tensile strain, respectively, that are more than 100 meV below the values for unstrained Ge. For all three capacitors the interface trap density is reasonably low, since neither a frequency dependent $V_{fb}$ shift nor a CV stretch-out are observable. This indicates, that the Fermi-level is not pinned at the surface, thus, the properties of the semiconductor can be investigated. In the case of the nearly unstrained Ge MOSCAP a frequency dispersion in weak inversion is obtained due to the interaction of trapped

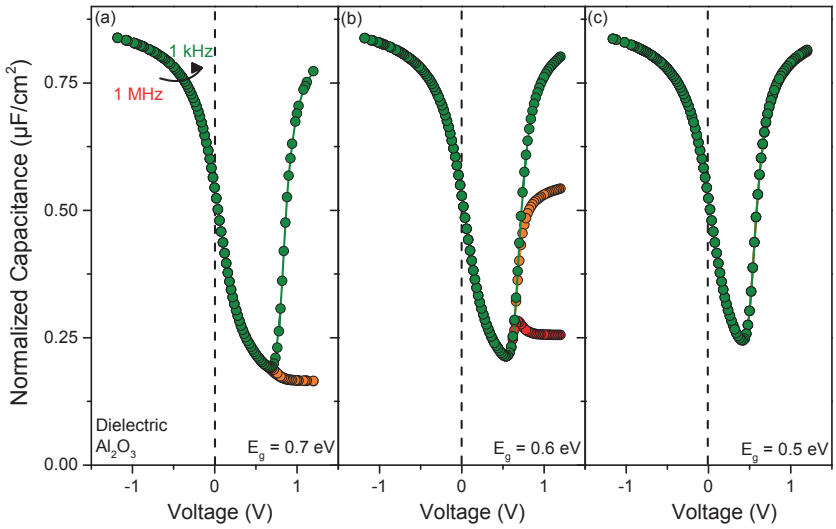


**Figure 3.41:** Simulation of frequency dependent CV characteristics at room temperature for different bandgaps: (a) 0.7 eV (b) 0.6 eV and (c) 0.5 eV. $Al_2O_3$ (5 nm) has been used as gate dielectric.

carriers with the energy bands induced by the low bandgap of Ge. In addition, a constant inversion capacitance in strong inversion can be seen comparable to Fig. 3.33 (b) indicating diffusion induced inversion response. At high frequencies, i.e. 500 kHz and 1 MHz, the CV characteristics resembles that of a Si MOSCAP without weak or strong inversion response. For the highly strained devices $C_{min}$ increases due to the enhanced background doping. The $V_{fb}$-shift increases for increasing strain according to the reduced bandgap energy. More important, the U-shape of the CV characteristic appears also at high frequencies owed to the enhanced minority carrier diffusion towards the surface typical for low bandgap semiconductors or measurements at elevated temperatures.
Numerical calculations [139, 140, 141, 142] of CV characteristics may also strengthen this argument (c.f. Fig. 3.41). The simulations have been performed for three different frequencies 1 kHz, 316 kHz and 1 MHz as well as for three different bandgaps 0.7 eV, 0.6 eV and 0.5 eV for a 5 nm thick $Al_2O_3$ layer as gate dielectric. No interface trap density is assumed, hence no frequency dispersion in accumulation or depletion occurs as well as weak inversion response is thus not considered. For a "Ge-like" bandgap of 0.7 eV (Fig. 3.41 (a)) strong inversion response sets in at about 0.7 V for 1 kHz. If the bandgap is decreased, the influence of the minority carriers on the CV characteristic increases, that is, the onset of strong inversion response occurs at higher frequencies and at lower DC bias voltages, i.e. at 0.4 V for $E_g = 0.5$ eV, resulting in a spiky CV shape around $C_{min}$ as observed for highly tensile strained Ge MOSCAPs (c.f. Fig. 3.40 (c)).

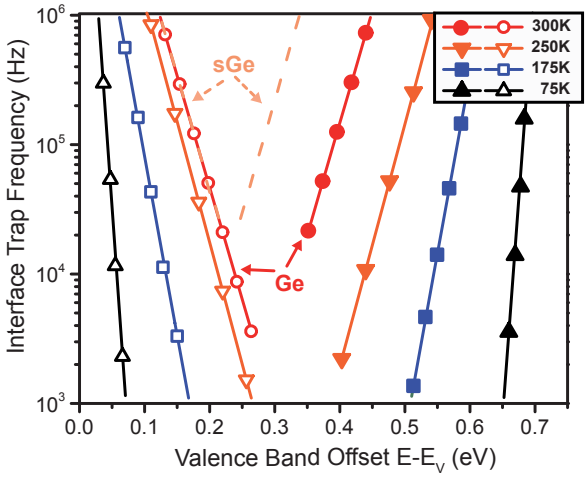


**Figure 3.42:** Interface trap frequency as function of the valence band offset and temperature.

In summary, these findings suggest, that the weak inversion response might be superimposed by the diffusion induced strong inversion response of minority carriers for highly strained, hence low bandgap Ge-based MOSCAPs. Moreover, reasonably low densities of interface states have been achieved avoiding Fermi-level pinning. However, it has to be kept in mind, that not all traps are able to respond to the probing AC signal at room temperature (c.f. chapter 3.2.2); mainly traps at midgap can be scanned. Hence, in the next section, temperature dependent CV measurements are presented.

### Temperature Dependence

As shown above, the minority carrier response severely affects admittance characteristics as well as $D_{it}$ determination. Especially for the strong inversion response this leads to an additional conductance besides the interface trap conductance (c.f. Fig. 3.33 (a)) hampering conventional methods like the *conductance method*. The influence of the minority carrier response can be significantly reduced by decreasing the temperature, since $G_d \propto n_i^2$ and $n_i \propto \exp(-1/k_B T)$. With decreasing temperature the intrinsic carrier concentration declines exponentially and so does the strong inversion response and its influence on the MOSCAP admittance. Moreover, interface traps may not be distributed equally in terms of energy throughout the bandgap, which may result in different $D_{it}$ levels near the conduction or valence band edge compared to midgap interface trap densities. This dramatically effects CV characteristics as will be described in the following.
In Fig. 3.42 the interface trap frequency as function of the valence band offset and temperature is displayed for Ge and sGe. The interface trap frequency is calculated using

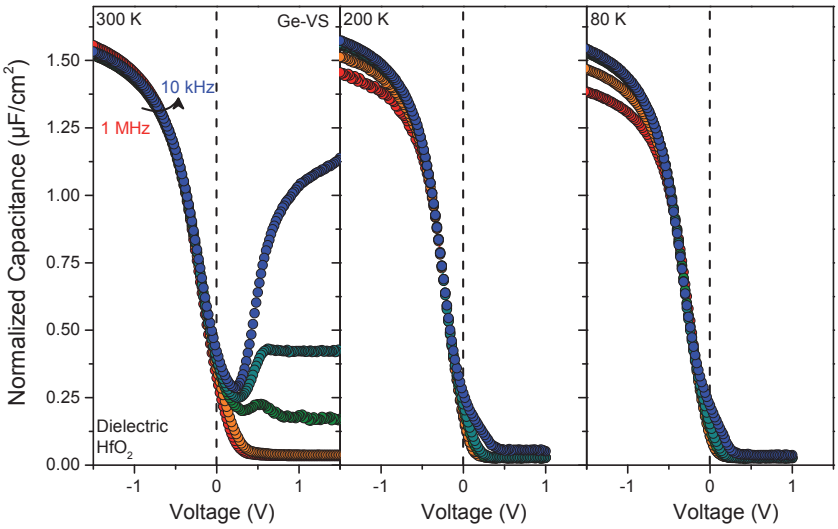


**Figure 3.43:** CV characteristics of a Ge-VS MOSCAP as function of temperature and frequency. $HfO_2$ is used as dielectric.

well-known material parameters (temperature dependent effective density of states of $E_C$ and $E_V$, electron thermal velocity and variation of the bandgap with temperature) for Ge [23] as well as a trap capture cross section of $1 \times 10^{-15}\,\mathrm{cm}^{-2}$ [119]. At room temperature traps in the middle of the bandgap are in resonance with the applied AC signal ($1\,\mathrm{kHz} - 1\,\mathrm{MHz}$), but traps near the band edges remain invisible, because their resonance frequency is too high. By decreasing the temperature one shrinks the energetically observable window for interface traps and shifts the region towards the band edges. The resonance frequency for traps near the band edges is reduced with lowering the temperature and they become visible in the applied frequency window. Now, traps near midgap exhibit a too low resonance frequency. This explains that severe frequency dispersion may only be obtained for low temperatures, if the $D_{it}$ towards the band edges is much higher than at midgap.

The frequency dependences at three different temperatures (300 K, 200 K and 80 K) for a Ge-VS MOSCAP are shown in Fig. 3.43. A slight but increasing frequency dispersion in accumulation is observed for decreasing the temperature. For lower frequencies the accumulation capacitance increases indicating an elevated density of interface states towards the band edges of the Ge-VS. Furthermore, a small horizontal shift of the CV curves towards negative voltages is visible, which is another hint for an enhanced $D_{it}$ near the band edge. At lower temperatures the Fermi-level gets closer to the valence band with a higher $D_{it}$ in its vicinity, so a higher DC bias is required to achieve the same band bending as for higher temperatures, where the Fermi-level is located in a lower $D_{it}$ region. However,

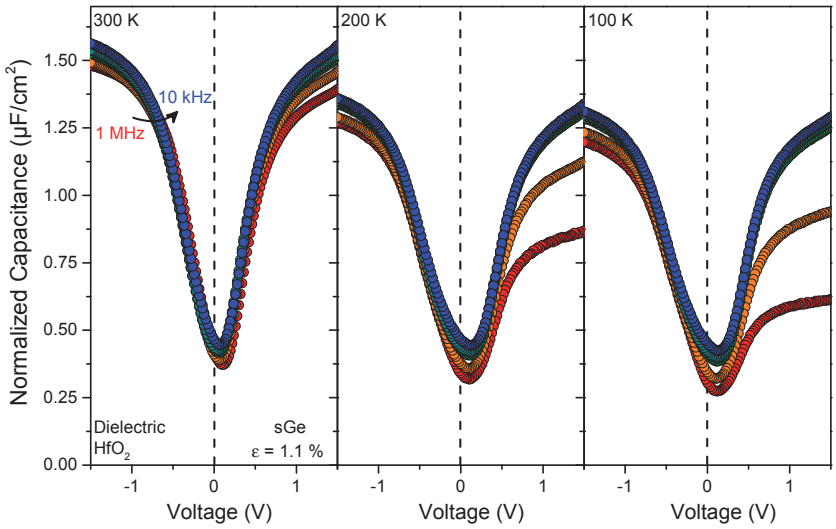


**Figure 3.44:** CV characteristics of a sGe ($\epsilon = 1.1\,\%$) MOSCAP as function of temperature and frequency. $HfO_2$ is used as dielectric.

in depletion no dispersion at any temperature is seen. Also the dispersion in inversion is strongly reduced for lower temperatures due to the reduced minority carrier response. At 80 K no dispersion occurs in strong inversion and a small weak inversion hump becomes visible. Obviously, the strong inversion response could be completely suppressed for the Ge-VS MOSCAP with a bandgap close to unstrained Ge.
A different temperature dependence is observed for the strained Ge MOSCAPs with a smaller bandgap (c.f. Fig. 3.44 and 3.45). A frequency dispersion in accumulation is found for both devices comparable to the Ge-VS MOSCAP. Though the dispersion is smaller and interestingly enough, the slightest dispersion is observed for the capacitor exhibiting the smallest bandgap. In addition, the horizontal shift is reduced. Both these findings indicate that the increase of the $D_{it}$ towards the band edges is larger for the Ge-VS MOSCAP than for the sGe MOSCAPs. Again, no frequency dispersion in depletion is observed, although a slight stretch-out of the CV curve may be seen for the sGe device with 1.1 % biaxial tensile strain. In inversion, the strong inversion response due to minority carriers is strongly reduced. According to the bandgap energies, this effect is smaller for the 1.4 % strained sample. In the case of the sGeSn MOSCAP with a calculated fundamental direct bandgap of 0.57 eV comparable to the 1.1 % strained Ge layer, the strong inversion response is completely suppressed at low temperatures and high frequencies of 1 MHz and 500 kHz as demonstrated in Fig. 3.46 (a) and (b). This could be an indication that the minority carrier mobility (here electrons) in highly strained Ge might be higher than in strained GeSn with the same bandgap. Further, the quality of the $HfO_2$-sGeSn

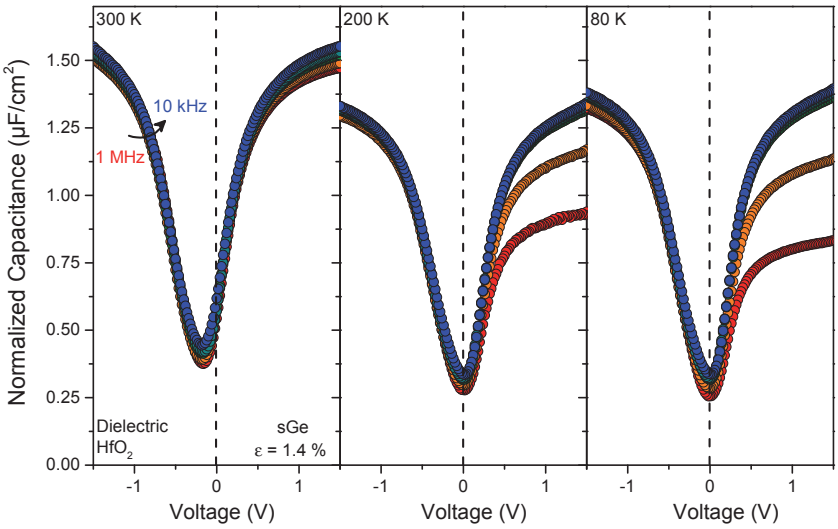


**Figure 3.45:** CV characteristics of a sGe ($\epsilon = 1.4\,\%$) MOSCAP as function of temperature and frequency. $HfO_2$ is used as dielectric.

interface seems to be higher due to the absence of frequency dispersion in accumulation and depletion at any investigated temperature.

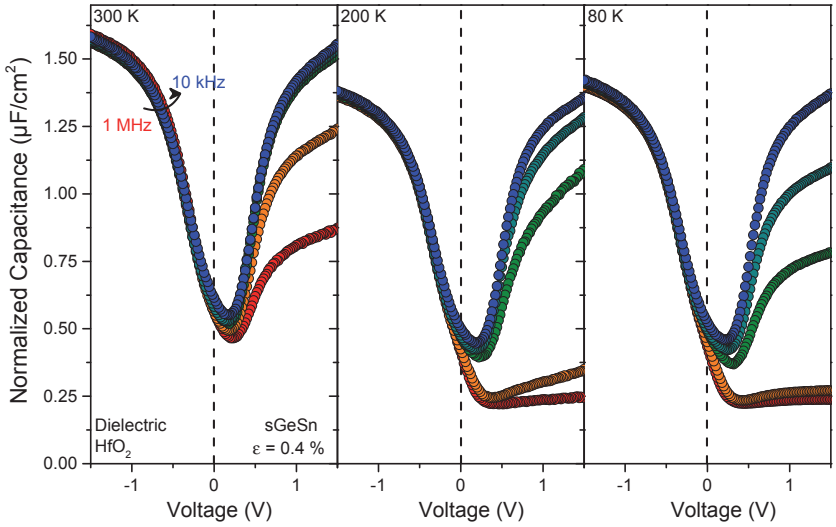


**Figure 3.46:** CV characteristics of a sGeSn ($\epsilon = 0.4\,\%$) MOSCAP as function of temperature and frequency. $HfO_2$ is used as dielectric.

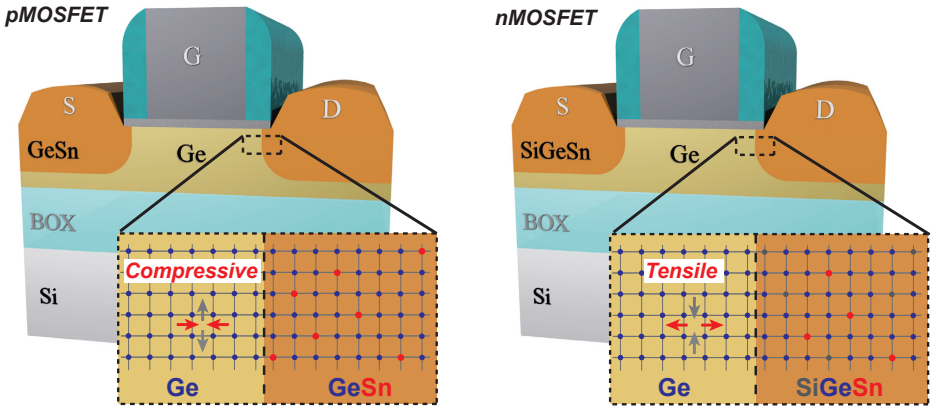


(a) sGe p-MOSFET with GeSn S/D stressors (b) sGe n-MOSFET with SiGeSn S/D stressors

**Figure 3.47:** Sketches of sGe MOSFETs with uniaxially (a) compressive and (b) tensile strained channels using GeSn and SiGeSn source/drain stressors, respectively.

## 3.3 Contact Engineering

Another important step towards the integration of a novel channel material is the formation of source (S) and drain (D) metal contacts. The requirements for metal contacts are defined by the transistor process. Therefore, S/D contacts must be formed at low temperatures and provide low sheet and contact resistances as well as a good thermal stability. Gaudet *et al.* [143] have investigated the reaction of Ge with transition metals and found out that Pd and Ni are the most promising candidates to fulfill all these requirements. So, in this section the formation of NiGeSn and NiSiGeSn contact layers are studied. Special emphasis is put on high Sn content ($\geq 6$ at.% Sn) (Si)GeSn epilayers and on the influence of Si on the contact formation. Highly lattice mismatched layers to Ge are favorable, since theoretical investigations [102] have shown that strain engineering is required in future Ge-MOS devices in order to outperform high performance strained Si FETs. For the latter several straining techniques have been developed like SiN liners [144] or embedded S/D stressor layers with larger (SiGe) or smaller (Si:C) lattice constants compared to unstrained Si to introduce compressive or tensile strain in short gate length Si devices, respectively. This enables enhanced hole and electron mobilities in Si channels, hence ultimately high performance n- and p-type MOSFETs on the very same chip [145]. In the case of Ge the technique of S/D stressors is poorly studied yet, due to the lack of suitable large lattice parameter group IV semiconductors. The growth technique developed in this thesis enables the growth of high quality GeSn binary and SiGeSn ternary alloys exhibiting larger and smaller lattice constants than Ge. In Fig. 3.47 schematics of sGe p- (Fig. 3.47 (a)) and n-type (Fig. 3.47 (b)) MOSFETs are shown.

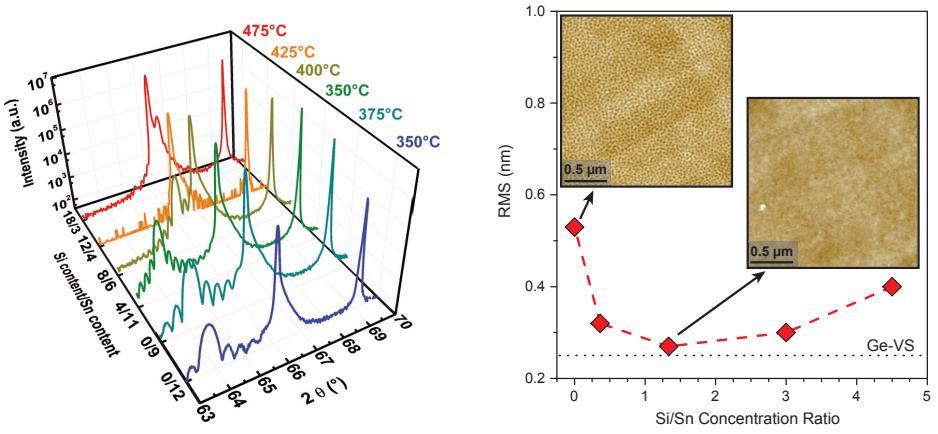


**Figure 3.48:** (a) XRD $\theta/2\theta$ scans of the as-grown GeSn and SiGeSn epilayers under investigation. (b) AFM results indicating improved layer morphology with increasing Si concentration.

The zoom-in views present the lattice of the Ge/GeSn heterojunction at the edge of the channel. Since the lattice constant of cubic GeSn, $a_{GeSn}$, is larger than the lattice constant of Ge, $a_{Ge}$, the out-of-plane lattice constant of pseudomorphically grown GeSn on Ge, $a_{GeSn,\perp}$, becomes larger than the in-plane lattice constant, $a_{GeSn,\neg}$, which equals $a_{Ge}$. This results in an increased and decreased out-of-plane and in-plane lattice of Ge at the edge of the channel, respectively. Finite-element studies on SiGe S/D stressors [146] have shown that this uniaxial strain extends to the center of the channel. In the case of SiGeSn stressors, the out-of-plane lattice constant, $a_{SiGeSn,\perp}$, of coherently grown SiGeSn with a large Si/Sn concentration ratio on Ge is smaller than $a_{Ge}$ leading to uniaxial tensile strain in the channel. By using these techniques a theoretical compressive stress of 2.357 GPa can be achieved in short channel Ge devices with $Ge_{0.9}Sn_{0.1}$ S/D stressors [147].

### 3.3.1 Sample Preparation

Several SiGeSn and GeSn layers (c.f. table 3.2) are pseudomorphically grown on Ge-VS with thicknesses ranging between 26 nm and 65 nm. Here, the growth temperature is varied according to the desired Si and Sn concentration. For higher Sn concentrations the temperature is reduced to 350 °C, whereas for higher Si concentrations the epilayers are grown at elevated temperatures up to 475 °C. The XRD $\theta/2\theta$ scans in Fig. 3.48 (a) provide evidence for the high crystalline quality of the epilayers under investigation containing Sn and Si concentrations between 4 at.% – 12 at.% and 4 at.% – 18 at.%, respectively. Besides

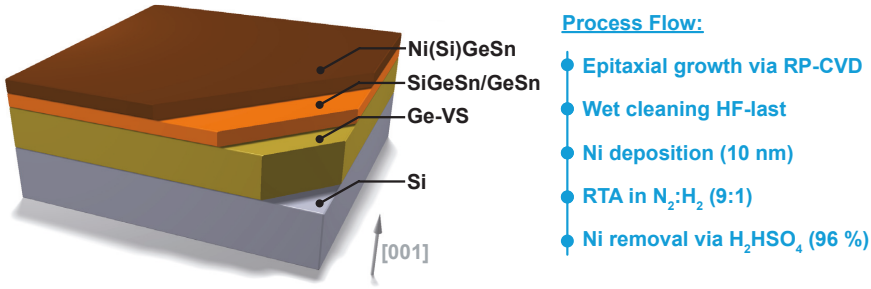


**Figure 3.49:** (left) Sketch of the layer stack after (Si)GeSn contact formation. (right) Process flow of the contact formation.

the Si and Ge-VS peaks, well-defined GeSn and SiGeSn peaks are observed surrounded by thickness fringes. According to the incorporated strain, which is measured by XRD-RSM and summarized in table 3.2, the (Si)GeSn peaks shift towards smaller or higher angles for a higher Sn or Si content, respectively. In Fig. 3.48 (b), the results of the AFM analysis for some of these epilayers are presented. Without adding Si and a Sn concentration of 12 at.% the rms-roughness amounts to 0.53 nm, whereas the surface roughness decreases to 0.27 nm by incorporating Si atoms into the lattice. After the epitaxial growth the layers are cleaned using HF. Subsequently, 10 nm of Ni are deposited by EBE and the whole stack is annealed in a *rapid thermal processing* system (RTP) in an $N_2$:$H_2$ ambient at temperatures between 250 °C and 400 °C for 10 s or 30 s. In order to remove unconsumed Ni on the surface, the samples are finally dipped in $H_2SO_4$. The final layer stack as well as a summary of the process can be found in Fig. 3.49.

| Sample | $x_{Si}$ (at.%) | $x_{Sn}$ (at.%) | Thickness (nm) | Strain (%) |
|---|---|---|---|---|
| A | 0 | 6 | 45 | -0.9 |
| B | 0 | 9 | 27 | -1.3 |
| C | 0 | 12 | 26 | -1.7 |
| D | 18 | 3 | 65 | +0.36 |
| E | 12 | 4 | 45 | 0 |
| F | 8 | 6 | 54 | -0.6 |
| G | 4 | 11 | 53 | -1.6 |

**Table 3.2:** GeSn and SiGeSn layers used for the contact formation.

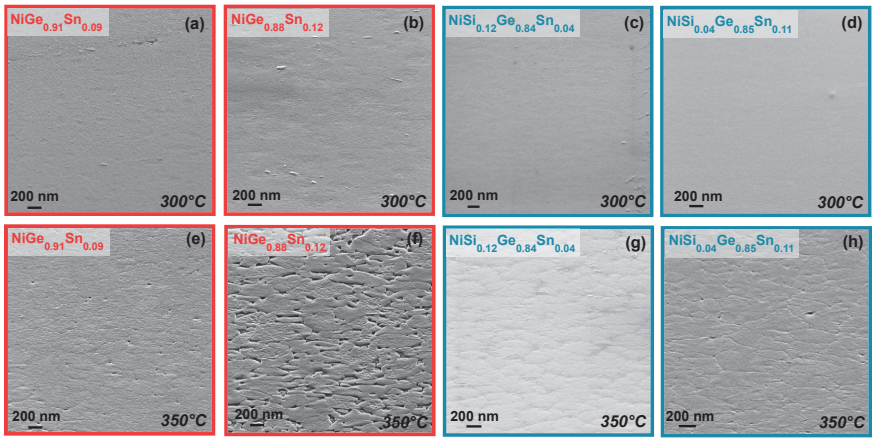


**Figure 3.50:** Scanning electron micrographs of (a) and (e) $NiGe_{0.91}Sn_{0.09}$, (b) and (f) $NiGe_{0.88}Sn_{0.12}$, (c) and (g) $NiSi_{0.12}Ge_{0.84}Sn_{0.04}$, (d) and (h) $NiSi_{0.04}Ge_{0.85}Sn_{0.11}$ after a 10 s anneal at 300 °C and 350 °C.

### 3.3.2 Layer Morphology

In order to investigate the surface morphology of the processed NiGeSn and NiSiGeSn layers SEM micrographs are employed, see Fig. 3.50. Samples B and C as well as E and G are presented after a 10 s anneal RTA at 300 °C (upper row in Fig. 3.50) and 350 °C (lower row in Fig. 3.50). For the lower annealing temperature smooth and continuous metal layers are observed without any cracks or agglomeration on the surface independent on the Sn concentration. If the annealing temperature is increased by 50 °C the layers become rough and cracked. This degradation strongly depends on the Sn concentration. For the NiGeSn sample with 12 at.% Sn discontinuities become visible. By adding Si at a comparable Sn content (Fig. 3.50 (h)) discontinuities are avoided. Hence Si seem to slightly increase the thermal stability in terms of morphology. For an annealing temperature of 400 °C also the surface of sample A with the lowest Sn concentration of 6 at.% starts to crack. Recent studies on stanogermanides with Sn concentrations ranging from 5.3 at.% to 8 at.% indicate smooth surfaces up to annealing temperatures of 350 °C [147, 148, 149]. In comparison to Ni germanides, where the layer degradation sets in at 580 °C [143] the thermal stability of Ni stanogermanides are reduced by more than 200 °C indicating a strong influence of Sn atoms on the contact formation. Thus, the temperature window for the formation of smooth and continuous NiGeSn layer shrinks for increasing Sn concentrations necessitating process adjustments for future high Sn content GeSn MOSFETs or S/D stressors.

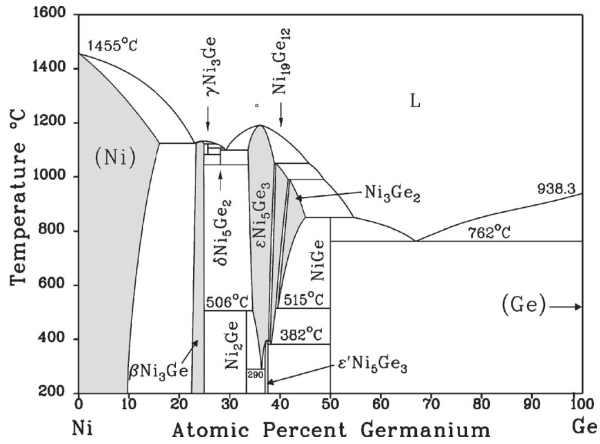


**Figure 3.51:** NiGe phase diagram taken from [150].

### 3.3.3 Phase Formation

Data on the phase formation of stanogermanides and stanogermanosilicides are less comprehensive so far. However the phase formation of NiGe is supposed to be quite similar, since Sn concentrations below 15 at.% are used. Here, four phases are known to be thermodynamically stable at room temperature (c.f. Fig. 3.51) - cubic $\beta$-$Ni_3Ge$, orthorhombic $Ni_2Ge$, monoclinic $Ni_5Ge_3$ and orthorhombic NiGe - whereas five phases are stable at elevated temperatures - $\gamma$-$Ni_3Ge$, hexagonal $Ni_5Ge_2$, hexagonal $Ni_5Ge_3$, orthorhombic $Ni_{19}Ge_{12}$ and hexagonal $Ni_3Ge_2$. The general phase sequence starts with a Ni-rich phase that changes at a certain temperature into a phase with the largest amount of Ge when all the Ni is consumed. For bulk processes and long annealings all thermodynamically stable phases at a certain temperature grow simultaneously in a diffusion controlled regime. In thin film processes with reduced temperatures as well as annealing times the phases grow sequentially mainly due to the reduced dimensions and the stronger influence of interfaces and surfaces. A number of studies have been carried out in order to investigate the phase formation in thin Ni germanides. It has been found that there are two possible phase sequences depending on the Ni film thickness, microstructure of the Ni film and the annealing conditions. Wittmer *et al.* [151] showed that for $100 - 150$ nm thick Ni films a $Ni_2Ge$ phase is formed first before it turns into the phase with the largest possible amount of Ge, namely NiGe. In contrast, for thinner metal depositions the initial phase is $Ni_5Ge_3$ [152, 153, 154].

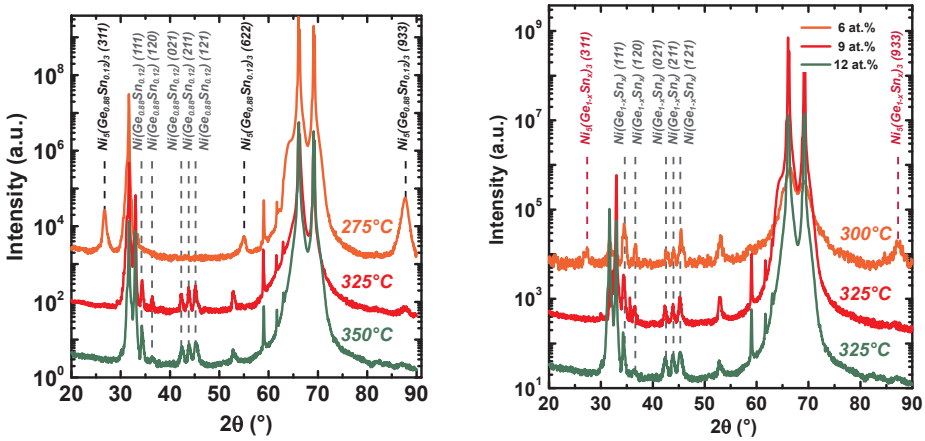


(a) (b)

**Figure 3.52:** XRD $\theta/2\theta$ scans presenting the NiGeSn phase formation at (a) constant Sn concentration, 12 at.%, and annealing temperatures between 275 °C and 350 °C as well as at (b) different Sn concentrations and annealing temperatures between 300 °C and 325 °C.

### Ni Stanogermanides

The phase formation in NiGeSn is analyzed using XRD $\theta/2\theta$ scans as presented in Fig. 3.52 (a) for $NiGe_{0.88}Sn_{0.12}$ (sample C). Here, measurements are shown for samples processed at annealing temperatures between 275 °C and 350 °C. Besides the (200) and (400) substrate peaks from Si and Ge an additional set of peaks is observed at $T_a$ = 275 °C, which is assigned to the Ni-rich $Ni_5(Ge_{0.88}Sn_{0.12})_3$ phase. Its first, second and third order peaks appear at 26.9°, 55.2° and 88.2°, respectively. This initial phase is also observed for lower Sn concentrations, i.e. sample A and B. The strong intensity of the peaks, especially of the first and third order peaks, indicates a well-ordered layer. If the annealing temperature is increased to 325 °C, this phase transforms into the final Ge-rich $Ni_1(Ge_{0.88}Sn_{0.12})_1$ phase identified by the emerging second set of peaks around 35° and 45° in the green and red scans in Fig. 3.52 (a). Rocking curves around the peaks at 34.6° and 45.5° show that these metal layers are polycrystalline with randomly oriented grains. In Fig. 3.52 (b) the curve for $NiGe_{0.94}Sn_{0.06}$ annealed at 300 °C suggests that both phases coexist at this temperature, which indicates a diffusion controlled growth regime [143]. In addition, the Ni-rich phase disappears at 325 °C for all Sn concentrations. Hence the observed phase transformation from $Ni_5(GeSn)_3$ to $Ni_1(GeSn)_1$ - similar to Ni germanides [152, 153, 154] - does not depend on the Sn content. However, the formation of the final Ge-rich phase starts at slightly lower temperatures for stanogermanides, 300 °C, as compared

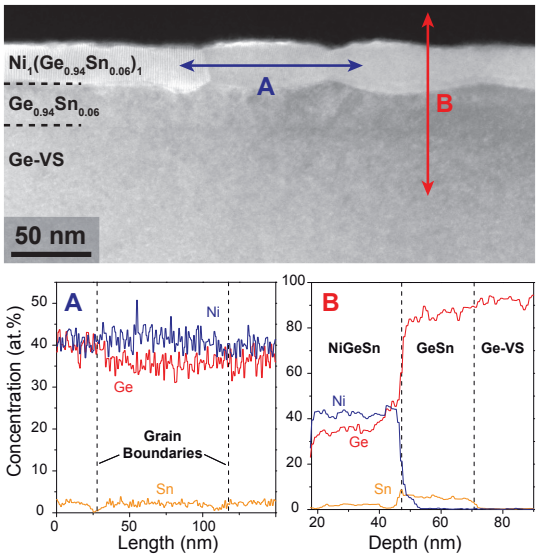


**Figure 3.53:** STEM image of a $NiGe_{0.94}Sn_{0.06}$ layer (sample A) annealed for 10 s at 300 °C. Below the energy dispersive X-ray spectroscopy results are shown for a horizontal (A) and vertical (B) cut through the sample.

to germanides, 325 °C [143]. The morphology as well as the atomic distribution of Ni, Sn and Ge throughout the stanogermanides are studied using *scanning transmission electron microscopy* (STEM) and *energy dispersive X-ray spectroscopy* (EDX). In Fig. 3.53 the results of the STEM and EDX analysis for a $Ni_1(Ge_{0.94}Sn_{0.06})_1$ layer (sample A) annealed for 10 s at 300 °C are displayed. In the top part of the figure an STEM image exhibits a smooth surface of the 25 nm thick stanogermanide. Obviously, not the whole $Ge_{0.94}Sn_{0.06}$ layer has been consumed during the annealing process, since underneath the metal layer there is still single crystalline GeSn. The interface between this GeSn and the NiGeSn layer is rather rough due to the polycrystallinity of the topmost metal layer. Differently oriented grains are clearly visible. In the bottom of the figure EDX line scans along (A) and perpendicular (B) to the grains are shown. Sn atoms are homogeneously distributed throughout a single grain in the vertical as well as in the horizontal scan. However, towards grain boundaries and the surface the Sn content is slightly reduced, whereas more Sn atoms are observed at the NiGeSn/GeSn interface as well as throughout the residual GeSn layer. A constant Ni signal is observed throughout the complete NiGeSn layer in vertical and horizontal direction even at the interfaces. Moreover, a nearly 1:1 stoichiometry between the Ni and the GeSn is observed in the NiGeSn layer. The RBS random and aligned spectra of the 45 nm thick as grown layer containing 6 at.% Sn (sample A) and its stanogermanides annealed at 300 °C, 350 °C and 400 °C for 10 s are presented in Fig. 3.54. The plateau in the Sn signal of the random spectrum indicates a homogeneous

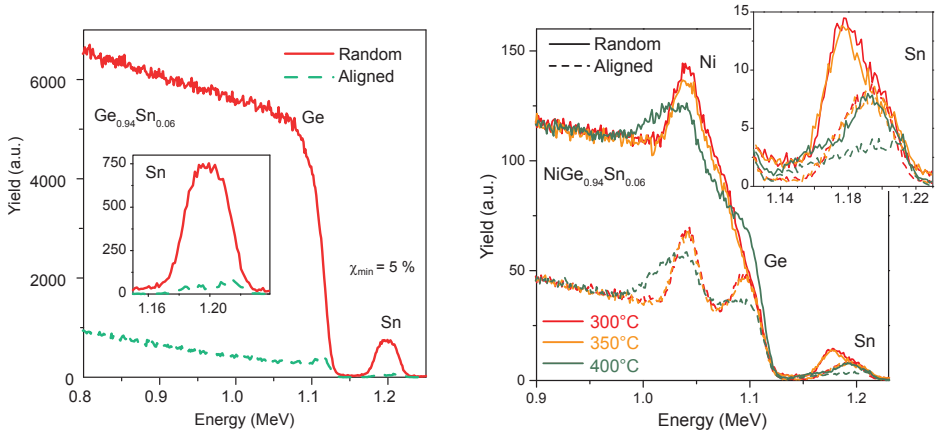


**Figure 3.54:** RBS/c spectra of the (a) as grown sample A and (b) the $NiGe_{0.94}Sn_{0.06}$ layers annealed at different temperatures, 300 °C, 350 °C and 400 °C for 10 s.

Sn distribution throughout the as grown $Ge_{0.94}Sn_{0.06}$ layer. Furthermore the minimum yield value of 5 %, which is close to the value of pseudomorphically grown SiGe on Si(001), evidence high single crystalline quality and nearly perfect substitutional incorporation of Sn atoms on Ge lattice sites. After the annealing process, the spectra become more complex, see Fig. 3.54 (b). Here, spectra for samples annealed at 300 °C and 350 °C (red and orange lines) are nearly identical. A higher Sn concentration of 5.5 at.% is measured within the 26 nm thick residual GeSn layer compared to the topmost metal layer with $x_{Sn} = 2.3 - 2.5$ at.% and a thickness of about 30 nm. The stoichiometry of the NiGeSn layer is nearly 1:1 confirming the EDX results and the Ge to Sn ratio in the NiGeSn layer is close to the ratio in the as grown layer. The latter indicates that Sn is soluble in NiGe as well as it suggests that the dominant diffusing species is probably Ni [155]. Moreover, for these low and moderate annealing temperature the yield of the aligned spectrum within the Sn signal increases towards the surface due to the polycrystalline structure of the NiGeSn phase. In contrast, the Sn concentration increases going from the residual GeSn layer to the NiGeSn for an annealing temperature of 400 °C (green line), and at the same time the minimum yield value decreases. In addition, as has been discussed in chapter 3.3.2 the layers start to exhibit cracks on the surface for this annealing temperature. These results may provide evidence for a starting agglomeration of NiGeSn at 400 °C with crystalline GeSn areas reaching the surface leading to the observed reduced $\chi_{min}$.

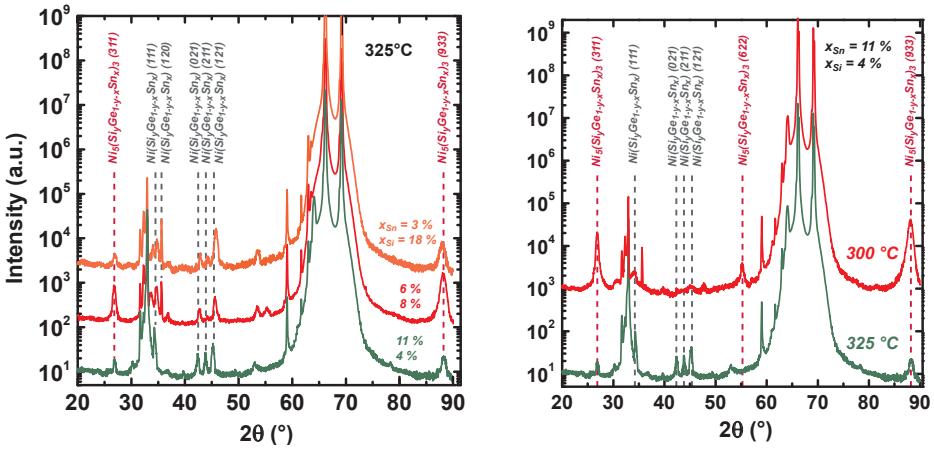


**Figure 3.55:** XRD $\theta/2\theta$ scans presenting the NiSiGeSn phase formation at (a) 325 °C and different Si and Sn concentrations and (b) different annealing temperatures.

### Ni Stanogermanosilicides

For the formation of Ni germanosilicides, which have been extensively studied for the implementation as S/D stressors in p-type SiGe MOSFETs, it is well-known that Ge tends to condensate at the alloy boundary due to the thermodynamically more favorable formation of NiSi [156]. In order to avoid this effect and to mediate the Ni-Si and Ni-Ge reactions, the incorporation of C, Al or Pt have been employed for improved layer morphology and enhanced thermal stability of the NiSiGe [157]. Thus, the contact formation on SiGeSn layers might differ from their NiGeSn counterparts. Indeed, a slightly different phase formation is observed as shown in Fig. 3.55. At an annealing temperature of 300 °C, as shown in Fig. 3.55 (b), only the XRD peaks for the Ni-rich $Ni_5(Si_xGe_ySn_{1-x-y})_3$ are observed for all Si/Sn compositions ranging from Si-rich (sample D) to Sn-rich ternary alloys (sample G). The formation of the Ge-rich phase starts at 325 °C, see Fig. 3.55 (a). At this annealing temperature both phases occur as it has been seen for NiGeSn at 300 °C. Above 325 °C only the $Ni_1(SiGeSn)_1$ phase remains. Again the phase formation is independent on the Si as well as Sn concentration. No Ge condensation is observed indicating that Sn might serve as mediator between the Ni-Si and Ni-Ge phase formation. Compared to the formation of Ni stanogermanides the initial $Ni_5(Si_xGe_ySn_{1-x-y})_3$ phase shows a slightly higher thermal stability up to 325 °C comparable to phase formation of Ni germanides.

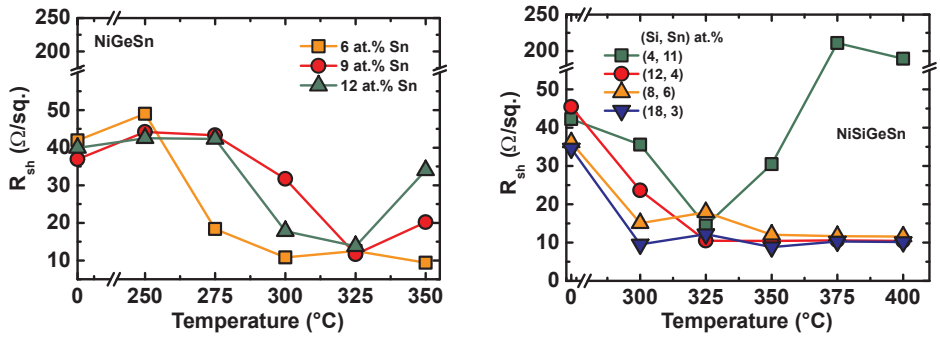


(a) (b)

**Figure 3.56:** Sheet resistance as function of annealing temperature for (a) NiGeSn and (b) NiSiGeSn layers.

### 3.3.4 Electrical Characterization

The sheet resistance as function of annealing temperature for NiGeSn and NiSiGeSn layers is presented in Fig. 3.56. The sample with the lowest Sn concentration (sample A) shows the largest temperature window, 275−350 °C, for low sheet resistances, $< 20\,\Omega$/sq., among the stanogermanides (Fig. 3.56 (a)). For sample B and C, the low sheet resistance regime shrinks to $300 - 325\,°C$. If the samples are annealed at even higher temperatures, the layer morphology degradation (c.f. chapter 3.3.2) leads to high sheet resistances. In terms of conductive properties a strong Sn dependence is thus observed. Adding Si significantly improves these properties as displayed in Fig. 3.56 (b). For samples D to F the low sheet resistance region extends to 400 °C. In contrast, for sample G with the highest Sn concentration a reasonably low sheet resistance is only observed at 325 °C. Assuming a stanogermanide and stanogermanosilicide thickness of about 25 nm the minimum specific resistivity of $20 - 25\,\mu\Omega$cm is obtained at 325 °C.

### 3.3.5 Discussion

The presented process for the contact formation on GeSn and SiGeSn layers using 10 nm Ni results in a 25 nm thick metal layer. During this process, i.e. for sample A, $15 - 19$ nm GeSn is consumed according to the EDX results (c.f. Fig. 3.53), which is close to the consumption ratio of Ni and Ge of 1 nm Ni + 2.05 nm Ge → 2.42 nm NiGe [158]. A phase sequence from an initial $Ni_5((Si)GeSn)_3$ to a final Ni stanogermanide or stanogermanosilicide is observed. The same sequence has been demonstrated by other groups [155, 159] for Sn concentration below 9 at.%. Neither NiGeSn formation above 10 at.% nor NiSiGeSn

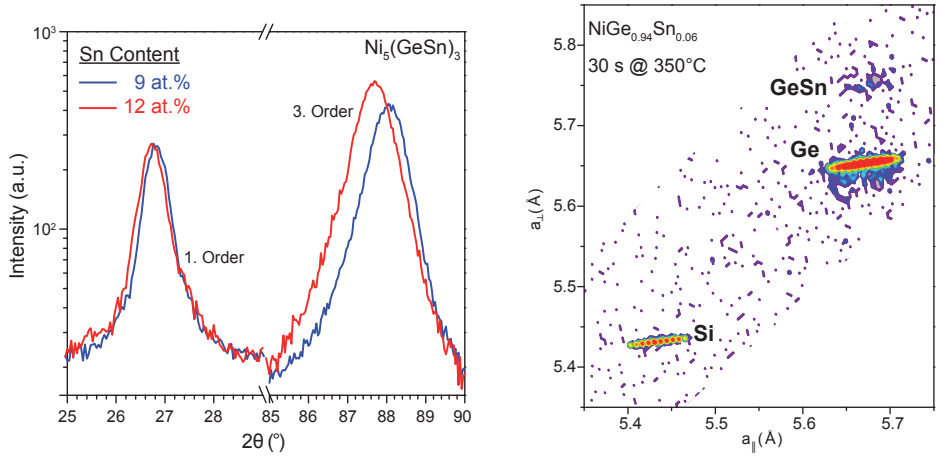


**Figure 3.57:** (a) First and third order XRD diffraction peaks of the $Ni_5(GeSn)_3$ phase for 9 at.% and 12 at.% Sn annealed at 275 ° for 10 s. (b) XRD-RSM of a $NiGe_{0.94}Sn_{0.06}$ layer annealed at 350 ° for 30 s.

formation have been reported before. A slightly different sequence with an initial epitaxial $Ni_2(GeSn)$ phase for $x_{Sn} = 3.6$ at.% has been determined in Refs [160, 148], which has not been observed in this study. Certain phases may exist solely in narrow process windows [143], so different phase sequences determined for the same material system is well-known. Regarding the mechanisms of the phase formation, Demeulemeester *et al.* [155] found that Sn atoms are incorporated in an initial $Ni_5Ge_3$ to form $Ni_5(GeSn)_3$ using *in-situ* real-time XRD and RBS measurements. However, it has not been clarified whether Sn atoms (i) substitute Ge in $Ni_5Ge_3$, (ii) are segregated at grain boundaries or (iii) are dissolved as $Ni_3Sn_2$ in $Ni_5Ge_3$. From the presented EDX results it can be excluded that Sn segregates at grain boundaries, since it has been found, that the Sn concentration decreases towards the NiGeSn grain boundaries. In addition, XRD results, shown in Fig. 3.57 (a), indicate a shift of $Ni_5(GeSn)_3$ diffraction peaks towards lower angles for increasing Sn content. This shift is caused by an increased amount of Sn atoms substitutionally incorporated into the $Ni_5(GeSn)_3$ with increasing Sn concentration, which in turn results in a larger lattice spacing. The same shift is observed for the NiGeSn phase. These results provide evidence for the assumption that Sn atoms indeed occupy Ge or Ni lattice sites in NiGeSn confirming the above process (i). The subsequent phase formation to Ni(Si)GeSn is supposed to occur by dissociation of the Ni-rich initial phase and the reaction between Ni and the (Si)GeSn epilayer. Interestingly enough, the formation temperature of the low resistive NiGeSn is lower compared to NiGe formation [143] but independent on the Sn content within $x_{Sn} = 6 - 12$ at.%. In the case of NiSiGeSn the formation temperature

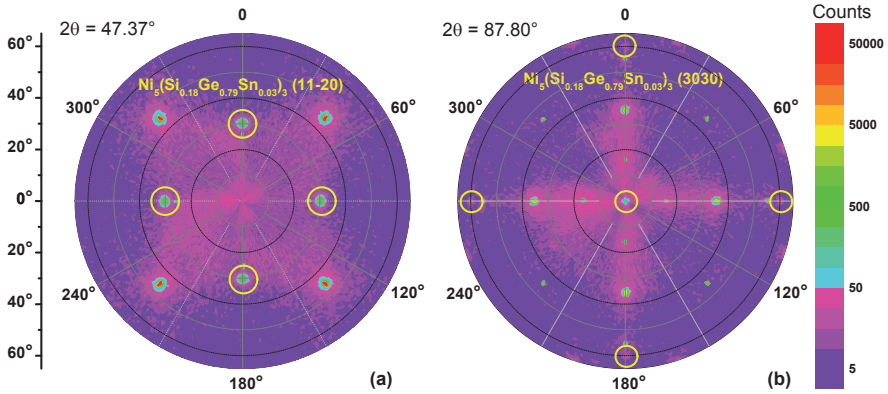


**Figure 3.58:** Pole figures of a $NiSi_{0.18}Ge_{0.79}Sn_{0.03}$ layer at (a) $2\theta = 47.37\,°$ and (b) $2\theta = 87.80\,°$.

is comparable to NiGe. It has also been shown that NiGeSn layers do not prevent Sn diffusion or segregation [155], so Sn atoms continue to redistribute throughout the structure for further increasing the annealing temperature. Sn tends to accumulate at the NiGeSn/GeSn interface as proven by EDX (chapter 3.3.3) and severe Sn precipitation occurs above 450 °C [160]. It has been observed throughout this study that the XRD diffraction peaks start to shift towards higher angles at 350 °C, so Sn diffusion out of NiGeSn may be triggered at these temperatures. On the other hand XRD-RSM (Fig. 3.57 (b)) shows that the underlying, residual GeSn layer is still fully strained and exhibits a Sn concentration of nearly 6 at.%.

Very recently, it has been shown that an epitaxial $Ni_5(SiGe)_3$ phase can be formed by introducing Al [161]. By means of plan view HR-TEM they identified two domains of the $Ni_5(SiGe)_3$ crystal that are rotated in-plane by 90 °. The determination of this crystalline structure is, however, challenging, because two different phases - hexagonal and monoclinic - with nearly identical XRD peaks are thermodynamically stable at the same time. In the case of Ni(Si)GeSn the expected XRD peaks of both phases fit the experimental data as presented in table 3.3 if a (10-10) or a (311) crystal orientation is assumed for the hexagonal or monoclinic phase, respectively. Thus, XRD pole figures are carried out (Fig. 3.58) at Bragg angles of $2\theta = 47.37\,°$ and $2\theta = 87.80\,°$ for a $NiSi_{0.18}Ge_{0.79}Sn_{0.03}$ layer annealed at 275 °C for 10 s. Diffraction peaks corresponding to the NiSiGeSn layer are marked in yellow and all reflections without a mark stem from the Si substrate and the Ge-VS. The measurement shown in Fig. 3.58 (a) exhibits a 90 ° symmetry, which might provide an indication for the assumption that the $Ni_5(SiGeSn)_3$ phase may be hexagonal with domains rotated in-plane by 90 °. Furthermore, the 180 ° symmetry observed in Fig. 3.58 (b) could be assigned to the hexagonal (3030) reflection, whereas the monoclinic (933) reflection (see table 3.3) would have appeared only once.

The lowest sheet resistance as well as sheet resistivity of about 10 Ωsq. and $20 - 25\,\mu\Omega$cm, respectively, are comparable to NiGe results [153, 154, 143, 150]. Here, the initial Ni-rich

| | Exp. | | Hexagonal | | | Monoclinic | | |
|---|---|---|---|---|---|---|---|---|
| | $2\theta$ (°) | $\chi$ (°) | Reflex | $2\theta$ (°) | $\chi$ (°) | Reflex | $2\theta$ (°) | $\chi$ (°) |
| 1. Peak | 26.9 | 0 | 10-10 | 26.3 | 0 | 311 | 26.8 | 0 |
| 2. Peak | 55.2 | 0 | 20-20 | 54.2 | 0 | 622 | 55.2 | 0 |
| 3. Peak | 88.2 | 0 | 30-30 | 86.3 | 0 | 933 | 88.1 | 0 |
| 4. Peak | 46.6 | 30 | 11-20 | 46.5 | 30 | 602 | 46.4 | 31 |

**Table 3.3:** Expected and experimental XRD diffraction peak positions of the hexagonal and monoclinic phase of $Ni_5(SiGeSn)_3$.

as well as the observed multiphase of Ni(Si)GeSn and $Ni_5((Si)GeSn)_3$ show higher resistivities compared to the (Si)GeSn-rich phase as expected from NiGe- and NiSi- as well as from recent NiGeSn-studies [159]. According to the observed distinct transformation to the (Si)GeSn-rich phase, the sheet resistance drops at an annealing temperature of 325 °C and > 325 °C for NiGeSn and NiSiGeSn, respectively. For metal layers with the highest Sn concentration of 12 at.% the resistance increases immediately for slightly higher temperatures than 325 °C. Since a further phase transition to another Ge(Sn)-rich phase is impossible for higher temperatures, the increasing resistivity of the layers might be due to morphology degradation [162], i.e. NiGe(Sn) agglomeration or Sn segregation. In the case of NiGeSn this critical temperature is shifted to higher values for lower Sn concentrations, which is in accordance with the results on the layer morphology. Compared to NiGe the thermal stability of NiGeSn is reduced by about 150 °C. Zhang *et al.* [162] have ascribed the reduced thermal stability of NiGe compared to NiSi to agglomeration, and they suggested that the lower activation energy of NiGe agglomeration is attributed to a lower activation energy of Ge epitaxy compared to Si epitaxy. They believe that epitaxial Ge grows between the NiGe grains. In the case of NiGeSn this activation energy might be further reduced by the strong tendency of Sn atoms to segregate towards the surface. In contrast, the thermal stability of low resistive NiSiGeSn is significantly higher apart from sample G containing the highest Sn concentration. For future Ge MOSFET processes including raised S/D stressors NiSiGeSn layers with the appropriate Sn to Si concentration ratio may provide sufficiently high thermal stability and large uniaxial compressive as well as tensile strain levels. In order to further increase the thermal stability of NiGeSn the use of Pt has been suggested recently by Wang *et al.* [149]. The stronger chemical bond of Pt-Ge compared to Ni-Ge might reduce the breaking of bonds at grain boundaries enhancing the morphological stability [149].

## 3.4 Summary

Novel, highly tensile strained - up to 1.4 % strain - Ge and GeSn layers grown on GeSn SRBs have been investigated in the first part of this chapter regarding their implementation as channel material for high mobility MOSFET or TFET devices. Therefore, electronic band structure calculations and MOSCAP characterization at room and low temperature have been carried out.

- It has been shown that the effective masses of holes and electrons significantly decrease for sGe as well as for sGeSn compared to unstrained Ge. Here, the lowest effective hole masses can be achieved by a combination of moderate tensile strain, 0.4 %, and Sn alloying, $x_{Sn} = 6$ at.%. In terms of effective electron mass sGe is advantageous.
- A TFET structure based on Si-Ge-Sn alloys has been proposed. It has been found that $sGe_{0.94}Sn_{0.06}$ with $\epsilon = 0.4\,\%$ becomes a fundamental direct bandgap semiconductor, which makes it an ideal channel material for TFET devices. For the drain, $Si_{0.12}Ge_{0.84}Sn_{0.04}$ has been suggested owed to its larger and indirect bandgap compared to sGe(Sn).
- The thermal budget for the sGe(Sn) MOSCAP process is restricted to 300 °C. At higher temperatures, i.e. 350 °C, severe Sn and Ge diffusion as well as strain relaxation occur.
- Room temperature CV characteristics have exhibited strong inversion response due to the narrow bandgap of the layers under investigation. This effect has been suppressed at lower temperatures. In addition, only a slight frequency dispersion in accumulation and depletion at any temperature between 80 K and 300 K indicates reasonably low $D_{it}$ values and no Fermi-level pinning. Avoiding Fermi-level pinning should allow good control over the carriers in the channel and good sub-threshold slopes as well as high drive currents.

In the second part of this chapter, the contact formation on pseudomorphically grown GeSn and SiGeSn layers on Ge-VS have been studied. Here, the Sn and Si concentrations range from 3 at.% to 12 at.% and 0 at.% to 18 at.%, respectively. The incorporated strain varies accordingly from 0.4 % (tensile) to −1.7 % (compressive). The NiGeSn and NiSiGeSn metal layers have been analyzed regarding their formation temperature, phase evolution, sheet resistance and thermal stability.

- Smooth and continuous NiGeSn layers have been found for formation temperatures $< 350$ °C. The morphological degradation above this temperature strongly depends on the Sn concentration. By adding Si the layers remain smooth up to 350 °C.

- A phase evolution from $Ni_5((Si)GeSn)_3$ to $Ni_1((Si)GeSn)_1$ is observed. Here, a lower phase formation temperature of 300 °C is determined for the low resistive $Ni_1(GeSn)_1$ phase compared to $Ni_1(SiGeSn)_1$ (325 °C). The phase formation does not depend on the Sn concentration and at 400 °C agglomeration is likely to appear.
- A specific resistivity of $20 - 25\,\mu\Omega$cm has been achieved for a process temperature of 325 °C for NiGeSn and NiSiGeSn layers.
- The residual (Si)GeSn layers remain fully strained after the metallization process which is essential for their use as S/D stressors in sGe-MOSFETs.

# Chapter 4

## Lasing In Direct Bandgap GeSn Grown On Si(001)

The most common materials for state-of-the-art semiconductor laser diodes are InP-, GaN- and GaAs-based III/V compounds grown on InP or GaAs wafers, due to their fundamental direct bandgap. This direct bandgap nature is widely known as being the prerequisite for achieving population inversion at low injection current densities. Group IV semiconductors, like Si or Ge, provide an indirect bandgap, which makes it very challenging to achieve population inversion or lasing. The main motivation for alloying Ge with Sn is to fabricate a fundamental direct bandgap group IV semiconductor. Already in the late 1980's Jenkins and Dow [163] predicted this transition to occur at Sn concentrations of approx. 20 at.%. They employed a *virtual-crystal approximation* (VCA) and a second-nearest-neighbor tight-binding model. Spectroscopic ellipsometry and photoreflectance studies [164] reveal a large direct bandgap bowing due to disorder induced potential fluctuations [26], which have to be accounted for in the band structure calculations. Hence, more recent simulations predict the indirect to direct bandgap transition in unstrained single crystals for Sn concentrations between 6 at.% and 11 at.% [165, 26, 166, 167, 4]. Subsequently, several groups have tried to experimentally verify the predictions [168, 169, 86, 170, 171] for (Si)GeSn alloys, but an unambiguous proof is still missing. In the following chapter the experimental verification of the transition from an indirect to a fundamental direct bandgap in GeSn and SiGeSn alloys is demonstrated using temperature dependent PL measurements. Sn concentrations up to 12.6 at.% in mild compressively strained GeSn epilayers grown on Si(001) are sufficient to pull the Γ-valley below the L-valleys. Gain measurements using the *variable stripe length* (VSL) method provide evidence for stimulated emission in these direct bandgap group IV semiconductors grown on Si(001). Finally, GeSn cavities are optically excited. Threshold behavior of the emitted intensity as well as linewidth for increasing excitation power in combination with a consistent cavity mode pattern reveal unambiguous lasing action.

Parts of the results presented in this chapter have been published in [172]. The experiments as well as the data interpretation have been carried out in strong collaboration with the Paul Scherrer Institut, Switzerland. Band structure calculations and gain predictions have been provided by the University of Leeds, United Kingdom.

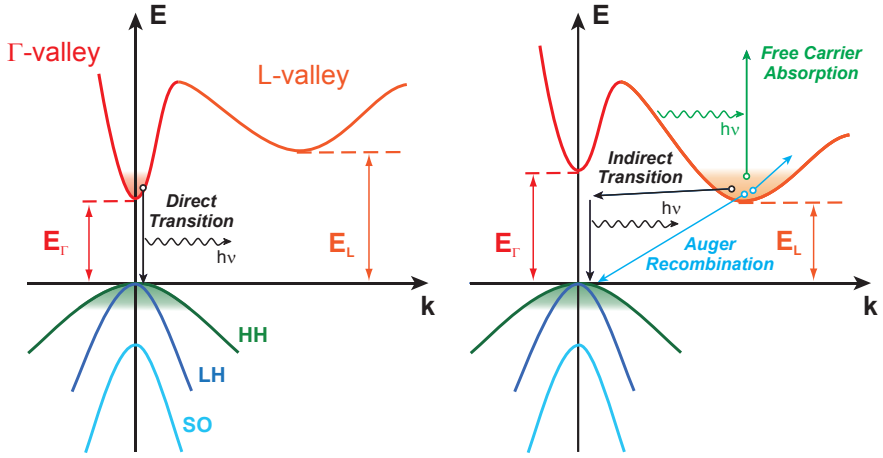


**Figure 4.1:** Sketch of the band structures of direct and indirect semiconductors. In direct semiconductors radiative transitions are more favorable compared to radiative transitions in materials with an indirect bandgap. Here, a phonon is required to conserve momentum hence nonradiative transitions, i.e. Auger recombination, and losses, i.e. free carrier absorption, dominate the electron-hole pair recombination.

## 4.1 Background

Si and Ge are inefficient light emitters due to an unfavorable electronic band structure leading to an accumulation of electrons with too high a momentum to recombine via emission of a photon. In contrast to direct bandgap semiconductors like most compounds comprising elements of groups III and V of the Periodic Table, so-called III/V semiconductors, the conduction band minimum is not located at the center of the Brillouin zone, namely the Γ-point, just as the valence band maximum, but at the L-point. Therefore, radiative interband transitions of electrons from the conduction into the valence band in indirect semiconductors are second order processes. The emission or absorption of a quantized lattice vibration, called *phonon*, is required for these transitions in order to conserve momentum (c.f. Fig. 4.1) resulting in a low radiative transition probability compared to first order electronic interband transitions occurring in direct bandgap semiconductors. These transition probabilities might be translated into radiative carrier recombination lifetimes $\tau_r$. Consequently, direct bandgap materials provide much shorter $\tau_r$ in the order of ns [173] compared to indirect materials with $\tau_r$ of a few ms [174]. On the other hand, electron-hole pairs may also recombine nonradiatively with a nonradiative carrier recombination lifetime $\tau_{nr}$. There are two nonradiative recombination categories, namely *intrinsic* (such as *Auger recombination*) and *extrinsic* (such as *Shockley-Read-Hall recombination* (SRH)). As indicated in Fig. 4.1 an electron-hole recombination is called Auger recombination if the resultant energy is transferred to another electron or hole in the

conduction or valence band without photon emission. This process becomes dominant for high carrier injection. In the case of high doping levels, loss mechanisms (such as the *free carrier absorption* (FCA)) are relevant. If a photon is absorbed by an excited carrier in the conduction band and the latter subsequently occupies an elevated state, this is termed FCA. In this context, the internal quantum efficiency $\eta_i$, defined as the ratio of the radiative recombination rate over the total recombination rate, is a key parameter for light emission and can be written as:

$$\eta_i = \frac{\tau_{nr}}{\tau_{nr} + \tau_r} . \tag{4.1}$$

$\tau_{nr}$ might be in the order of nanoseconds in Si, which is orders of magnitude shorter than $\tau_r$ of the second order radiative recombination process, due to recombination via defect induced deep level traps. With above numbers we obtain $\eta_i$ of about $10^{-6}$.
Thus, recent research interest focused on either decreasing the radiative or increasing the nonradiative lifetime in group IV semiconductors. Especially in the case of Si the latter option is a prominent route, since band engineering Si towards a direct bandgap semiconductor and hence decreasing $\tau_r$ is difficult due to the large energy difference between the conduction band minima at the Γ- and X-point of approximately 2.2 eV [23]. A method to increase $\tau_{nr}$ in Si and hence decrease the mean free path of carriers within the material is to spatially confine carriers via nanocrystals [175, 176, 177, 178], rare-earth doped Si [179, 180], porous Si [181, 182, 183, 184] or superlattices [185]. Amongst others, promising results have been published by Pavesi *et al.* [177] who measured optical gain values of $(100 \pm 10)\,\mathrm{cm}^{-1}$ as well as linewidth narrowing in Si quantum dots (QDs) dispersed in a $SiO_2$ matrix. However, neither lasing action nor efficient bipolar electrical injection have been achieved so far. All these techniques exhibit one common drawback, namely the poor brightness due to the unchanged high radiative lifetime requiring phonon emission or absorption.
In 2004 *stimulated Raman scattering* (SRS) has been successfully employed to demonstrate stimulated emission in Si [186, 187, 188, 189]. The large Raman scattering cross-section in Si allows to achieve significant gain values and even lasing in Si. This effect, though, has to be stimulated by an external optical pump, which prohibits large scale integration.
Ge attracted lots of research effort in recent years, owed to the low energy offset of approximately 140 meV between the L- and the Γ-valley in the conduction band [23]. This makes band engineering towards a direct bandgap in Ge, that is, decreasing the radiative lifetime, more promising in contrast to Si. Here, the most commonly used approach is to either introduce uniaxial [190, 191, 192] or biaxial [193, 29, 194, 195, 13] tensile strain in order to pull the Γ- below the L-valleys. Despite efforts made, an unambiguous proof for a direct bandgap in Ge has not been published up to now. Another way to populate the conduction band valley with electrons in the center of the Brillouin zone is to fill all states in the L-valleys up to the Γ-valley via heavy n-type doping [196]. For moderate tensile strain, induced by the mismatch of the lattice thermal expansion coefficient between Si and Ge, in combination with n-type doping levels between $1 \cdot 10^{19}\,\mathrm{cm}^{-3}$ and $4 \cdot 10^{19}\,\mathrm{cm}^{-3}$ optically [197] and electrically [198] pumped lasing action in Ge has been

claimed. However, the large threshold current densities of $280\,\mathrm{kA/cm^2}$ implies unfeasibly short device lifetimes. In addition, the obtained gain values of approximately $50\,\mathrm{cm^{-1}}$ are under debate. Carroll *et al.* [199] investigated the optical gain in Ge as a function of carrier density, strain and doping as well as the role of valence intraband absorption via pump-probe measurements. They have shown that in Ge, a photoexcited carrier density of approx. $10^{20}\,\mathrm{cm^{-3}}$ is required to achieve population inversion (c.f. chapter 4.4), which entails strong parasitic absorption effects prohibiting optical amplification in Ge. No research group has been able to reproduce or confirm the results of gain and lasing in Ge so far [200, 201].

## 4.2 Photoluminescence in Semiconductors

Basically, there are three different optical processes in semiconductors regarding band to band transitions between the conduction and valence band called *absorption*, *spontaneous emission* and *stimulated emission*. In equilibrium, absorption and spontaneous emission, which are the fundamental mechanisms for example in photodetectors and *light emitting diodes* (LED), respectively, are predominant. These two mechanisms also represent the basis for PL measurements, which are used in this section to investigate radiative transitions in GeSn. Here, the sample is illuminated by laser light in order to photoexcite electron-hole pairs by absorption that subsequently diffuse and relax into quasi-equilibrium distributions and finally recombine radiatively or nonradiatively. Hence, photoluminescence can be divided into three main processes, that are (i) electron-hole pair excitation, (ii) electron-hole pair thermalization and diffusion and (iii) electron-hole pair recombination. Electrons might be photoexcited from any valence band near the center of the Brillouin zone, i.e. light hole (LH), heavy hole (HH) or split-off (SO) valence band, into all conduction bands via direct or indirect transitions. In this connection, the absorption via indirect transitions in indirect semiconductors requires phonon absorption or emission, which results in a rather weak absorption and in turn in large penetration depths. The carrier generation can be expressed by Beer's law [173]:

$$G(z, \hbar\omega_e) = [1 - R(\hbar\omega_e)]\alpha(\hbar\omega_e)\Phi(0)\exp[-\alpha(\hbar\omega_e)z]\ . \tag{4.2}$$

$\mathrm{R}(\hbar\omega_e)$ is the reflectivity, $\Phi(0)$ is the incident photon flux and $\alpha(\hbar\omega_e)$ is the absorption coefficient at the excitation energy $\hbar\omega_e$. The excited carriers have a higher kinetic energy compared to the average thermal energy of the lattice, since $\hbar\omega_e > E_g$. All excited carriers relax subsequently to the band edges in a three step thermalization process. In an initial very fast relaxation, the carriers thermalize among themselves resulting in a so-called hot carrier distribution exhibiting a higher temperature compared to the lattice. This hot distribution cools down towards the lattice temperature in the second step via optical phonons. These first two relaxation processes take place on a time scale shorter than 100 ps. The final cooling of the distribution to the lattice temperature via acoustic phonons takes about nanoseconds and, thus, compete with the depletion of carriers via

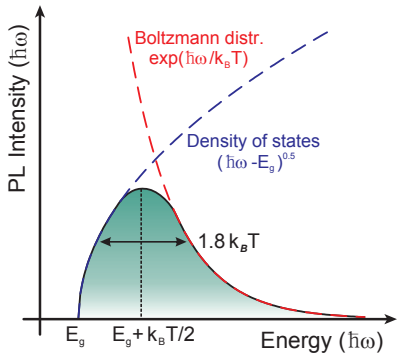


**Figure 4.2:** Sketch of the theoretical spectrum of spontaneous emission. (After [202])

recombination. During thermalization excited carriers can diffuse throughout the whole sample that could lead to carrier loss via nonradiative recombination.

### 4.2.1 Radiative Recombination

Since PL measurements are sensitive to radiative recombination paths of photoexcited electron-hole pairs only, the measured PL intensity within an energy range $[\hbar\omega, \hbar\omega + d\hbar\omega]$ is directly related to the *spontaneous emission rate* $\mathrm{R}_{sp}(\hbar\omega)$. This rate can be expressed via [203]:

$$R_{sp}(\hbar\omega)d\hbar\omega \propto \sum_{\mathbf{k_e},\mathbf{k_h}} |\mathcal{H}(\mathbf{k_e},\mathbf{k_h})|^2 \, F_C(\mathbf{k_e})[1 - F_V(\mathbf{k_h})]\delta(E_C(\mathbf{k_e}) - E_V(\mathbf{k_h}) - \hbar\omega)d\hbar\omega, \quad (4.3)$$

here $\mathcal{H}(\mathbf{k_e},\mathbf{k_h})$ is the dipole matrix element for the transition from the conduction band into the valence band with $\mathbf{k_e}$ and $\mathbf{k_h}$ being the wave vectors of the electrons and holes, respectively, and $F_{C,V}(\mathbf{k_{e,h}})$ are the carrier occupation functions. Although, one has to consider non-equilibrium conditions in a PL measurement, the thermalization of electrons and holes among themselves takes place prior to the electron-hole recombination, hence *Fermi-Dirac distributions* can be used as occupation functions:

$$F_C(\mathbf{k_e}) = \frac{1}{1 + \exp[(E_C(\mathbf{k_e}) - E_{f,e})/k_B T]}, \quad (4.4)$$

$$F_V(\mathbf{k_h}) = \frac{1}{1 + \exp[(E_V(\mathbf{k_h}) - E_{f,h})/k_B T]} \, . \quad (4.5)$$

Where $E_{f,e}$ and $E_{f,h}$ are the quasi Fermi levels of the electrons and holes, respectively, and $k_B$ is the Boltzmann constant. Finally, for the total spontaneous emission rate $\mathrm{R}_{sp}(\hbar\omega)$ has to be integrated over all photon energies [203]:

$$R_{sp} = \int R_{sp}(\hbar\omega)d\hbar\omega \, . \quad (4.6)$$

Equation 4.3 can be simplified for direct bandgap semiconductors. First, only vertical transitions in the k-space have to be considered and since the momentum of a photon is negligible the two sums over $\mathbf{k}_e$ and $\mathbf{k}_h$ can be replaced by an integral over $\mathbf{k}$ and the remaining sum accounts for LH, HH and SO valence bands:

$$R_{sp}(\hbar\omega) \propto \sum_{v=LH,HH,SO} |\mathcal{H}|^2 F_C(\mathbf{k})[1 - F_V(\mathbf{k})]\delta(E_C(\mathbf{k}) - E_V(\mathbf{k}) - \hbar\omega)d^3k \,. \tag{4.7}$$

The energy dependence of the dipole matrix element can be neglected for low excitation energies [203], and for parabolic bands the density of states is proportional to $\sqrt{\hbar\omega - E_g}$. Moreover, in this work merely undoped GeSn samples are investigated, which means that the carrier energy is well above the Fermi-level. Therefore, the Fermi-Dirac distribution can be approximated by the Boltzmann factor $\exp[-(\hbar\omega)/(k_BT)]$. The spectral spontaneous emission rate for fundamental direct bandgap semiconductors can thus be written as:

$$R_{sp}(\hbar\omega) \propto \sqrt{\hbar\omega - E_g} \exp\left(-\frac{\hbar\omega - E_g}{k_BT}\right) . \tag{4.8}$$

In Fig. 4.2 the theoretical direct transition PL spectrum of the spontenous emission is shown. The peak energy of the spectra is related to the bandgap of the semiconductor via $\hbar\omega_p = E_g + 1/2k_BT$, whereas the half width is $\Delta E = 1.8\,\mathrm{k_B T}$. The carrier temperature can be extracted from the high energy tail that is proportional to $\exp[-(\hbar\omega - E_g)/(k_BT)]$. In the case of indirect semiconductors no momentum restriction is imposed by the dipole matrix element and the spontaneous emission rate reads:

$$R_{sp}(\hbar\omega) \propto \int dE_C \int dE_V \rho(E_C)\rho(E_V)F_C(E_C)[1 - F_V(E_V)]\delta(E_C - E_V - \hbar\omega \pm \hbar\omega_q), \tag{4.9}$$

here $\rho(E_{V,C})$ are the densities of states of the valence and conduction bands and $\pm\hbar\omega_q$ accounts for the absorption (+) and emission (-) of phonons during the recombination. Again, the integrals can be solved under the same assumption of an energy independent dipole matrix element, parabolic bands and a non-degenerated semiconductor:

$$\begin{aligned} R_{sp}(\hbar\omega) \;\propto\; & \frac{(\hbar\omega + \hbar\omega_q - E_g)^2}{1 - \exp\left(-\frac{\hbar\omega_q}{k_BT}\right)} \exp\left[-\frac{(\hbar\omega + \hbar\omega_q - E_g)}{k_BT}\right] \\ + \; & \frac{(\hbar\omega - \hbar\omega_q - E_g)^2}{\exp\left(\frac{\hbar\omega_q}{k_BT}\right) - 1} \exp\left[-\frac{(\hbar\omega - \hbar\omega_q - E_g)}{k_BT}\right] . \end{aligned} \tag{4.10}$$

Here, the two summands consider phonon absorption and emission. The peak energy and the half width of the PL spectrum in this case are $\hbar\omega_p = E_g - \hbar\omega_q + 2k_BT$ and $\Delta E \cong 3.4\,\mathrm{k_B T}$, respectively.

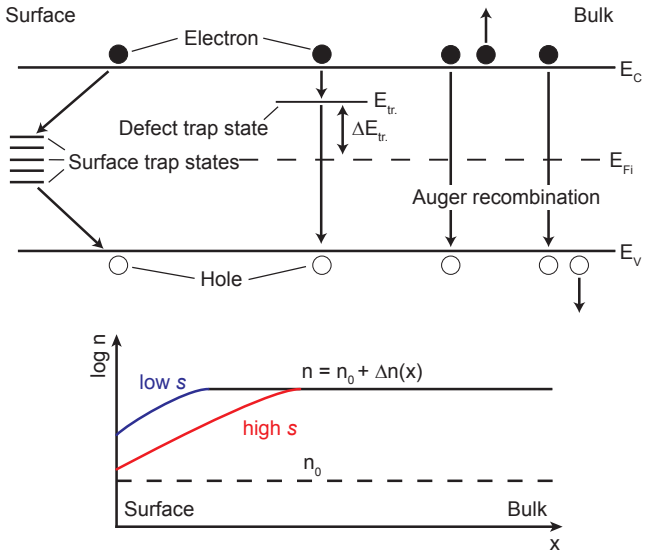


**Figure 4.3:** Sketch of extrinsic nonradiative recombination processes in semiconductors. Electrons may recombine with holes via surface or defect trap states without emission of a photon. $s$ depicts the surface recombination velocity. (After [202])

### 4.2.2 Nonradiative Recombination

The main mechanisms of nonradiative carrier recombination are the following: Auger recombination, defect and surface recombination. For high injection rates, Auger recombination is the predominant process. This recombination mechanism is called intrinsic and is always present even in a perfect crystal. Besides the unavoidable Auger recombination the effect of extrinsic nonradiative transitions like surface or defect recombination on the luminescence of group IV heterostructures depict a serious challenge. Especially in the present case of GeSn and SiGeSn alloys grown at very low temperatures, as discussed in chapter 2, a significant number of point defects might be introduced during growth. Moreover, since efficient light emission is much more favorable for unstrained or tensile strained alloys due to the reduced difference in energy between the Γ- and L-valleys [26], misfit dislocations are present in the investigated (Si)GeSn/Ge/Si(001) heterostructures induced by the strain relaxation process (c.f. chapter 2). As displayed in Fig. 4.3 defects might form energy levels deep inside the bandgap. In this context, the most common defects are dislocations, native defects, point defects, defect complexes, foreign atoms and interstitials or vacancies. Trap states located within the bandgap open an additional nonradiative recombination path for electron-hole pairs and reduce the luminescence efficiency. The rate

of this SRH recombination is given by [204, 205]:

$$R_{SRH} = \frac{p_0\Delta n + n_0\Delta p + \Delta n\Delta p}{(N_T\nu_p\sigma_p)^{-1}(n_0 + n_l + \Delta n) + (N_T\nu_n\sigma_n)^{-1}(p_0 + p_l + \Delta p)} , \tag{4.11}$$

where $\nu_n$ and $\nu_p$ are the electron and hole thermal velocities, $\sigma_n$ and $\sigma_p$ are the capture cross sections for electrons and holes, $\Delta n$ and $\Delta p$ are the excess carrier concentrations due to low excitation, $N_T$ is the trap concentration and $n_l$ and $p_l$ are the electron and hole concentrations if the Fermi energy is located at the trap level. $n_0$ and $p_0$ depict the equilibrium electron and hole concentration, respectively. For intrinsic semiconductors and small deviation from equilibrium, i.e. low excitation, ($\Delta n \ll p_0$) the nonradiative carrier lifetime under the assumptions of $\nu_n\sigma_n = \nu_p\sigma_p$ and $\tau_{n0} = \tau_{p0}$ is given by:

$$\tau = \tau_{n0}\left[1 + \cosh\left(\frac{E_T - E_{Fi}}{k_BT}\right)\right] . \tag{4.12}$$

Here, $E_{Fi}$ is the intrinsic Fermi level and $\tau_{n0}$ depicts the minority carrier lifetime. Obviously, the nonradiative carrier lifetime based on SRH recombination is minimized to $\tau = 2\tau_{n0}$ if $E_T - E_{Fi} = 0$. Hence, deep trap levels close to midgap are effective recombination centers. Moreover, equation 4.12 shows that for elevated temperatures the SRH recombination rate increases, since $\tau$ declines. As a consequence indirect and direct bandgap semiconductors exhibit the highest luminescence efficiency at cryogenic temperatures.

In Fig. 4.3 another nonradiative recombination mechanism is indicated. The energy stemming from an electron-hole recombination might be dissipated by the excitation of a free electron or hole to higher or lower energy states within the energy bands, respectively. This is called Auger recombination. For low excitation levels the Auger recombination rate can be written as [202]:

$$R_{Auger} = C_p np^2 \quad \text{(p-type)}, \tag{4.13}$$

$$R_{Auger} = C_n n^2 p \quad \text{(n-type)}, \tag{4.14}$$

where the Auger coefficients $C_n$ and $C_p$ differ in general and energy as well as momentum conservation must be true. In the case of high excitation, where the non-equilibrium carrier concentration is higher than the equilibrium concentration the Auger recombination rate is given by [202]:

$$R_{Auger} = (C_p + C_n)n^3 = Cn^3 . \tag{4.15}$$

Hence, the Auger recombination becomes significant for high excitation intensities or injection currents.

Finally, electron-hole recombination at the surface may lead to a reduced luminescence efficiency. Surface reconstruction due to dangling bonds [202] results in surface trap states within the bandgap, see Fig. 4.3. The carrier concentration as function of the distance $x$ from the surface for low excitation can be expressed via [202]:

$$n = n_0 + \Delta n(x) . \tag{4.16}$$

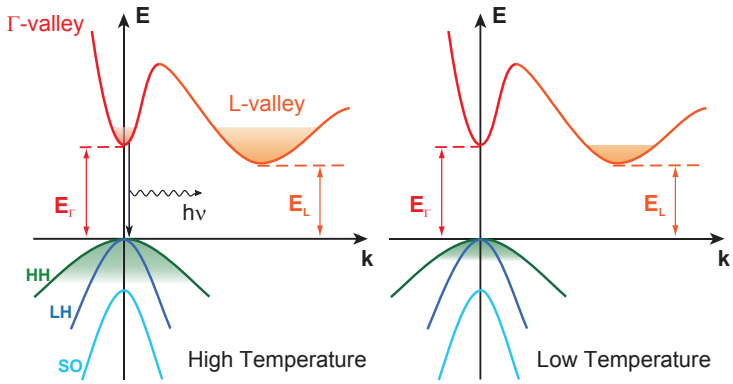


**Figure 4.4:** Sketch of the carrier distributions in an indirect semiconductor at two different temperatures. At 300 K the distribution is smeared out resulting in carrier population of the Γ-valley allowing radiative transitions.

Here, $\Delta n(x)$ depends on the surface recombination velocity $s$ and exponentially on $x$. As illustrated in the bottom of Fig. 4.3, for low $s$ ($s \to 0$) the minority carrier concentration equals the bulk concentration $n(0) \to n_0 + \Delta n$, whereas for a high surface recombination velocity $n(0) \to n_0$. Surface recombination leads to both a reduced luminescence efficiency and a surface heating owing to their nonradiative nature. Typical values for $s$ are $10^4$ m/s for GaAs or 0.1 m/s for Si. Very recently, Geiger *et al.* [200] have determined surface recombination velocities for Ge layers grown on Si and for germanium-on-insulator of $490 - 920$ m/s by means of synchrotron based pump-probe transmission spectroscopy.

### 4.2.3 Temperature Dependent Photoluminescence

As depicted in Fig. 4.4 low optical pumping (far below transparency) at elevated temperatures of quasi-direct bandgap semiconductors, i.e. heavy n-type doped Ge layers [85], tensile strained Ge [190] or low concentrated GeSn alloys [86], results in electronic population within the Γ-valley of the conduction band, due to the temperature dependence of the Fermi-Dirac distribution (c.f. equation 4.4). As a consequence, electron-hole pairs may recombine radiatively without the need of a phonon. If the temperature is decreased the Fermi-Dirac distribution becomes more and more a step function prohibiting the population of the Γ-valley and, thus, radiative recombination decays exponentially according to the temperature dependence of $F_C(E)$. Consequently, as shown by Sun *et al.* [85], the PL intensity of indirect bandgap Ge or GeSn declines for decreasing temperature. In contrast, electronic transitions in fundamental direct bandgap materials, such as III-V semiconductors, occur at the center of the Brillouin zone at any temperature. Furthermore, the number of carriers per $dk$ in reciprocal space is decreased with increasing temperature,

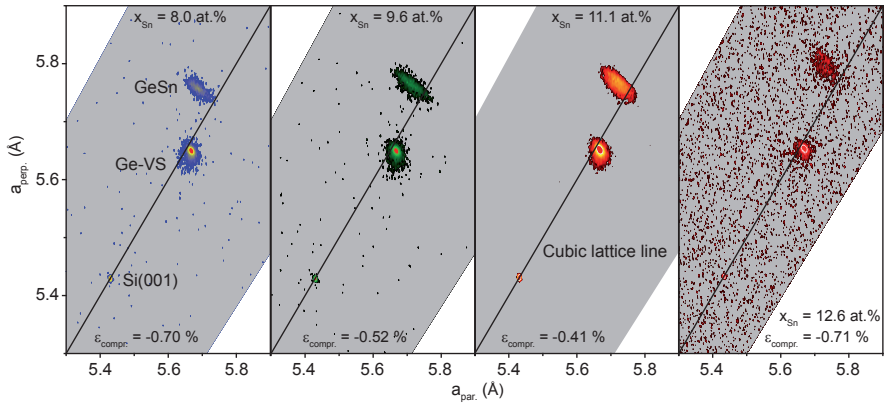


**Figure 4.5:** XRD-RSM around the asymmetric (224) reflection of sample A to D. For all layers a residual compressive strain is measured; the GeSn peaks are right above the diagonal cubic lattice line.

due to the large tail of the Fermi-Dirac distribution at elevated temperatures. This results in a reduced recombination probability at elevated temperatures, since the number of holes available for electrons to recombine at equal momentum is reduced [202]. In addition, the reduction of the nonradiative recombination rate at lower temperatures in semiconductors leads to an additional increase of the luminescence for decreasing temperature.

## 4.3 Indirect to Direct Bandgap Transition in (Si)GeSn

One reason for the lack of direct bandgap GeSn materials so far was the trade-off between high Sn concentration, incorporated strain and crystalline quality. As has been discussed before (c.f. chapter 2) incorporating a high concentration of Sn atoms substitutionally into the Ge lattice and preserving high single crystalline quality of the epilayers at the same time is a challenging task. In addition, achieving complete strain relaxation in metastable GeSn alloys seems to be even more difficult, because rapid thermal annealing will lead to Sn precipitation due to the fast Sn diffusion in Ge. Hence, the unavoidable residual compressive strain, which is counterproductive in terms of fundamental direct bandgap GeSn, has to be overcompensated by a larger Sn content within the alloy. During this work, a CVD growth process has been developed, that enables the epitaxial growth of partially relaxed, single crystalline GeSn layers with high Sn concentrations, c.f. chapter 2.
An elegant way to provide evidence that a semiconductor has a fundamental direct bandgap is obtained from a study of the temperature dependent PL. For this study a set of four GeSn samples (A,B,C and D) grown on Si(001) have been measured. Lay-

| Sample | $a_{par.}$ (Å) | $a_{perp.}$ (Å) | $x_{Sn,XRD}$ (at.%) | $x_{Sn,RBS}$ (at.%) | $\epsilon_{XRD}$ (%) |
|---|---|---|---|---|---|
| A | 5.688 | 5.757 | 8.0 | 8.0 | -0.70 |
| B | 5.712 | 5.765 | 9.6 | 10.3 | -0.52 |
| C | 5.731 | 5.773 | 11.1 | 11.5 | -0.41 |
| D | 5.727 | 5.799 | 12.6 | 13.0 | -0.71 |

**Table 4.1:** Layer properties determined by RBS and XRD.

ers with thicknesses between 200 nm and 300 nm, well above the critical thickness for strain relaxation, have been selected for these investigations. In order to reduce the defect density induced via plastic relaxation, i.e. keep the threading dislocation density below $5 \cdot 10^6\,\mathrm{cm}^{-2}$, within the GeSn layers, Ge-VS have been used (c.f. chapter 2). The Sn concentrations are set between 8 at.% and 13 at.% as determined by RBS. In Fig. 4.5 XRD-RSM around the asymmetric (224) reflection for all four samples are presented. The diagonal lines represent cubic crystal structures, i.e. unstrained lattices. In all samples a residual compressive strain is measured for GeSn epilayers and a slight tensile strain for the Ge-VS. The Sn concentrations determined by XRD support the RBS results within the experimental uncertainties. All values concerning the residual compressive strain and Sn concentrations of samples A to D are listed in table 4.1.

### 4.3.1 Band Structure Calculations

The electronic band structures for all four samples around the Γ-point are calculated using the 8 band k·p method described in [109, 206]. Strain effects are included in order to account for the measured residual compressive strain of the layers, hence conduction band valleys off the Brillouin zone center may split. The employed alloy parameters are calculated using Vegard's type extrapolation for the deformation potentials with bowing correction (quadratic) for the bandgaps and lattice constants from elemental Ge and Sn values. The Luttinger parameters $\gamma$ have been taken from [165]. In Fig. 4.6 band structure schematics for samples A-D are displayed including the calculated energies for the Γ- and L-valleys. Note, the heavy hole valence band is shifted towards higher energies in comparison to the light hole band due to the residual compressive strain. For sample A the energy difference between the Γ- and L-valleys, $\Delta E_{calc.} = E_L - E_\Gamma$, is negative, namely $-50\,\mathrm{meV}$, hence this GeSn layer is supposed to be an indirect bandgap semiconductor. In the case of sample B the offset between the Γ- and L-valleys is reduced to $-8\,\mathrm{meV}$ which can be compensated by the thermal energy at room temperature ($k_B T \approx 26\,\mathrm{meV}$). According to these band structure calculations a fundamental direct bandgap is expected for sample C and D with $\Delta E_{calc.} = 26\,\mathrm{meV}$ and $\Delta E_{calc.} = 28\,\mathrm{meV}$, respectively.

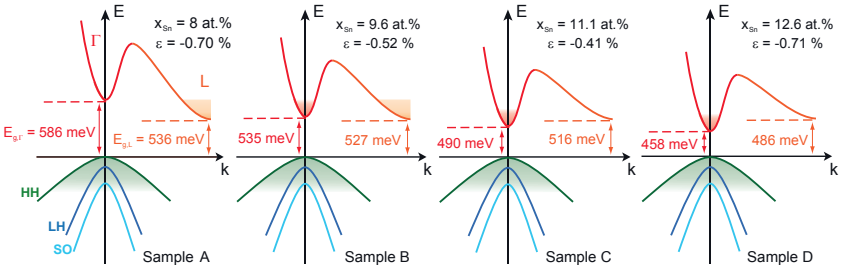


**Figure 4.6:** Scheme of the band structures for samples A to D. The energies at critical points within the Brillouin zone, i.e. the Γ-valley and L-valley are calculated using the 8 band k·p method.

### 4.3.2 Temperature Dependent Photoluminescence of GeSn Alloys

In order to carry out PL measurements from room temperature to 20 K and to demonstrate the indirect to direct bandgap transition in GeSn alloys, the four samples (A, B, C and D) are mounted into a $^4$He-cooled cold finger cryostat. The excitation is provided in the same way as described in chapter 2. Figure 4.7 displays the PL intensity of the direct transition as function of energy within the investigated temperature range for all four samples. Here, the y-scale is kept constant to enable a direct comparison between the samples. The insets present the spectra with a different scale for better readability. The luminescence of sample A declines continuously with decreasing temperature similar to the results in Refs. [85, 86]. Especially the spectrum of sample A exhibits multiple peaks due to Fabry-Perot resonances. By using $\Delta\nu = c/(2d_{Ge-VS}n)$, the resonance distance can be estimated to 50 meV corresponding to the observed peak spacing. Around 0.4 eV an additional weak, broad peak can be seen, which might stem from defects, i.e. from strain relaxation induced misfit dislocations. Well-shaped PL peaks with a strong PL onset are observed for samples B to D at temperatures below 250 K. Moreover, a 350-times higher peak intensity is determined comparing the peaks of sample A at room temperature and of sample D at 20 K. The main observation, however, is the significant peak intensity increase of samples B, C and D with decreasing temperature.
A detailed temperature dependent peak analysis of sample B to D is presented in Fig. 4.8. The normalized PL intensity as function of energy for sample D (c.f. Fig. 4.8 (a)) exhibits a clear blue-shift in energy for decreasing temperature as well as a linewidth narrowing. In the top part of Fig. 4.8 (b) it can be seen that the *full width at half maximum* (FWHM) significantly increases from 30 meV (sample D), 32 meV (sample C) and 38 meV (sample B) to 74 meV (sample D), 64 meV (sample C) and 73 meV (sample B), respectively, for rising temperatures as a consequence of the thermal broadening of the Fermi-Dirac distribution. In the bottom of this figure, the temperature dependence of the PL peak position is depicted, which correlates with the temperature dependent variation of the energy gap. The bandgaps of all three alloys increase with decreasing temperature due to temperature

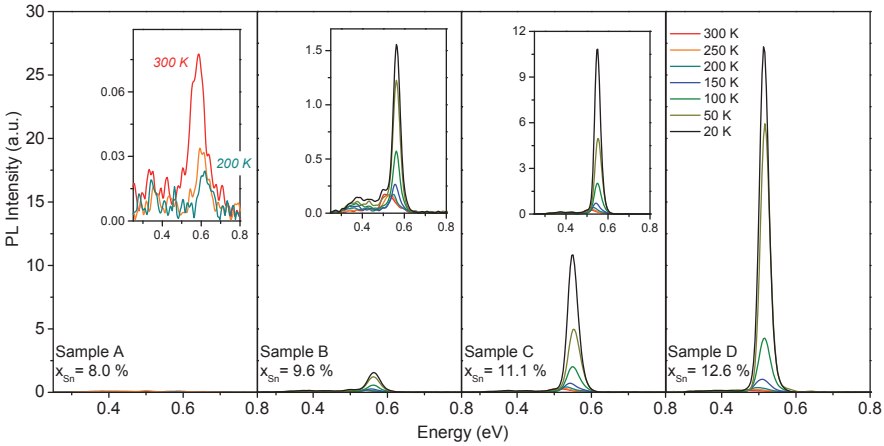


**Figure 4.7:** Photoluminescence spectra as function of temperature (20 K – 300 K) for sample A to D. Only for sample A the PL intensity declines with decreasing temperature.

dependent electron-lattice interaction and the temperature induced dilation of the lattice [207]. This temperature dependence of the bandgap of semiconductors has been found by Varshni and can be expressed by [207]:

$$E_\Gamma(T) \quad = \quad E_\Gamma(0) - \frac{\alpha T^2}{T+\beta}\,. \tag{4.17}$$

Here, $\alpha$ and $\beta$ are material constants and $E_\Gamma(0)$ is the bandgap at 0 K. The data presented in Fig. 4.8 are fit using $\beta = 296\,\mathrm{K}$ [208]. The thus obtained values for $\alpha$ lie between 2.8 eV/K and 3.4 eV/K in good agreement with the results of Ryu *et al.* [86].

### 4.3.3 Modeling of Luminescence Spectra

The quantitative analysis of the temperature dependent PL spectra regarding the Γ- and L-valley crossover is carried out using the integrated PL intensity (Fig. 4.9). The experimental data (symbols in Fig. 4.9 (a)) are normalized to unity at room temperature. For sample A, which is predicted to be an indirect bandgap semiconductor, the integrated intensity strongly decreases with lowering the temperature, whereas a steady increase is observed for the integrated luminescence of sample D. However, the temperature dependence of the integrated PL intensities of samples B and C is more complex. For high temperatures, $\geq 150\,\mathrm{K}$, the intensities remain constant and start to increase for lower temperatures. In order to understand this behavior and relate the temperature dependence to the difference in energy between the Γ- and L-valleys, a *joint density of states* (JDOS) model has been developed at the Paul Scherrer Institut. By means of this model

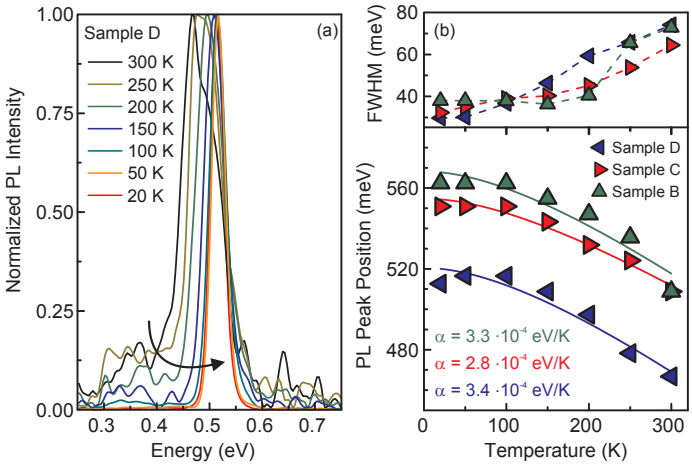


**Figure 4.8:** (a) Normalized PL intensity of sample D as function of energy in the investigated temperature range. (b) Full width at half maximum (FWHM) and PL peak position as function of temperature for samples B, C and D. The latter is fit using $E_\Gamma(T) = E_\Gamma(0) - \alpha T^2/(T+\beta)$ with a fixed $\beta = 296\,\mathrm{K}$[207].

the spontaneous emission rate derived in chapter 4.2 can be calculated:

$$JDOS(\hbar\omega) = C m_{red}^{3/2} E_p \sqrt{\hbar\omega - (E_C - E_V)}\, F_C(E'_C, E_{f,e}, T) F_V(E'_V, E_{f,h}, T), \quad (4.18)$$

$$C = \frac{2e^2 n}{\pi m_e^2 \epsilon_0 h^2 c^3} \left(\frac{2m_{red}}{\hbar^2}\right)^{3/2}. \quad (4.19)$$

Here, $m_{red}$ is the reduced mass weighted by 1/3 of the longitudinal and 2/3 of the transversal mass, $n$ is the refractive index, $E_p$ is the dipole matrix element, $E_C$ as well as $E_V$ are the band edges of conduction and valence bands, respectively, and $E_{f,e/h}$ are the quasi Fermi levels according to:

$$E_{f,e}(n_e) = \frac{\hbar^2}{2m_e}(3\pi^2 n_e)^{2/3}, \quad (4.20)$$

$$E_{f,h}(n_h) = \frac{\hbar^2}{2m_h}(3\pi^2 n_h)^{2/3}, \quad (4.21)$$

which are calculated for a given carrier density at a corresponding temperature. The Fermi-Dirac distributions $F_{C,V}$ for electrons and holes (c.f. equation 4.5) are determined at primed energies:

$$E'_C = E_C + \frac{m_{red}}{m_C}[\hbar\omega - (E_C - E_V)], \quad (4.22)$$

$$E'_V = E_V + \frac{m_{red}}{m_V}[\hbar\omega - (E_C - E_V)]. \quad (4.23)$$

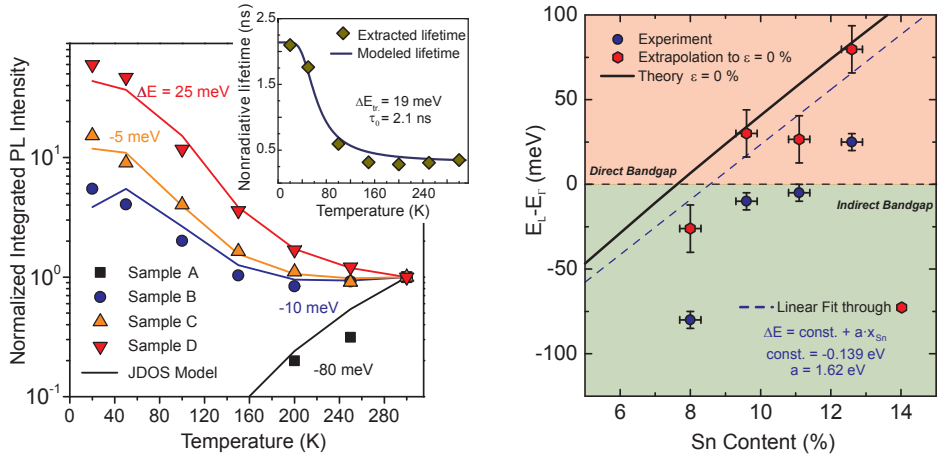


(a) (b)

**Figure 4.9:** (a) Temperature dependent integrated PL intensity normalized to the corresponding intensity at room temperature. In the inset the recombination time as function of the temperature is shown. (b) Difference in energy between L- and Γ-valley, $\Delta E$, as function of the Sn concentration.

In cooperation with the University of Leeds 8 band k·p band structure simulations for the four GeSn samples have been conducted and the resulting effective masses (see table 4.2) are used for the JDOS model. For equation 4.18 heavy hole and light hole valence bands are considered and the integration is carried out over the entire energy spectrum. The values calculated as above are subsequently normalized to unity at 300 K for comparison with the experimental data.
The conduction band offset $\Delta E$ between the Γ- and L-valleys along with the injected carrier concentration $n_c(T)$ are used as fitting parameters in a recursive approach as described in the following. The key parameters within this model are the injected carrier concentrations $n_{e,h}$. Here, $n_e$ strongly depends on the energy difference between the conduction band extrema and can be written as:

$$n_e(T, E_{f,e}) = \int_{min[E_L, E_\Gamma]}^{\infty} e[\rho_{e,L}(E, E_L, m_{C,L}) + \rho_{e,\Gamma}(E, E_\Gamma, m_{C,\Gamma})] F_C(E, T, E_{f,e}) dE. \quad (4.24)$$

Where $\rho_{e,L}$ and $\rho_{e,\Gamma}$ are the densities of states for the as assumed parabolic Γ- and L-valleys. Moreover, nonradiative electron-hole pair recombinations are supposed to play a significant role in the overall recombination rate. So, the first step of the recursive JDOS calculation is to calculate the quasi Fermi levels of electrons and holes for a given band offset and temperature via:

$$n_c(T) = \frac{n_0}{\tau_0} \cdot \tau(T) \; . \quad (4.25)$$

| Sample | $m_{\Gamma,x/y}/m_0$ | $m_{\Gamma,z}/m_0$ | $m_{L,x/y}/m_0$ | $m_{L,z}/m_0$ | $\Delta(E_{HH}\text{-}E_{LH})$ (meV) |
|---|---|---|---|---|---|
| A | 0.029 | 0.034 | 0.080 | 1.563 | 65 |
| B | 0.025 | 0.029 | 0.080 | 1.560 | 50 |
| C | 0.024 | 0.027 | 0.080 | 1.559 | 41 |
| D | 0.021 | 0.028 | 0.080 | 1.558 | 67 |

**Table 4.2:** Effective masses and valence band offsets used in the JDOS model.

The density of carriers and recombination time at room temperature are represented by $n_0$ and $\tau_0 = \tau(300\,\mathrm{K})$, respectively. The temperature dependent recombination time $\tau(T)$ is assumed to be the same for all samples and similar to the temperature dependence of the Shockley-Read-Hall (SRH) recombination process (c.f. chapter 4.2.2). Now, the JDOS (equation 4.19) for a given band offset as well as temperature can be calculated and compared with the experimental results. The best fit is finally obtained by recursively adjusting the quasi Fermi level using $n_c(T)$ and $\Delta E$ and can be seen in Fig. 4.9 (a) (solid lines).
The best fit is obtained at an injected carrier concentration of $n_0 \approx 4 \cdot 10^{17}\,\mathrm{cm}^{-3}$ at room temperature, which goes along with a nonradiative lifetime of 0.35 ns. The thus obtained $\tau_{nr}$ is found to be consistent with surface recombination velocities obtained for Ge on Si [200]. According to the fit, the Γ-valley of sample D is 25 meV below the L-valleys, hence **sample D is a fundamental direct bandgap group IV semiconductor**. This is also in excellent agreement with the theoretical prediction shown in Figure 4.6. Energy differences of $\Delta E = -10\,\mathrm{meV}$ and $\Delta E = -5\,\mathrm{meV}$ for sample B and C are found, respectively. Also, the assumed indirect bandgap of sample A with $\Delta E = -80\,\mathrm{meV}$ is confirmed by the JDOS-model. In the inset of Figure 4.9 (a) the recombination time $\tau(T)$ is shown (symbols) that has been employed to fit the experimental results for all four samples. The extracted values can be fairly described using the SRH model:

$$\tau(T) = \left( \frac{1}{\tau_0} + \frac{A}{\tau_{SRH}(T)} \right)^{-1} . \tag{4.26}$$

At low temperatures the lifetime is determined by $\tau_0$, whereas $\tau_{SRH}(T)$ depicts the decay due to the capture of charge carriers by midgap states:

$$\tau_{SRH}(T) = 1 + \cosh\left( \frac{\Delta E_{tr.}}{k_B T} \right) . \tag{4.27}$$

The difference between the trap level energy and the intrinsic Fermi level is given by $\Delta E_{tr.}$ and $A$ is used to normalize $\tau(300\,\mathrm{K})$ to 350 ps. As can be seen in the inset of Fig. 4.9 (a) $\tau_0 = 2.1\,\mathrm{ns}$ and $\Delta E_{tr.} = 19\,\mathrm{meV}$. However, the weak decline of the lifetime with decreasing temperature for $150\,\mathrm{K} \leq T \leq 300\,\mathrm{K}$ cannot be explained with the employed JDOS model. These results show clearly that the steady increase of the integrated PL intensity for sample D can only be explained by the crossover between the Γ- and L-valleys, so the

transition from an indirect to a fundamental direct semiconductor. At higher temperature, a large fraction of electrons occupies states in the fourfold degenerate L-valleys due to the large density of states even for a direct bandgap semiconductor with $\Delta E = 25\,\text{meV}$ such as sample D [28]. By lowering the temperature, the Fermi tails become smaller, i.e. the Fermi function approaches more and more a step function, and electrons gather at the Γ-point leading to a steady increase of the photoluminescence. The nonradiative lifetime starts increasing for temperatures below 100 K resulting in an additional increase of the integrated PL. This causes the increase of the PL for samples B and C - having bandgaps that are still slightly indirect - in spite of the reduction of the occupation of the states at the Γ conduction band minimum. For sample A the typical temperature dependence of indirect bandgap Ge epilayers is observed, that is, only at elevated temperatures electrons may also populate the Γ-valley and recombine radiatively.
In the following, we extrapolate the experimental offset data to the zero strain case, shown in Fig. 4.9 (b) in order to separate the dependencies on strain from the dependence on Sn concentration. Here, $\Delta E$ as function of the Sn content for various strain values is presented. The energy of the Γ- and L-point in strained semiconductors can be determined via [28]:

$$E^{L,\Gamma} = \frac{1}{3}\Delta_{SO} + E_g^{L,\Gamma} + \Delta E_h^{L,\Gamma} \text{with} \tag{4.28}$$

$$\Delta E_h^{L,\Gamma} = \left(a_c^{L,\Gamma} - a_v\right)\left(2\epsilon_{\parallel} + \epsilon_{\perp}\right) , \tag{4.29}$$

where the indirect and direct bandgaps of bulk Ge are $E_g^L$ and $E_g^\Gamma$, respectively. The deformation potentials for various bands are $a_{c,v}^{L,\Gamma}$ and $\epsilon_{\parallel}$ as well as $\epsilon_{\perp}$ are the in-plane and perpendicular components of the strain tensor. From these equations an energy difference between Γ- and L-valleys of $\Delta E = 77\,\text{meV}$ per unit strain [29] results and can be used to extrapolate the experimental data (red circles) to 0 % strain (blue diamonds). By means of a linear fit of the extrapolated values, the offset in energy between the Γ- and L-valleys can be related to the applied strain and incorporated Sn concentration via:

$$\Delta E(\epsilon, x_{Sn}) = -0.139\,\text{eV} + 7.7\,\text{eV} \cdot \epsilon + 1.62\,\text{eV} \cdot x_{Sn} , \tag{4.30}$$

where $-0.139\,\text{eV}$ is $\Delta E$ for unstrained Ge and 1.62 eV represents the slope of the linear fit (c.f. Fig. 4.9 (b)). According to this equation, the required Sn concentration in order to achieve a fundamental direct bandgap in unstrained GeSn alloys amounts to 8.6 at.%. This finding is in good agreement with the band structure calculations discussed above (c.f. Fig. 4.6) as plotted for comparison (green line).
In literature, the theoretically predicted Sn concentrations required for the indirect to direct bandgap transition in GeSn alloys vary considerably from 6.3 at.% to $> 20$ at.% [163, 107, 17, 165, 167, 26, 209]. One of the main reasons for this discrepancy is the nonlinear Sn composition dependency of the bandgap energies leading to large bowing parameters compared to other group IV alloys like SiGe. The direct bandgap bowing parameter has been determined experimentally to 2.8 eV [48, 210], which is indeed one order

of magnitude larger than for SiGe [17]. Taking this large bowing parameter into consideration the transition has been predicted for a smaller variance in Sn content: $6.3-17$ at.%. Several groups tried to determine the transition experimentally using spectroscopic ellipsometry and photoreflectance measurements [51, 164, 211]. However, these techniques are not as straight forward as the PL determination employed here and, thus, may be considered as being less accurate. After all, for data interpretation the dielectric function of GeSn has to be modeled using a large number of adjustable parameters [164]. Moreover, the aim of those measurements was rather to determine the bowing parameter of the direct transition, which is subsequently used for the extrapolation of the bandgaps. As a consequence, D'Costa *et al.* [164] only provide an upper limit of 11 at.% Sn for the indirect to direct transition.
Furthermore, room temperature PL has been applied. Whereas Mathews *et al.* [212] measured GeSn alloys grown directly on Si(001) only up to 3 at.% Sn, Grzybowski *et al.* [213] also investigated partially relaxed $Ge_{0.92}Sn_{0.08}$ layers, but found no clear indication of a fundamental direct bandgap in their samples. Nearly fully strain-relaxed GeSn layers (300 nm) with $x_{Sn}$ ranging from 0 at.% to 8.6 at.% have been investigated using room temperature PL by Chen *et al.* [169]. They observed a monotonic increase in the PL intensity with increasing Sn concentration resulting in a 30 times higher integrated PL intensity for $Ge_{0.914}Sn_{0.086}$ compared to Ge layers. Again, the extracted bowing parameter has been used to theoretically estimate the indirect to direct bandgap transition. Furthermore, low temperature PL results of pseudomorphic Ge/GeSn heterostructures [166] have provided evidence for the indirect to direct transition at about 17 at.% for fully strained GeSn epilayers. None of these studies have presented an unambiguous experimental proof for a direct bandgap group IV semiconductor. Hence, the here presented temperature dependent steady increase of the integrated PL intensity for sample D is the first proof of a fundamental direct bandgap group IV alloy.

### Power Dependent PL

In Figure 4.10 power dependent PL spectra at low temperature (20 K) are shown for samples B, C and D. As depicted in the inset of Figure 4.10 the integrated PL intensity increases with excitation power. In general the power dependence of the PL can be expressed via $I \propto P^a$, where $P$ is the excitation power and $I$ the PL intensity. The exponents of all three samples have been determined by means of linear fits in the entire pump power window and amount to 0.99 (sample B), 0.96 (sample C) and 0.82 (sample D). Notably, the lowest value is observed for sample D. Former studies ascribe the decline of the power factor to an increasing impact of Auger recombination at higher excitations [214, 215]. Owing to the fact that a significant decrease is only observed for sample D, it is hard to believe, that increasing Auger recombination is the explanation in the present case.

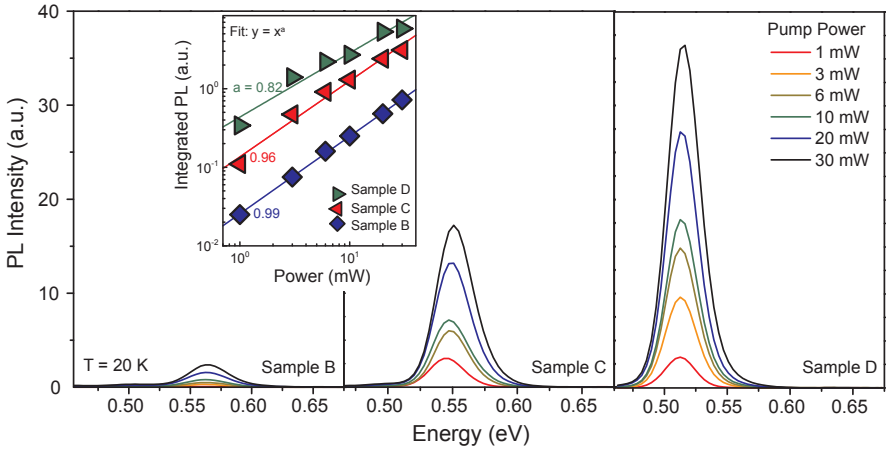


**Figure 4.10:** Power dependent PL spectra of samples B, C and D measured at 20 K. The inset shows the integrated PL intensity vs. excitation power.

### 4.3.4 Direct Bandgap Group IV Ternary Alloys

SiGeSn ternary alloys offer several advantages regarding photonics compared to their GeSn and SiGe binary counterparts. As theoretically shown by Moontragoon *et al.* [24] adding Sn to SiGe, a fundamental direct bandgap can be achieved. Moreover, Gibb's free energy calculations have shown that SiGeSn alloys are thermodynamically more stable than GeSn [75]. An important advantage of these ternary alloys is that band engineering can be decoupled from the lattice constant, i.e. by choosing the appropriate ratio between Si and Sn concentration the Γ-valley can be pulled below the L-valleys along with matching the lattice constant of Ge. In other words, SiGeSn alloys could be grown pseudomorphically on Ge without constraints in terms of layer thickness or defect formation. Hence, nearly defect-free and fundamental direct bandgap group IV epilayers exhibiting almost perfect optical quality could be grown on Ge-buffered Si(001).
As shown in chapter 2, with the growth process developed in this thesis, Sn and Si concentrations up to 13 at.% and 18 at.% are achievable, respectively. For temperature dependent PL measurements a $Si_{0.04}Ge_{0.83}Sn_{0.13}$/Ge-VS heterostructure has been chosen. The ternary alloy is approximately 245 nm thick and RSM measurements indicate an in-plane lattice constant of 5.73 Å. This can be translated into a residual compressive strain of −0.54 % using bowing corrected Vegard's law. Here the bowing parameters $b_{SiGe}$ and $b_{GeSn}$ were taken from [24, 74], whereas $b_{SiSn}$ was set to zero. This layer might be comparable to sample D from chapter 4.2.3 to a certain extent. Due to the incorporated Si the bandgap should be slightly higher and the offset between the Γ- and L-valleys gets smaller compared to sample D.
In Fig. 4.11 (a) the measured PL spectra as function of the temperature are presented.

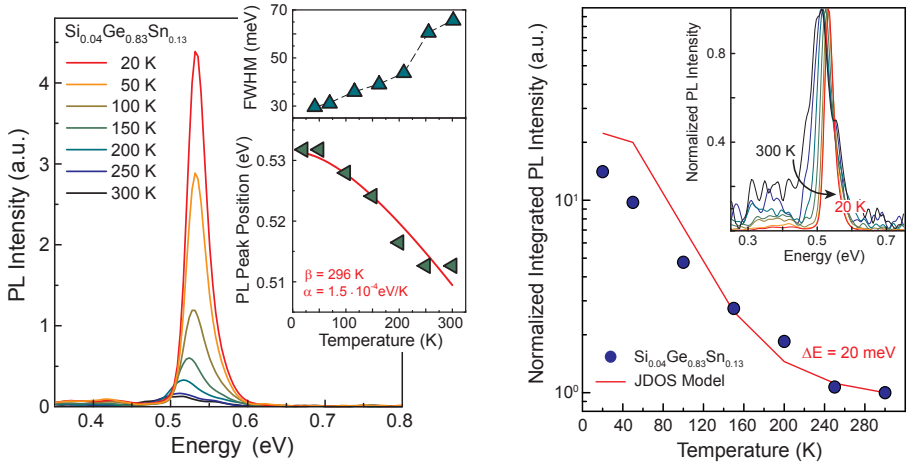


(a) (b)

**Figure 4.11:** (a) Temperature dependent PL spectra of a $Si_{0.04}Ge_{0.83}Sn_{0.13}$/Ge-VS heterostructure. The inset shows the FWHM and the peak position as function of the temperature. (b) Experimental and modeled normalized integrated PL intensity as function of the temperature. In the inset the normalized PL spectra are shown.

Strong PL onsets are observed as well as a PL intensity increase for lower temperature, comparable to the results of sample D. According to the bandgap dependence on the temperature the PL peak is blue-shifted at lower temperatures. By fitting the peak position using Varshni's rule (c.f. equation 4.17) $\alpha$ is determined to $1.5 \cdot 10^{-4}$ eV/K, see inset of Figure 4.11 (a). Compared to the results for GeSn this value is two times smaller, that is, the incorporation of Si reduces the temperature dependence of the bandgap. As expected, the peak energies, hence the bandgap, are slightly larger than for sample D. The linewidth of the strong direct band to band transition peak declines from 66 meV at room temperature to 30 meV at 20 K (upper part of the inset in Figure 4.11 (a)). A second broad peak around 0.4 eV (inset of Figure 4.11 (b)) is attributed to defect levels inside the bandgap as for the case of GeSn.

Figure 4.11 (b) displays the normalized integrated PL intensity indicating a steady increase for decreasing temperature. Applying the JDOS model (chapter 4.3.3) a difference in energy between the Γ- and L-valleys of $\Delta E = 20$ meV is obtained assuming the identical temperature dependent carrier injection density $n_C(T)$ as for the GeSn binary alloys. Hence, this indicates the experimental proof of a fundamental direct bandgap ternary group IV alloy. However, a two times higher carrier injection of $8 \times 10^{17}$ cm$^{-3}$ at room temperature has to be employed for the modeling. In addition, the model overestimates the normalized integrated PL intensity for $T < 150$ K. These findings suggest that the defect density could have been reduced compared to GeSn epilayers. A lower defect den-

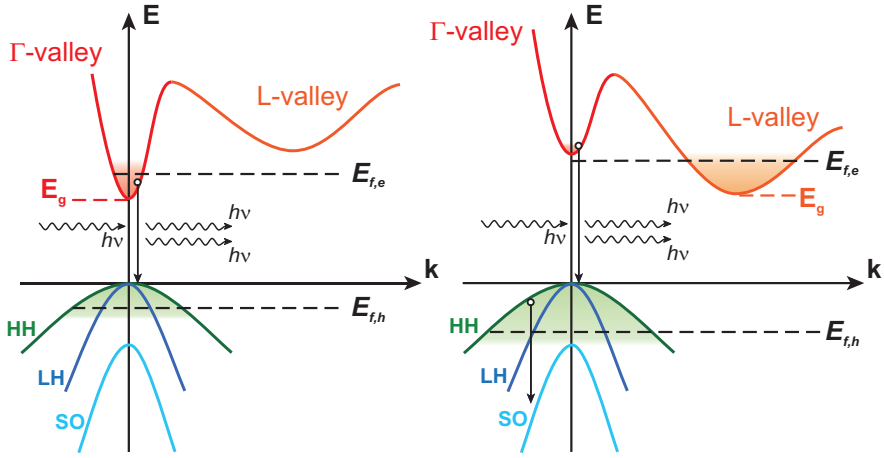


**Figure 4.12:** Sketch of the band structures of direct and indirect semiconductors with non-equilibrium carrier distributions. In the case of indirect semiconductors, much stronger pumping compared to direct semiconductors is required to fill up the Γ-valley, which in turn results in strong intravalence band absorption.

sity results in a longer carrier lifetime and, thus, a higher carrier density.
Prior to this study, merely the group of Kouvetakis at the Arizona State University published room temperature PL studies on this material system grown directly on Si(001) [216] and on Ge-VS [171, 170]. In order to investigate their material with Si and Sn concentrations ranging from $0-7\,\text{at.}\%$ and $0-8.3\,\text{at.}\%$, respectively, using room temperature PL, they have grown at least 500 nm thick layers [170]. By fitting the peaks of the direct and indirect band to band recombination and extrapolation, they predict a transition from an indirect to a fundamental direct semiconductor in nearly unstrained $Si_{0.04}Ge_{0.96-y}Sn_y$ for $y \approx 9\,\text{at.}\%$ in agreement with the experimental proof presented here.

## 4.4 GeSn Alloys as Optical Gain Media

In this section, luminescence of fundamental direct bandgap GeSn under high-level excitation is investigated. If the semiconductor is pumped electrically or optically the excited electrons start to populate the lowest available states in the conduction band and the previously filled (empty) electron (hole) states in the valence band will be depopulated (populated). Hence, similar to the case discussed in chapter 4.2 quasi Fermi levels, $E_{f,e}$ and $E_{f,h}$ (c.f. equation 4.21), have to be introduced for the description. The conduction band is filled with electrons up to $E_{f,e}$ and the valence band is depopulated down to $E_{f,h}$ (see Fig. 4.12). Even though the assumption of a total thermal equilibrium is not valid anymore, the carriers within a given energy band (and probably also over different bands)

remain in thermal equilibrium among themselves just as in the case of low-level excitation (c.f. chapter 4.2), thus, Fermi-Dirac distributions (c.f. equation 4.5) can be used for the occupation probability of a state in the conduction and valence band. For increasing carrier concentration, induced by external pumping, $E_{f,e}$ ($E_{f,h}$) gets closer to the conduction (valence) band edge. If absorption, characterized by the *absorption coefficient* $\alpha(\hbar\omega)$, via electron-hole pairs for $\hbar\omega = E_g$ is no longer possible so-called *transparency* is reached and $\alpha(\hbar\omega)$ equals zero. Now, light with an energy close to the bandgap can only be absorbed via scattering at impurities or heterojunctions known as *internal optic losses* $\alpha_{int}$. If the external excitation is further increased, $\alpha(\hbar\omega)$ becomes negative, that is, *gain* sets in. An incoming photon is now able to stimulate a band to band transition of an excited electron from the conduction band to the valence band, which results in the emission of an additional photon with identical momentum and phase to the initial photon namely *coherent light*. The condition for population inversion can be derived from the rate equations for absorption and stimulated emission in a semiconductor [111]:

$$R_{abs} = B_{12} \int (1 - F_C) F_V \rho_C \rho_V N_\gamma dE, \tag{4.31}$$

$$R_{st} = B_{21} \int F_C (1 - F_V) \rho_C \rho_V N_\gamma dE \; . \tag{4.32}$$

Here, $B_{12}$, $A_{21}$ and $B_{21}$ depict the Einstein coefficients and $\rho_C$ and $\rho_V$ are the density of states for the conduction and valence band, respectively. Obviously, the condition for amplification is fulfilled if $R_{st} > R_{abs}$ which becomes the *Bernard-Duraffourg* (BD) condition [217]:

$$E_g < \hbar\omega < E_{f,e} - E_{f,h} \; . \tag{4.33}$$

From the implied condition $E_{f,e} > E_{f,h}$ one may derive the requirement for population inversion as $n_e n_p > n_i^2$. As long as the BD condition is fulfilled the stimulated emission is a self amplifying process and the electron-hole pair density remains at the threshold level. All excess carriers recombine via stimulated emission, meaning that a further increase of the excitation leads rather to an increased photon density than to a higher carrier pair density.

As can be seen in Fig. 4.12 for direct semiconductors the states in the Γ-valley will be occupied right away, whereas for indirect semiconductors the fourfold degenerate L-valleys with their large density of states have to be filled up first before electrons may occupy the Γ-valley. Hence, much higher pumping is necessary to achieve transparency and finally population inversion in indirect semiconductors. Liu *et al.* [196] suggested, that doping, i.e. n-type doping, in combination with tensile strain in indirect bandgap Ge facilitate a condition to achieve transparency. The substitutional incorporation of Phosphorous (P) atoms, acting as electron donors, helps increasing the quasi Fermi level for electrons towards the Γ-valley, whereas tensile strain decreases the Γ- and L-valley energy as well as the difference in energy between them. Actually, gain values of $50\,\mathrm{cm}^{-1}$ have been claimed [197] using this approach. In contrast, Carroll *et al.* [199] have not been able to confirm

these results. They have measured a significant direct-gap gain of up to $(850 \pm 50)\,\mathrm{cm}^{-1}$, but due to the high optical pumping unipolar transitions between the heavy hole and the split off band occur leading to so-called *pump-induced absorption* (PIA) losses of approximately $7000\,\mathrm{cm}^{-1}$ prohibiting light amplification by stimulated emission in Ge. In this context, the use of direct bandgap GeSn binary alloys as gain media represent a more promising alternative on the road towards an efficient electrically pumped group IV laser diode as will be shown in this section.

### 4.4.1 Gain Calculations

Several theoretical studies investigated the potential of GeSn binary alloys to be employed as optically active gain medium in laser diodes [25, 167, 218, 219]. Dutt *et al.* [167] found that unstrained GeSn layers with a Sn concentration ranging from 0 at.% to 10 at.% show a significantly higher differential gain, $dg/dn_{inj}$, compared to Ge. Moreover, the theoretical optical gain of SiGeSn/GeSn double heterostructure [218] or multi-quantum-wells [25] also indicates possible lasing within strain relaxed or compressively strained GeSn wells containing 6 at.% and 16 at.%, respectively. However, the effect of tensile strain on the optical gain in GeSn has received less attention. During this work, optical gain calculations have been carried out in order to investigate the effect of Sn concentration, n-type doping, applied strain (compressive and tensile) and *intra-valence band* (IVB) transitions in close collaboration with the University of Leeds, where the simulation code has been developed. The total absorption coefficient, hence the optical gain $g$ (for $\alpha < 0$), consists of two main contributions, i.e. the interband transitions $\alpha^{bb}$ and the free carrier IVB transitions $\alpha^{fc}$ [28]:

$$g(\hbar\omega) = -\alpha(\hbar\omega) = \alpha^{bb}(\hbar\omega) + \alpha^{fc}(\hbar\omega)\ . \tag{4.34}$$

In the case of quasi-direct or just direct semiconductors, the consideration of the free carrier absorption is mandatory due to the required higher carrier injection densities as well as n-type doping levels compared to III/V compounds with a large offset in energy between the Γ- and L-valleys in the conduction band. Theoretical [220, 28] and experimental [199] studies have shown that the free carrier absorption is indeed the main obstacle for laser emission in Ge-based devices. The interband transition $\alpha^{bb}$ depends on the direct, $\alpha^{\Gamma_V\Gamma_C}(\hbar\omega)$, and indirect absorption coefficient, $\alpha^{\Gamma_V L_C}(\hbar\omega)$:

$$\alpha^{bb}(\hbar\omega) = \alpha^{\Gamma_V\Gamma_C}(\hbar\omega) + \alpha^{\Gamma_V L_C}(\hbar\omega)\ . \tag{4.35}$$

Whereas for the indirect absorption coefficient, photon absorption and stimulated photon emission contributions have to be taken into account for phonon absorption (abs) and emission (em) [28]:

$$\alpha^{\Gamma_V L_C}(\hbar\omega) = \underbrace{\alpha_{abs}^{\Gamma_V L_C} + \alpha_{em}^{\Gamma_V L_C}}_{\text{Photon Absorption}} - \underbrace{\alpha_{abs}^{L_C\Gamma_V} - \alpha_{em}^{L_C\Gamma_V}}_{\text{Stimulated Emission}}\ , \tag{4.36}$$

to the lowest order the direct absorption coefficient may be written as:

$$\alpha^{\Gamma_V\Gamma_C}(\hbar\omega) = \frac{e^2 E_p m_{red}}{\pi n \epsilon_0 m_0^2 \hbar^2 c\omega} \int_0^{k^{dir}} dk_\perp [F_C(k_\perp, E_C, E_{f,e}, T) - F_V(k_\perp, E_V, E_{f,h}, T)] \; . \quad (4.37)$$

Here $n$ is the refractive index and for $k^{dir}$ is given by:

$$k^{dir} = \sqrt{\frac{2m_{red}}{\hbar^2}[\hbar\omega - (E_C - E_V)]} \; . \quad (4.38)$$

For the required band structure parameters, an 8x8 k·p model, derived by Bahder [109, 206], including strain effects, is employed. Material parameters of GeSn have been taken from [221], besides the Luttinger's parameter, which were taken from [165]. Since transitions between all bands are taken into account within the employed model, the obtained gain values consider interband transitions including valence to conduction band transitions as well as Auger recombination and unipolar IVB transitions like heavy hole to light hole or to split off valence band transitions, respectively. In addition, the code includes FCA, which means free-electron intravalley absorption due to scattering on acoustic and optical phonons as well as impurity scattering. Moreover, FCA from intervalley and alloy disorder scattering is consider just as hole intraband absorption and indirect interband absorption, i.e. from the valence band at the Γ-valley to the conduction band at the L-valley.
Figure 4.13 shows the thus calculated optical gain values as function of the n-type doping and carrier injection density for unstrained and differently tensile strained ($\epsilon = 0.4-1.0\,\%$) $Ge_{0.94}Sn_{0.06}$ layers. The assumed strain levels can be achieved experimentally to some extent via a partially strain relaxed GeSn buffer layer with a higher Sn concentration as presented in chapter 2. In the case of unstrained $Ge_{0.94}Sn_{0.06}$, see Fig. 4.13 (a), gain can only be obtained for a significant n-type doping level above $2 \cdot 10^{19}\,cm^{-3}$ and an injected carrier density above $5 \cdot 10^{18}\,cm^{-3}$ at the same time. Electronic states in the L-valleys still have to be filled up before a population inversion at the center of the Brillouin zone can be built up. For the investigated electronic configuration a maximum gain of about $2500\,cm^{-1}$ is attainable.
According to band structure calculations (c.f. chapter 3) the incorporation of moderate tensile strain, i.e. $0.4\,\%$ is sufficient to achieve a direct bandgap semiconductor in $Ge_{0.94}Sn_{0.06}$. Hence, the states in the conduction band at the Γ-valley can be filled immediately via external pumping which is supposed to soften the requirements for transparency in terms of doping and carrier injection, making the BD relation (equation 4.33) easier to achieve. Indeed, in $0.4\,\%$ tensile strained $Ge_{0.94}Sn_{0.06}$ (c.f. Fig. 4.13 (b)) a significant optical gain above $400\,cm^{-1}$ can be obtained for an n-type doping of $1.4 \cdot 10^{19}\,cm^{-3}$ and a carrier injection of $2 \cdot 10^{19}\,cm^{-3}$. Also the aforementioned maximum gain is exceeded reaching $g > 4000\,cm^{-1}$.
Figures 4.13 (c) and (d) display the effect of $0.8\,\%$ and $1.0\,\%$ tensile strain on the optical gain. The layers have to be heavily doped between $4 \cdot 10^{19}\,cm^{-3}$ and $8 \cdot 10^{19}\,cm^{-3}$, respectively, in order to achieve population inversion.

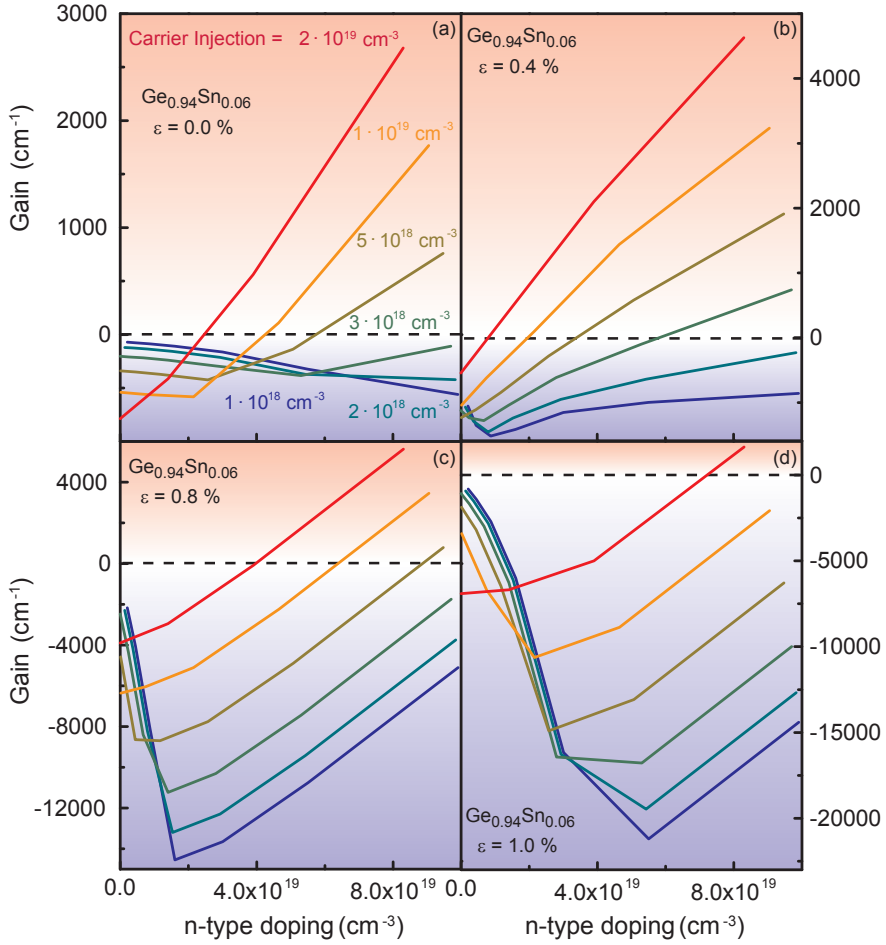


**Figure 4.13:** Optical gain as function of the n-type doping and injected carrier density for (a) unstrained, (b) 0.4 % tensile strained, (c) 0.8 % tensile strained and (d) 1.0 % tensile strained $Ge_{0.94}Sn_{0.06}$. For the investigated carrier injection densities n-type doping is required for all four strain cases. The intra-valence band absorption strongly increases with increasing strain.

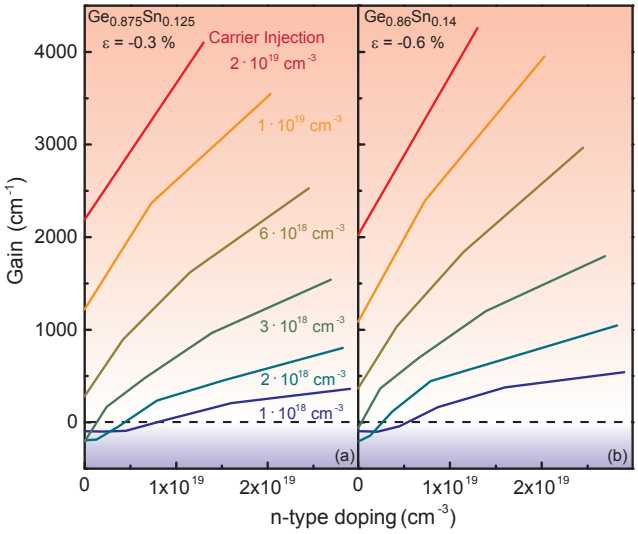


**Figure 4.14:** Optical gain as function of the n-type doping and injected carrier density for (a) $-0.3\,\%$ compressively strained $Ge_{0.875}Sn_{0.125}$ and (b) $-0.6\,\%$ compressively strained $Ge_{0.86}Sn_{0.14}$.

Another possibility to achieve a direct bandgap GeSn alloy and hence to reach transparency without the need of heavy n-type doping is to grow thick, partially strain-relaxed GeSn layers on Ge virtual substrates. Since growing fully relaxed GeSn epilayers is hard to achieve, the layers remain slightly compressively strained. In Fig. 4.14 (a) and (b) the gain simulation results are shown for $Ge_{0.875}Sn_{0.125}$ and $Ge_{0.86}Sn_{0.14}$ with $\epsilon = -0.3\,\%$ and $\epsilon = -0.6\,\%$, respectively. As discussed above higher Sn concentrations compared to the unstrained case are needed in order to achieve a fundamental direct bandgap semiconductor. Apparently, gain can now be achieved in undoped material in contrast to unstrained and tensile strained GeSn with lower Sn concentration. Here, the required injected carrier density amounts to $4 - 5 \cdot 10^{18}\,\mathrm{cm}^{-3}$, nearly one order of magnitude lower than before. Maximum gain values of $> 4000\,\mathrm{cm}^{-1}$ for an injected carrier concentration of $2 \cdot 10^{19}\,\mathrm{cm}^{-3}$ are calculated. Overall, the gain values as a function of the n-type doping and carrier injection of these two differently alloyed layers are nearly identical.

### 4.4.2 Variable Stripe Length (VSL) Method

A common way to experimentally verify whether a material, i.e. a semiconductor, exhibits gain is to fabricate laser structures and analyze the threshold conditions. However, merely gain measurements may deliver information regarding optimizing important mate-

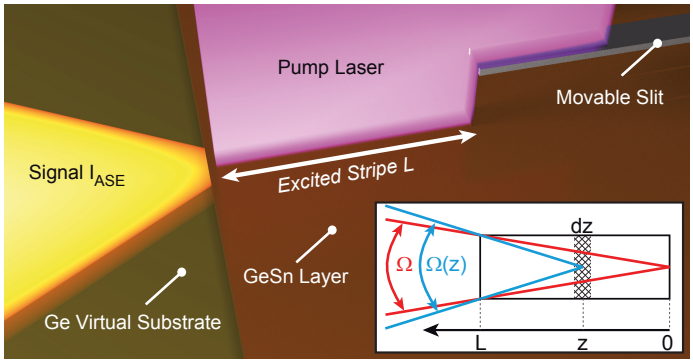


**Figure 4.15:** Sketch of the variable stripe length method. The pump lasing light is focused on the sample by means of a cylindrical lens. The length, $L$, of the resulting excitation stripe is varied via a movable slit. The inset displays an illustration of an 1d-amplifier, which is the underlying model of the variable stripe length method.

rial parameters such as doping, composition or strain. Additionally, those measurements are essential to understand loss and saturation characteristics of the material under investigation.

In this section the *variable stripe length* (VSL) method is used. Here, as shown in Fig. 4.15, the sample is excited by means of a pump laser. Its light is focused by a cylindrical lens in order to excite the carriers in the sample along a stripe. The stripe length in turn can be varied via a movable slit. The resulting *amplified spontaneous emission*, $\mathrm{I}_{ASE}$, is collected from the sample edge. If the material exhibits gain, spontaneously emitted photons from excited electron-hole pairs lead to a light amplification along the stripe due to stimulated emission. This single-pass amplified spontaneous emission (ASE) increases exponentially with increasing stripe length $L$ [222, 223, 224]. Additionally, the ASE spectra are supposed to show a significantly reduced full width at half maximum for longer excitation lengths, due to the coherence of the stimulated emission. If the material is just transparent, modal gain = −modal loss = 0, a linear dependence of the ASE on the excitation length is observed. The VSL method is based on the one dimensional amplifier, sketched in the inset of Figure 4.15 and can be mathematically described using the propagation intensity equation [225]:

$$\frac{dI}{dz} = (\Gamma g_m - \alpha)I + \left(\frac{R_{sp}N^*h\nu\Omega(z)}{4\pi}\right) . \tag{4.39}$$

Here, the first and second summand correspond to the stimulated and spontaneous emission intensity within the solid angle $\Omega(z)$, respectively. The gain of the material is denoted by $\mathrm{g}_m$, $\Gamma$ is the confinement factor, $\alpha$ is the propagation loss coefficient, $\mathrm{R}_{sp}$ is the spontaneous emission rate and $N^*$ the excited state population density. This equation can be

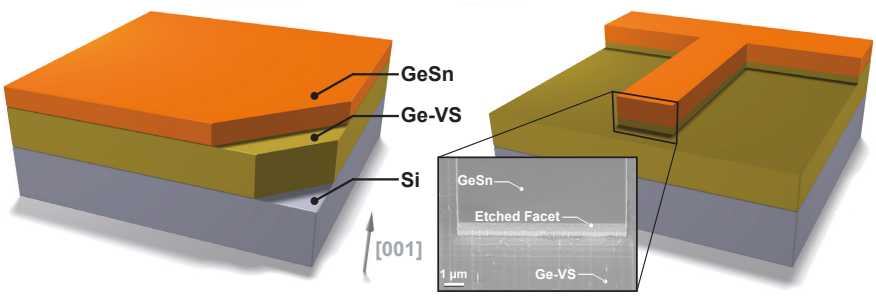


**Figure 4.16:** (left) Sketch of the GeSn-based heterostructure used for the VSL measurements. A 560 nm $Ge_{0.874}Sn_{0.126}$ epilayer has been grown on a Ge-VS. (right) Sketch and scanning electron micrograph taken at PSI of a dry-etched waveguide structure.

analytically integrated under two assumptions. At first:

$$\Omega(z) \cong \Omega = \frac{S}{L^2} \,, \tag{4.40}$$

which means that the collection efficiency of $I_{ASE}$ has to be constant over the pumping length $z$, where $S$ is the cross sectional area of the one dimensional amplifier. This is certainly true for optical fibers or 2d waveguides but not necessarily for planar waveguides [225]. For the investigated structures in this thesis, this assumption is assured, since the predominant portion of the collected light originates at $\Omega(0)$ (see inset of Figure 4.15). On the other hand, the gain coefficient as well as the pump intensity have to be constant over the pumping length $z$. The analytical integration of equation 4.39 finally reads:

$$I_{ASE}(z) = \frac{I_{sp}(\Omega)}{g}[\exp(g \cdot z) - 1] \,, \tag{4.41}$$

where g is called *modal gain* and equals $(\Gamma g_m - \alpha)$ and $I_{sp}$ is the spontaneous emission intensity. Hence, fitting the ASE as function of the excitation length provides the modal gain of the material. In the following the results of VSL measurements on direct bandgap GeSn waveguide structures will be presented and discussed.

### 4.4.3 High Modal Gain in Direct Bandgap GeSn

For the VSL measurements a $Ge_{0.874}Sn_{0.126}$/Ge/Si(001) heterostructure is used (Fig. 4.16). The thickness of the GeSn epilayer is measured by RBS and amounts to 560 nm. The obtained minimum yield of $5 - 6\,\%$ indicate nearly perfect crystalline quality and Sn substitutionality. The XRD-RSM measurements show a residual compressive strain of

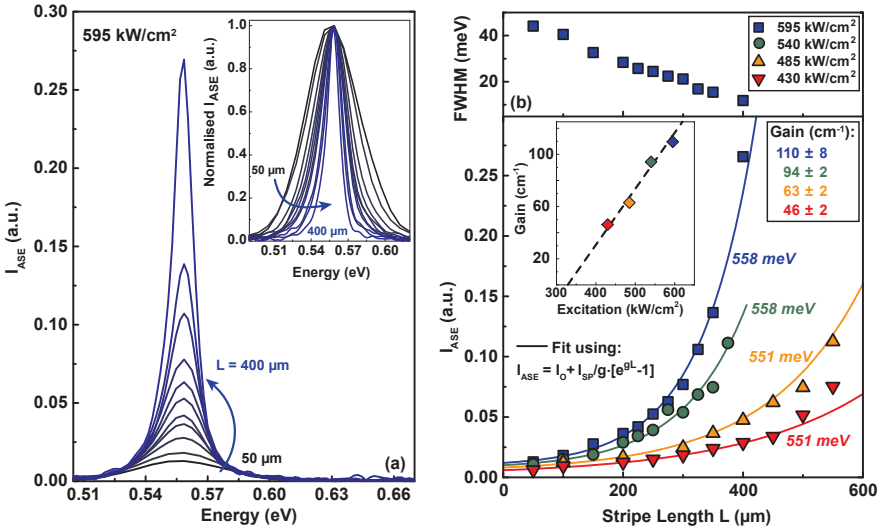


**Figure 4.17:** (a) Amplified spontaneous emission (ASE) spectra measured at 20 K. (b) Top: decreasing FWHM of the spectra presented in (a). Bottom: ASE intensities at peak energies (551 meV and 558 meV) as function of the stripe length.

$\epsilon = -0.57\,\%$. Since this layer exhibits a higher degree of relaxation compared to sample D from chapter 4.2.3 the offset between the Γ- and L-valleys is also supposed to be larger. According to the band structure calculations an offset of 39 meV is supposed. The heterostructure is patterned into several mm long and 5 $\mu$m wide stripe structures (c.f. Fig. 4.16) using a Cr hardmask and e-beam lithography at the Paul Scherrer Institut. The steep sidewalls and facets of the 900 nm deep waveguides (c.f. SEM image in Fig. 4.16) are dry-etched by reactive ion etching (RIE) using a gas mixture of $SF_6$ and $C_4F_8$. For the optical excitation a pulsed Nd:YAG laser (5 ns) with a wavelength of 1064 nm is focused by means of a cylindrical lens on a variable slit. This slit is subsequently imaged 1:1 onto the waveguide by a biconvex lens. The measurements are performed at 20 K, thus, as for the low temperature PL measurements, the sample is mounted in a helium cold-finger cryostat.

It turned out that too high excitation power densities and too long excitation length lead to stimulated feedback by backscattered light from the waveguide sidewalls. Moreover, if the excited stripe is too long, gain saturation sets in, thus, the gain coefficient depends on the excitation length and the analytical integration (equation 4.41) is not valid anymore. Therefore the excitation power density as well as the excitation length are limited to 600 kW/cm$^2$ and 550 $\mu$m, respectively. In Figure 4.17 (a) the amplified spontaneous emission spectra (ASE) for excitation length between 50 $\mu$m and 400 $\mu$m at an excitation power density of 595 kW/cm$^2$ are shown. A superlinear increase of the ASE is observed. The inset of Figure 4.17 (a) displays the normalized spectral ASE. With increasing pump-

ing length the linewidth becomes narrower. As shown in the top of Figure 4.17 (b) the FWHM decreases as function of stripe length from 44 meV at 50 $\mu$m to 12 meV at 400 $\mu$m. These two findings are a clear indication of gain in the material. The difference in energy between the Γ- and L-valleys in this direct bandgap semiconductor is high enough in order to achieve population inversion at the Γ-point by the employed excited power density. This enables the stimulated emission of photons along the stripe induced by spontaneously emitted photons at the end of the stripe ($z = 0$).
For a quantitative analysis of the material's modal gain, ASE intensities at 551 meV and 558 meV and power densities between 430 kW/cm$^2$ and 595 kW/cm$^2$ are fitted, c.f. bottom of Fig. 4.17 (b), using:

$$I_{ASE}(L) = I_O + \frac{I_{sp}}{g}[\exp(g \cdot L) - 1] \, . \tag{4.42}$$

This equation differs slightly from equation 4.41 due to contributions of higher order modes and of collected light from the sidewalls of the waveguides. These contributions are taken into account by inserting $I_O$. A peak gain value of $(110 \pm 8)\,\mathrm{cm}^{-1}$ is found for 558 meV at an excitation of 595 kW/cm$^2$. For an approx. 30 % lower excitation value of 430 kW/cm$^2$ the measured gain decreases by more than a factor of two and shifts towards 551 meV. The inset of Fig. 4.17 (b) shows the modal gain as function of the excitation. By means of a linear fit a differential gain of $(0.40 \pm 0.04)$ cm/kW is obtained as well as a gain onset of about 325 kW/cm$^2$. At this threshold excitation density (325 kW/cm$^2$) the difference between the quasi Fermi-levels of electrons and holes is about to overcome the bandgap energy (BD condition, see equation 4.33), thus, transparency is achieved. Further excitation increase leads to population inversion.
The main obstacle to achieve gain in group IV semiconductors is their indirect bandgap nature. In order to meet the condition for population inversion in the center of the Brillouin zone ($E_{C,\Gamma} > E_{f,e} - E_{f,h}$) high excitation is needed. Whereas in direct semiconductors rather low carrier injection densities of $< 10^{19}\,\mathrm{cm}^{-3}$ are required, in indirect semiconductors this value is close to $1 \times 10^{20}\,\mathrm{cm}^{-3}$ [199] inducing severe losses due to FCA and Auger recombination. However, Cloutier *et al.* [226] have observed optical gain and stimulated emission in nanopatterned SOI samples. By means of VSL they have been able to measure modal gain values between 88 cm$^{-1}$ and 260 cm$^{-1}$ at cryogenic temperatures ranging from 80 K to 10 K. Although a complete understanding of the origin of the gain has not been provided, the enhanced radiative transitions have been ascribed to radiative recombination due to defect states located 0.17 eV below the conduction band. Furthermore, electrical carrier injection of these structures remained an unsolved problem, yet.
More recently, the group of Michel *et al.* has reported on the first observation of gain from the Γ-valley in Ge epilayers grown directly on Si by combining mild tensile strain (0.23 %) and heavy n-type doping ($1 \times 10^{19}\,\mathrm{cm}^{-3}$) [227]. Room temperature pump-probe transmission measurements have indicated optical gain values of $(56 \pm 25)\,\mathrm{cm}^{-1}$ at a pump power density of approx. 7.0 kW/cm$^2$ and a wavelength of 1605 nm. These results on indirect semiconductors with high n-type doping, however, have not been reproduced so far [199, 200, 201].

The key to avoid severe losses due to excessive excitation is to reduce the offset between the Γ- and L-valleys in order to increase the occupation ratio between Γ-and L-valleys either by applying tensile strain [190] or/and Sn-alloying, since in unstrained, undoped bulk Ge only approx. 0.01% of electrons populate the Γ-valley at room temperature [220]. Using $Si_3N_4$ as stressor layer de Kersauson *et al.* [228] have obtained a modal gain of $(80 \pm 20)\,cm^{-1}$ in tensile strained Ge wires grown on GaAs substrates with an n-type doping level of $3 \times 10^{19}\,cm^{-3}$. Theoretically it has been shown that 2 % biaxial tensile strain increases the occupation of the Γ-valley by three orders of magnitude [28]. For a strain level of 1.4 % and a doping level of $1 \times 10^{20}\,cm^{-3}$ an optical gain of $2000\,cm^{-1}$ is achievable. If the tensile strain in Ge is further increased to 3 % no doping and merely moderate carrier injection densities of about $10^{18}\,cm^{-3}$ are predicted to attain $g > 3000\,cm^{-1}$ [29], because the transition from an indirect to a fundamental direct bandgap semiconductor has been passed by far. A combination of $1 \times 10^{19}\,cm^{-3}$ n-type doping and $1 \times 10^{19}\,cm^{-3}$ carrier injection might lead to $g = 460\,cm^{-1}$ in 3.1 % uniaxially tensile strain Ge microbridges [190].
As presented above, for $Ge_{0.94}Sn_{0.06}$ alloys much lower tensile strain levels (0.4 %) are required in order to obtain significantly high gain values of about $1000\,cm^{-1}$ at a carrier injection and n-type doping level of $2 \times 10^{19}\,cm^{-3}$. In fact, it is observed that applying too high tensile strain the gain declines. This is due to several reasons. Applying more tensile strain reduces the offset in energy between the Γ- and L-valleys, but at the same time the bandgap shrinks. This in turn leads to a reduced effective mass of electrons and holes and, more importantly, to a smaller density of states. The latter implies that the possibility of electron-hole recombination at a certain wavelength is decreased. Furthermore the FCA becomes stronger for smaller bandgaps and the IVB absorption may increase. In the case of unstrained GeSn alloys, Dutt *et al.* [167] found that the ratio of electrons populating the Γ- and L-valleys is increased by three orders of magnitude by increasing the Sn-content from 0 at.% to 10 at.%, which is comparable to the effect of 2 % tensile strain in Ge. Additionally, the optimum n-type doping level decreases by two orders of magnitude. As presented in chapter 2, unstrained GeSn layers containing 8 at.% can be grown on partially relaxed GeSn layers even though limited in thickness by the critical thickness for strain relaxation, which makes mode confinement rather challenging. The most promising materials in terms of gain as function of doping level and carrier injection density as well as experimental feasibility are partially relaxed GeSn layers with Sn concentrations above 12 at.%. Due to the direct bandgap nature, as shown in the previous section, no n-type doping is required to achieve transparency. Indeed, modal gain values between $46\,cm^{-1}$ and $110\,cm^{-1}$ are measured at 20 K in $Ge_{0.874}Sn_{0.126}$ waveguide structures. Thus, these layers are used in the following section, in order to proof lasing in GeSn alloys.

## 4.5 Lasing in GeSn

In general, a laser (*light amplification by stimulated emission*) device consists of a gain medium and a resonator. In a semiconductor gain medium, electron-hole pairs are generated by means of electrical or optical excitation, as described before. The light emitted by electron-hole recombination is guided through the gain medium back and forth by a resonator. In this connection, the simplest design of a resonator consisting of two mirrors is called *Fabry-Pérot* (FP) *resonator* or *cavity*. At low excitation, no light amplification occurs and spontaneous emission is dominant. Once population inversion is achieved - at high excitation - light can be amplified by stimulated emission in the gain medium and the resonator provides feedback of the light. As soon as the amplification overcomes the losses of the resonator the device starts to lase. Photons generated by stimulated emission may have identical phase, direction, wavelength and polarization and are, thus, spatially and temporally coherent. The emitted light of a laser device shows the following distinctive characteristics [229] in contrast to light of i.e. LEDs or incandescent lamps based on spontaneous emission:

- narrow linewidth,
- the output consists of a beam,
- clear threshold in output power and linewidth,
- the light emission is characteristic of and influenced by the gain medium and resonator.

Therefore, the required experiments to recognize lasing action include emission spectra as well as the output power as function of the pump power and the measurement of the divergence of the laser beam. Lasing action is not to be confused with ASE, described in chapter 4.4.3, which is also based on stimulated emission and shows similar characteristics as lasing, i.e. linewidth narrowing and directionality. For the single-pass ASE measurements, however, no resonator have been used, hence lasing cannot be attained.

### 4.5.1 Optically Pumped GeSn Laser

The same $Ge_{0.874}Sn_{0.126}$(560 nm)/Ge heterostructures as for the VSL measurements are used for the fabrication of GeSn cavities by means of a Cr hard mask, e-beam lithography and RIE dry-etching (gas mixture: $SF_6/C_4F_8$), as sketched in Fig. 4.18 (a). The processing was done at the Paul Scherrer Institut. The etched GeSn stripes act as FP resonators and the induced roughness of the 900 nm deep structures is sufficiently low to achieve mirror-like facets at the ends of the cavities. The lengths, $L_C$, of the 5 $\mu$m wide ($W_C$) cavities vary between 250 $\mu$m and 1 mm. A waveguide mode solver based on a 2D

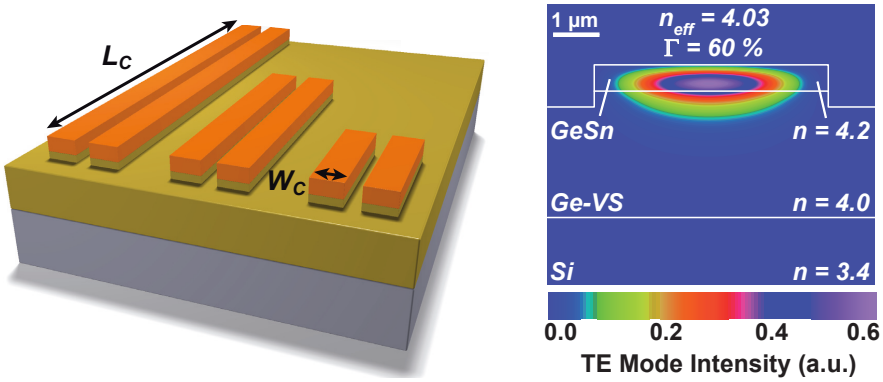


(a) (b)

**Figure 4.18:** (a) Sketch of dry-etched $Ge_{0.874}Sn_{0.126}$(560 nm)/Ge/Si(001) waveguide structures. The widths of the waveguides, $W_C$, is 5 $\mu$m and the lengths, $L_C$, vary between 250 $\mu$m and 1 mm. (b) Calculated intensity of the fundamental TE mode within a 5 $\mu$m wide and 900 nm deep waveguide.

plane-wave expansion method [230, 231] is used to calculate the mode overlap. Figure 4.18 (b) presents the calculated intensity of the fundamental TE mode in the GeSn cavities using a refractive index of 4.2 for GeSn (obtained from ellipsometry measurements), 4.0 for Ge and 3.4 for Si. A mode overlap of $\Gamma = 60\,\%$ within the GeSn layer and an effective refractive index of 4.03 are obtained. The mode confinement at the surface is good, due to the large difference between the refractive indices of air ($\sim$1) and the GeSn cavity ($\sim$4.2). Additional mirror losses of the cavity can be calculated via:

$$\alpha_C = \frac{1}{L_C} \cdot ln\left(\frac{1}{R}\right) \ , \tag{4.43}$$

where $R$ is the reflectivity at an ideal facet and can be estimated to be 37 % considering the index contrast between Ge and air [197]. Under these assumptions, the cavity losses are 40 cm$^{-1}$, 20 cm$^{-1}$ and 10 cm$^{-1}$ for cavity lengths of 250 $\mu$m, 500 $\mu$m and 1 mm, respectively. The mirror losses are thus much lower than the measured modal gain of $(110 \pm 8)$ cm$^{-1}$ (c.f. chapter 4.4.3). For the optical excitation the same setup is used as for the gain measurements. The GeSn waveguides are entirely illuminated and the emitted light is detected at one facet of the waveguides as illustrated in Fig. 4.19 (a). In Fig. 4.19 (b) PL spectra - measured at 20 K - as function of the optical excitation for a 1 mm long cavity are shown. Here, spectra below 310 kW/cm$^2$ are multiplied by a factor of 200 for better readability. For low excitations a rather broad emission peak is observed. Population inversion is not achieved, yet; the emission is governed by spontaneous emission. At 308 kW/cm$^2$ (dark cyan line) several peaks above the broadband PL appear with a mode spacing of about 3 meV. If the optical excitation is further increased, above 320 kW/cm$^2$,

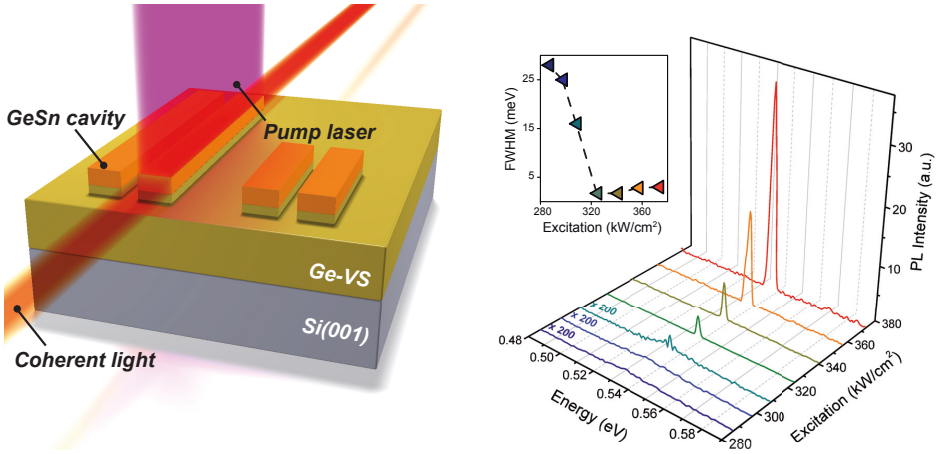


(a) (b)

**Figure 4.19:** (a) Sketch of the optically excited GeSn (12.6 at.%) cavities. (b) PL spectra of a homogeneously excited 1 mm long cavity as a function of the excitation power density at 20 K. The inset displays the FWHM drop as function of the excitation.

a dramatic increase of one of these peaks indicates lasing threshold behavior. Notably, the PL peak intensity increases by a factor of 8000 if the excitation is raised by 30 %, i.e. from 286 kW/cm$^2$ to 373 kW/cm$^2$. The corresponding integrated PL intensity is 1500 times higher. Additionally, a threshold behavior in linewidth is found, see inset of Fig. 4.19 (b). Close to the lasing threshold, the FWHM drops by a factor of 16 to 1.7 meV. The FWHM decrease of the ASE measured by the VSL method results in a minimum FWHM of 12 meV still much larger than for the lasing action described here. The peak positions of the spectra are between 535 meV and 537 meV, thus, significantly blue-shifted (20 meV) compared to the PL peak of sample D (c.f. Fig. 4.7) at low excitation. The integrated PL intensity as function of the excitation, also known as *light-light* or *L-L curve*, for three different cavity lengths (250 $\mu$m, 500 $\mu$m and 1 mm) is shown in Fig. 4.20. On the linear scale (Fig. 4.20 (a)) a clear knee-behavior is observed for all three cavities indicating lasing threshold. The kinks occur at excitation values between 300 kW/cm$^2$ and 325 kW/cm$^2$ depending on the cavity length. Whereas below the threshold light is emitted by spontaneous emission, the light wave passes the complete cavity and lasing sets in as soon as the gain equals the internal losses of the cavity. For higher excitations the integrated PL intensity increases linearly (lasing regime) up to approx. 600 kW/cm$^2$ until gain saturation leads to a second kink in the L-L curve. Most likely, heating of the sample leads to this saturation at those high excitation levels. In Fig. 4.20 (b) the L-L curves are shown on a double logarithmic scale. As long as spontaneous emission is predominant the integrated PL intensity increases linearly with optical excitation, but when the lasing threshold is passed a strong increase of more than three orders of magnitude is observed.

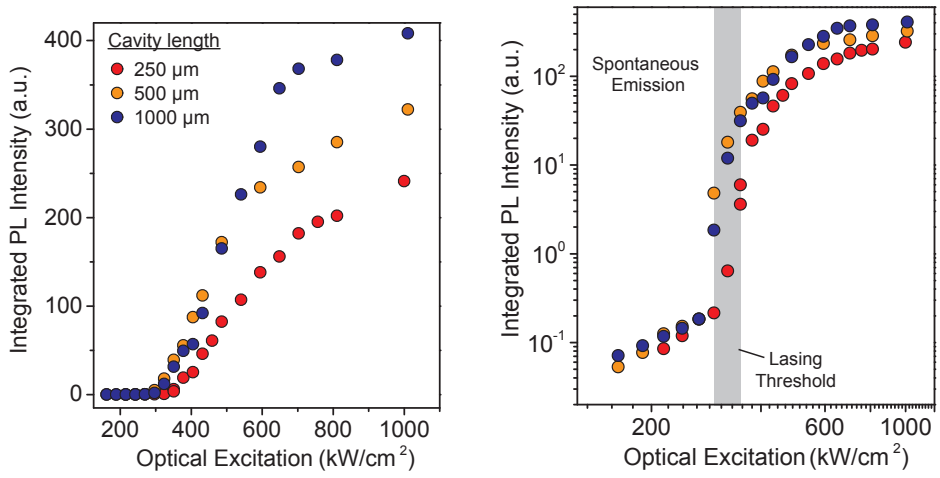


(a) (b)

**Figure 4.20:** Integrated PL intensity as function of optical excitation displayed on a (a) linear and (b) logarithmic scale for three different cavity lengths ranging between 250 $\mu$m and 1000 $\mu$m.

From these measurements the lasing threshold values are estimated to 345 kW/cm$^2$ ($L_C$ = 250 $\mu$m), 312 kW/cm$^2$ (500 $\mu$m) and 338 kW/cm$^2$ (1 mm). The slight disagreement with respect to the VSL results are most probably owed to shot-to-shot variations of the pump laser observed during the measurements. Whereas this instability is averaged out during VSL measurements, it leads to a "smearing" of the threshold values for the waveguide measurements. The final evidence for lasing is displayed in Fig. 4.21 (a). Here, two high resolution (1 cm$^{-1}$ and 0.5 cm$^{-1}$) spectra of excited (500 kW/cm$^2$) 5 $\mu$m wide cavities with lengths of 250 $\mu$m and 500 $\mu$m are plotted. A large number of FP modes are observed over 7 meV indicating a broad gain spectrum of the GeSn. Especially for the shorter waveguide the peaks are nicely separated with a FWHM of approx. 0.2 meV. The peak distances, obtained by means of linear fits (c.f. inset of Fig. 4.21 (a)), exhibit that the spacing is nearly doubled for the 250 $\mu$m compared to the 500 $\mu$m long cavity. This verifies that the emission is characteristic of the resonator modes [229]. Moreover, a group mode refractive index of 4.5 is determined via $\Delta\nu = c/(2Ln)$. Temperature dependent PL spectra for a 1 mm long cavity measured at 1000 kW/cm$^2$ between 20 K and 100 K are presented in Fig. 4.21 (b). Whereas narrow linewidth spectra are obtained for temperatures $\leq$ 90 K, the FWHM rises abruptly by a factor of 13 from 2.7 meV to 36 meV at 100 K and the PL intensity drops. The peak intensity at 20 K is about 10000 times higher than at 100 K. These two findings suggest a temperature dependent lasing threshold for an excitation of 1000 kW/cm$^2$ between 90 K and 100 K. As presented in chapter 4.2.3 the activation temperature for SRH recombination also amounts to approximately 100 K. The, thus,

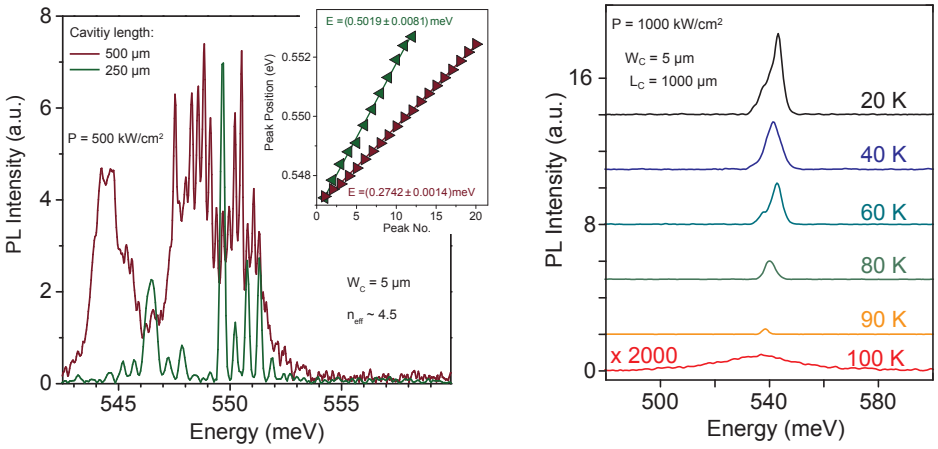


**Figure 4.21:** (a) High resolution spectra measured at 20 K and 500 kW/cm$^2$ for cavity lengths of 250 $\mu$m and 500 $\mu$m. (b) Temperature dependent PL spectra at an excitation density of 1000 kW/cm$^2$.

reduced carrier lifetime might be an explanation for the quenching of the lasing.
An emitted peak power of 12 mW at an excitation of 1000 kW/cm$^2$ for these GeSn lasers is measured using a 1 mm$^2$ detector in a distance of 60 mm from the facet. This is converted to an external quantum efficiency of approx. 1.5 %.

### Discussion

All required attributes for lasing in direct bandgap $Ge_{0.874}Sn_{0.126}$ cavities have been presented in the previous section including a narrow linewidth as well as threshold behavior in output power and linewidth. In addition, it has been demonstrated that the light emission is a characteristic of the resonator and the gain medium. In this regard, the emission peaks with the highest intensity at an excitation of 500 kW/cm$^2$ shown in Fig. 4.21 (a) obtained around 550 meV are in very good agreement with the emission energy of 551 meV for the highest gain values measured at 485 kW/cm$^2$ (c.f. Fig. 4.17). Furthermore, a blueshift of about 10 meV is observed going from threshold (c.f. Fig. 4.19) to 500 kW/cm$^2$ in Fig. 4.21 owed to increased gain at higher energies for elevated excitation, that is, higher carrier densities [197, 196]. It is not possible to measure the polarization of the laser light with the employed setup, however, most likely *transverse-electric* (TE) modes are most efficient, since the HH is the predominant band for hole population, which favors TE gain [108, 232].

The observation of an optically excited lasing threshold has been claimed in 2010 for the first time from the Γ-valley in indirect Ge [197] by using high n-type doping levels ($1 \times 10^{19}\,\mathrm{cm}^{-3}$) and slight tensile strain (0.24 %). In 1.6 $\mu$m wide and 4.8 mm long selectively grown Ge waveguides with *chemical-mechanical polished* (CMP) facets a lasing threshold has been reported. Owing to the direct growth on Si the optical confinement amounts to 90 %, that is about 50 % higher than for the $Ge_{0.874}Sn_{0.126}$ cavities. However, no unambiguous FP mode pattern has been presented. Further on, the peak intensity rises by a factor of approx. 20 from spontaneous emission to lasing action. For the here presented GeSn cavities, this raise extends over more than three orders of magnitude even for the integrated luminescence.
Very recently, studies using GeSn as gain medium are based on microdisk structures [233, 108]. Chen *et al.* [108] have employed $Ge/Ge_{0.92}Sn_{0.08}/Ge$ quantum wells pseudomorphically grown on Ge-VS and have observed *whispering-gallery-mode* (WGM) resonances without indication of lasing. Although they have been able to reduce the energy difference between the Γ- and L-valleys by introducing 8 at.% Sn and hence increasing the quantum efficiency, a fundamental direct bandgap has not been achieved due to the large compressive strain. In addition, since these layers are coherently grown on Ge the thickness of the GeSn layer amounts solely 20 nm enabling high crystalline quality but at the same time a low mode overlap with the GeSn active region. Hence, the FCA in the Ge cladding layers dominates the possible gain in the GeSn.
To conclude, the here presented optically pumped $Ge_{0.874}Sn_{0.126}$ cavities are, thus, the **first direct bandgap group IV laser devices**.
Although lasing is demonstrated here at cryogenic temperatures, there are several ways to optimize these simple FP resonators towards technologically relevant room temperature lasing action. First of all, the GeSn waveguides do not provide any capping that would allow carrier lifetime enhancement by preventing severe surface recombination. Moreover, the simulated mode confinement of 60 % can be significantly improved using thicker GeSn active layers or suitable cladding layers, which act as a heterostructure and, thus, provide not only a mode but also carrier confinement. The lasing quenching around 90 K strikingly correlates with the activation of SRH recombination deduced from the temperature dependent PL measurements. Thus, further improvements regarding the crystalline quality of (Si)GeSn epilayers may increase the carrier lifetime at elevated temperatures and consequently shift the lasing quenching towards higher temperatures.

## 4.6 Summary

- **Direct bandgap group IV semiconductors**
  Via temperature dependent PL measurements, a fundamental direct bandgap has been proven in $Ge_{0.874}Sn_{0.126}$ and $Si_{0.04}Ge_{0.83}Sn_{0.13}$ epilayers grown on Si(001). By means of a joint density of states model differences in energy between the L- and Γ-valley of 25 meV and 20 meV are observed for GeSn and SiGeSn, respectively. The transition from an indirect to direct bandgap semiconductor in cubic GeSn alloys have been determined to occur at 8.6 at.%.

- **Gain in direct bandgap group IV semiconductors**
  Band structure calculations have indicated that significant gain values are achievable in partially relaxed GeSn layers with $x_{Sn} \geq 12.5$ at.% without the requirement of n-type doping. Gain measurements using the variable stripe length method indicates modal gain values between 46 $cm^{-1}$ and 110 $cm^{-1}$ in $Ge_{0.874}Sn_{0.126}$ at an emission energy of 558 meV and 551 meV, respectively.

- **Lasing in direct bandgap group IV semiconductors**
  Unambiguous lasing action in optically pumped $Ge_{0.874}Sn_{0.126}$ cavities have been demonstrated at 20 K. Threshold behavior in emitted intensity along with a strong linewidth narrowing and a consistent cavity mode pattern have been measured. An increase of PL intensity by a factor of 8000 is observed if the lasing threshold is passed. Lasing action is obtained for temperatures $\leq$ 90 K around 550 meV. Here, the peak intensity is increased by a factor of 10000 going from 100 K to 20 K. An external quantum efficiency of the optically pumped laser of approx. 1.5 % is estimated.

# Chapter 5

## Conclusion And Outlook

Within the framework of this thesis the applicability of epitaxial GeSn and SiGeSn layers for nano- and optoelectronic devices has been investigated. The main focus has been placed on the development and study of epitaxial growth processes for the fabrication of high Sn-content layers with the ultimate goal to achieve a fundamental direct bandgap group IV semiconductor. In addition, through layer characterization exhaustive analysis has provided deep insight into key material properties such as Sn incorporation into Ge- and SiGe host lattices, crystalline quality, lattice constants, strain relaxation, optical quality, doping or thermal stability. Moreover, regarding the integration of (Si)GeSn alloys as novel high mobility channel materials in MOSFETs/TFETs or as source/drain stressors the electrical and structural quality of strained Ge- and strained GeSn-high-k interfaces as well as the metallization of high Sn content epilayers are investigated. Temperature dependent photoluminescence measurements reveal the fundamental direct bandgap nature of the grown layers and optically excited GeSn cavities exhibit lasing action.

Due to the low solid solubility of diamond lattice $\alpha$-Sn in Ge ($< 1\,\%$) as well as in Si ($< 0.1\,\%$) the synthesis of GeSn binary and SiGeSn ternary alloys is challenging. The large lattice mismatch far above $15\,\%$ hampers additionally the epitaxial growth of monocrystalline Sn-based group IV layers. In this thesis it has been shown that reduced pressure chemical vapor deposition using a precursor combination of $Ge_2H_6$, $Si_2H_6$ and $SnCl_4$ along with a vertical reactor design enables epitaxial growth of single crystalline GeSn and SiGeSn on Si(001) and Ge-buffered Si(001) (Ge-VS) in a growth temperature window of $325 - 475\,^{\circ}\mathrm{C}$. However, for the lowest growth temperatures, $T_{gr}$, i.e. $< 375\,^{\circ}\mathrm{C}$, Ge-VS is mandatory. The Sn incorporation into Ge- and SiGe host lattices strongly depends on the partial pressure ratios between $Ge_2H_6$, $Si_2H_6$ and $SnCl_4$ as well as on the growth temperature; for decreasing $T_{gr}$ a higher Sn concentration is obtained. In this regard, the highest values for $x_{Sn}$ and $x_{Si}$ are 13 at.% and 19 at.%, respectively, whereas the Si concentration within the layers increases with increasing temperature at constant partial pressure ratios. Depending on the employed $p_{SnCl_4}$ the epitaxial activation energies for GeSn and SiGeSn vary between 0.4 eV and approx. 0.6 eV. The higher the amount of $SnCl_4$ within the growth chamber the lower the activation energy.
It has been found that the crystalline quality of the GeSn and SiGeSn epilayers is significantly improved on Ge-VS, due to a reduction of the lattice mismatch. Minimum yield values of coherently grown (Si)GeSn alloys, measured with Rutherford backscattering spectrometry in the ion channeling mode, of approx. $5\,\%$ close to pseudomorphic

SiGe on Si indicate excellent monocrystalline quality. Complementary transmission electron micrographs evidence defect-free (Si)GeSn/Ge-VS interfaces. Compressive strain of max. $-1.9\,\%$ is obtained by X-ray diffraction. This high distortion is advantageous for nanoelectronic applications, i.e. p-MOSFETs, due to the reduced phonon scattering of holes induced by the large split of the valence bands.
However, since coherently grown (Si)GeSn on Ge might not provide a fundamental direct bandgap, the strain relaxation of these materials at low growth temperatures have been investigated. In contrast to the well-known SiGe/Si system these epilayers appear to plastically relax nearly exclusively via $90\,^\circ$ misfit dislocations, spatially limited close to the (Si)GeSn/Ge interface, rather than via $60\,^\circ$ threading dislocations reaching the sample surface. Consequently, the (Si)GeSn layers slightly above the (Si)GeSn/Ge interface exhibit a nearly perfect monocrystalline quality with threading dislocation density of approx. $5 \times 10^6\,\mathrm{cm}^{-2}$. Pseudomorphic as well as partially relaxed layers show a strong PL peak at room temperature confirming high crystalline quality.
Another route to achieve direct bandgap group IV semiconductors with high carrier mobility is to pseudomorphically grow Ge or GeSn epilayers on top of high Sn content and partially relaxed GeSn buffer layers in order to introduce biaxial tensile strain. The use of $250 - 265\,\mathrm{nm}$ thick GeSn buffers with Sn concentrations between 11 at.% and 12 at.% enables tensile strain values up to $1.4\,\%$ in coherently overgrown Ge and GeSn epilayers. Since these highly strained Ge(Sn) (sGe, sGeSn) layers are promising channel materials for n- and p-MOSFETs, owing to their potentially high carrier mobility and the split of valence bands, MOS capacitors have been fabricated in order to study the quality of the sGe(Sn)-high-k interface which represents the key issue in implementing novel channel materials apart from Si. Secondary ion mass spectrometry measurements of processed MOS capacitors show that the thermal budget for the sGe(Sn)/GeSn/Ge/Si heterostructures is limited to approx. $300\,^\circ\mathrm{C}$. For higher temperatures, severe Sn and Ge diffusion towards the surface and strain relaxation of the topmost epilayers has been observed. Room temperature admittance characterization has indicated a strong inversion response due to the low bandgap of the highly strained semiconductors. Moreover, temperature dependent CV measurements between $80 - 300\,\mathrm{K}$ have provided evidence to conclude that no Fermi-level pinning - caused by excessive interface trap densities - occurs.
Regarding contact formation, smooth Ni-stanogermanides and -stanogermanosilicides with Sn concentrations up to 12 at.% have been synthesized at formation temperatures between $275\,^\circ\mathrm{C}$ and $350\,^\circ\mathrm{C}$. Above the latter temperature the degradation strongly depends on the Sn concentration of the as grown GeSn and SiGeSn layers. A lower formation temperature of $300\,^\circ\mathrm{C}$ of a low resistive $\mathrm{Ni}_1((\mathrm{Si})\mathrm{GeSn})_1$ phase has been determined for NiGeSn ternaries compared to NiSiGeSn quaternaries. The min. specific resistivity of $20 - 25\,\mu\Omega\mathrm{cm}$ at process temperatures of $325\,^\circ\mathrm{C}$ (NiGeSn) and $350\,^\circ\mathrm{C}$ (NiSiGeSn) is comparable to values for NiGe.
Via temperature dependent photoluminescence measurements and a set of above mentioned partially relaxed high quality GeSn layers with Sn concentrations between 8 at.% and 12.6 at.% the transition from an indirect to a fundamental direct bandgap group IV

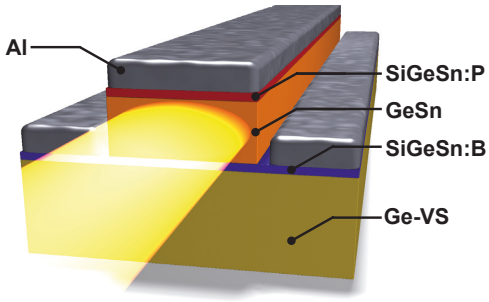


**Figure 5.1:** Sketch of an electrically pumped SiGeSn/GeSn/SiGeSn double heterostructure laser.

semiconductor has been experimentally proven for the first time. Whereas a significant reduction of the difference in energy, $\Delta E$, between the L- and Γ-valley has been determined for $-0.52\,\%$ strained $Ge_{0.904}Sn_{0.096}$ ($\Delta E = -10\,\text{meV}$) and $-0.41\,\%$ strained $Ge_{0.889}Sn_{0.111}$ ($\Delta E = -5\,\text{meV}$), the Γ-valley of a $Ge_{0.874}Sn_{0.126}$ epilayer with a residual compressive strain of $-0.71\,\%$ lies approx. 25 meV below the L-valleys. From these data the transition from an indirect to direct bandgap semiconductor in cubic GeSn is assumed to occur at approx. 8.6 at.%. For slightly thicker, 560 nm, and intentionally undoped direct bandgap $Ge_{0.874}Sn_{0.126}$ modal gain has been proven experimentally by the variable stripe length method. At emission energies of 558 meV and 551 meV gain values of $46\,\text{cm}^{-1}$ and $110\,\text{cm}^{-1}$ have been determined, respectively. Consequently, this $Ge_{0.874}Sn_{0.126}$ layer is predestined to show lasing and indeed unambiguous lasing action have been obtained in optically pumped $Ge_{0.874}Sn_{0.126}$ Fabry-Perot cavities at temperatures $\leq 90\,\text{K}$. A threshold behavior in emitted intensity and linewidth with increasing optical power along with a consistent longitudinal cavity mode pattern has been observed for the first time in a group IV semiconductor. The PL intensity increases by a factor of 8000 when passing the lasing threshold. Moreover, the lasing action provides self-contained evidence for the fundamental direct bandgap nature of this group IV semiconductor. The proof of a fundamental direct bandgap group IV semiconductor that exhibits high modal gain in order to enable lasing provide the largest impact among the results of this work.

These achievements represent an exciting starting point for group IV laser devices as well as low power nanoelectronics with an enormous potential particularly in terms of monolithic integration. Interfacial qualities to high-k dielectrics comparable with state of the art Ge-high-k interfaces along with CMOS compatible thermal budgets and contact formation are essential first steps towards the integration of such novel highly tensile strained, narrow bandgap semiconductors. Further studies on the interfacial quality are, however, essential in order to comply with the prevalent high requirements in the field of low power nanoelectronics.
In respect to optics, due to the fact that the simplest heterostructures have been em-

ployed for the demonstration of lasing the development of efficient group IV laser devices has just started. The next logical steps on that route are the introduction of suitable cladding layers such as SiGeSn epilayers presented in chapter 2 and the n-type doping of the gain medium to further enhance the modal gain. SiGeSn/GeSn/SiGeSn double heterostructures (DHS) (c.f. Fig. 5.1) would allow stronger carrier as well as mode confinement. Another way to enhance the gain is to increase energy difference between the L- and Γ-valley, i.e. the "directness". One option to achieve this, is to incorporate even higher Sn concentrations by a further development of the epitaxial growth process towards lower growth temperatures. Moreover, techniques to further enhance the degree of strain relaxation would be highly advantageous in this regard.

# Bibliography


[1] "Visual Networking Index (VNI) 2012-2017, Cisco Systems. URL www.cisco.com."

[2] A. M. Ionescu and H. Riel, "Tunnel field-effect transistors as energy-efficient electronic switches.," *Nature*, vol. 479, pp. 329–37, Nov. 2011.

[3] K. Kao, A. Verhulst, W. Vandenberghe, B. Sorée, G. Groeseneken, and K. D. Meyer, "Direct and indirect band-to-band tunneling in germanium-based TFETs," *IEEE Transactions on Electron Devices*, vol. 59, no. 2, pp. 292–301, 2012.

[4] R. Kotlyar, U. E. Avci, S. Cea, R. Rios, T. D. Linton, K. J. Kuhn, and I. A. Young, "Bandgap engineering of group IV materials for complementary n and p tunneling field effect transistors," *Applied Physics Letters*, vol. 102, no. 11, p. 113106, 2013.

[5] F. Xia, L. Sekaric, and Y. Vlasov, "Ultracompact optical buffers on a silicon chip," *Nature Photonics*, vol. 1, pp. 65–71, Jan. 2007.

[6] S. Assefa, F. Xia, and Y. A. Vlasov, "Reinventing germanium avalanche photodetector for nanophotonic on-chip optical interconnects.," *Nature*, vol. 464, pp. 80–4, Mar. 2010.

[7] Q. Xu, B. Schmidt, S. Pradhan, and M. Lipson, "Micrometre-scale silicon electro-optic modulator.," *Nature*, vol. 435, pp. 325–7, May 2005.

[8] A. W. Fang, H. Park, O. Cohen, R. Jones, M. J. Paniccia, and J. E. Bowers, "Electrically pumped hybrid AlGaInAs-silicon evanescent laser.," *Optics Express*, vol. 14, pp. 9203–10, Oct. 2006.

[9] C. Goodman, "Direct-gap group IV semiconductors based on tin," *IEE Proceedings I Solid State and Electron Devices*, vol. 129, no. 5, p. 189, 1982.

[10] J. P. Fleurial and A. Borshchevsky, "Si-Ge-Metal Ternary Phase Diagram Calculations," *Journal of The Electrochemical Society*, vol. 137, no. 9, p. 2928, 1990.

[11] S. Wirths, D. Buca, A. Tiedemann, B. Holländer, P. Bernardy, T. Stoica, D. Grützmacher, and S. Mantl, "Epitaxial Growth of $Ge_{1-x}Sn_x$ by Reduced Pressure CVD Using $SnCl_4$ and $Ge_2H_6$," *ECS Transactions*, vol. 50, pp. 885–893, Mar. 2012.

[12] S. Wirths, D. Buca, G. Mussler, A. T. Tiedemann, B. Holländer, P. Bernardy, T. Stoica, D. Grützmacher, and S. Mantl, "Reduced Pressure CVD Growth of Ge and $Ge_{1-x}Sn_x$ Alloys," *ECS Journal of Solid State Science and Technology*, vol. 2, pp. N99–N102, Mar. 2013.

[13] S. Wirths, A. T. Tiedemann, Z. Ikonic, P. Harrison, B. Holländer, T. Stoica, G. Mussler, M. Myronov, J. M. Hartmann, D. Grützmacher, D. Buca, and S. Mantl, "Band engineering and growth of tensile strained Ge/(Si)GeSn heterostructures for tunnel field effect transistors," *Applied Physics Letters*, vol. 102, no. 19, p. 192103, 2013.

[14] S. Wirths, Z. Ikonic, A. T. Tiedemann, B. Holländer, T. Stoica, G. Mussler, U. Breuer, J. M. Hartmann, A. Benedetti, S. Chiussi, D. Grützmacher, S. Mantl, and D. Buca, "Tensely strained GeSn alloys as optical gain media," *Applied Physics Letters*, vol. 103, no. 19, p. 192110, 2013.

[15] S. Wirths, D. Buca, Z. Ikonic, P. Harrison, A. Tiedemann, B. Holländer, T. Stoica, G. Mussler, U. Breuer, J. Hartmann, D. Grützmacher, and S. Mantl, "SiGeSn growth studies using reduced pressure chemical vapor deposition towards optoelectronic applications," *Thin Solid Films*, vol. 557, pp. 183–187, Apr. 2014.

[16] S. Wirths, Z. Ikonic, N. von den Driesch, G. Mussler, U. Breuer, A. Tiedemann, P. Bernardy, B. Holländer, T. Stoica, J.-M. Hartmann, D. Grützmacher, S. Mantl, and D. Buca, "Growth Studies of Doped SiGeSn/Strained Ge(Sn) Heterostructures," *ECS Transactions*, vol. 64, pp. 689–696, Sept. 2014.

[17] P. Moontragoon, Z. Ikonic, and P. Harrison, "Band structure calculations of Si-Ge-Sn alloys: achieving direct band gap materials," *Semiconductor Science and Technology*, vol. 22, pp. 742–748, July 2007.

[18] L. Ansari, G. Fagas, J.-P. Colinge, and J. C. Greer, "A proposed confinement modulated gap nanowire transistor based on a metal (tin).," *Nano Letters*, vol. 12, pp. 2222–7, May 2012.

[19] H. Höchst and I. Hernández-Calderón, "Angular resolved photoemission of InSb(001) and heteroepitaxial films of $\alpha$-Sn(001)," *Surface Science*, vol. 126, pp. 25–31, Mar. 1983.

[20] R. Farrow, D. Robertson, G. Williams, A. Cullis, G. Jones, I. Young, and P. Dennis, "The growth of metastable, heteroepitaxial films of $\alpha$-Sn by metal beam epitaxy," *Journal of Crystal Growth*, vol. 54, pp. 507–518, Sept. 1981.

[21] S. Groves and W. Paul, "Band structure of gray tin," *Physical Review Letters*, vol. 11, no. 5, pp. 194–196, 1963.

[22] X. Li, X. Wang, L. Zhang, S. Lee, and H. Dai, "Chemically derived, ultrasmooth graphene nanoribbon semiconductors.," *Science (New York, N.Y.)*, vol. 319, pp. 1229–32, Feb. 2008.

[23] "Ioffe physical technical institute, semiconductors on nsm. url http://www.ioffe.rssi.ru/sva/nsm/semicond/."

[24] P. Moontragoon, R. A. Soref, and Z. Ikonic, "The direct and indirect bandgaps of unstrained $Si_xGe_{1-x-y}Sn_y$ and their photonic device applications," *Journal of Applied Physics*, vol. 112, no. 7, p. 073106, 2012.

[25] G.-E. Chang, S.-W. Chang, and S. L. Chuang, "Strain-Balanced $Ge_zSn_{1-z}$-$Si_xGe_ySn_{1-x-y}$ Multiple-Quantum-Well Lasers," *IEEE Journal of Quantum Electronics*, vol. 46, pp. 1813–1820, Dec. 2010.

[26] S. Gupta, B. Magyari-Köpe, Y. Nishi, and K. C. Saraswat, "Achieving direct band gap in germanium through integration of Sn alloying and external strain," *Journal of Applied Physics*, vol. 113, no. 7, p. 073707, 2013.

[27] T. F. Kuech, L. J. Mawst, and A. S. Brown, "Mixed semiconductor alloys for optical devices.," *Annual review of chemical and biomolecular engineering*, vol. 4, pp. 187–209, Jan. 2013.

[28] M. Virgilio, C. L. Manganelli, G. Grosso, G. Pizzi, and G. Capellini, "Radiative recombination and optical gain spectra in biaxially strained n-type germanium," *Physical Review B*, vol. 87, p. 235313, June 2013.

[29] M. El Kurdi, G. Fishman, S. Sauvage, and P. Boucaud, "Band structure and optical gain of tensile-strained germanium based on a 30 band k.p formalism," *Journal of Applied Physics*, vol. 107, no. 1, p. 013710, 2010.

[30] E. A. Fitzgerald, Y.-H. Xie, M. L. Green, D. Brasen, A. R. Kortan, J. Michel, Y.-J. Mii, and B. E. Weir, "Totally relaxed $Ge_xSi_{1-x}$ layers with low threading dislocation densities grown on Si substrates," *Applied Physics Letters*, vol. 59, no. 7, p. 811, 1991.

[31] R. Loo, G. Wang, L. Souriau, J. Lin, S. Takeuchi, G. Brammertz, and M. Caymax, "Epitaxial Ge on Standard STI Patterned Si Wafers: High Quality Virtual Substrates for Ge pMOS and III/V nMOS," *ECS Transactions*, vol. 25, no. 7, pp. 335–350, 2009.

[32] G. Wang, F. E. Leys, L. Souriau, R. Loo, M. Caymax, D. P. Brunco, J. Geypen, H. Bender, M. Meuris, W. Vandervorst, and M. Heyns, "Selective Epitaxial Growth of Germanium on Si Wafers with Shallow Trench Isolation: An Approach for Ge Virtual Substrates," *ECS Transactions*, vol. 16, pp. 829–836, Aug. 2008.

[33] J. M. Hartmann, A. Abbadie, A. Papon, P. Holliger, G. Rolland, T. Billon, J. Fédéli, M. Rouviere, L. Vivien, and S. Laval, "Reduced pressure-chemical vapor deposition of Ge thick layers on Si(001) for 1.3-1.55-$\mu$m photodetection," *Journal of Applied Physics*, vol. 95, no. 10, p. 5905, 2004.

[34] L. Colace, G. Masini, F. Galluzzi, G. Assanto, G. Capellini, L. Di Gaspare, E. Palange, and F. Evangelisti, "Metal-semiconductor-metal near-infrared light detector based on epitaxial Ge/Si," *Applied Physics Letters*, vol. 72, no. 24, p. 3175, 1998.

[35] V. Shah, A. Dobbie, M. Myronov, and D. Leadley, "High quality relaxed Ge layers grown directly on a Si(001) substrate," *Solid-State Electronics*, vol. 62, pp. 189–194, Aug. 2011.

[36] R. W. Olesinski and G. J. Abbaschian, "The Ge-Sn (Germanium-Tin) system," *Bulletin of Alloy Phase Diagrams*, vol. 5, pp. 265–271, June 1984.

[37] E. Kasper, J. Werner, M. Oehme, S. Escoubas, N. Burle, and J. Schulze, "Growth of silicon based germanium tin alloys," *Thin Solid Films*, vol. 520, pp. 3195–3200, Feb. 2012.

[38] S. Takeuchi, A. Sakai, O. Nakatsuka, M. Ogawa, and S. Zaima, "Tensile strained Ge layers on strain-relaxed $Ge_{1-x}Sn_x$/virtual Ge substrates," *Thin Solid Films*, vol. 517, pp. 159–162, Nov. 2008.

[39] S. Oguz, W. Paul, B.-Y. Tsaur, and D. Murphy, "Synthesis of metastable, semiconducting Ge-Sn alloys by pulsed UV laser crystallization," *Applied Physics Letters*, vol. 43, no. 9, p. 848, 1983.

[40] S. Shah, J. Greene, L. Abels, Q. Yao, and P. Raccah, "Growth of single-crystal metastable $Ge_{1-x}Sn_x$ alloys on Ge(100) and GaAs(100) substrates," *Journal of Crystal Growth*, vol. 83, pp. 3–10, May 1987.

[41] E. A. Fitzgerald, P. E. Freeland, M. T. Asom, W. P. Lowe, R. A. Macharrie, B. E. Weir, A. R. Kortan, F. A. Thiel, Y. H. Xie, A. M. Sergent, S. L. Cooper, G. A. Thomas, and L. C. Kimerling, "Epitaxially stabilized $Ge_xSn_{1-x}$ diamond cubic alloys," *Journal of Electronic Materials*, vol. 20, pp. 489–501, June 1991.

[42] W. Wegscheider, "Fabrication and properties of epitaxially stabilized Ge / $\alpha$-Sn heterostructures on Ge(001)," *Journal of Crystal Growth*, vol. 123, pp. 75–94, Sept. 1992.

[43] A. Harwit, P. Pukite, J. Angilello, and S. Iyer, "Properties of diamond structure SnGe films grown by molecular beam epitaxy," *Thin Solid Films*, vol. 184, pp. 395–401, 1990.

[44] M. Taylor and G. He, "Solid phase epitaxy of diamond cubic $Sn_xGe_{1-x}$ alloys," *Journal of Applied Physics*, vol. 80, no. 8, pp. 96–100, 1996.

[45] O. Gurdal, P. Desjardins, J. R. A. Carlsson, N. Taylor, H. H. Radamson, J.-E. Sundgren, and J. E. Greene, "Low-temperature growth and critical epitaxial thicknesses

of fully strained metastable $Ge_{1-x}Sn_x$ ($x \leq 0.26$) alloys on Ge(001)2×1," *Journal of Applied Physics*, vol. 83, no. 1, p. 162, 1998.

[46] G. He and H. A. Atwater, "Synthesis of epitaxial $Sn_xGe_{1-x}$ alloy films by ion-assisted molecular beam epitaxy," *Applied Physics Letters*, vol. 68, no. 5, p. 664, 1996.

[47] R. Ragan and H. A. Atwater, "Measurement of the direct energy gap of coherently strained $Sn_xGe_{1-x}$/Ge(001) heterostructures," *Applied Physics Letters*, vol. 77, no. 21, p. 3418, 2000.

[48] G. He and H. Atwater, "Interband Transitions in $Sn_xGe_{1-x}$ Alloys," *Physical Review Letters*, vol. 79, pp. 1937–1940, Sept. 1997.

[49] K. A. Bratland, Y. L. Foo, T. Spila, H.-S. Seo, R. T. Haasch, P. Desjardins, and J. E. Greene, "Sn-mediated Ge/Ge(001) growth by low-temperature molecular-beam epitaxy: Surface smoothening and enhanced epitaxial thickness," *Journal of Applied Physics*, vol. 97, no. 4, p. 044904, 2005.

[50] J. Taraci, J. Tolle, J. Kouvetakis, M. R. McCartney, D. J. Smith, J. Menendez, and M. A. Santana, "Simple chemical routes to diamond-cubic germanium-tin alloys," *Applied Physics Letters*, vol. 78, no. 23, p. 3607, 2001.

[51] M. Bauer, J. Taraci, J. Tolle, A. V. G. Chizmeshya, S. Zollner, D. J. Smith, J. Menéndez, C. Hu, and J. Kouvetakis, "Ge-Sn semiconductors for band-gap and lattice engineering," *Applied Physics Letters*, vol. 81, no. 16, p. 2992, 2002.

[52] M. Bauer, C. Ritter, P. S. Crozier, J. Ren, J. Menéndez, G. Wolf, and J. Kouvetakis, "Synthesis of ternary SiGeSn semiconductors on Si(100) via $Sn_xGe_{1-x}$ buffer layers," *Applied Physics Letters*, vol. 83, no. 11, p. 2163, 2003.

[53] B. Vincent, F. Gencarelli, H. Bender, C. Merckling, B. Douhard, D. H. Petersen, O. Hansen, H. H. Henrichsen, J. Meersschaut, W. Vandervorst, M. Heyns, R. Loo, and M. Caymax, "Undoped and in-situ B doped GeSn epitaxial growth on Ge by atmospheric pressure-chemical vapor deposition," *Applied Physics Letters*, vol. 99, no. 15, p. 152103, 2011.

[54] J. Mathews, R. Roucka, C. Weng, R. Beeler, J. Tolle, J. Menendez, and J. Kouvetakis, "Near IR Photodiodes with Tunable Absorption Edge Based on Ge Sn Alloys Integrated on Silicon," *ECS Transactions*, vol. 33, no. 6, pp. 765–773, 2010.

[55] R. Roucka, J. Mathews, R. T. Beeler, J. Tolle, J. Kouvetakis, and J. Menéndez, "Direct gap electroluminescence from $Si/Ge_{1-y}Sn_y$ p-i-n heterostructure diodes," *Applied Physics Letters*, vol. 98, no. 6, p. 061109, 2011.

[56] R. T. Beeler, G. J. Grzybowski, R. Roucka, L. Jiang, J. Mathews, D. J. Smith, J. Menéndez, A. V. G. Chizmeshya, and J. Kouvetakis, "Synthesis and Materials

Properties of Sn/P-Doped Ge on Si(100): Photoluminescence and Prototype Devices," *Chemistry of Materials*, vol. 23, pp. 4480–4486, Oct. 2011.

[57] A. Gassenq, F. Gencarelli, J. Van Campenhout, Y. Shimura, R. Loo, G. Narcy, B. Vincent, and G. Roelkens, "GeSn/Ge heterostructure short-wave infrared photodetectors on silicon," *Optics Express*, vol. 20, pp. 27297–303, Dec. 2012.

[58] R. T. Beeler, C. Xu, D. J. Smith, G. Grzybowski, J. Menéndez, and J. Kouvetakis, "Compositional dependence of the absorption edge and dark currents in $Ge_{1-x-y}Si_xSn_y$/Ge(100) photodetectors grown via ultra-low-temperature epitaxy of $Ge_4H_{10}$, $Si_4H_{10}$, and $SnD_4$," *Applied Physics Letters*, vol. 101, no. 22, p. 221111, 2012.

[59] S. Gupta, B. Vincent, B. Yang, D. Lin, F. Gencarelli, J.-Y. J. Lin, R. Chen, O. Richard, H. Bender, B. Magyari-Kope, M. Caymax, J. Dekoster, Y. Nishi, and K. C. Saraswat, "Towards high mobility GeSn channel nMOSFETs: Improved surface passivation using novel ozone oxidation method," in *2012 International Electron Devices Meeting*, pp. 16.2.1–16.2.4, IEEE, Dec. 2012.

[60] A. C. Jones and M. L. Hitchman, eds., *Chemical Vapour Deposition*. Cambridge: Royal Society of Chemistry, 2008.

[61] M. Dauelsberg, C. Martin, H. Protzmann, A. Boyd, E. Thrush, J. Käppeler, M. Heuken, R. Talalaev, E. Yakovlev, and A. Kondratyev, "Modeling and process design of III-nitride MOVPE at near-atmospheric pressure in close coupled showerhead and planetary reactors," *Journal of Crystal Growth*, vol. 298, pp. 418–424, Jan. 2007.

[62] R. Loo, G. Wang, L. Souriau, J. C. Lin, S. Takeuchi, G. Brammertz, and M. Caymax, "High Quality Ge Virtual Substrates on Si Wafers with Standard STI Patterning," *Journal of The Electrochemical Society*, vol. 157, no. 1, p. H13, 2010.

[63] J. Hartmann, A. Papon, V. Destefanis, and T. Billon, "Reduced pressure chemical vapor deposition of Ge thick layers on Si(001), Si(011) and Si(111)," *Journal of Crystal Growth*, vol. 310, pp. 5287–5296, Dec. 2008.

[64] J. Hartmann, J. Damlencourt, Y. Bogumilowicz, P. Holliger, G. Rolland, and T. Billon, "Reduced pressure-chemical vapor deposition of intrinsic and doped Ge layers on Si(001) for microelectronics and optoelectronics purposes," *Journal of Crystal Growth*, vol. 274, pp. 90–99, Jan. 2005.

[65] J.-F. Damlencourt, "Low Temperature Epitaxy of Si and SiGe Using Disilane Based Chemistry for Electronic Purposes," *ECS Transactions*, vol. 28, pp. 343–348, Feb. 2010.

[66] B. Vincent, R. Loo, W. Vandervorst, G. Brammertz, and M. Caymax, "Low temperature Si homo-epitaxy by reduced pressure chemical vapor deposition using dichlorosilane, silane and trisilane," *Journal of Crystal Growth*, vol. 312, pp. 2671–2676, Sept. 2010.

[67] J. C. Sturm and K. H. Chung, "Chemical Vapor Deposition Epitaxy of Silicon-based Materials using Neopentasilane," *ECS Transactions*, vol. 16, pp. 799–805, Aug. 2008.

[68] F. Gencarelli, B. Vincent, L. Souriau, O. Richard, W. Vandervorst, R. Loo, M. Caymax, and M. Heyns, "Low-temperature Ge and GeSn Chemical Vapor Deposition using $Ge_2H_6$," *Thin Solid Films*, vol. 520, pp. 3211–3215, Feb. 2012.

[69] R. F. Spohn and C. B. Richenberg, "Tin Deuteride ($SnD_4$) Stabilization," *ECS Transactions*, vol. 50, pp. 921–927, Mar. 2013.

[70] J. Kouvetakis, J. Menendez, and A. Chizmeshya, "TIN-BASED GROUP IV SEMICONDUCTORS: New Platforms for Opto- and Microelectronics on Silicon," *Annual Review of Materials Research*, vol. 36, pp. 497–554, Aug. 2006.

[71] H. Radamson, M. Noroozi, A. Jamshidi, and M. Ostling, "Strain Engineering in GeSnSi Materials," *ECS Transactions*, vol. 50, pp. 527–531, Mar. 2012.

[72] R. Roucka, J. Tolle, C. Cook, A. V. G. Chizmeshya, J. Kouvetakis, V. D'Costa, J. Menendez, Z. D. Chen, and S. Zollner, "Versatile buffer layer architectures based on $Ge_{1-x}Sn_x$ alloys," *Applied Physics Letters*, vol. 86, no. 19, p. 191912, 2005.

[73] J. M. Hartmann, A. Abbadie, N. Cherkashin, H. Grampeix, and L. Clavelier, "Epitaxial growth of Ge thick layers on nominal and 6° off Si(0 0 1); Ge surface passivation by Si," *Semiconductor Science and Technology*, vol. 24, p. 055002, May 2009.

[74] F. Gencarelli, B. Vincent, J. Demeulemeester, A. Vantomme, A. Moussa, A. Franquet, A. Kumar, H. Bender, J. Meersschaut, W. Vandervorst, R. Loo, M. Caymax, K. Temst, and M. Heyns, "Crystalline Properties and Strain Relaxation Mechanism of CVD Grown GeSn," *ECS Journal of Solid State Science and Technology*, vol. 2, pp. P134–P137, Jan. 2013.

[75] J. Xie, A. V. G. Chizmeshya, J. Tolle, V. R. D'Costa, J. Menéndez, and J. Kouvetakis, "Synthesis, Stability Range, and Fundamental Properties of Si-Ge-Sn Semiconductors Grown Directly on Si(100) and Ge(100) Platforms," *Chemistry of Materials*, vol. 22, pp. 3779–3789, June 2010.

[76] A. V. Chizmeshya and J. Kouvetakis, "(Invited) Practical Strategies for Tuning Optical, Structural and Thermal Properties in Group IV Ternary Semiconductors," in *ECS Transactions 33 (6)*, vol. 33, pp. 717–728, ECS, 2010.

[77] R. People and J. C. Bean, "Calculation of critical layer thickness versus lattice mismatch for $Ge_xSi_{1-x}$/Si strained-layer heterostructures," *Applied Physics Letters*, vol. 47, no. 3, p. 322, 1985.

[78] R. People and J. C. Bean, "Erratum: Calculation of critical layer thickness versus lattice mismatch for $Ge_xSi_{1-x}$/Si strained-layer heterostructures [Appl. Phys. Lett. 47, 322 (1985)]," *Applied Physics Letters*, vol. 49, no. 4, p. 229, 1986.

[79] E. A. Fitzgerald, "Influence of strain on semiconductor thin film epitaxy," *Journal of Vacuum Science & Technology A: Vacuum, Surfaces, and Films*, vol. 15, p. 1048, May 1997.

[80] F. LeGoues, B. Meyerson, and J. Morar, "Anomalous strain relaxation in SiGe thin films and superlattices.," *Physical Review Letters*, vol. 66, pp. 2903–2906, June 1991.

[81] F. K. LeGoues, J. A. Ott, K. Eberl, and S. S. Iyer, "In situ study of relaxation of SiGe thin films by the modified Frank-Read mechanism," *Applied Physics Letters*, vol. 61, no. 2, p. 174, 1992.

[82] F. K. LeGoues, K. Eberl, and S. S. Iyer, "Relaxation by the modified Frank-Read mechanism in compositionally uniform thin films," *Applied Physics Letters*, vol. 60, no. 23, p. 2862, 1992.

[83] K. K. Linder, F. C. Zhang, J.-S. Rieh, P. Bhattacharya, and D. Houghton, "Reduction of dislocation density in mismatched SiGe/Si using a low-temperature Si buffer layer," *Applied Physics Letters*, vol. 70, no. 24, p. 3224, 1997.

[84] D. Gerthsen, D. Biegelsen, F. Ponce, and J. Tramontana, "Misfit dislocations in GaAs heteroepitaxy on (001) Si," *Journal of Crystal Growth*, vol. 106, pp. 157–165, Nov. 1990.

[85] X. Sun, J. Liu, L. C. Kimerling, and J. Michel, "Direct gap photoluminescence of n-type tensile-strained Ge-on-Si," *Applied Physics Letters*, vol. 95, no. 1, p. 011911, 2009.

[86] M.-Y. Ryu, T. R. Harris, Y. K. Yeo, R. T. Beeler, and J. Kouvetakis, "Temperature-dependent photoluminescence of Ge/Si and $Ge_{1-y}Sn_y$/Si, indicating possible indirect-to-direct bandgap transition at lower Sn content," *Applied Physics Letters*, vol. 102, no. 17, p. 171908, 2013.

[87] R. Chen, Y.-C. Huang, S. Gupta, A. C. Lin, E. Sanchez, Y. Kim, K. C. Saraswat, T. I. Kamins, and J. S. Harris, "Material characterization of high Sn-content, compressively-strained GeSn epitaxial films after rapid thermal processing," *Journal of Crystal Growth*, vol. 365, pp. 29–34, Feb. 2013.

[88] S. Takeuchi, Y. Shimura, O. Nakatsuka, S. Zaima, M. Ogawa, and A. Sakai, "Growth of highly strain-relaxed $Ge_{1-x}Sn_x$/virtual Ge by a Sn precipitation controlled compositionally step-graded method," *Applied Physics Letters*, vol. 92, no. 23, p. 231916, 2008.

[89] Y. Bai, K. E. Lee, C. Cheng, M. L. Lee, and E. A. Fitzgerald, "Growth of highly tensile-strained Ge on relaxed $In_xGa_{1-x}As$ by metal-organic chemical vapor deposition," *Journal of Applied Physics*, vol. 104, no. 8, p. 084518, 2008.

[90] Y.-Y. Fang, J. Tolle, R. Roucka, A. V. G. Chizmeshya, J. Kouvetakis, V. R. D'Costa, and J. Menéndez, "Perfectly tetragonal, tensile-strained Ge on $Ge_{1-y}Sn_y$ buffered Si(100)," *Applied Physics Letters*, vol. 90, no. 6, p. 061915, 2007.

[91] H. Trinkaus, D. Buca, B. Holländer, R. A. Minamisawa, S. Mantl, and J. M. Hartmann, "Strain tensors in layer systems by precision ion channeling measurements," *Journal of Applied Physics*, vol. 107, no. 12, p. 124906, 2010.

[92] B. S. Meyerson, "Phosphorus-Doped Polycrystalline Silicon via LPCVD," *Journal of The Electrochemical Society*, vol. 131, no. 10, p. 2366, 1984.

[93] S. Gupta, Y.-C. Huang, Y. Kim, E. Sanchez, and K. C. Saraswat, "Hole Mobility Enhancement in Compressively Strained $Ge_{0.93}Sn_{0.07}$ pMOSFETs," *IEEE Electron Device Letters*, vol. 34, pp. 831–833, July 2013.

[94] S. Gupta, R. Chen, J. S. Harris, and K. C. Saraswat, "Atomic layer deposition of $Al_2O_3$ on germanium-tin (GeSn) and impact of wet chemical surface pre-treatment," *Applied Physics Letters*, vol. 103, no. 24, p. 241601, 2013.

[95] C. Merckling, X. Sun, Y. Shimura, A. Franquet, B. Vincent, S. Takeuchi, W. Vandervorst, O. Nakatsuka, S. Zaima, R. Loo, and M. Caymax, "Molecular beam deposition of $Al_2O_3$ on p-Ge(001)/$Ge_{0.95}Sn_{0.05}$ heterostructure and impact of a Ge-cap interfacial layer," *Applied Physics Letters*, vol. 98, no. 19, p. 192110, 2011.

[96] K. C. Saraswat, C. O. Chui, T. Krishnamohan, A. Nayfeh, and P. Mcintyre, "Ge based high performance nanoscale MOSFETs," *Microelectronic Engineering*, vol. 80, pp. 15–21, 2005.

[97] R. Pillarisetty, "Academic and industry research progress in germanium nanodevices.," *Nature*, vol. 479, pp. 324–8, Nov. 2011.

[98] D. P. Brunco, B. De Jaeger, G. Eneman, J. Mitard, G. Hellings, A. Satta, V. Terzieva, L. Souriau, F. E. Leys, G. Pourtois, M. Houssa, G. Winderickx, E. Vrancken, S. Sioncke, K. Opsomer, G. Nicholas, M. Caymax, A. Stesmans, J. Van Steenbergen, P. W. Mertens, M. Meuris, and M. M. Heyns, "Germanium MOSFET Devices: Advances in Materials Understanding, Process Development, and Electrical Performance," *Journal of The Electrochemical Society*, vol. 155, no. 7, p. H552, 2008.

[99] O. Hashemi, W. Chern, H.-S. Lee, J. T. Teherani, Y. Zhu, J. Gonsalvez, G. G. Shahidi, and J. L. Hoyt, "Ultrathin Strained-Ge Channel P-MOSFETs With High-k/Metal Gate and Sub-1-nm Equivalent Oxide Thickness," *IEEE Electron Device Letters*, vol. 33, pp. 943–945, July 2012.

[100] T. Krishnamohan, Z. Krivokapic, K. Uchida, Y. Nishi, and K. Saraswat, "High-mobility ultrathin strained Ge MOSFETs on bulk and SOI with low band-to-band tunneling leakage: experiments," *IEEE Transactions on Electron Devices*, vol. 53, pp. 990–999, May 2006.

[101] M. V. Fischetti and S. E. Laux, "Band structure, deformation potentials, and carrier mobility in strained Si, Ge, and SiGe alloys," *Journal of Applied Physics*, vol. 80, no. 4, p. 2234, 1996.

[102] D. A. Antoniadis and A. Khakifirooz, "MOSFET performance scaling: Limitations and future options," in *2008 IEEE International Electron Devices Meeting*, pp. 1–4, IEEE, Dec. 2008.

[103] G. Han, S. Su, C. Zhan, and Q. Zhou, "High-mobility germanium-tin (GeSn) P-channel MOSFETs featuring metallic source/drain and sub-370°C process modules," in *2011 IEEE International Electron Devices Meeting*, pp. 402–404, IEEE, 2011.

[104] X. Gong, G. Han, F. Bai, S. Su, P. Guo, Y. Yang, R. Cheng, D. Zhang, G. Zhang, C. Xue, B. Cheng, J. Pan, Z. Zhang, E. S. Tok, D. Antoniadis, and Y.-C. Yeo, "Germanium-Tin (GeSn) p-Channel MOSFETs Fabricated on (100) and (111) Surface Orientations With Sub-400 °C $Si_2H_6$ Passivation," *IEEE Electron Device Letters*, vol. 34, pp. 339–341, Mar. 2013.

[105] R. R. Lieten, J. W. Seo, S. Decoster, A. Vantomme, S. Peters, K. C. Bustillo, E. E. Haller, M. Menghini, and J.-P. Locquet, "Tensile strained GeSn on Si by solid phase epitaxy," *Applied Physics Letters*, vol. 102, no. 5, p. 052106, 2013.

[106] R. R. Lieten, T. Maeda, W. Jevasuwan, H. Hattori, N. Uchida, S. Miura, M. Tanaka, and J.-P. Locquet, "Tensile-Strained GeSn Metal-Oxide-Semiconductor Field-Effect Transistor Devices on Si(111) Using Solid Phase Epitaxy," *Applied Physics Express*, vol. 6, p. 101301, Oct. 2013.

[107] J. Sau and M. Cohen, "Possibility of increased mobility in Ge-Sn alloy system," *Physical Review B*, vol. 75, pp. 1–7, Jan. 2007.

[108] R. Chen, S. Gupta, Y.-C. Huang, Y. Huo, C. W. Rudy, E. Sanchez, Y. Kim, T. I. Kamins, K. C. Saraswat, and J. S. Harris, "Demonstration of a Ge/GeSn/Ge quantum-well microdisk resonator on silicon: enabling high-quality Ge(Sn) materials for micro- and nanophotonics.," *Nano Letters*, vol. 14, pp. 37–43, Jan. 2014.

[109] T. Bahder, "Eight-band k·p model of strained zinc-blende crystals," *Physical Review B*, vol. 41, pp. 11992–12001, June 1990.

[110] J. Knoch and J. Appenzeller, "A novel concept for field-effect transistors-the tunneling carbon nanotube FET," *Device Research Conference Digest*, vol. 1, pp. 153–156, 2005.

[111] S. Sze and K. Ng, *Physics of Semiconductor Devices*. John Wiley & Sons, 3 ed., 2006.

[112] J. Knoch, S. Mantl, and J. Appenzeller, "Impact of the dimensionality on the performance of tunneling FETs: Bulk versus one-dimensional devices," *Solid-State Electronics*, vol. 51, pp. 572–578, Apr. 2007.

[113] M. Zhao, R. Liang, J. Wang, and J. Xu, "Improved electrical properties of Ge metal-oxide-semiconductor devices with $HfO_2$ gate dielectrics using an ultrathin $GeSnO_x$ film as the surface passivation layer," *Applied Physics Letters*, vol. 102, no. 14, p. 142906, 2013.

[114] E. P. Gusev, H. Shang, M. Copel, M. Gribelyuk, C. D'Emic, P. Kozlowski, and T. Zabel, "Microstructure and thermal stability of $HfO_2$ gate dielectric deposited on Ge(100)," *Applied Physics Letters*, vol. 85, no. 12, p. 2334, 2004.

[115] M. K. Hudait and Y. Zhu, "Energy band alignment of atomic layer deposited $HfO_2$ oxide film on epitaxial (100)Ge, (110)Ge, and (111)Ge layers," *Journal of Applied Physics*, vol. 113, no. 11, p. 114303, 2013.

[116] E. Nicollian and J. Brews, *MOS (Metal Oxide Semiconductor) Physics and Technology*. Wiley, 2002.

[117] K. Martens, C. O. Chui, G. Brammertz, B. De Jaeger, D. Kuzum, M. Meuris, M. Heyns, T. Krishnamohan, K. Saraswat, H. E. Maes, and G. Groeseneken, "On the Correct Extraction of Interface Trap Density of MOS Devices With High-Mobility Semiconductor Substrates," *IEEE Transactions on Electron Devices*, vol. 55, pp. 547–556, Feb. 2008.

[118] D. Schroder, *Semiconductor Material and Device Characterization*. John Wiley & Sons, 3 ed., 2006.

[119] K. Martens, *Electrical Characterization and Modelling of Ge/III-V - Dielectric Interfaces*. PhD thesis, Katholieke Universiteit Leuven, 2009.

[120] K. Martens, W. Wang, K. De Keersmaecker, G. Borghs, G. Groeseneken, and H. Maes, "Impact of weak Fermi-level pinning on the correct interpretation of III-V MOS C-V and G-V characteristics," *Microelectronic Engineering*, vol. 84, pp. 2146–2149, Sept. 2007.

[121] P. Batude, X. Garros, L. Clavelier, C. Le Royer, J. M. Hartmann, V. Loup, P. Besson, L. Vandroux, Y. Campidelli, S. Deleonibus, and F. Boulanger, "Insights on fundamental mechanisms impacting Ge metal oxide semiconductor capacitors with high-k/metal gate stacks," *Journal of Applied Physics*, vol. 102, no. 3, p. 034514, 2007.

[122] C. Garrett and W. Brattain, "Physical Theory of Semiconductor Surfaces," *Physical Review*, vol. 99, pp. 376–387, July 1955.

[123] L. Terman, "An investigation of surface states at a silicon/silicon oxide interface employing metal-oxide-silicon diodes," *Solid-State Electronics*, vol. 5, pp. 285–299, Sept. 1962.

[124] C. Garrett, "High-Frequency Relaxation Processes in the Field-Effect Experiment," *Physical Review*, vol. 107, pp. 478–487, July 1957.

[125] E. H. Nicollian and A. Goetzberger, "The Si-$SiO_2$ Interface - Electrical Properties as Determined by the Metal-Insulator-Silicon Conductance Technique," *Bell System Technical Journal*, vol. 46, pp. 1055–1133, July 1967.

[126] T. Sawada and H. Hasegawa, "Anomalous frequency dispersion of MOS capacitors formed on n-type GaAs by anodic oxidation," *Electronics Letters*, vol. 12, no. 18, p. 471, 1976.

[127] H. Hasegawa and T. Sawada, "Electrical modeling of compound semiconductor interface for FET device assessment," *IEEE Transactions on Electron Devices*, vol. 27, pp. 1055–1061, June 1980.

[128] J. Reed, Z. Fan, G. B. Gao, A. Botchkarev, and H. Morkoc, "GaAs metal insulator semiconductor capacitors and high transconductance metal insulator semiconductor field effect transistors," *Applied Physics Letters*, vol. 64, no. 20, p. 2706, 1994.

[129] N. Wu, Q. Zhang, C. Zhu, C. C. Yeo, S. J. Whang, D. S. H. Chan, M. F. Li, B. J. Cho, A. Chin, D.-L. Kwong, A. Y. Du, C. H. Tung, and N. Balasubramanian, "Effect of surface $NH_3$ anneal on the physical and electrical properties of $HfO_2$ films on Ge substrate," *Applied Physics Letters*, vol. 84, no. 19, p. 3741, 2004.

[130] A. Delabie, A. Alian, F. Bellenger, M. Caymax, T. Conard, A. Franquet, S. Sioncke, S. Van Elshocht, M. Heyns, and M. Meuris, "$H_2O$- and $O_3$-Based Atomic Layer Deposition of High-$\kappa$ Dielectric Films on $GeO_2$ Passivation Layers," *Journal of The Electrochemical Society*, vol. 156, no. 10, p. G163, 2009.

[131] R. Zhang, T. Iwasaki, N. Taoka, M. Takenaka, and S. Takagi, "Suppression of ALD-Induced Degradation of Ge MOS Interface Properties by Low Power Plasma Nitridation of $GeO_2$," *Journal of The Electrochemical Society*, vol. 158, no. 8, p. G178, 2011.

[132] B. De Jaeger, R. Bonzom, F. Leys, O. Richard, J. V. Steenbergen, G. Winderickx, E. V. Moorhem, G. Raskin, F. Letertre, T. Billon, M. Meuris, and M. Heyns, "Optimisation of a thin epitaxial Si layer as Ge passivation layer to demonstrate deep sub-micron n- and p-FETs on Ge-On-Insulator substrates," *Microelectronic Engineering*, vol. 80, pp. 26–29, June 2005.

[133] N. Wu, Q. Zhang, C. Zhu, D. S. H. Chan, M. F. Li, N. Balasubramanian, A. Chin, and D.-L. Kwong, "Alternative surface passivation on germanium for metal-oxide-semiconductor applications with high-k gate dielectric," *Applied Physics Letters*, vol. 85, no. 18, p. 4127, 2004.

[134] R. Zhang, T. Iwasaki, N. Taoka, M. Takenaka, and S. Takagi, "$Al_2O_3/GeO_x$/Ge gate stacks with low interface trap density fabricated by electron cyclotron resonance plasma postoxidation," *Applied Physics Letters*, vol. 98, no. 11, p. 112902, 2011.

[135] R. Zhang, N. Taoka, M. Takenaka, and S. Takagi, "1-nm-thick EOT high mobility Ge n- and p-MOSFETs with ultrathin $GeO_x$/Ge MOS interfaces fabricated by plasma post oxidation," in *2011 International Electron Devices Meeting*, pp. 28.3.1–28.3.4, IEEE, Dec. 2011.

[136] R. Zhang, T. Iwasaki, N. Taoka, M. Takenaka, and S. Takagi, "High-Mobility Ge pMOSFET With 1-nm EOT $Al_2O_3/GeO_x$/Ge Gate Stack Fabricated by Plasma Post Oxidation," *IEEE Transactions on Electron Devices*, vol. 59, pp. 335–341, Feb. 2012.

[137] S. Takagi, R. Zhang, and M. Takenaka, "Ge gate stacks based on Ge oxide interfacial layers and the impact on MOS device properties," *Microelectronic Engineering*, vol. 109, pp. 389–395, Sept. 2013.

[138] S. Gupta, X. Gong, R. Zhang, Y.-C. Yeo, S. Takagi, and K. C. Saraswat, "New materials for post-Si computing: Ge and GeSn devices," *MRS Bulletin*, vol. 39, pp. 678–686, Aug. 2014.

[139] N. D. Nguyen and M. Schmeits, "Numerical simulation of impedance and admittance of OLEDs," *physica status solidi (a)*, vol. 203, pp. 1885–1885, June 2006.

[140] B. Baert, O. Nakatsuka, S. Zaima, and N. Nguyen, "Impedance Spectroscopy of GeSn-based Heterostructures," *ECS Transactions*, vol. 50, no. 9, pp. 481–490, 2013.

[141] M. Schmeits, N. D. Nguyen, and M. Germain, "Competition between deep impurity and dopant behavior of Mg in GaN Schottky diodes," *Journal of Applied Physics*, vol. 89, no. 3, p. 1890, 2001.

[142] M. Sakhaf and M. Schmeits, "Capacitance and conductance of semiconductor heterojunctions with continuous energy distribution of interface states," *Journal of Applied Physics*, vol. 80, no. 12, p. 6839, 1996.

[143] S. Gaudet, C. Detavernier, A. J. Kellock, P. Desjardins, and C. Lavoie, "Thin film reaction of transition metals with germanium," *Journal of Vacuum Science & Technology A: Vacuum, Surfaces, and Films*, vol. 24, no. 3, p. 474, 2006.

[144] T. Ghani, M. Armstrong, C. Auth, M. Bost, P. Charvat, G. Glass, T. Hoffmann, K. Johnson, C. Kenyon, J. Klaus, B. McIntyre, K. Mistry, A. Murthy, J. Sandford, M. Silberstein, S. Sivakumar, P. Smith, K. Zawadzki, S. Thompson, and M. Bohr, "A 90nm high volume manufacturing logic technology featuring novel 45nm gate length strained silicon CMOS transistors," in *2003 IEEE International Electron Devices Meeting*, vol. M, pp. 11.6.1–11.6.3, IEEE, Dec. 2003.

[145] Y.-C. Yeo, "Enhancing CMOS transistor performance using lattice-mismatched materials in source/drain regions," *Semiconductor Science and Technology*, vol. 22, pp. S177–S182, Jan. 2007.

[146] Y.-C. Yeo and J. Sun, "Finite-element study of strain distribution in transistor with silicon-germanium source and drain regions," *Applied Physics Letters*, vol. 86, no. 2, p. 023103, 2005.

[147] B. Vincent, Y. Shimura, S. Takeuchi, T. Nishimura, G. Eneman, A. Firrincieli, J. Demeulemeester, A. Vantomme, T. Clarysse, and O. Nakatsuka, "Characterization of GeSn materials for future Ge pMOSFETs source/drain stressors," *Microelectronic Engineering*, vol. 88, pp. 342–346, Apr. 2011.

[148] S. Takeuchi, Y. Shimura, T. Nishimura, B. Vincent, G. Eneman, T. Clarysse, J. Demeulemeester, A. Vantomme, J. Dekoster, M. Caymax, R. Loo, A. Sakai, O. Nakatsuka, and S. Zaima, "$Ge_{1-x}Sn_x$ stressors for strained-Ge CMOS," *Solid-State Electronics*, vol. 60, pp. 53–57, June 2011.

[149] L. Wang, G. Han, S. Su, Q. Zhou, Y. Yang, P. Guo, W. Wang, Y. Tong, P. S. Y. Lim, B. Liu, E. Y.-J. Kong, C. Xue, Q. Wang, B. Cheng, and Y.-C. Yeo, "Thermally Stable Multi-Phase Nickel-Platinum Stanogermanide Contacts for Germanium-Tin Channel MOSFETs," *Electrochemical and Solid-State Letters*, vol. 15, no. 6, p. H179, 2012.

[150] S. Gaudet, C. Detavernier, C. Lavoie, and P. Desjardins, "Reaction of thin Ni films with Ge: Phase formation and texture," *Journal of Applied Physics*, vol. 100, no. 3, p. 034306, 2006.

[151] M. Wittmer, M.-A. Nicolet, and J. Mayer, "The first phase to nucleate in planar transition metal-germanium interfaces," *Thin Solid Films*, vol. 42, pp. 51–59, Apr. 1977.

[152] J. Patterson, B. Park, K. Ritley, H. Xiao, L. Allen, and A. Rockett, "Kinetics of Ni/a-Ge bilayer reactions," *Thin Solid Films*, vol. 253, pp. 456–461, Dec. 1994.

[153] J. Spann, R. Anderson, T. Thornton, G. Harris, S. Thomas, and C. Tracy, "Characterization of nickel Germanide thin films for use as contacts to p-channel Germanium MOSFETs," *IEEE Electron Device Letters*, vol. 26, pp. 151–153, Mar. 2005.

[154] S.-L. Hsu, C.-H. Chien, M.-J. Yang, R.-H. Huang, C.-C. Leu, S.-W. Shen, and T.-H. Yang, "Study of thermal stability of nickel monogermanide on single- and polycrystalline germanium substrates," *Applied Physics Letters*, vol. 86, no. 25, p. 251906, 2005.

[155] J. Demeulemeester, A. Schrauwen, O. Nakatsuka, S. Zaima, M. Adachi, Y. Shimura, C. M. Comrie, C. Fleischmann, C. Detavernier, K. Temst, and A. Vantomme, "Sn diffusion during Ni germanide growth on $Ge_{1-x}Sn_x$," *Applied Physics Letters*, vol. 99, no. 21, p. 211905, 2011.

[156] F. De Boer, R. Boon, W. Mattens, A. Miedema, and A. Niessen, *Cohesion in Metals: Transition Metal Alloys*. Amsterdam: North-Holland, 1988.

[157] B. Zhang, W. Yu, Q. T. Zhao, G. Mussler, L. Jin, D. Buca, B. Holländer, J. M. Hartmann, M. Zhang, X. Wang, and S. Mantl, "Epitaxial growth of $Ni(Al)Si_{0.7}Ge_{0.3}$ on $Si_{0.7}Ge_{0.3}$/Si(100) by Al interlayer mediated epitaxy," *Applied Physics Letters*, vol. 98, no. 25, p. 252101, 2011.

[158] V. Carron, M. Ribeiro, P. Besson, G. Rolland, J.-M. Hartmann, V. Loup, S. Minoret, L. Clavelier, C. Leroyer, and T. Billon, "Nickel Selective Etching Studies for Self-Aligned Silicide Process in Ge and SiGe-Based Devices," *ECS Transactions*, vol. 3, pp. 643–654, June 2006.

[159] Y. Liu, H. Wang, J. Yan, and G. Han, "Reduction of Formation Temperature of Nickel Mono-Stanogermanide [Ni(GeSn)] by the Incorporation of Tin," *ECS Solid State Letters*, vol. 3, pp. P11–P13, Dec. 2013.

[160] T. Nishimura, O. Nakatsuka, Y. Shimura, S. Takeuchi, B. Vincent, A. Vantomme, J. Dekoster, M. Caymax, R. Loo, and S. Zaima, "Formation of $Ni(Ge_{1-x}Sn_x)$ layers with solid-phase reaction in $Ni/Ge_{1-x}Sn_x/Ge$ systems," *Solid-State Electronics*, vol. 60, pp. 46–52, June 2011.

[161] L. Liu, L. Jin, L. Knoll, S. Wirths, A. Nichau, D. Buca, G. Mussler, B. Holländer, D. Xu, Z. Feng Di, M. Zhang, Q.-T. Zhao, and S. Mantl, "Ultrathin highly uniform Ni(Al) germanosilicide layer with modulated B8 type $Ni_5(SiGe)_3$ phase formed on strained $Si_{1-x}Ge_x$ layers," *Applied Physics Letters*, vol. 103, no. 23, p. 231909, 2013.

[162] Q. Zhang, N. Wu, T. Osipowicz, L. K. Bera, and C. Zhu, "Formation and Thermal Stability of Nickel Germanide on Germanium Substrate," *Japanese Journal of Applied Physics*, vol. 44, pp. L1389–L1391, Oct. 2005.

[163] D. Jenkins and J. Dow, "Electronic properties of metastable $Ge_xSn_{1-x}$ alloys," *Physical Review B*, vol. 36, pp. 7994–8000, Nov. 1987.

[164] V. D'Costa, C. Cook, A. Birdwell, C. Littler, M. Canonico, S. Zollner, J. Kouvetakis, and J. Menéndez, "Optical critical points of thin-film $Ge_{1-y}Sn_y$ alloys: A comparative $Ge_{1-y}Sn_y/Ge_{1-x}Si_x$ study," *Physical Review B*, vol. 73, no. 12, p. 125207, 2006.

[165] K. Lu Low, Y. Yang, G. Han, W. Fan, and Y.-C. Yeo, "Electronic band structure and effective mass parameters of $Ge_{1-x}Sn_x$ alloys," *Journal of Applied Physics*, vol. 112, no. 10, p. 103715, 2012.

[166] A. A. Tonkikh, C. Eisenschmidt, V. G. Talalaev, N. D. Zakharov, J. Schilling, G. Schmidt, and P. Werner, "Pseudomorphic GeSn/Ge(001) quantum wells: Examining indirect band gap bowing," *Applied Physics Letters*, vol. 103, no. 3, p. 032106, 2013.

[167] B. Dutt, H. Lin, D. S. Sukhdeo, B. M. Vulovic, S. Gupta, D. Nam, K. C. Saraswat, and J. S. Harris Jr., "Theoretical Analysis of GeSn Alloys as a Gain Medium for a Si-Compatible Laser," *IEEE Journal of Selected Topics in Quantum Electronics*, vol. 19, pp. 1502706–1502706, Sept. 2013.

[168] S. Gupta, R. Chen, Y.-C. Huang, Y. Kim, E. Sanchez, J. S. Harris, and K. C. Saraswat, "Highly Selective Dry Etching of Germanium over Germanium-Tin ($Ge_{1-x}Sn_x$): A Novel Route for $Ge_{1-x}Sn_x$ Nanostructure Fabrication.," *Nano Letters*, vol. 13, pp. 3783–90, Aug. 2013.

[169] R. Chen, H. Lin, Y. Huo, C. Hitzman, T. I. Kamins, and J. S. Harris, "Increased photoluminescence of strain-reduced, high-Sn composition $Ge_{1-x}Sn_x$ alloys grown by molecular beam epitaxy," *Applied Physics Letters*, vol. 99, no. 18, p. 181125, 2011.

[170] L. Jiang, C. Xu, J. D. Gallagher, R. Favaro, T. Aoki, J. Menéndez, and J. Kouvetakis, "Development of Light Emitting Group IV Ternary Alloys on Si Platforms for Long Wavelength Optoelectronic Applications," *Chemistry of Materials*, vol. 26, pp. 2522–2531, Apr. 2014.

[171] J. D. Gallagher, C. Xu, L. Jiang, J. Kouvetakis, and J. Menéndez, "Fundamental band gap and direct-indirect crossover in $Ge_{1-x-y}Si_xSn_y$ alloys," *Applied Physics Letters*, vol. 103, no. 20, p. 202104, 2013.

[172] S. Wirths, R. Geiger, N. von den Driesch, G. Mussler, T. Stoica, S. Mantl, Z. Ikonic, M. Luysberg, S. Chiussi, J. Hartmann, H. Sigg, J. Faist, D. Buca, and D. Grützmacher, "Lasing in direct bandgap GeSn alloy grown on Si(001)," *Nature Photonics*, vol. 9, pp. 88–92, Jan. 2015.

[173] L. Pavesi and M. Guzzi, "Photoluminescence of $Al_xGa_{1-x}As$ alloys," *Journal of Applied Physics*, vol. 75, no. 10, pp. 4779–4842, 1994.

[174] L. Pavesi, "Silicon-Based Light Sources for Silicon Integrated Circuits," *Advances in Optical Technologies*, vol. 2008, pp. 1–12, 2008.

[175] M. Fujii, M. Yoshida, Y. Kanzawa, S. Hayashi, and K. Yamamoto, "1.54 $\mu$m photoluminescence of $Er^{3+}$ doped into $SiO_2$ films containing Si nanocrystals: Evidence for energy transfer from Si nanocrystals to $Er^{3+}$," *Applied Physics Letters*, vol. 71, no. 9, p. 1198, 1997.

[176] W. L. Wilson, P. F. Szajowski, and L. E. Brus, "Quantum confinement in size-selected, surface-oxidized silicon nanocrystals.," *Science (New York, N.Y.)*, vol. 262, pp. 1242–4, Nov. 1993.

[177] L. Pavesi, L. Dal Negro, C. Mazzoleni, G. Franzò, and F. Priolo, "Optical gain in silicon nanocrystals.," *Nature*, vol. 408, pp. 440–4, Nov. 2000.

[178] F. Iacona, A. Irrera, G. Franz, D. Pacifici, I. Crupi, M. Miritello, C. D. Presti, and F. Priolo, "Silicon-Based Light-Emitting Devices: Properties and Applications of Crystalline, Amorphous and Er-Doped Nanoclusters," *IEEE Journal of Selected Topics in Quantum Electronics*, vol. 12, pp. 1596–1606, Nov. 2006.

[179] B. Zheng, J. Michel, F. Y. G. Ren, L. C. Kimerling, D. C. Jacobson, and J. M. Poate, "Room-temperature sharp line electroluminescence at $\lambda$=1.54 $\mu$m from an erbium-doped, silicon light-emitting diode," *Applied Physics Letters*, vol. 64, no. 21, p. 2842, 1994.

[180] O. Jambois, F. Gourbilleau, A. J. Kenyon, J. Montserrat, R. Rizk, and B. Garrido, "Towards population inversion of electrically pumped Er ions sensitized by Si nanoclusters.," *Optics Express*, vol. 18, pp. 2230–5, Feb. 2010.

[181] U. Gösele and V. Lehmann, "Light-emitting porous silicon," *Materials Chemistry and Physics*, vol. 40, pp. 253–259, May 1995.

[182] L. T. Canham, "Silicon quantum wire array fabrication by electrochemical and chemical dissolution of wafers," *Applied Physics Letters*, vol. 57, no. 10, p. 1046, 1990.

[183] A. G. Cullis and L. T. Canham, "Visible light emission due to quantum size effects in highly porous crystalline silicon," *Nature*, vol. 353, pp. 335–338, Sept. 1991.

[184] K. D. Hirschman, L. Tsybeskov, S. P. Duttagupta, and P. M. Fauchet, "Silicon-based visible light-emitting devices integrated into microelectronic circuits," *Nature*, vol. 384, pp. 338–341, Nov. 1996.

[185] Z. H. Lu, D. J. Lockwood, and J.-M. Baribeau, "Quantum confinement and light emission in $SiO_2$/Si superlattices," *Nature*, vol. 378, pp. 258–260, Nov. 1995.

[186] O. Boyraz and B. Jalali, "Demonstration of a silicon Raman laser.," *Optics Express*, vol. 12, pp. 5269–73, Oct. 2004.

[187] H. Rong, A. Liu, R. Jones, O. Cohen, D. Hak, R. Nicolaescu, A. Fang, and M. Paniccia, "An all-silicon Raman laser.," *Nature*, vol. 433, pp. 292–4, Jan. 2005.

[188] O. Boyraz and B. Jalali, "Demonstration of directly modulated silicon Raman laser.," *Optics Express*, vol. 13, pp. 796–800, Feb. 2005.

[189] H. Rong, R. Jones, A. Liu, O. Cohen, D. Hak, A. Fang, and M. Paniccia, "A continuous-wave Raman silicon laser.," *Nature*, vol. 433, pp. 725–8, Feb. 2005.

[190] M. J. Süess, R. Geiger, R. A. Minamisawa, G. Schiefler, J. Frigerio, D. Chrastina, G. Isella, R. Spolenak, J. Faist, and H. Sigg, "Analysis of enhanced light emission from highly strained germanium microbridges," *Nature Photonics*, vol. 7, pp. 466–472, Apr. 2013.

[191] D. S. Sukhdeo, D. Nam, J.-H. Kang, M. L. Brongersma, and K. C. Saraswat, "Direct bandgap germanium-on-silicon inferred from 5.7 % $\langle 100 \rangle$ uniaxial tensile strain," *Photonics Research*, vol. 2, p. A8, Apr. 2014.

[192] J. R. Jain, A. Hryciw, T. M. Baer, D. A. B. Miller, M. L. Brongersma, and R. T. Howe, "A micromachining-based technology for enhancing germanium light emission via tensile strain," *Nature Photonics*, vol. 6, pp. 398–405, May 2012.

[193] G. Capellini, G. Kozlowski, Y. Yamamoto, M. Lisker, C. Wenger, G. Niu, P. Zaumseil, B. Tillack, A. Ghrib, M. de Kersauson, M. El Kurdi, P. Boucaud, and T. Schroeder, "Strain analysis in SiN/Ge microstructures obtained via Si-complementary metal oxide semiconductor compatible approach," *Journal of Applied Physics*, vol. 113, no. 1, p. 013513, 2013.

[194] D. Nam, D. Sukhdeo, S.-L. Cheng, A. Roy, K. Chih-Yao Huang, M. Brongersma, Y. Nishi, and K. Saraswat, "Electroluminescence from strained germanium membranes and implications for an efficient Si-compatible laser," *Applied Physics Letters*, vol. 100, no. 13, p. 131112, 2012.

[195] J. R. Sánchez-Pérez, C. Boztug, F. Chen, F. F. Sudradjat, D. M. Paskiewicz, R. B. Jacobson, M. G. Lagally, and R. Paiella, "Direct-bandgap light-emitting germanium in tensilely strained nanomembranes.," *Proceedings of the National Academy of Sciences of the United States of America*, vol. 108, pp. 18893–8, Nov. 2011.

[196] J. Liu, X. Sun, D. Pan, X. Wang, L. C. Kimerling, T. L. Koch, and J. Michel, "Tensile-strained, n-type Ge as a gain medium for monolithic laser integration on Si.," *Optics Express*, vol. 15, pp. 11272–7, Sept. 2007.

[197] J. Liu, X. Sun, R. Camacho-Aguilera, L. C. Kimerling, and J. Michel, "Ge-on-Si laser operating at room temperature.," *Optics Letters*, vol. 35, pp. 679–81, Mar. 2010.

[198] R. E. Camacho-Aguilera, Y. Cai, N. Patel, J. T. Bessette, M. Romagnoli, L. C. Kimerling, and J. Michel, "An electrically pumped germanium laser.," *Optics Express*, vol. 20, pp. 11316–20, May 2012.

[199] L. Carroll, P. Friedli, S. Neuenschwander, H. Sigg, S. Cecchi, F. Isa, D. Chrastina, G. Isella, Y. Fedoryshyn, and J. Faist, "Direct-Gap Gain and Optical Absorption in Germanium Correlated to the Density of Photoexcited Carriers, Doping, and Strain," *Physical Review Letters*, vol. 109, p. 057402, Aug. 2012.

[200] R. Geiger, J. Frigerio, M. J. Süess, D. Chrastina, G. Isella, R. Spolenak, J. Faist, and H. Sigg, "Excess carrier lifetimes in Ge layers on Si," *Applied Physics Letters*, vol. 104, p. 062106, Feb. 2014.

[201] M. Schmid, M. Oehme, M. Gollhofer, R. Körner, M. Kaschel, E. Kasper, and J. Schulze, "Effect of heavy doping and strain on the electroluminescence of Ge-on-Si light emitting diodes," *Thin Solid Films*, vol. 557, pp. 351–354, Apr. 2014.

[202] E. Schubert, *Light-Emitting Diodes*. Cambridge University Press, 2nd ed., 2006.

[203] H. Bebb, "Photoluminescence I: Theory," in *Semiconductors and Semimetals, Vol. 8* (R. Willardson and A. Beer, eds.), ch. 4, pp. 181–320, New York: Academic, 1972.

[204] W. Shockley and W. Read, "Statistics of the Recombinations of Holes and Electrons," *Physical Review*, vol. 87, pp. 835–842, Sept. 1952.

[205] R. Hall, "Electron-Hole Recombination in Germanium," *Physical Review*, vol. 87, pp. 387–387, July 1952.

[206] T. Bahder, "Erratum: Eight-band k·p model of strained zinc-blende crystals [Phys. Rev. B 41, 11 992 (1990)]," *Physical Review B*, vol. 46, pp. 9913–9913, Oct. 1992.

[207] Y. Varshni, "Temperature dependence of the energy gap in semiconductors," *Physica*, vol. 34, pp. 149–154, Jan. 1967.

[208] M. E. Levinshtein, S. L. Rumyantsev, and M. Shur, *Handbook Series on Semiconductor Parameters: Si, Ge, C (Diamond), GaAs, GaP, GaSb, InAs, InP, InSb*. Handbook Series on Semiconductor Parameters, World Scientific, 1996.

[209] W.-J. Yin, X.-G. Gong, and S.-H. Wei, "Origin of the unusually large band-gap bowing and the breakdown of the band-edge distribution rule in the $Sn_xGe_{1-x}$ alloys," *Physical Review B*, vol. 78, p. 161203, Oct. 2008.

[210] M. R. Bauer, J. Tolle, C. Bungay, A. V. Chizmeshya, D. J. Smith, J. Menéndez, and J. Kouvetakis, "Tunable band structure in diamond-cubic tin-germanium alloys grown on silicon substrates," *Solid State Communications*, vol. 127, pp. 355–359, July 2003.

[211] H. Lin, R. Chen, W. Lu, Y. Huo, T. I. Kamins, and J. S. Harris, "Investigation of the direct band gaps in $Ge_{1-x}Sn_x$ alloys with strain control by photoreflectance spectroscopy," *Applied Physics Letters*, vol. 100, no. 10, p. 102109, 2012.

[212] J. Mathews, R. T. Beeler, J. Tolle, C. Xu, R. Roucka, J. Kouvetakis, and J. Menéndez, "Direct-gap photoluminescence with tunable emission wavelength in $Ge_{1-y}Sn_y$ alloys on silicon," *Applied Physics Letters*, vol. 97, no. 22, p. 221912, 2010.

[213] G. Grzybowski, R. T. Beeler, L. Jiang, D. J. Smith, J. Kouvetakis, and J. Menéndez, "Next generation of $Ge_{1-y}Sn_y$ (y = 0.01-0.09) alloys grown on Si(100) via $Ge_3H_8$ and $SnD_4$: Reaction kinetics and tunable emission," *Applied Physics Letters*, vol. 101, no. 7, p. 072105, 2012.

[214] R. Lieten, K. Bustillo, T. Smets, E. Simoen, J. Ager, E. Haller, and J.-P. Locquet, "Photoluminescence of bulk germanium," *Physical Review B*, vol. 86, p. 035204, July 2012.

[215] W. Klingenstein and H. Schweizer, "Direct gap recombination in germanium at high excitation level and low temperature," *Solid-State Electronics*, vol. 21, pp. 1371–1374, Nov. 1978.

[216] C. Xu, L. Jiang, J. Kouvetakis, and J. Menéndez, "Optical properties of $Ge_{1-x-y}Si_xSn_y$ alloys with y > x: Direct bandgaps beyond 1550 nm," *Applied Physics Letters*, vol. 103, no. 7, p. 072111, 2013.

[217] M. G. A. Bernard and G. Duraffourg, "Laser Conditions in Semiconductors," *physica status solidi (b)*, vol. 1, no. 7, pp. 699–703, 1961.

[218] G. Sun, R. A. Soref, and H. H. Cheng, "Design of an electrically pumped SiGeSn/GeSn/SiGeSn double-heterostructure midinfrared laser," *Journal of Applied Physics*, vol. 108, no. 3, p. 033107, 2010.

[219] Y.-H. Zhu, Q. Xu, W.-J. Fan, and J.-W. Wang, "Theoretical gain of strained $GeSn_{0.02}/Ge_{1-x-y'}Si_xSn_{y'}$ quantum well laser," *Journal of Applied Physics*, vol. 107, no. 7, p. 073108, 2010.

[220] B. Dutt, D. S. Sukhdeo, D. Nam, B. M. Vulovic, and K. C. Saraswat, "Roadmap to an Efficient Germanium-on-Silicon Laser: Strain vs. n-Type Doping," *IEEE Photonics Journal*, vol. 4, pp. 2002–2009, Oct. 2012.

[221] S.-W. Chang and S. L. Chuang, "Theory of Optical Gain of Ge-$Si_xGe_ySn_{1-x-y}$ Quantum-Well Lasers," *IEEE Journal of Quantum Electronics*, vol. 43, pp. 249–256, Mar. 2007.

[222] K. Shaklee, R. Nahory, and R. Leheny, "Optical gain in semiconductors," *Journal of Luminescence*, vol. 7, pp. 284–309, Jan. 1973.

[223] K. Shaklee, R. Leheny, and R. Nahory, "Stimulated Emission from the Excitonic Molecules in CuCl," *Physical Review Letters*, vol. 26, pp. 888–891, Apr. 1971.

[224] K. L. Shaklee, "Direct Determination of Optical Gain in Semiconductor Crystals," *Applied Physics Letters*, vol. 18, no. 11, p. 475, 1971.

[225] L. Negro, P. Bettotti, M. Cazzanelli, D. Pacifici, and L. Pavesi, "Applicability conditions and experimental analysis of the variable stripe length method for gain measurements," *Optics Communications*, vol. 229, pp. 337–348, Jan. 2004.

[226] S. G. Cloutier, P. A. Kossyrev, and J. Xu, "Optical gain and stimulated emission in periodic nanopatterned crystalline silicon.," *Nature Materials*, vol. 4, pp. 887–91, Dec. 2005.

[227] J. Liu, X. Sun, L. C. Kimerling, and J. Michel, "Direct-gap optical gain of Ge on Si at room temperature.," *Optics Letters*, vol. 34, pp. 1738–40, June 2009.

[228] M. de Kersauson, M. El Kurdi, S. David, X. Checoury, G. Fishman, S. Sauvage, R. Jakomin, G. Beaudoin, I. Sagnes, and P. Boucaud, "Optical gain in single tensile-strained germanium photonic wire," *Optics Express*, vol. 19, pp. 17925–34, Sept. 2011.

[229] I. D. W. Samuel, E. B. Namdas, and G. A. Turnbull, "How to recognize lasing," *Nature Photonics*, vol. 3, pp. 546–549, Oct. 2009.

[230] U. T. Schwarz, M. Pindl, E. Sturm, M. Furitsch, A. Leber, S. Miller, A. Lell, and V. Härle, "Influence of ridge geometry on lateral mode stability of (Al,In)GaN laser diodes," *physica status solidi (a)*, vol. 202, pp. 261–270, Jan. 2005.

[231] U. T. Schwarz and B. Witzigmann, "Optical properties of edge-emitting lasers: measurement and simulation," in *Nitride Semiconductor Devices* (J. Piprek, ed.), Wiley-VCH, 2007.

[232] S. L. Chuang, *Physics of Photonic Devices*. Wiley Series in Pure and Applied Optics, John Wiley & Sons, 2009.

[233] S. Cho, R. Chen, S. Koo, G. Shambat, H. Lin, N. Park, J. Vuckovic, T. I. Kamins, B.-G. Park, and J. S. Harris, "Fabrication and Analysis of Epitaxially Grown $Ge_{1-x}Sn_x$ Microdisk Resonator With 20-nm Free-Spectral Range," *IEEE Photonics Technology Letters*, vol. 23, pp. 1535–1537, Oct. 2011.

# Acknowledgments

I would like to thank all the people, who helped and supported me throughout the entire process of this thesis. I am deeply grateful for this time, since on that way I learned a lot about science, gathered new experiences and found new friends.
First of all I would like to thank my doctoral adviser Prof. Siegfried Mantl for offering me a position in his group. He provided outstanding support and gave me the freedom to achieve my goals and scientific results. Special thanks to Prof. Detlev Grützmacher for giving me the opportunity to work in his institute, fruitful discussions and advices as well as inspirational conferences. I would like to thank Prof. Morgenstern for undertaking the Korreferat of this work. I would like to express my deep thanks and appreciation for my daily supervisor Dr. Dan Buca. Thank you Dan for your help writing publications, introducing me to your scientific network, for your advices concerning experiments, your endless support and trust as well as for being a great mentor and friend! I am also very grateful for all the daily help and support provided by the Waldschlösschen crew: Andreas Tiedemann, Patric Bernardy and Karl-Heinz Deussen. Without your great commitment the results for this work could not have been achieved. I would like to thank Dr. Jürgen Schubert, Dr. Bernd Holländer and Dr. Qing-Tai Zhao for their help regarding XRD, RBS, cleanroom processes, fruitful discussions and advices along that journey. Furthermore, I would like to thank Steffi Lenk for her great support as well as for preparing and measuring countless TEM samples for me. Special thanks also to Dr. Gregor Mussler for all his excellent XRD measurements being the foundation for the fast progress in GeSn-based epitaxy. Also thanks to Dr. Toma Stoica and Dr. Uwe Breuer for their help and support regarding PL, Raman spectroscopy and ToF-SIMS analyses. A big thank you to my colleagues in the GeSn-group: Nils von den Driesch, Daniela Stange, Maria-Angela Pampillón, René Troitsch, Christian Schulte-Braucks, Denis Rainko, Markus Hagedorn, Emily Hofmann. It was a great pleasure working with all of you. Thank you to all the members and former colleagues of the group: Brigitte Modolo, Willi Zander, Anna Schäfer, Vinh Luong, Sebastian Blaeser, Linjie Liu, Joachim Wermuth, Thomas Lehndorff, Stefan Glass, Uli Tromm, Felix Krämer, Felix Rothe, Dr. Renato Minamisawa, Dr. Lars Knoll, Dr. Simon Richter, Dr. Matthias Schmidt, Dr. Stefan Habicht, Dr. Sebastian Feste, Dr. Alexander Nichau and Dr. Eylem Durğun Özben. I would also like to thank Dr. Martina Luysberg for her TEM studies. For the technical support concerning the RBS and implantations I would like to thank Andre Dahmen, Christian Scholtysik and Katja Palmen. Thank you to the whole cleanroom team for their help and assistance. Of course, a special thanks to all our external collaborators, especially Dr. Jean-Michel Hartmann for providing excellent Ge virtual substrates and his help during writing publications, Dr. Zoran Ikonic for his band structure and gain calculations, Dr. Stefano Chiussi, Prof. Oussama Moutanabbir and Prof. Jeremy Witzens. I would like to specially mention Dr. Hans Sigg and Richard Geiger, who introduced me to spectroscopy and provided extraordinary help

and support concerning inter alia experiments, data analysis and writing papers. Thank you Hans and Richard, it was a great and unforgettable time working and spending time with you at PSI; I really enjoyed it and I am very grateful for that.
Of course without the support and encouragement of my family this work would not have been possible, thank you. I would like to express my deepest thanks to Verena. Thank you so much for your love, patience and your endless belief in me!

# Publications

- S. Wirths, R. Geiger, N. von den Driesch, G. Mussler, T. Stoica, S. Mantl, Z. Ikonic, M. Luysberg, S. Chiussi, J. Hartmann, H. Sigg, J. Faist, D. Buca, and D. Grützmacher, "Lasing in direct-bandgap GeSn alloy grown on Si", *Nature Photonics* **9**, 88-92 (2015).

- S. Wirths, D. Stange, M.A. Pampillon, A.T. Tiedemann, G. Mussler, A. Fox, U. Breuer, B. Baert, E. San Andres, N.D. Nguyen, J.-M. Hartmann, Z. Ikonic, S. Mantl, and D. Buca, "High-k gate stacks on low bandgap tensile strained Ge and GeSn alloys for Field Effect Transistors", *ACS Applied Materials & Interfaces* **7**, 62-67 (2015).

- S. Wirths, R. Troitsch, G. Mussler, J.M. Hartmann, P. Zaumseil, T. Schroeder, S. Mantl, and D. Buca, "Ternary and Quaternary Ni(Si)Ge(Sn) Contact Formation for Highly Strained Ge p- and n-MOSFETs", *Semiconductor Science and Technology* **30**, 055003 (2015).

- N. von den Driesch, D. Stange, S. Wirths, G. Mussler, B. Holländer, Z. Ikonic, J. M. Hartmann, T. Stoica, S. Mantl, D. Grützmacher, and D. Buca, "Direct Bandgap Group IV Epitaxy on Si for Laser Applications", *Chemistry of Materials*, in press (doi: 10.1021/acs.chemmater.5b01327).

- L. Di Gaspare, D. Sabbagh, M. De Seta, A. Sodo, S. Wirths, D. Buca, P. Zaumseil, T. Schroeder, and G. Capellini, "Epi-cleaning of Ge/GeSn heterostructures", *Journal of Applied Physics* **117**, 045306 (2015).

- L. Liu, L. Knoll, S. Wirths, D. Xu, G. Mussler, U. Breuer, B. Holländer, Z. Di, M. Zhang, S. Mantl, and Q-T. Zhao, "Homogeneous $NiSi_{1-x}Ge_x$ layer formation on strained SiGe with ultrathin Ni layers", *Microelectronic Engineering* **139**, 26-30 (2015).

- L. Liu, L. Jin, L. Knoll, S. Wirths, D. Buca, G. Mussler, B. Holländer, D. Xu, Z. F. Di, M. Zhang, S. Mantl, and Q-T. Zhao, "Ultrathin homogeneous Ni(Al) germanosilicide layer formation on strained SiGe with Al/Ni multi-layers", *Microelectronic Engineering* **137**, 88-91 (2015).

- L. Knoll, S. Richter, A. Nichau, S. Trellenkamp, A. Schäfer, S. Wirths, S. Blaeser, D. Buca, K.K. Bourdelle, Q.-T. Zhao, and S. Mantl, "Strained silicon based complementary tunnel-FETs: Steep slope switches for energy efficient electronics", *Solid-State Electronics* **98**, 32-37 (2014).

- S. Stefanov, C. Serra, A. Benedetti, J.C. Conde, J. Werner, M. Oehme, J. Schulze, S. Wirths, D. Buca, and S. Chiussi, "Structure and composition of Silicon-Germanium-Tin microstructures obtained through Mask Projection assisted Pulsed Laser Induced Epitaxy", *Microelectronic Engineering* **125**, 18-21 (2014).

- S. Wirths, D. Buca, Z. Ikonic, P. Harrison, A.T. Tiedemann, B. Holländer, T. Stoica, G. Mussler, U. Breuer, J.M. Hartmann, D. Grützmacher, and S. Mantl, "SiGeSn growth studies using reduced pressure chemical vapor deposition towards optoelectronic applications", *Thin Solid Films* **557**, 183-187 (2014).

- K. Weis, S. Wirths, A. Winden, K. Sladek, H. Hardtdegen, H. Lüth, D. Grützmacher, and T. Schäpers, "Quantum dots in InAs nanowires induced by surface potential fluctuations", *Nanotechnology* **25**, 135203 (2014).

- S. Wirths, Z. Ikonic, N. von den Driesch, G. Mussler, U. Breuer, A. T. Tiedemann, P. Bernardy, B. Holländer, T. Stoica, J.-M. Hartmann, D. Grützmacher, S. Mantl, and D. Buca, "Growth studies of doped SiGeSn/strained Ge(Sn) heterostructures", *ECS Transactions* **64**, 689-696 (2014).

- S. Wirths, R. Troitsch, G. Mussler, P. Zaumseil, J.-M. Hartmann, T. Schroeder, S. Mantl, and D. Buca, "Ni(SiGeSn) Metal Contact Formation on Low Bandgap Strained (Si)Ge(Sn) Semiconductors", *ECS Transactions* **64**, 107-112 (2014).

- J.-H. Fournier-Lupien, D. Chagnon, P. Levesque, A.A. Al Mutairi, S. Wirths, E. Pippel, G. Mussler, J.-M. Hartmann, S. Mantl, D. Buca, and O. Moutanabbir, "In Situ Studies of Germanium-Tin and Silicon-Germanium-Tin Thermal Stability", *ECS Transactions* **64**, 903-911 (2014).

- D. Grützmacher, S. Wirths, T. Rieger, D. Buca, T. Stoica, M.I. Lepsa, Q.T. Zhao, and S. Mantl, "Epitaxy-Based Strain-Engineering Methods for Advanced Devices", *ECS Transactions* **64**, 85-96 (2014).

- S. Wirths, R. Geiger, Z. Ikonic, A.T. Tiedemann, G. Mussler, J.-M. Hartmann, S. Mantl, H. Sigg, D. Grützmacher, and D. Buca, "Epitaxy and photoluminescence studies of high quality GeSn heterostructures with Sn concentrations up to 13 at.%", *11th Int. Conf. Group IV Photonics* (IEEE, 2014), pp. 15-16.

- D. Buca, S. Wirths, D. Stange, A.T. Tiedemann, G. Mussler, Z. Ikonic, S. Chiussi, J.M. Hartmann, D. Grützmacher, and S. Mantl, "Si-Ge-Sn heterostructures: growth and applications", *2014 7th Int. Silicon-Germanium Technol. Device Meet.* (IEEE, 2014), pp. 163-164.

- S. Wirths, M.A. Pampillon, E. San Andres, D. Stange, A.T. Tiedemann, G. Mussler, A. Fox, U. Breuer, J.-M. Hartmann, S. Mantl, and D. Buca, "Growth and interface engineering of highly strained low bandgap group IV semiconductors", *2014 7th Int. Silicon-Germanium Technol. Device Meet.* (IEEE, 2014), pp. 13-14.

- S. Wirths, D. Stange, R. Geiger, Z. Ikonic, T. Stoica, G. Mussler, J.-M. Hartmann, H. Sigg, D. Grützmacher, S. Mantl, and D. Buca, "Strain engineering for direct bandgap GeSn alloys", *11th Int. Conf. Group IV Photonics* (IEEE, 2014), pp. 13-14.

- J.-H. Fournier-Lupien, S. Mukherjee, S. Wirths, E. Pippel, N. Hayazawa, G. Mussler, J.M. Hartmann, P. Desjardins, D. Buca, and O. Moutanabbir, "Strain and composition effects on Raman vibrational modes of silicon-germanium-tin ternary alloys", *Applied Physics Letters* **103**, 263103 (2013).

- L. Liu, L. Jin, L. Knoll, S. Wirths, A. Nichau, D. Buca, G. Mussler, B. Holländer, D. Xu, Z. Feng Di, M. Zhang, Q.-T. Zhao, and S. Mantl, "Ultrathin highly uniform Ni(Al) germanosilicide layer with modulated B8 type $Ni_5(SiGe)_3$ phase formed on strained $Si_{1-x}Ge_x$ layers", *Applied Physics Letters* **103**, 231909 (2013).

- M. Oehme, D. Buca, K. Kostecki, S. Wirths, B. Holländer, E. Kasper, and J. Schulze, "Epitaxial growth of highly compressively strained GeSn alloys up to 12.5 % Sn", *Journal of Crystal Growth* **384**, 71-76 (2013).

- S. Wirths, Z. Ikonic, A.T. Tiedemann, B. Holländer, T. Stoica, G. Mussler, U. Breuer, J.M. Hartmann, A. Benedetti, S. Chiussi, D. Grützmacher, S. Mantl, and D. Buca, "Tensely strained GeSn alloys as optical gain media", *Applied Physics Letters* **103**, 192110 (2013).

- A. Nichau, A. Schäfer, L. Knoll, S. Wirths, T. Schram, L.-Å. Ragnarsson, J. Schubert, P. Bernardy, M. Luysberg, A. Besmehn, U. Breuer, D. Buca, and S. Mantl, "Reduction of silicon dioxide interfacial layer to 4.6 Å EOT by Al remote scavenging in high-k/metal gate stacks on Si", *Microelectronic Engineering* **109**, 109-112 (2013).

- G. V. Luong, S. Wirths, S. Stefanov, B. Holländer, J. Schubert, J.C. Conde, T. Stoica, U. Breuer, S. Chiussi, M. Goryll, D. Buca, and S. Mantl, "Study of dopant activation in biaxially compressively strained SiGe layers using excimer laser annealing", *Journal of Applied Physics* **113**, 204902 (2013).

- S. Wirths, A.T. Tiedemann, Z. Ikonic, P. Harrison, B. Holländer, T. Stoica, G. Mussler, M. Myronov, J.M. Hartmann, D. Grützmacher, D. Buca, and S. Mantl, "Band engineering and growth of tensile strained Ge/(Si)GeSn heterostructures for tunnel field effect transistors", *Applied Physics Letters* **102**, 192103 (2013).

- S. Wirths, D. Buca, A.T. Tiedemann, P. Bernardy, B. Holländer, T. Stoica, G. Mussler, U. Breuer, and S. Mantl, "Low temperature RPCVD epitaxial growth of $Si_{1-x}Ge_x$ using $Si_2H_6$ and $Ge_2H_6$", *Solid-State Electronics* **83**, 2-9 (2013).

- S. Wirths, D. Buca, G. Mussler, A.T. Tiedemann, B. Holländer, P. Bernardy, T. Stoica, D. Grützmacher, and S. Mantl, "Reduced Pressure CVD Growth of Ge and $Ge_{1-x}Sn_x$ Alloys", *ECS Journal of Solid State Science and Technology* **2**, N99-N102 (2013).

- S. Wirths, D. Buca, A.T. Tiedemann, B. Holländer, P. Bernardy, T. Stoica, D. Grützmacher, and S. Mantl, "Epitaxial Growth of $Ge_{1-x}Sn_x$ by Reduced Pressure CVD Using $SnCl_4$ and $Ge_2H_6$", *ECS Transactions* **50**, 885-893 (2012).

- Q.T. Zhao, L. Knoll, S. Richter, M. Schmidt, S. Blaeser, G. V. Luong, S. Wirths, A. Nichau, A. Schäfer, S. Trellenkamp, J.-M. Hartmann, K.K. Bourdelle, D. Buca, and S. Mantl, "Strained Si nanowire tunnel FETs and inverters", *2013 Third Berkeley Symp. Energy Effic. Electron. Syst.* (IEEE, 2013), pp. 1-2.

- S. Mantl, L. Knoll, M. Schmidt, S. Richter, A. Nichau, S. Trellenkamp, A. Schäfer, S. Wirths, S. Blaeser, D. Buca, and Q.T. Zhao, "Si based tunnel field effect transistors: recent achievements", *2013 14th Int. Conf. Ultimate Integration on Silicon* (IEEE, 2013), pp. 15-20.

- S. Mantl, L. Knoll, S. Richter, M. Schmidt, S. Wirths, A. Nichau, A. Schäfer, S. Blaeser, S. Trellenkamp, J.-M. Hartmann, K.K. Bourdelle, D. Buca, and Q.T. Zhao, "Si based tunneling field effect transistors and inverters", *71st Device Research Conf.* (IEEE, 2013), pp. 193-194.

- S. Wirths, D. Buca, A.T. Tiedemann, P. Bernardy, B. Holländer, T. Stoica, G. Mussler, U. Breuer, and S. Mantl, "Low temperature RPCVD epitaxial growth of $Si_{1-x}Ge_x$ and Ge using $Si_2H_6$ and $Ge_2H_6$", *2012 Int. Silicon-Germanium Technol. Device Meet.* (IEEE, 2012), pp. 1-2.

- S. Wirths, M. Mikulics, P. Heintzmann, A. Winden, K. Weis, C. Volk, K. Sladek, N. Demarina, H. Hardtdegen, D. Grützmacher, and T. Schäpers, "Preparation of ohmic contacts to GaAs/AlGaAs-core/shell-nanowires", *Applied Physics Letters* **100**, 042103 (2012).

- K. Sladek, A. Winden, S. Wirths, K. Weis, C. Blömers, Ö. Gül, T. Grap, S. Lenk, M. von der Ahe, T.E. Weirich, H. Hardtdegen, M.I. Lepsa, A. Lysov, Z.-A. Li, W. Prost, F.-J. Tegude, H. Lüth, T. Schäpers, and D. Grützmacher, "Comparison of InAs nanowire conductivity: influence of growth method and structure", *Physica Status Solidi (c)* **9**, 230-234 (2012).

- S. Wirths, K. Weis, A. Winden, K. Sladek, C. Volk, S. Alagha, T.E. Weirich, M. von der Ahe, H. Hardtdegen, H. Lüth, N. Demarina, D. Grützmacher, and T. Schäpers, "Effect of Si-doping on InAs nanowire transport and morphology", *Journal of Applied Physics* **110**, 053709 (2011).

Band / Volume 109
**Study on the electroforming and resistive switching behaviour of nickel oxide thin fims for non-volatile memory applications**
R. Weng (2015), xxi, 159 pp
ISBN: 978-3-95806-062-3

Band / Volume 110
**Microswimmers – From Single Particle Motion to Collective Behaviour**
Lecture Notes of the DFG SPP Summer School 2015
edited by G. Gompper, C. Bechinger, S. Herminghaus, R. E. Isele-Holder, U.B. Kaupp, H. Löwen, H. Stark, R. G. Winkler (2015)
ISBN: 978-3-95806-083-8

Band / Volume 111
**Long range order in 3D nanoparticle assemblies**
E. Josten (2015), 238 pp
ISBN: 978-3-95806-087-6

Band / Volume 112
**Silicon nanowire structures for neuronal cell interfacing**
S. Pud (2015), 153 pp
ISBN: 978-3-95806-089-0

Band / Volume 113
**Memristive Phenomena - From Fundamental Physics to Neuromorphic Computing**
Lecture Notes of the 47$^{th}$ IFF Spring School 2016
22 February – 04 March 2016, Jülich, Germany
ed. by R. Waser and M. Wuttig (2016), ca 1000 pp
ISBN: 978-3-95806-091-3

Band / Volume 114
**Single-Cell Analysis of Microbial Production Strains in Microfluidic Bioreactors**
A. M. Grünberger (2015), XIX, 225 pp
ISBN: 978-3-95806-092-0

Band / Volume 115
**Magnetic order and spin dynamics in the extended kagome system $CaBaCo_2Fe_2O_7$**
J. Reim (2015), viii, 144 pp
ISBN: 978-3-95806-097-5

Band / Volume 116
**Structural and electronic investigations on homo- and hetero-organic layers involving CuPc on silver single crystal surfaces**
K. M. Schönauer (2015), x, 148 pp
ISBN: 978-3-95806-112-5

Band / Volume 117
**First-principles investigation of inelastic magnetic excitations in nanostructures deposited on surfaces**
B. J. Schweflinghaus (2016), v, 204 pp
ISBN: 978-3-95806-115-6

Band / Volume 118
**Magnetic, structural, and electronic properties of $NiFe_2O_4$ ultrathin films**
M. Hoppe (2016), vii, 118 pp
ISBN: 978-3-95806-122-4

Band / Volume 119
**First-principle investigation of displacive response in complex solids**
D. A. Klüppelberg (2016), xi, 179 pp
ISBN: 978-395806-123-1

Band / Volume 120
**Beam Cooling at COSY and HESR** - Theory and Simulation -
Part 1 Theory
H. Stockhorst, T. Katayama and R. Maier (2016), v, 192 pp
ISBN: 978-3-95806-127-9

Band / Volume 121
**Scanning tunneling microscopy of single-molecule magnets and hybrid-molecular magnets: Two approaches to molecular spintronics**
V. Heß (2016), x, 127 pp
ISBN: 978-3-95806-128-6

Band / Volume 122
**Bulk and surface sensitive energy-filtered photoemission microscopy using synchrotron radiation for the study of resistive switching memories**
M. C. Patt (2016), viii, 247 pp
ISBN: 978-3-95806-130-9

Band / Volume 123
**Group IV Epitaxy for Advanced Nano- and Optoelectronic Applications**
S. Wirths (2016), vi, 116, XXX pp
ISBN: 978-3-95806-132-3

Schlüsseltechnologien /
Key Technologies
Band / Volume 123
ISBN 978-3-95806-132-3